Background discrimination of EDELWEISS-III cryogenic Ge-detectors for dark matter search

Zur Erlangung des akademischen Grades eines
DOKTORS DER NATURWISSENSCHAFTEN
von der Fakultät für Physik
des Karlsruher Instituts für Technologie

genehmigte

DISSERTATION

von

Dipl.-Phys. Benjamin Ernst Ludwig Schmidt

aus Freiburg im Breisgau

Tag der mündlichen Prüfung: 24.04.2015

Referent: Prof. Dr. Johannes Blümer, IKP
Korreferent: Prof. Dr. Wim de Boer, EKP

I declare that I have developed and written the enclosed thesis completely by myself, and have not used sources or means without declaration in the text.

Karlsruhe, 16.03.2015

. . . .
Benjamin Schmidt

Contents

Abstract

Dark matter searches together with neutrino oscillation experiments, neutrinoless double β decay searches and proton decay experiments are leading the non accelerator based effort to discover and illuminate the nature of particle physics beyond the standard model.

First direct dark matter search experiments in the 1980's used simple setups with a single ionization Ge detector and passive shielding [1] trying to detect the scattering of a dark matter particle with the target. This thesis is set in the framework of the generation of experiments that employ 10's or 100's of kg of target material in large detector arrays or with liquid spherical and cylindrical target volumes. In practice, the EDELWEISS-III experiment [2] is currently taking data with 36 800 g Ge detectors installed in a cryostat in the underground laboratory of Modane. For each event, the information on 10 different channels (8 ionization, 2 phonon) is saved by the data acquisition system. For the next generation of cryogenic dark matter search experiments, arrays with 100's of detectors are foreseen. This scaling motivated the realization of a data processing in a scalable, multi-user framework, with automated tracking of processing information and meta data on a dedicated CouchDB database [3]. The KData framework has been finalized with improved ionization signal processing and the verification of the processing, within this thesis. This builds the basis for the main project of this thesis, the analysis of the surface event background and EDELWEISS-III FID detector discrimination capabilities.

For the processing of EDELWEISS-III data, several new pulse processing algorithms were implemented along with calibration and analysis routines. The results were evaluated over a three month commissioning dataset in 2013/2014 and compared with an existing processing of the Lyon analysis group. The comparison and subsequent analysis of the rejection performance of the EDELWEISS-III FID detectors has been restricted to the data with relevant operating conditions at 8 V bias: 12 days of γ calibration data and 5 days of dark matter (WIMP) search data.

Within this work, a perfect statistical consistency of the evaluated γ background data compared to the existing processing was observed, and an overall improvement on the individual baseline resolution of the ionization channels of 22% down to 920 eV was achieved. The total ionization resolution was improved by 9.7%, the bulk ionization and heat resolutions were compatible in both processings. Further technical modifications of the processing that can lead to a similar improvement on the bulk ionization are easily feasible, and several ideas are given in this thesis. Such an improvement could boost the sensitivity to the WIMP-nucleon spin independent scattering cross-section by up to a factor 10 for WIMPs with masses below $10\,\mathrm{GeV/c^2}$. The improved processing within KData was used for a first physics analysis of the FID detector discrimination capabilities in EDELWEISS-III and an earlier version of the software has been used in the analysis of muon-induced events in EDELWEISS-II [4]. During this thesis the analysis of muon-induced events was completed extracting a detector response model and interfacing the model with a preexisting Geant4 simulation [5, 6], leading to a muon flux[1] of $\Phi_\mu = 5.4 \pm 0.2(\mathrm{stat})^{+0.5}_{-0.9}(\mathrm{syst.})\,\mu/\mathrm{m^2/d}$ [7].

---

[1]through a horizontal plane

Taking the data from this commissioning run alone, a first γ discrimination measurement in the full EDELWEISS-III setup with 27% lower threshold (11 keV) than in the EDELWEISS-II setup could be performed. The discrimination was evaluated to a remaining misidentified signal contribution R of

$$R_\gamma^{11\,\text{keV}} < 2.0 \cdot 10^{-5} \quad (90\%\,\text{C.L.}). \tag{0.1}$$

per γ event. A combination of the results with previous measurements improves the previous limit by 22% to a rejection of

$$R_\gamma^{15\,\text{keV}} < 4.4 \cdot 10^{-6} \quad (90\%\,\text{C.L.}), \tag{0.2}$$

above 15 keV threshold energy.

The main physics case of this thesis is the determination of the EDELWEISS-III FID detector rejection performance for surface events. The analyzed commissioning run features the only dataset for the analysis of surface event background in FID detectors in the full EDELWEISS-III setup. The detailed understanding of this event population or the complete rejection is crucial for the analysis of dark matter search experiments. WIMP signal claims in both the CRESST and CoGeNT experiments seem to rely heavily on the understanding of surface event populations [8, 9, 10]. In this thesis, the surface event rejection has been measured experimentally with a ^{210}Pb source implanted on copper tape glued to the detector holders of a single detector. With the improved resolutions in the EDELWEISS-III setup, a rejection down to an analysis threshold of 10.5 keV could be demonstrated, leading to a limit of the ratio of misidentified surface background of

$$R_\text{surface}^{10.5\,\text{keV}} < 1.5 \cdot 10^{-4} \quad (90\%\,\text{C.L.}) \tag{0.3}$$

for all relevant background events (α, β, Pb-recoils). The specific analysis features an efficiency which reaches a value of 50% at an ionization energy of 4.6 keV. For charge-quenched nuclear recoils this translates to a 50% efficiency at 15 keV recoil energy. The efficiency loss at small energies is solely dominated by the resolution achieved on the 100 kHz ionization channels and can certainly be improved for dedicated low WIMP mass analyses. Accounting for the efficiency loss and adding statistics from earlier data in EDELWEISS-II, an overall rejection performance for FID detectors of

$$R_\text{surface}^{15\,\text{keV}} < 3.4 \cdot 10^{-5} \quad (90\%\,\text{C.L.}), \tag{0.4}$$

has been validated. This combined rejection is the best measured surface event rejection for cryogenic dark matter search experiments. Specifically, it is 12% better than the discrimination demonstrated with SuperCDMS iZIP detectors[2][11].

With the improved statistics in background discrimination, the envisaged background free data taking of 3000 kg·d in EDELWEISS-III seems well feasible. The projected 30% improvement on the ionization resolution with respect to EDELWEISS-II could be achieved on some of the 12 detectors in this commissioning run. With such resolutions, a minimal spin independent WIMP-nucleon cross-section of $\sigma = 2.4 \cdot 10^{-9}$ pb can be probed at a WIMP mass of $60\,\text{GeV}/c^2$. This envisaged sensitivity can be further improved, especially for lower mass WIMPs, with the anticipated better stability during WIMP data taking, additional improvements on the data processing and including the selection of low noise periods and dedicated detectors with the best resolutions.

---

[2]Note that the SuperCDMS collaboration has a different normalization of the rejection R and the results need to be scaled accordingly.

Zusammenfassung

Die Suche nach Physik jenseits des Standardmodells der Teilchenphysik ist aktuell die größte Herausforderung auf dem Gebiet der Teilchenphysik. Abseits der Hochenergiefront an Teilchenbeschleunigern gibt es einige der wichtigsten Hinweise auf neue Physik aus dem Bereich der Astronomie und Kosmologie sowie aus der Neutrinophysik. Die experimentelle Suche nach dunkler Materie zusammen mit Experimenten zur Suche nach dem neutrinolosen Doppelbetazerfall, nach dem Zerfall des Protons und mit Experimenten zur Untersuchung der Neutrinooszillationen sind einige der vielversprechendsten Möglichkeiten, um weitere Hinweise auf Physik jenseits des Standardmodells der Teilchenphysik zu erhalten.

Erste Experimente zur direkten Detektion des Energieeintrags der Streuung eines dunkle Materie Teilchens wurden bereits in den 1980er Jahren mit einzelnen Ge-Diodendetektoren und passiven Abschirmungen realisiert [1]. Seither wurden die experimentellen Techniken verfeinert, und aktuelle Experimente nutzen einige dutzend oder hunderte kg an Detektionsmaterial in vielen Modulen oder in flüssigen Targets. Das EDELWEISS-III Experiment, in dessen Rahmen diese Arbeit stattfand, nimmt Daten mit 36 Detektoren mit jeweils 800 g Masse. Für jedes Ereignis in einem Detektor werden die Pulsspuren von 10 Kanälen aufgezeichnet (8 Ionisiation, 2 Phononen). Für die Zukunft sind kryogene Experimente mit hunderten von Detektoren geplant. Diese Skalierung der Exposition und damit der Sensitivität der Experimente geht mit einer Vergrößerung der Komplexität, der Menge an Daten und der Größe der Kollaborationen einher. Dies motivierte die Entwicklung eines neuen Frameworks zur Datenanalyse und Datenverarbeitung in der EDELWEISS Kollaboration, welches modular aufgebaut ist und sich leicht für die Multi-Nutzer Umgebung an verschiedenen Instituten in einem Experiment der nächsten Generation skalieren lässt.

Die Fertigstellung dieses Frameworks mit der Implementierung einer ersten Rohdatenanalysekette mit verbesserter Energieauflösung in den Ionisationskanälen, die Validierung der Rohdatenverarbeitung und eine erste Physikanalyse der Untergrunddiskriminierung der EDELWEISS-III FID Detektoren sind Teil dieser Promotion. Datenmanagement und -verarbeitung werden im KData genannten Framework über eine CouchDB-Datenbank kontrolliert und erlauben einen einfachen Überblick mittels Web-Interface sowie die Automatisierung verschiedener Verarbeitungsschritte. Der Code ist modular aufgebaut, um eine hohe Wiederverwendbarkeit zu erreichen und bietet Schnittstellen zur Nutzung des TESLA Computerclusters am KIT und des Tier2 (LHC) Computerzentrums in Lyon. Eine Beschreibung der grundlegenden Konzepte findet sich in [3].

Für die Datenverarbeitung in EDELWEISS-III wurden mehrere neue Pulsformanalyse- und Rauschunterdrückungsalgorithmen implementiert. Kalibrations- und Analyseroutinen wurden erstellt. Die Datenverarbeitung wurde anhand einer Drei-Monatsperiode an Kommissionsdaten im EDELWEISS-III Setup mit einer in Lyon existierenden Analyse verglichen. Zu diesem Vergleich der Ergebnisse und einer Analyse der Untergrunddiskriminierung wurden nur Daten mit relevanten Betriebsparametern verwendet. Damit standen 12 Tage an γ-Kalibrationsdaten und 5 Tage an Daten zur Suche nach dunkler Materie zur Verfügung.

In einem statistischen Vergleich der gemessenen Rate von γ-Untergrund wurde verifiziert, dass die implementierte Datenverarbeitungslösung kompatible Ergebnisse zu einer bestehenden Analyse liefert und keine technischen Probleme wie Datenverlust vorliegen. Gleichzeitig konnte die Energieauflösung an der Nulllinie der Ionisationskanäle um 22% auf 920 eV verbessert werden. Die Energieauflösung der Summe aller Ionisationskanäle wurde um 9.7% verbessert, und die Auflösung des Energieeintrags in den Wärmekanälen sowie im Ionisationssignal für Ereignisse im Innern der Detektoren ist in beiden Datenverarbeitungslösungen vergleichbar. Weitere technische Verbesserungsmöglichkeiten der Rohdatenverarbeitung werden im Rahmen dieser Arbeit diskutiert. Eine hierdurch zu erwartende Verbesserung der Energieauflösung um 10% für das Ionisationssignal von Ereignissen im Innern der Detektoren sollte die Untergrunddiskriminierung bei Ereignissen geringer Energie deutlich verbessern. So zeigen erste Projektionen eine Steigerung der Sensitivität auf den spinunbahängigen WIMP-Nukleon Streuquerschnitt von bis zu einem Faktor 10 für WIMPs geringer Masse ($m_\chi < 10\,\mathrm{GeV/c^2}$).

Das KData Framework wurde zum ersten Mal im Rahmen einer Koinzidenzstudie zur Indentifizierung Myon-induzierten Untergrundes in EDELWEISS-II angewandt [4]. Diese Studie des Myon-induzierten Untergrundes wurde in dieser Arbeit mit der Kalibration der 46 Plastikszintillatormodule des Myon-Veto-Systems und der Bestimmung der individuellen Moduleffizienzen fortgeführt. Mit Hilfe dieser Daten und einer Geant4 MC-Simulation [5, 6] konnte eine erste Messung des Myon-Flusses

$$\Phi_\mu = 5.4 \pm 0.2(\mathrm{stat})^{+0.5}_{-0.9}(\mathrm{syst.})\,\mu/\mathrm{m^2/d} \qquad (0.5)$$

und eine Extrapolation des Myon-induzierten Untergrundes für EDELWEISS-III durchgeführt werden [7]. Auch für EDELWEISS-III wurde die erfolgreiche Identifizierung Myon-induzierter Ereignisse validiert.

Die verbesserte Energieauflösung wurde genutzt, um die Untergrunddiskriminierung der EDELWEISS FID Detektoren bei niedrigeren Energien als zuvor zu untersuchen. Mit dem vorliegenden Datensatz wurde die Ereignisdiskriminierung für γ-Ereignisse im Kristall ab einer 27% niedrigeren Energieschwelle von 11 keV im Vergleich zu vorherigen Messungen mit FID Detektoren im EDELWEISS-II Setup untersucht. Nach Anwendung aller Kriterien wurde kein Ereignis in der Signalregion beobachtet. Dies entspricht statistisch einer Obergrenze

$$R_\gamma^{11\,\mathrm{keV}} < 2.0 \cdot 10^{-5} \quad (90\%\ \mathrm{C.L.}) \qquad (0.6)$$

der Rate misidentifizierter γ-Untergrundereignisse, die fälschlicherweise als Signal interpretiert werden. Eine statistische Kombination dieser Messung mit vorherigen Ergebnissen erhöht die Gesamtstatistik um 22% zu einer demonstrierten Untergrunddiskriminierung von

$$R_\gamma^{15\,\mathrm{keV}} < 4.4 \cdot 10^{-6} \quad (90\%\ \mathrm{C.L.}) \qquad (0.7)$$

für Ereignisse $E_{\mathrm{Rec}} > 15\,\mathrm{keV}$.

Die Unterdrückung von Untergrund durch oberflächennahe Ereignisse ist eine zentrale Aufgabe bei der Suche nach dunkler Materie. So hat sich in Analysen der CoGeNT und CRESST Daten gezeigt, dass das Verständnis und die Demonstration der Kontrolle dieses Untergrundes von überragender Bedeutung für die Interpretation von Daten zur Suche nach dunkler Materie sind [8, 9, 10]. Die Studie zur Diskriminierung oberflächennaher Ereignisse in dieser Arbeit ist zusätzlich von besonderer Bedeutung, da die untersuchten Daten des commissioning Runs (Oktober 2013 - Januar 2014) die einzigen Daten im vollständigen EDELWEISS-III Setup sind, bei der ein Detektor mit einer ^{210}Pb-Quelle ausgestattet war.

Mit der verbesserten Datenanalyse im vollen EDELWEISS-III Setup konnte die Untergrunddiskriminierung bis zu einer Analyse-Schwelle von $E_{\text{Rec}} = 10.5\,\text{keV}$ untersucht werden. Auch in diesem Datensatz wurde kein misidentifiziertes Ereignis in der Signalregion gefunden und eine Obergrenze von

$$R_{\text{surface}}^{10.5\,\text{keV}} < 1.5 \cdot 10^{-4} \quad (90\%\,\text{C.L.}) \qquad (0.8)$$

an misidentifizierten Ereignissen pro Zerfall von ^{210}Pb zu ^{210}Bi, zu ^{210}Po und schließlich zu ^{206}Pb gesetzt. Die Analyse erreicht eine Signalakzeptanz von 50% bei 4.6 keV Ionisationsenergie, was 15 keV an Energie für eine WIMP-Kernstreuung entspricht. Diese recht geringe Akzeptanz bei niedrigen Rückstoßenergien wird allein durch die Energieauflösung im 100 kHz-Ionisationssignal bestimmt und kann für die Suche nach WIMPs von geringer Masse noch optimiert werden. Eine statistische Kombination der Ergebnisse mit vorherigen Messungen führt zu einer Grenze von

$$R_{\text{surface}}^{15\,\text{keV}} < 3.4 \cdot 10^{-5} \quad (90\%\,\text{C.L.}) \qquad (0.9)$$

für Ereignisse mit $E_{\text{Rec}} > 15\,\text{keV}$. Diese Diskriminierung ist die beste bisher gemessene Unterdrückung von oberflächennahen Ereignissen in einem kryogenen Experiment zur Suche nach dunkler Materie. Insbesondere sind die hier erzielten Ergebnisse um 12% besser als die Ergebnisse der SuperCDMS iZIP Detektoren[3]. Die demonstrierte Diskriminierung ist damit schon jetzt für eine geplante Exposition von $0.3\,\text{t}\cdot\text{Jahre}$ im Rahmen eines gemeinsamen Experiments von EDELWEISS und SuperCDMS in einer kryogenen Infrastruktur im Untergrundlabor SNOLAB ausreichend.

Diese Arbeit zeigt, dass für EDELWEISS-III die verbesserte Untergrundunterdrückung der Detektoren ausreicht um 3000 kg·d an Exposition aufzunehmen. Die zuvor projizierte 30%ige Verbesserung der Auflösung der Ionisationskanäle im Vergleich zu EDELWEISS-II konnte in dieser Arbeit für einige der 12 Detektoren demonstriert werden. Mit dieser Auflösung sollte eine Sensitivität auf den Wechselwirkungsquerschnitt für WIMP-Nukleon-Streuung bis zu $2.4 \cdot 10^{-9}$ pb für WIMPs mit $\text{m}_\chi = 60\,\text{GeV/c}^2$ erreicht werden. Eine Selektion stabiler Perioden mit geringem Rauschen und guter Detektoren, während der EDELWEISS-III WIMP Suche sollte die Sensitivität, speziell für WIMPs geringer Masse, noch deutlich verbessern.

---

[3]Die SuperCDMS Kollaboration verwendet eine unterschiedliche Normierung des Diskriminierungsfaktors R, weshalb Ergebnisse nur nach Skalierung verglichen werden können.

1. The case for dark matter

Where does life come from? What is the Universe made of? Which are the laws that govern its behavior?

These are just some of the questions that have enthralled the interest of philosophers and scientists throughout human history. While some questions might never be answered, we do have a good grasp of others. Today's standard model of particle physics perfectly describes the matter content, the behavior and interactions of fundamental particles, except for very few unsolved mysteries. This chapter is dedicated to the particular mystery of the existence of an additional non luminous matter component, termed dark matter. Although having a 5 times higher density than baryonic matter, this matter component has never been observed directly. The only indication of its existence is its gravitational effect. This effect, however, has been observed on all scales in the universe and is of fundamental importance for the formation of structure.

In this chapter, astrophysical evidence of the existence and nature of dark matter will be reviewed. Specific examples of the evidence for dark matter in galaxies and galaxy clusters will be discussed. The results of the application of such dynamical mass estimates on the local dark matter density will be given. The resulting insights into the nature of dark matter were incorporated into the cosmological standard model, ΛCDM (Λ Cold Dark Matter, a Universe dominated by the cosmological constant Λ and a cold dark matter component), of Big Bang cosmology. In combination with the highest precision measurements of the cosmic microwave background (CMB) from the PLANCK satellite, the most accurate estimate of several parameters including the total amount of dark matter, the allowed baryonic matter component and the neutrino component will be given. Prospects on further constraining dark matter properties like the warm dark matter and cold dark matter scenarios from precision astronomy and simulations will be discussed.

Given the observational evidence for particle dark matter, several possible particle candidates from extensions of the standard model of particle physics will be discussed. Detection possibilities for the well motivated supersymmetric neutralino will be reviewed. We will focus on summarizing the status of direct detection experiments like the EDELWEISS experiment, but also present some of the recent results of indirect dark matter searches. For the direct searches the discussion of obtained results will be split into a section about standard WIMP search results for $O(100\,\mathrm{GeV}/c^2)$ dark matter particles and a section about lower mass dark matter searches. Special focus will be paid on surface event rejection capabilities since it is known that this is an intricate population to be understood, which can easily mimic a possible WIMP signature.

1.1. Dark matter - observational evidence

Observational evidence for dark matter dates back to publications investigating the dynamics of our local neighborhood in the Milky Way in 1922 [12] and that of nearby galaxy clusters in 1933 [13]. These early results showed that a large fraction of the mass in these systems was not observed in stars and visible matter, but had to be present in some other form. While this is an astonishing result in its own, its impact on cosmology and particle physics became apparent only much later.

In fact, up to the detailed investigation of galactic rotation curves by Vera Rubin in 1980 [14], renewing the evidence for additional non-luminous matter, only little progress was made. From that time on, both experimental [1] and astrophysical observations made rapid progress to build our current understanding of dark matter in the universe. The following discussion will not follow the chronological path. Instead, a few selected astrophysical key observations will be explained. Current best parameter estimates in the cosmological standard Big Bang model and the role of high precision astronomy in combination with large scale N-body simulations will be touched.

1.1.1. Dark matter in galaxy clusters

The study of galaxy clusters as representative objects of the universe has had several key impacts on our understanding of dark matter and our understanding of Big Bang cosmology.

Most notably the Coma galaxy cluster was the first large scale object where a significant quantity of missing mass was found [13]. Using the Doppler technique, Fritz Zwicky measured the speed of several of the constituent galaxies and noted their large velocities. Assuming that the Coma galaxy cluster had time to virialize, he could compute the mass of the system from the virial theorem to

$$M = \frac{5R}{6G} \langle v^2 \rangle. \tag{1.1}$$

With average velocities of at least $\sqrt{\langle v^2 \rangle} \geq 1000 \, \text{km/s}$ for individual galaxies and a radius of $10^{24} \, \text{cm}$, he found a mass to light ratio of M/L = 400. One could argue about the assumption that the system reached a stationary state and that the virial theorem holds. A relaxation of this assumption can, however, not alter the result by more than a factor two which demonstrates the significance of the observation.

From further dynamical evidence of galaxy clusters and the evidence from rotation curves of galaxies (sec. 1.1.2) dark matter became later accepted as part of the standard model of cosmology. Assuming a flat universe and calculating the baryon content in terms of a thermal Big Bang expansion model, a baryon content of $\Omega_b = 0.0125h$ was estimated (result from [15]). Ω_b hereby denotes the baryon matter/energy density normalized over the critical density $\rho_{c,0} = \frac{3H_0^2}{8\pi G}$ needed to obtain a flat universe. $h = 0.677 \pm 0.05$ [16] parametrizes the uncertainty of the current-time Hubble constant, $H_0 = h \cdot 100 \, \text{km/s/Mpc}$, and G is the gravitational constant. For a standard introduction to cosmology and further details of Big Bang nucleosynthesis we refer the reader to [17].

With the advent of x-ray satellite measurements (ROSAT ∼1992), the baryon and dark matter fraction of galaxy clusters could be quantified for the first time. Being the largest typical structures of the Universe, the results were directly transferred to the matter content of the Universe and compared to Big Bang cosmology. Using x-ray measurements from the ROSAT satellite [18] of the hydrogen gas inside the Coma galaxy cluster, S. White and collaborators measured the baryon to total mass ratio of such a typical cluster
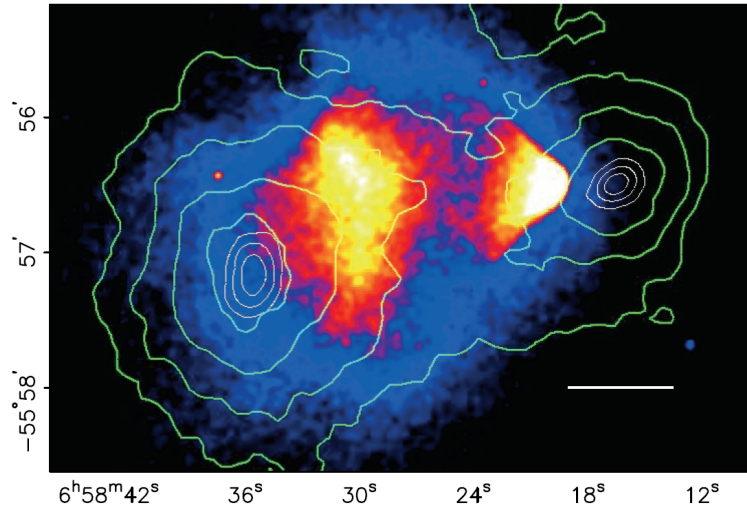
Figure 1.1.: Chandra X-ray image of the Bullet Cluster (1E 0675-558). The white bar indicates a distance of 200 kpc, green contours show weak lensing mass reconstructions (κ reconstruction) and in white the 68.3%, 95.5% and 99.7% confidence level contours for the peak position of the whole gravitational matter are given. The convergence κ is the shape independent increase in the size of a galaxy image. The hot gas (luminous matter) has its maximum density at the red to white spots, well separated from the gravitational centers. Figure from [19].

[15]. The measurements of $M_{gal} = 1.0 \pm 0.2 \cdot 10^{13} h^{-1} M_\odot$, $M_{gas} = 5.45 \pm 0.98 \cdot 10^{13} h^{-5/2} M_\odot$ were compared to a total mass estimate of M_{tot} ranging from $M_{tot} = 6.7 \pm 1.0 \cdot 10^{14} h^{-1} M_\odot$ to $M_{tot} = 1.1 \pm 0.18 \cdot 10^{15} h^{-1} M_\odot$ depending on the model. The resulting baryon fraction $M_b/M_{tot} \geq 0.009 \pm 0.050 h^{-3/2}$ confirms the existence of a dominant contribution of dark matter in the Universe. However, it is in conflict with the baryon fraction estimated from the standard model of cosmology at the time (Big Bang nucleosynthesis) and severely challenged the assumptions of either a flat Universe or a negligible cosmological constant, $\Omega_\Lambda = 0$. The measurements ultimately contributed to the acceptance and introduction of the cosmological constant Λ or dark energy into the current cosmological standard model.

Finally with the advent of the new observational technique of weak gravitational lensing the dark matter component of the Universe could be imaged more directly instead of an inference from the dynamics of astrophysical objects or from the hydrogen gas temperature in x-ray measurements. The investigation of colliding galaxy clusters with a multiwavelength technique using weak gravitational lensing from optical imaging, as well as x-ray techniques, established the model of non baryonic particle dark matter as the standard framework today. In fig. 1.1 an x-ray false color image of the Bullet cluster [19] is shown. Matter density contours from weak lensing have been overlaid in green and 1,2,3 sigma contours for local peak positions of the matter densities were added in white. Astrophysicists believe that the image shows two galaxy clusters about 100 Myr after their collision. Galaxies (not shown) as well as the dominant matter component passed dissipationless through each other. On the other hand, the main baryonic matter component (the hydrogen gas) was shocked, heated and stripped from the gravitational center of the clusters.

Alternative explanations of the dark matter problem in form of scale dependent modified theories of gravity, MOND [20, 21], or in form of a relativistic theory TeVeS [22], do not allow a similarly straight forward explanation. To bring astrophysical observations of different scales (galaxies and galaxy clusters) into agreement they often require large neutrino mass contributions or some kind of sub-dominant dark matter component in clusters.

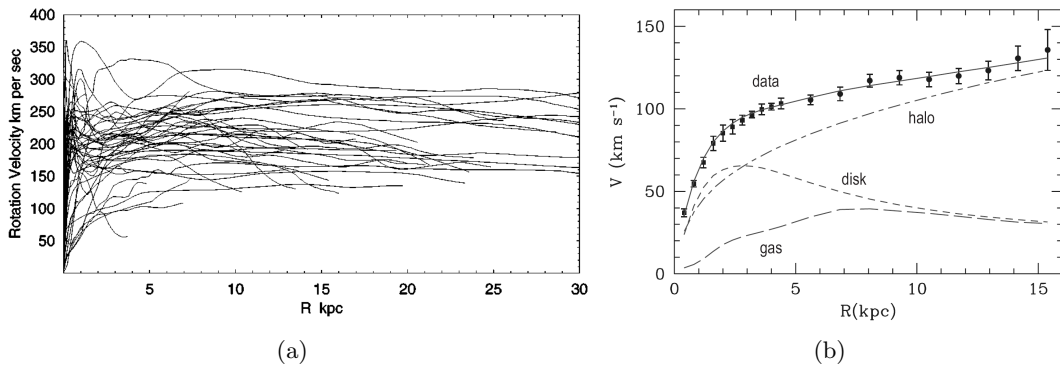(a)   (b)

Figure 1.2.: (a) Rotational velocity versus distance for a collection of galaxies. Figure from [26]. (b) Rotational velocity versus distance for M33 (data points) as well as expected rotational velocities for the individual components from luminous matter in the disk and inside the hydrogen gas. The constant or increasing velocity of the rotation curves can be best explained by an additional dark matter halo. Figure adapted from [27].

We want to note that the Bullet cluster is not the only astrophysical object where colliding galaxy clusters could be imaged in various stages of their collisions. In fact, at least half a dozen well observable colliding galaxy clusters have been collected by the "Merging Cluster Collaboration". Most of these objects can easily fit the particle dark matter hypothesis, while two of them are more difficult to interpret and are under controversial discussion (see [23, 19, 24]). Many of the observations are used to extract additional dark matter properties, e.g. to constrain the self-interaction cross-sections (see for example [25]).

1.1.2. Dark matter in galaxies

A historically important measurement is the analysis of the rotational velocity of galaxies. The measurement and analysis of dozens of individual rotation curves in the 1980's and 1990's proved a dark matter halo as universal feature of all observed galaxies. Given our place in the solar neighborhood of our galaxy, this triggered both an experimental and phenomenological effort in understanding the dark matter profile of galaxies as well as the effort to experimentally detect the local dark matter component [1].

Starting from measurements in the 1980's, Vera Rubin and others sampled dozens of individual rotation curves of different types of galaxies (see for example [14]). Instead of an expected Keplerian fall off of the velocity for objects beyond the radius of the dominant matter component in the disk, a constant rotational velocity or even a slight increase was observed (see fig. 1.2). The required gravitational potential could be deduced from accurate observations and transferred into a dark matter density profile. The dominant technique driving this progress employed the Doppler shifts observed in optical spectroscopy of the hydrogen emission lines of stars and gas. The technique was extended to the central regions of galaxies using the millimeter wavelength of carbon monoxide rotational transition lines that do not suffer from dust extinction, as the optical observations do. See [26] and references therein for details. Using these techniques, a universal rotation curve of spiral galaxies was derived dependent on a single parameter only, the global luminosity of the galaxy. Analyzing a sample of ~ 1100 rotation curves, Persic and Salucci found that the universal rotation curve predicts the radial velocity at radius R with a relative accuracy of the order of 4% for different galaxies ranging over a factor of 150 in luminosity [28]. At the same time, N-body simulations were used to derive the dark matter halo density profile in the framework of the gravitational collapse in the cold dark matter cosmological framework [29]. From such simulations, Navarro, Frenk and White proposed in 1996 the

following dark matter halo density parametrization:

$$\rho(r) = \frac{\rho_{\mathrm{crit}} \cdot \delta_{\mathrm{c}}}{(r/r_s)(1 + r/r_s)^2} \tag{1.2}$$

Herein ρ_{crit} is the critical density needed for a flat universe, $r_s = r_{200}/c$ where r_{200} is the radius where the mass of the galaxy has a characteristic overdensity of 200 times the critical density and c is a dimensionless parameter. $\delta_c = \frac{200}{3} \frac{c^3}{(ln(1+c) - c/(1+c))}$ parametrizes the characteristic overdensity of the halo. The proposed halo profile works well with most observed rotational velocities and is widely used up to date as a standard halo model. It is worthy to note though that the authors already noted a discrepancy between simulation and observed rotational velocities for irregular dwarf galaxies. A second problem was noted concerning the large number of galaxy sized dark matter halos observed in the simulation of a cold dark matter CDM cosmological model with respect to the observations.

Since the 1990's the cosmological standard model changed to include the cosmological constant Λ to explain the accelerated expansion of the Universe observed in supernovae Type-Ia and resolve some of the problems encountered in the CDM framework concerning structure formation in simulation and observation. See also the discussion on galaxy clusters in the previous section.

From the improvements in simulations including the usage of the current cosmological ΛCDM model, several small modifications of the density profile were proposed, leading to slightly different profiles. Many of these profiles are more similar to an existing experimental parametrization from Einasto $\rho(r) \, \alpha \, e^{-Ar^\beta}$ [30]. A review discussing several of the proposed modifications as well as the original parametrization from Einasto is given in [31]. However, for a large part, the differences only concern the central and very far outer regions of the halo.

In spite of the tremendous progress in computing power and experimental observation in the last 20 years, the understanding of the dark matter profile close to the galactic center is still a matter of active debate. Specifically, cored or cusped profiles are still discussed in detail. Also the effect of substructures, e.g. clumpy dark matter is a point of current interest both for galaxy halos and for clusters. See for instance [32] and references therein.

1.1.3. Dark matter in the Milky Way

Evidence for dark matter in our local astronomic neighborhood was found already in 1922 by J.H. Jeans [12]. He analyzed the motion of stars transverse to the galactic plane and concluded that there must be a similar amount of dark stars (dark matter) to explain the large peculiar velocities of stars. Remarkably enough, recent estimates employing the NFW model together with a global fit of the Milky Way's rotation curve [33] and purely local methods relying on much better observations [34] still give similar results today. Dependent on the method, local densities of $\rho(R_\odot) = 0.54 \pm 0.04 \, \mathrm{GeV/cm^3}$ (local estimation RAVE data 2014 [34]) and $\rho(R_\odot) = 0.23 \pm 0.03 \, \mathrm{GeV/cm^3}$ (NFW model with Milky Way's rotation curve 2012 [33]) have been derived. While there is still much variation between individual estimates, large progress is expected from the Gaia satellite mission in the near future. For details about the individual methods and a collection of further estimates I refer the reader to [35].

Some additional information on the nature of dark matter in the Milky Way could be derived from gravitational lensing: As already discussed in sec. 1.1.1 astrophysical observations prefer the particle dark matter hypothesis over modifications of gravity. One of the early candidates discussed within this paradigm were massive compact halo objects (MACHOs), e.g. primordial black holes or for example brown dwarf stars. Using the gravitational lensing effects, two independent searches have analyzed the possible abundance

of these objects within the Milky Way. While a few candidates were observed both by
the MACHO and EROS collaboration, they could not by far account for the entire dark
matter mass. Current limits constrain the contribution of MACHO dark matter to less
than 10% for objects in the range of 10^{-6} to 1 $M_\odot$ at 95% C.L. [36].

1.1.4. Dark matter in the early Universe and in cosmology

The current best quantitative probe of the matter and energy content of our Universe
is the cosmic microwave background (CMB) radiation interpreted in the ΛCDM cosmo-
logical framework. Calculated quantities are thus somewhat model dependent, but all
astrophysical parameter estimates are in good agreement with independent measurements
and add up to a consistent picture within this framework. See for example the particle
data group review on Big Bang cosmology [37]. Within this model, our Universe started
out from a hot dense plasma with particles and radiation in thermal equilibrium. The ob-
servable horizon was then blown up in a rapid expansion phase (Inflation), which explains
the isotropy which we observe today. Due to the expansion, the Universe adiabatically
cooled and after $\sim$380000 years it reached a temperature of $\sim$3000 K at which electrons
and protons could combine to neutral hydrogen (Recombination) and the Universe became
transparent. The thermal photons decoupled at the time and the wavelength was shifted
during the further expansion of the Universe. In 1964, Penzias and Wilson discovered this
uniform background radiation at 2.75 K as irreducible background in their radio telescope
[38]. Since the CMB observation was in fact already predicted in 1948 [39], its experi-
mental discovery and subsequent precise measurement with satellite missions are a corner
stone of the current cosmological ΛCDM model. Penzias and Wilson were awarded the
Nobel Prize for the discovery of the CMB in 1978, and George Smoot received the Nobel
Prize for the search for anisotropies in the CMB with the COBE satellite [40]. Since then,
the WMAP satellite [41] and the currently operating Planck satellite [42] improved on the
precision of the measurements by orders of magnitude and the CMB spectrum is the best
measured black-body spectrum today.

In today's Universe, homogeneity and isotropy are observed only at the largest scales, and
galaxies and galaxy clusters are in fact extremely non-homogeneous objects concerning
the average density of the Universe. Density perturbations that can lead to the observed
inhomogeneity need to be present already in the CMB and were indeed discovered by
the COBE satellite. In our current understanding of cosmology, quantum fluctuations in
the primordial fields are blown up by inflation to form these original density fluctuations.
Dependent on the matter and energy content and dependent on the geometry, e.g. the
flatness of the Universe, the growth of these fluctuations can be very different and hence
also the observable anisotropies in the CMB and in structures today. The most striking
feature expected in a flat ΛCDM model is a rather strong correlation of density and hence
observed temperature in the CMB at an angular scale of $\sim$1°. This scale corresponds
to the largest possible observable standing wave (acoustic horizon) in the baryon/photon
content at the time. Since thermal dark matter will already be decoupled from baryons
and photons at the time of Recombination, this component can drive these oscillations
and be the engine for further structure formation in a gravitational collapse scenario. Any
change from cold dark matter to hot neutrino-like dark matter, or a change in the flatness,
significantly alters the observable spectrum and disagrees both with the observation of
the CMB and with galaxy surveys today. See [17] for a pedagogical introduction into the
different effects that need to be considered analyzing the CMB radiation.

With the latest published measurements (fig. 1.3) of the Planck mission data from 2015
and further external constraints, the Planck collaboration obtained the following results
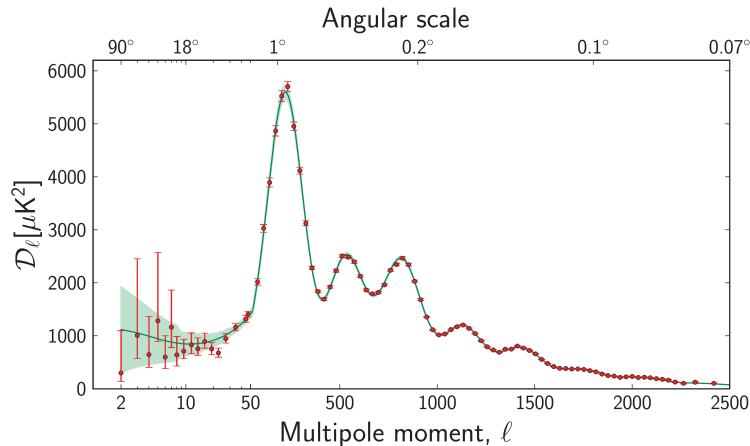
Figure 1.3.: Planck measurement of the CMB two point temperature correlation spectrum shown as an expansion in spherical harmonics. Deviations from the perfect isotropic blackbody are at the level of 10^{-5}. The correlation spectrum allows to extract the acoustic horizon from density fluctuations at the time of recombination. See text for details. Figure from [42].

[16] for the 6 parameters of the ΛCDM model

$$\Theta = (1.04093 \pm 0.0003) \cdot 10^{-2} \tag{1.3}$$

$$\Omega_b h^2 = 0.0223 \pm 0.00014 \tag{1.4}$$

$$\Omega_{cdm} h^2 = 0.1188 \pm 0.0010 \tag{1.5}$$

$$n_s = 0.967 \pm 0.004 \tag{1.6}$$

$$H_0 = 67.7 \pm 0.5 \, \text{km/s/Mpc} \tag{1.7}$$

$$\Omega_m = 0.309 \pm 0.006 \tag{1.8}$$

In their order of appearance the parameters are the angular scale of the sound horizon Θ, the baryon density Ω_b, the cold dark matter density Ω_{cdm}, the scalar spectral index n_s, the Hubble constant H_0 and the matter density Ω_m. The Planck collaboration also evaluated different cosmological models, but none provides a better fit to the data. If the curvature of the Universe is left as free parameter, the measurement of the angular horizon scale limits the curvature at a deviation of 1% with respect to the flat universe.

The matter content of the Universe is made up from baryonic matter in addition to cold and hot dark matter. However, due to its effect of washing out small scale density fluctuations, the effect of hot dark matter can be strongly constrained from the observations. Given the errors on Ω_b and Ω_{cdm}, and the measurement of Ω_m there is only negligible room for a hot dark matter component.

It is possible to use further data from Big Bang Nucleosynthesis and from structure surveys today in order to get a better handle on some degeneracies between parameters. The corresponding measurements are in agreement with the results from CMB data alone, but do not bring additional significant information for this discussion.

1.1.5. Inference of dark matter properties from precision astronomy

To summarize the previously discussed observations, they already pin down some of the dark matter properties. Observations on all scales show dynamical evidence for missing mass in galaxies, clusters and the Universe. Astrophysical observations of colliding galaxy clusters hint at a particle nature of this dark matter problem. In order to be consistent

with structure formation and CMB measurements, this particle species needs to be non-relativistic to allow the growth of small structures that develop into large ones (see also results from N-body simulations [43]). The dark matter particles cannot be accounted for in the baryon content of the Universe, and they show a more than 5 times higher density compared to the baryonic matter in the universe. The particle eluded detection and does not show strong self-coupling. In fact, in galaxy cluster collisions dark matter behaves as a frictionless fluid, and upper limits on the self interaction rate could be set so far.

With advances both in observations and computing power, simulations tracking structure formation from initial conditions to the current Universe at 14 billion years become more and more accurate and thus powerful. Statistical comparisons of observed structures at different scales can constrain the parameters like the velocity distributions of the fundamental particles driving structure formation.

Using this method, a few discrepancies were found in the ΛCDM scenario that led to discussions, whether a warm dark matter (WDM) model with non relativistic, but significantly faster dark matter particles could better explain the observations. In 1999, Klypin et al. noted that pure CDM gravitation simulations predicted much more galactic satellites [44] than are observed in our Galaxy. Later, a second discrepancy about the existence of very massive subhalos was found [45]. First simulations and analyses in a warm dark matter scenario helped reducing this discrepancy [46]. However, since then several investigations showed that a bias in observing faint subhalos, the very inaccurate estimate of the Milky Way's total mass, and inclusion of baryonic feedback [47] in CDM simulations together with improved tracking of subhalos in simulations can significantly alter these conclusions [48]. Thus, it is not possible to conclude on CDM versus WDM yet [49]. A very recent analysis claims that the WDM hypothesis is very unlikely to be able to explain all small scale structure anomalies (subhalos, cored/cusped halo profiles) [50].

Upcoming astrophysics experiments like the Gaia satellite are expected to reduce some uncertainties by an order of magnitude. If that will be valid, the error in the Milky Way's mass, would be reduced from a factor of 2 down to $\sim$20. However, dependent on the modeling of the dark matter content as smooth or with substructure systematic uncertainties much larger than the expected $\sim$20% nominal errors might persist [51]. In any case significant progress in these uncertainties will be essential for further results in the inference of dark matter properties from astronomy.

1.2. Dark matter candidates

As is the case for the discovery of the Higgs boson [52, 53], LHC-results and CMB observations continue to probe and validate the standard models both of particle physics and cosmology with better and better precision. The dark matter puzzle has become a lighthouse of new physics for particle physics theorists and phenomenologists. In this playground, a multitude of particle candidates have been devised, some motivated by mathematical elegance and naturalness versus fine tuning problems, others just devised to show the range of our ignorance and the theoretical possibilities. A somewhat old sketch (2007) of this particle zoo is shown in fig. 1.4. The characteristic properties of the proposed candidates vary in cross-section and mass by 50 to 60 orders of magnitude. Since there are excellent reviews, (see [54, 55, 56, 57, 58] and references therein), we will only briefly summarize the motivation and characteristic of two rather common scenarios, predicting the axion and WIMP dark matter particle candidates.

Different candidates can usually be divided according to their production mechanism. One class of candidates is produced as a thermal relic which means these candidates are in chemical equilibrium with the rest of the matter content in the early Universe,
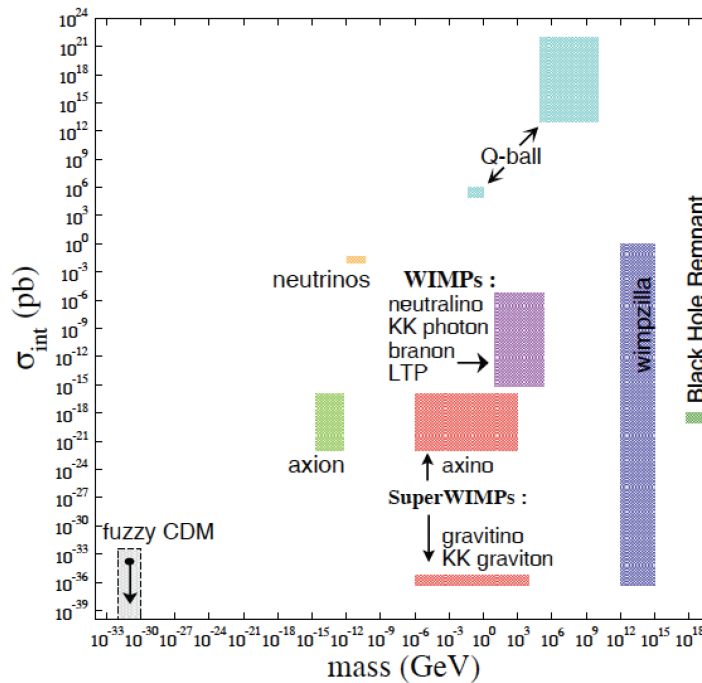
Figure 1.4.: Sketch showing different proposed dark matter candidates in the interaction cross-section versus mass plane. Figure originally prepared for the DMSAG report in 2007 (http://science.energy.gov/hep/hepap/reports/), reprinted from [55].

and the dark matter component drops out of equilibrium like the neutrino background or the cosmic microwave background, when the interaction rate drops below the Hubble expansion rate. The second class is produced non-thermally, for example through decays or radiation during a phase transition. Such a production mechanism allows therefore to produce non-relativistic dark matter without any direct bounds on its mass.

1.2.1. Non-thermal dark matter

The axion is a prime candidate in the class of non-thermal dark matter particle candidates. Originally, axions were invented as a by-product of symmetry investigations that could solve the so-called strong CP problem. The strong CP problem manifests itself in the vanishing electric dipole moment of the neutron, which is not required by standard model physics. In fact, current upper limits on the electric dipole moment of the neutron are 10 orders of magnitude smaller than expected for an angle parameter whose natural scale would be O(1). The Peccei-Quinn symmetry [59, 60] can explain the smallness of this value, and at the same time it introduces a pseudo Nambu-Goldstone boson. Production in the early Universe would have to be non-thermal to fulfill CDM and relic density constraints. A viable mechanism is the non-thermal production of axions during the so called Peccei-Quinn phase transition. This transition occurs when the temperature of the Universe cools to the characteristic value f_a that determines both the axion mass and coupling. Dependent on the time of this phase transition relative to inflation vacuum realignment, axion radiation from axionic string and domain wall decay contribute to the axion production [56].

Axions possess couplings to gluons and fermions and at loop level also to photons. They can contribute to invisible energy loss processes in stars and help explain astrophysical hints of the observation of highest energy TeV γ rays from distant AGN (active galactic nuclei) [61]. Major strategies to detect axion dark matter or axions produced in the sun
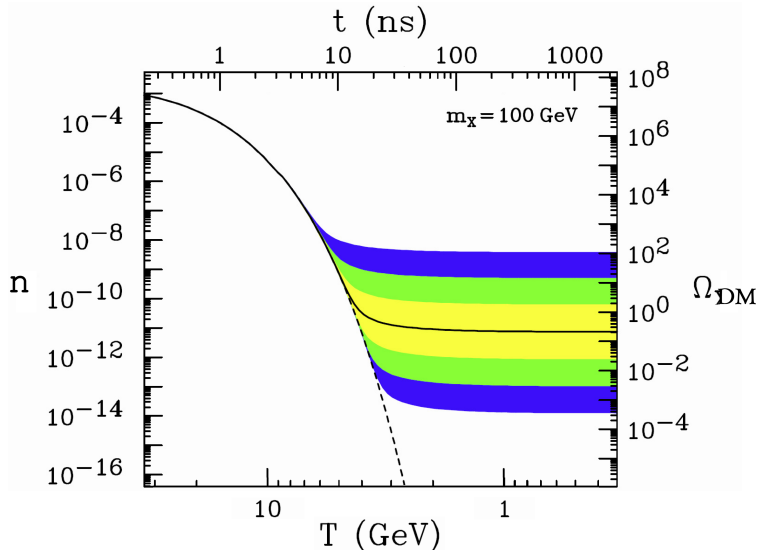
Figure 1.5.: The comoving number density n and resulting thermal relic density Ω_{DM} of a 100 GeV/c^2, P-wave annihilating WIMP as a function of the age of the universe (top) and temperature (bottom). Colored regions show deviations of a factor 10, 100 and 1000 in cross-section from the weak interaction cross-section. Figure from [56].

exploit the Primakoff conversion of axions to photons in a strong magnetic field. For a review we recommend [62]. Recently also axion like dark matter has come into closer focus and many direct dark matter searches have used dedicated analyses to constrain cross-sections of eV to keV scale axion like dark matter [63, 64].

1.2.2. Thermal dark matter - Weakly Interacting Massive Particles

Thermal production or freeze out of dark matter is an analogy to the known physics from the neutrino sector. In the early Universe, dark matter would be in chemical equilibrium with all other particles. Once the Universe cools such that $T < m_{\mathrm{DM}}$, the production becomes exponentially suppressed by Boltzmann statistics and the abundance drops exponentially due to dark matter annihilation: $n \sim e^{-m_{\mathrm{DM/T}}}$.

However, once the reaction rate for the annihilation drops below the expansion rate, the comoving number density n is frozen. This is described quantitatively by the Boltzmann equation

$$\frac{dn}{dt} = -3Hn - \langle \sigma_A v \rangle \left(n^2 - n_{\mathrm{eq}}^2 \right) \tag{1.9}$$

where $3Hn$ parametrizes the dilution in density due to the Hubble expansion H, $\langle \sigma_A v \rangle$ is the average thermal annihilation cross-section and the n^2 term arises from the annihilation reaction (DM+DM $\rightarrow$ SM+SM) into SM particles, and n_{eq}^2 arises from the opposite reaction which happens in chemical equilibrium (SM+SM $\rightarrow$ DM+DM). The thermal relic density is then determined by solving the Boltzmann equation numerically. Results for the comoving number density are plotted in fig. 1.5.

Defining the freeze out to be the time when $n \langle \sigma_A v \rangle = H$, an approximate solution can be obtained analytically. The number density at freeze out n_f is then

$$n_f \sim (m_{\mathrm{DM}} T_f)^{3/2} e^{-m_{DM}/T_f} \sim \frac{T_f^2}{M_{\mathrm{Pl}} \langle \sigma_A v \rangle} \tag{1.10}$$

The value of $x_f = m_{DM}/T_f$ exponentially influences the number density observed today and can hence be restricted very well, a typical value is $x_f \sim 20$. Today's relic density is

$$\Omega_{DM} = \frac{m_{DM}n_0}{\rho_c} = \frac{m_{DM}T_0^3 n_0}{\rho_c T_0^3} \sim \frac{m_{DM}T_0^3}{\rho_c}\frac{n_f}{T_f^3} \sim \frac{x_f T_0^3}{\rho_c M_{\text{Pl}}}\langle\sigma_A v\rangle^{-1} \qquad (1.11)$$

The subscript 0 denotes present day quantities. We note that the thermal relic density depends inversely on the thermal annihilation cross-section $\langle\sigma_A v\rangle$ and not directly to the mass m_{DM}. However, in many theories the mass enters into the thermal cross-section which can be written as

$$\langle\sigma_A v\rangle = k\frac{g_{\text{weak}}^4}{16\pi^2 m_{DM}^2}(1 \text{ or } \text{v}^2) \qquad (1.12)$$

with a constant k of O(1), the weak interaction gauge coupling $g_{\text{weak}} \cong 0.65$ and (1 or v^2) for S- or P- wave annihilation, respectively. This parametrization requires dark matter particles to have a mass of the order of 100 GeV - 1 TeV to account for the entire relic density. All particle candidates produced via the above mechanism are hence weakly interacting massive particles, WIMPs.

Amazingly, new physics setting in at 100 GeV to TeV energies would also help alleviate the gauge hierarchy problem. Assuming that the standard model is valid up to a theory of quantum gravity, loop corrections including momenta up to the Planck scale need to be taken into account in the calculation of the Higgs mass. The current value of $125\,\text{GeV}/\text{c}^2$ [65] requires that such loop corrections cancel out at the $1/10^{36}$ level. New physics at the weak scale could solve this problem.

A much discussed dark matter candidate is present in so-called Supersymmetry which introduces an additional symmetry between fermions and bosons that associates each boson with a supersymmetric partner and vice versa [37]. The symmetry needs to be broken since no super partner has been observed experimentally today. However, being broken at the weak scale, it could solve or at least alleviate the hierarchy problem, since bosonic and fermionic quantum corrections would cancel out in the calculation of the Higgs mass. Additionally, Supersymmetry allows for a unification of gauge couplings and could hence pave the way for a grand unification at the Planck scale [66]. A priori it would also allow for CP violating processes in contradiction to observations. However, a new quantum number can be introduced which being conserved prevents these processes and additionally ensures that the lightest supersymmetric particle, the LSP, is stable. Supersymmetry was not designed to explain dark matter. In fact in 1974 Wess and Zumino [67] studied the concept of arranging particles in spin multiplets. However, in all supersymmetric models where the LSP is neutral, it is an excellent dark matter candidate.

Today the particle physics community is divided about the validity of Supersymmetry. The parameter space of the simplest realizations of Supersymmetry the MSSM and CMSSM has been widely explored through combined efforts of the LHC, direct dark matter detection searches and including the dark matter relic density constraints. Hence, only very specific parameter combinations allow a consistent explanation today. This in turn can be seen as fine tuning of its own. The main motivation, the gauge hierarchy problem, is thus not entirely solved, but instead replaced by a weaker fine tuning problem. Some physicist hence urge the community to discuss new physics in a broader context [68, 69]. In supersymmetric models with extended Higgs sector or less stringent constraints, experimental bounds are much weaker. This comes at the expense of abandoning some of the elegance or naturalness of the simplest theories though. Many well known physicists still favor these scenarios [70, 71].

1.3. Dark matter detection techniques

Dark matter detection techniques depend on the underlying theory and properties of the dark matter candidates. While some candidates are practically inaccessible experimentally, the two previously discussed candidates, the axion and the WIMPs, show promising prospects for a plausible detection in the next decade. The following discussion will focus on WIMPs as they are the prime target of the EDELWEISS direct dark matter search.

1.3.1. Production

As discussed in the section of thermal production and freeze-out, the WIMP dark matter paradigm shows a tantalizing similarity between the required properties for dark matter and the required properties for new physics to solve the hierarchy problem. In fact, in addition to its prime goal of discovering the Higgs particle, the Large Hadron Collider (LHC) has been built to explore physics at the TeV scale and possibly solve the hierarchy problem.

If new physics and especially the production of a dark matter particle candidate becomes accessible at the energies of up to 14 TeV, a WIMP would manifest itself similarly to neutrinos by missing transverse energy and momentum. A prime search is the monojet search from the CMS and ATLAS experiments, which is not only sensitive to Supersymmetric dark matter but also to Kaluza-Klein/Universal Extra dimension models and other WIMP dark matter candidates. See e.g. the results from the 7 TeV data in 2012 [72].

A main drawback of new physics and dark matter searches at the LHC are model dependencies and difficulties in comparison with the results to direct dark matter searches. Combined experimental results of not only a single analysis at LHC, but also including the sensitivity of precision measurements to new physics which couples in Feynman loops and results from direct dark matter searches is done in specific models, like the CMSSM [73] [74]. A comparison of current results together with a prospect for the future 14 TeV LHC data and XENON1T sensitivity in the next to minimal supersymmetric standard model NMSSM is given in [75]. More general comparisons are under active discussions, but are not trivially obtained [76].

Collider searches are in general more sensitive to light WIMPs and have access to new physics, even if a discovered particle might not turn out to be the cosmological dark matter. They show a high complementary to other search strategies, but cannot conclude on the nature of dark matter on their own.

1.3.2. Indirect detection

For the WIMP paradigm we implicitly assumed, that dark matter, being made up from a single particle type is a Majorana particle that can annihilate into standard model particles and thereby produce the relic dark matter abundance during cooling and expansion. As discussed in sec. 1.1.3, current observations show clear evidence for a large overdensity of local dark matter in our neighborhood. For such regions, a continuous annihilation of dark matter particles is thus expected.

Indirect searches try to detect the signature of these decays by looking into various standard model decay products, maximizing the possible signal versus expected astrophysical background. Detection channels with low astrophysical background include antimatter but also detection channels with additional directional information like photons and neutrinos are very valuable, since overdense regions with low luminosities can be targeted in these searches. Explicit signatures are model dependent, but analyses within a specific model can use the multi messenger method to constrain signals in one observational channel with null results from different channels.

This is a very important feature since uncertainties on astrophysical sources and matter and antimatter propagation in cosmic rays is a field of active research. In case dark matter particles show a sizeable interaction cross-section with normal matter, particle accumulation inside of dense objects as the Sun and our Earth become possible. This opens another channel for the detection of neutrinos from dark matter annihilation.

In the following we will highlight observed anomalies or the strongest limit in each of the channels and refer the reader to [77] or [37] for a more thorough discussion.

In antimatter searches the highest statistics results are currently obtained by the AMS02 experiment on board of the international space station ISS. Recent results [78] focused on the analysis of an excess in the positron to electron fraction of cosmic rays first reported by the PAMELA experiment [79]. The AMS results [80] confirmed a positron excess rising from 8 GeV to 275 GeV. The shape of the spectrum after this rise is very important for the determination of the source characteristics. While annihilating dark matter could lead to a positron excess, usually a relatively sharp cutoff would be expected close to the dark matter particle mass. Furthermore, the observed excess would often be observed in anti protons as well, which it is not. Alternative astroparticle physics sources like local pulsars cannot be ruled out as the single source of this positron excess, especially as long as the positron excess at higher energies is not yet well determined. It seems unlikely that the entire large positron excess comes from dark matter annihilation, but it is an interesting observation nonetheless.

In photons, the Fermi satellite is driving the progress at energies up to a few 100 GeV, while TeV signals are being constrained by atmospheric Cherenkov telescopes. The most notable recent result is a diffuse gamma ray excess at about 2 GeV in the direction of the galactic center. This excess has been analyzed by several groups and has been under intense discussion [81]. While the signature is compatible with a variety of dark matter models and WIMP masses from a few tens to ~ 75 GeV, astrophysical sources have also been put forward. In particular, unresolved sources in the very center of the galaxy and a burst event injecting leptons and/or protons some kyears or Myears ago. Strongest constraints or confirmation is expected from the observation of dwarf spheroidals in our Galaxy. These objects have an extremely high matter-to-light ratio and are generally seen as much more robust targets than the galactic center which is subject to uncertainties in astrophysical sources and the shape of the dark matter halo. Current constraints [82] cannot limit the excess from the center, but a factor 2 to 3 stronger limits would provide a strong tension for the dark matter interpretation of the excess in the galactic center.

Another signal often discussed as a smoking gun is the annihilation of dark matter into 2 γ's which results in a line feature. Such a line was observed at 130 GeV in an external analysis of the FERMI data. However, in a careful reanalysis, the FERMI collaboration concluded that the observed excess has a global significance of only 1.5 σ [83] . In addition, the line shows a few unexpected features. Its width is smaller than the expected resolution and its morphology with respect to an expected halo is disputable.

In TeV γ-rays, the flux decreases and strongest limits are set by imaging atmospheric Cherenkov telescopes (IACTs) with high acceptance. While the current sensitivity does not reach the thermal annihilation cross-section, IACTs are a relatively young technique with a very high potential for astrophysics. The planned next generation Cherenkov telescope array CTA will boost the technique providing a factor 10 higher acceptance, better resolution and lower energy threshold. Latest results from the H.E.S.S. experiment already start to constrain some more exotic leptophilic models that would be required for a dark matter interpretation of the AMS and PAMELA positron excess [84].

Another interesting channel is the search for dark matter annihilation into neutrinos. The strongest experimental constraints in this channel come from the IceCube experiment [85].

As for TeV γ-ray searches, the IceCube experiment can constrain specific leptophilic models, but is not sensitive to the thermal annihilation cross-section yet. Interesting constraints can be set on the scenario of self-interacting dark matter, searching for neutrinos from the sun [86].

To sum up we may say that there are several indirect detection techniques and that there is clear progress towards the reference sensitivity of the thermal annihilation cross-section in several observation channels. At the same time there are several inconclusive measurements that can be interpreted as a dark matter signal or as new or unresolved astrophysical sources. In order to establish a robust dark matter interpretation, a multi-messenger observation will be essential.

1.3.3. Direct detection

The direct dark matter detection experiments are searching for the scattering of a WIMP on a target nucleus in well shielded detectors in underground facilities. Since this thesis is set in the context of the EDELWEISS direct dark matter detection experiment, we will go into much more detail in this section. After reviewing the mathematics and conventions for the comparison of signals or limits on the interaction cross-section with normal matter, the current status of different techniques will be summarized in a dedicated section.

The discussion of signal properties follows a review from Lewin and Smith [87] and a later update from Savage in 2006 [88]. We can also recommend the book from Bertone [57] for an instructive description. The physics of direct detection can generally be described in a simple parametrization using the non relativistic limit. Kurylov and Kamionkowski showed [89] that in this limit any WIMP with a Lorentz-invariant WIMP-nucleus interaction can be parametrized in terms of a spin-dependent and a spin-independent WIMP-nucleus interaction only. The non-relativistic limit is well justified in the cold dark matter scenario with expected recoil energies below $100\,\mathrm{keV}$. Hence, it allows a straight forward interpretation of experimental results and less model dependency than in the other cases of indirect dark matter detection or production at colliders.

The framework for the analysis and comparison of direct detection experiments is the so-called standard halo model which parametrizes the astrophysical uncertainties of the dark matter halo. It is certainly only an approximation to the real dark matter halo in our galaxy, but it allows the comparison of experimental results in a straightforward scenario with comparatively conservative assumptions. The model assumes that the dark matter halo of the Milky Way is an isotropic sphere. The WIMP velocity distribution is then given by a Maxwell Boltzmann distribution with a cutoff at the escape velocity v_{esc}:

$$f(\mathbf{v}) = \begin{cases} 1/N_0 \left(\frac{3}{2\pi\sigma_v^2} \right)^{3/2} e^{-3\mathbf{v}^2/2\sigma_v^2}, & \text{for } |\mathbf{v}| < v_{\mathrm{esc}} \\ 0, & \text{otherwise} \end{cases} \tag{1.13}$$

Traditionally, values of $v_{\mathrm{esc}} = 650\,\mathrm{km/s}$ and a local velocity dispersion of $\sigma_v = 270\,\frac{\mathrm{km}}{\mathrm{s}}$ were used, nowadays values of $v_{\mathrm{esc}} = 544\,\mathrm{km/s}$ and $\sigma_v = 230\,\frac{\mathrm{km}}{\mathrm{s}}$ are more common [90]. N_0 is a normalization parameter.

A rotation of the Sun in the Milky Way relative to the dark matter halo has to be considered for the kinematics of the WIMP nucleus scattering. This relative velocity is noted as $\mathbf{v}_{\mathrm{rel}}(t)$. In an elastic collision, the energy transfer is then calculated to

$$E_{\mathrm{Rec}} = \frac{\mu^2}{M_{\mathrm{N}}} v_{\mathrm{rel}}^2 \left(1 - cos\Theta \right). \tag{1.14}$$
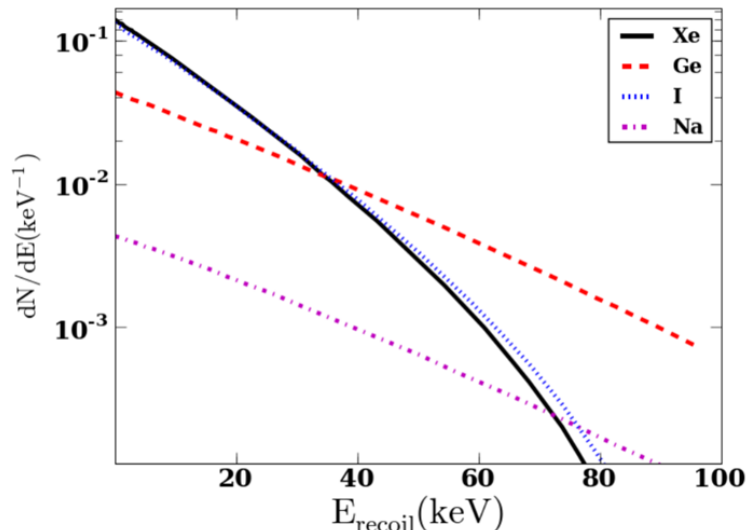
Figure 1.6.: Expected signal dN/dE for a $3000\,\mathrm{kg\cdot d}$ exposure and a cross-section of $\sigma_{\mathrm{SI}} = 10^{-9}\,\mathrm{pb}$ for a $100\,\mathrm{GeV/c^2}$ WIMP and different target nuclei. Signals are exponentially decreasing, and for higher momentum transfer the signals are further suppressed due to the nuclear form factor. The effect is more pronounced for the larger nuclei Xe and I than for Ge or Na. Figure created with the micrOMEGAs packet [91].

Here μ is the reduced mass $\mu = \frac{m_\chi m_N}{m_\chi + m_N}$ of the WIMP m_χ and the nucleus m_N and Θ is the scattering angle of the WIMP. For a WIMP with a typical mass $m_\chi = 100$ GeV/c^2 and a relative velocity of $v_{\mathrm{rel}} = 300\,\frac{\mathrm{km}}{\mathrm{s}}$ the maximum recoil energy for backscattering on a Ge nucleus is $E_{\mathrm{Rec}} = 65\,\mathrm{keV}$.

The total observable signal is determined by the Maxwell-Boltzmann distribution for the particle velocities convoluted with the energy transfer per scattering and the momentum dependent cross-section $\sigma(q)$.

$$\mathsf{R} = \frac{dR}{dE} = \frac{\sigma(q)}{2m_\chi \mu^2} \rho \eta(E, t) \tag{1.15}$$

The nuclear recoil rate is usually computed in units of events/kg/keV/d, using a local halo density of $\rho = 0.3\,\mathrm{GeV/c^2}$, with η parametrizing the dependency on the time dependent relative velocity distribution of WIMPs

$$\eta(E, t) = \int_{u > v_{\mathrm{min}}} \frac{f(\mathbf{u}, t)}{u} d^3 u \tag{1.16}$$

The integral starts from the minimal velocity $v_{\mathrm{min}} = \sqrt{\frac{ME}{\mu^2}}$ that can result in a recoil of energy E and stops at the maximal velocity parametrized by the escape velocity. In order to compute the signal shape R we need to take a second look at the cross-section.

As previously noted, the WIMP nucleus interaction can be parametrized by two possible couplings. First, the scalar interaction, where the WIMP couples to the mass of the nucleus, and secondly there is the axial-vector (spin) interaction. For supersymmetric dark matter, the scalar interaction is mediated dominantly by Higgs particles or by squarks as shown in the Feynman diagrams in figure 1.7. It is the dominant interaction in models with a large mixing of Higgsinos into the LSP. The cross-section reads

$$\sigma_{\mathrm{scalar}} = \frac{4\mu^2}{\pi} \left[Z f_{\mathrm{p}} + (A - Z) f_{\mathrm{n}} \right] \cdot F^2(q), \tag{1.17}$$
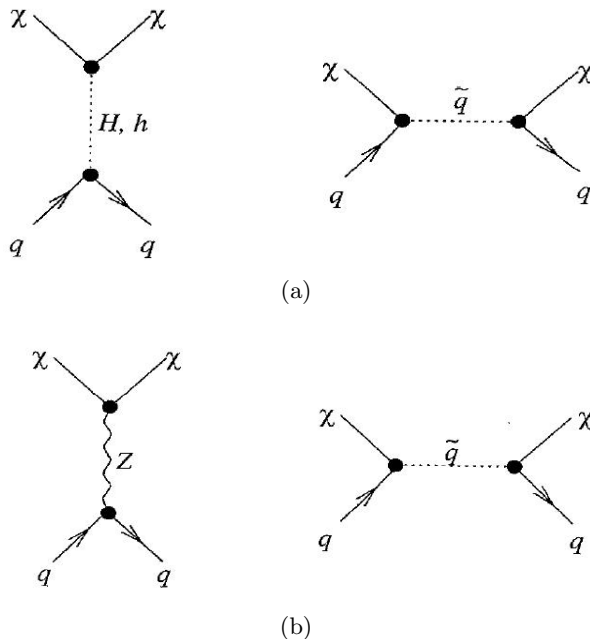
Figure 1.7.: Two main Feynman diagrams for scalar interactions (a) and axial vector (spin dependent) interactions (b). Figure from [92].

with the reduced mass μ, the atomic mass number A, the number of protons Z, the coupling of WIMPs to protons (neutrons) f_p (f_n) and the nuclear form factor $F(q)$. For the most straightforward assumption of $f_\mathrm{p} \approx f_\mathrm{n}$, $\sigma \propto A^2$, i.e. the cross-section profits from a quadratic enhancement with the number of nucleons. However, this quadratic enhancement is lost in case of high momentum transfer q, which is encoded in the nuclear form factor F with $F(q) \leq 1$. The underlying physics can be understood, noting that the de Broglie wave length of a $100\,\mathrm{GeV}/c^2$ WIMP with a velocity of $10^{-3}\,c$ is about $12\,\mathrm{fm}$. This length is very similar to the diameter of a large nucleus and is hence the length scale at which the transition from coherent scattering on the whole nucleus to scattering on nucleons/part of the nucleus sets in and interference effects have to be considered. Taking into account all these effects a featureless almost exponentially dropping signal is expected (see fig. 1.6).

For the spin interaction, the situation is more complex due to the spin structure of the nucleus. In this case, the interaction can be mediated by Z bosons as well as by squarks as depicted in the Feynman diagram fig. 1.7 (b). For Binos, or neutralinos with a large Bino mixing, this would be the dominant interaction. The cross-section is given as

$$\sigma_{\mathrm{spin}} = \frac{32}{\pi} G_\mathrm{F}^2 \mu^2 \lambda^2 J(J+1) \cdot F_\mathrm{S}^2(q), \quad \text{with} \tag{1.18}$$

$$\lambda = \frac{1}{J} \left[a_\mathrm{p} \langle S_\mathrm{p} \rangle + a_\mathrm{n} \langle S_\mathrm{n} \rangle \right]. \tag{1.19}$$

Here G_F is the Fermi constant, μ the WIMP-target nucleus reduced mass, J the total nuclear spin, $F_\mathrm{S}(q)$ parametrizes the momentum transfer dependence and a_p and a_n are effective WIMP-proton and WIMP-neutron couplings. $\langle S_\mathrm{p,n} \rangle$ are the expectation values of the proton, neutron spins within the nucleus. For each nucleus $\langle S_\mathrm{p,n} \rangle$ has to be calculated specifically, but most of the time the total nuclear spin is dominated by the last unpaired nucleon [92]. Since this total nuclear spin is much smaller than the number of nucleons, limits on the spin independent cross-sections are usually more than a factor 1000 stronger in current experiments.

So far, we only discussed the scattering of WIMPs on nuclei. Given the mass dependent
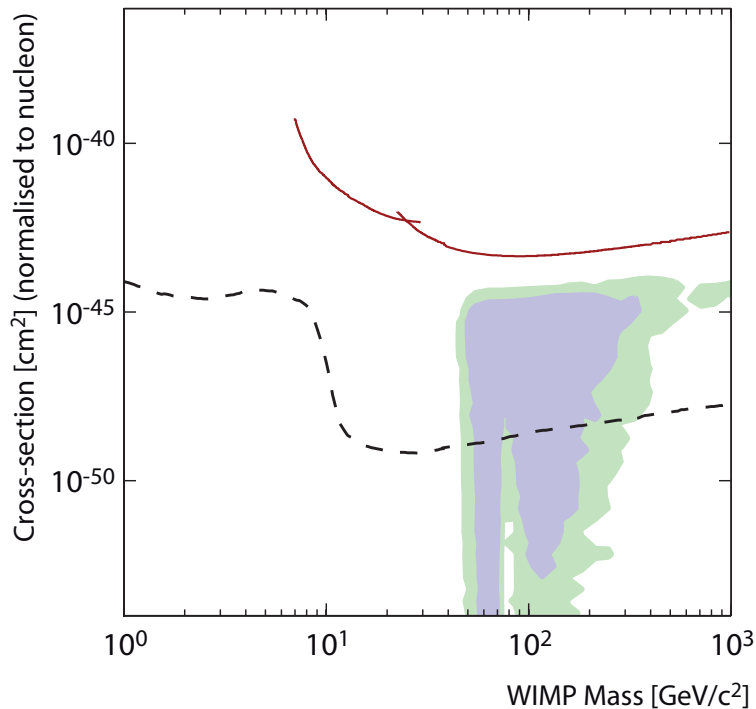
Figure 1.8.: 90% confidence limit on the spin independent scattering cross-section of WIMPs in the cross-section versus WIMP mass plane from the EDELWEISS experiment (solid red) [93, 94]. 68% C.L. (light blue) and 95% C.L. (green) contours of allowed WIMP parameter space in the MSSM-15 model [95]. Experimental limits of both colliders, the Planck relic density constraint and direct detection experiments have been included in this parameter scan. Cross-section limits corresponding to the first observation of an event from the coherent neutrino nucleus scattering as irreducible background have been added in black [96]. For details see text. Figure created with the micrOMEGAs packet [91].

coupling via Higgs exchange (see fig. 1.7 (a)) and the coherent enhancement for the scalar WIMP-nucleus interaction cross-section, it is evident that a scattering on single electrons with their much smaller lepton mass would be strongly suppressed for this interaction. But there is a second consideration why we neglected the WIMP electron scattering even for the spin dependent case. Considering a WIMP scattering on an electron, the reduced mass is approximately the mass of the electron and expected recoil energies are below the eV level. This energy is close to but below the energy needed to induce ionization or scintillation in semiconductor detectors and it is far below the usual trigger levels.

In any of the two cases, spin dependent and spin independent interaction, the recoil distribution is mainly an unspecific exponential distribution. Signal claims thus rely crucially on the suppression of all possible backgrounds.

In practice, WIMP searches are competitive in either the spin dependent or the scalar interaction only. For EDELWEISS with its Ge target with dominatntly $J = 0$, stronger limits can be set for scalar interactions. As long as no signal has been measured, the results are presented as an exclusion plot on a 2-dimensional plane of WIMP-nucleon cross-section versus WIMP mass (fig. 1.8). The plot shown herein is the exclusion plot for spin independent WIMP-nucleon cross-sections. The solid red lines signify the latest EDELWEISS limits. The parameter space above the lines is excluded at 90% C.L.. The light blue and green region is the currently (2014) favored parameter region for neutralino dark matter [95] in a phenomenological MSSM model with 15 parameters. Constraints from collider searches, the Planck relic density measurements and direct detection searches

are already included in this parameter scan.

The typical shape of the exclusion limits reflects detector threshold effects at low energies and the effect of decreasing WIMP number particle density for increasing dark matter particle mass. Best sensitivity can usually be obtained close to the matching of dark matter particle and target mass. In this case, both cross-section and kinematics are most favorable. Dedicated low mass dark matter searches use this effect and often rely on lighter targets than standard WIMP searches. For the shown EDELWEISS exclusion limit, low energy data, taking into account efficiency losses close to the threshold, and high energy data with constant efficiency close to 100% were analyzed separately leading to two independent limits.

1.4. Status of direct dark matter search experiments

Currently, there is a wealth of different techniques competing for the first detection of WIMPs, with at least a dozen experiments running and as many experiments in preparation. All of the experiments share the demand of background suppression. They are hence located in deep underground laboratories and employ active and passive shields for the reduction of remaining backgrounds. In addition, most experiments rely on an event by event discrimination of electron recoils from the dominant γ and β background versus nuclear recoils from WIMPs and neutron background. In particular, the material selection for the innermost instrumentation is key to achieve the required sensitivity to detect a signal of a few events within thousands of kg·d of exposure. In the following, recently operated and prospective future experiments will be characterized by their readout channel which is traditionally either phonons, ionization, scintillation or a combination of two out of these three. Nowadays, also bubble chambers are operated, and even DNA based nanometer tracking techniques have been proposed [97]. Directional techniques using large gaseous targets are actively developed, but do not achieve competitive sensitivity in the current situation. The tracking techniques will not be considered in the following. The discussion will be split focusing on the traditional WIMP paradigm with O(100) GeV/c^2 WIMPs first and then discussing on the progress towards low mass WIMP searches targeting WIMPs with masses less than $10\,\text{GeV/c}^2$.

Recent reviews can be found in [37, 98], and we also note the extensive discussion in [6]. The current situation is somewhat contradictory. Four collaborations published results with a signal excess that was interpreted in terms of dark matter parameters while other collaborations exclude the same parameter space in the naive scenario of WIMPs in a standard halo. 90% C.L. contours and exclusion limits for the various experiments are shown in fig. 1.9. Phenomenologists and theorists have investigated the possibility of putting all these results into a coherent picture, but a significant tweaking of all available parameters from dark matter particle properties to special astrophysical models is needed to at least reduce the tension between the observations. For the following discussion, we will adopt a skeptic's view and critically revise the observations and experimental constraints.

Scintillation - solid state detectors

Scintillating materials being read out by Photomultiplier Tubes (PMTs) have a long history in science. Due to the broad distribution of the technique it is not astonishing that the largest exposure in any dark matter search has been achieved using this technique. In fact, the DAMA/LIBRA collaboration claims a signal excess at the 9.3 σ C.L. in an exposure of 1.33 ton·years (485450 kg · d), accumulated in 13 years of data [99]. The interpretation of this excess as dark matter detection is, however, not widely accepted. Various other experiments have scanned the same parameter space and found no signal
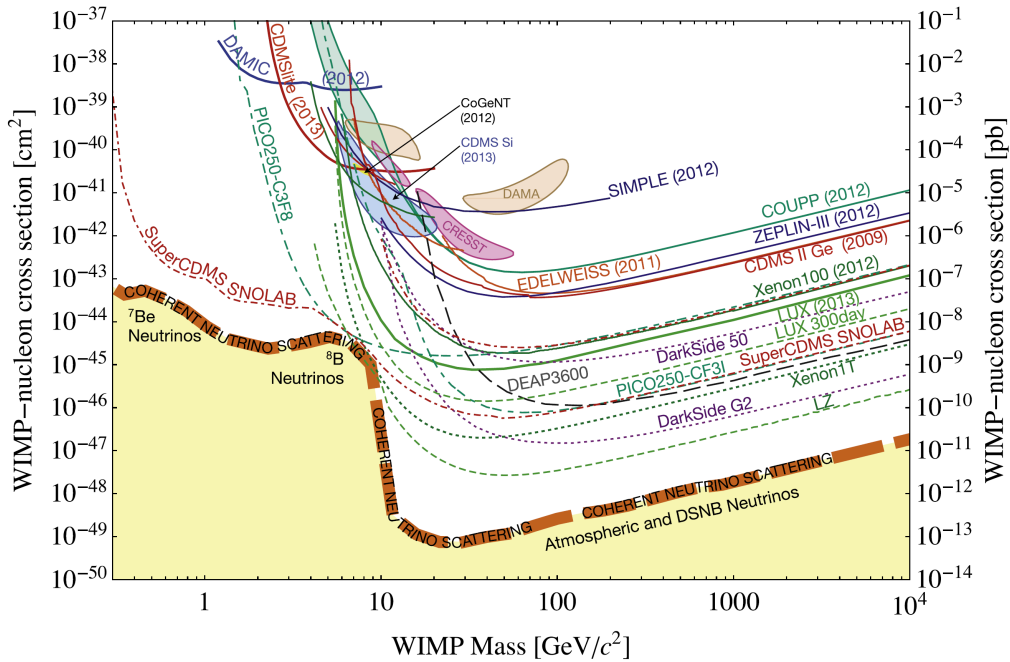
Figure 1.9.: Combination of limits and projected sensitivities of current and future direct dark matter search experiments on the spin independent WIMP-nucleon scattering cross-section. Figure from [98].

excess (see fig. 1.9). Even in the most extreme scenarios using special WIMP velocity profiles and tuning the cross-sections, e.g. the couplings to neutrons and protons, a severe tension remains. Furthermore, the DAMA/LIBRA experiment is not a background free experiment. The signal claim thus relies on an observed annual modulation of the data in their lowest energy bin. This modulation is consistent with the expected modulation in the WIMP interaction rate from the different relative velocities at which an observer on earth is moving through the dark matter halo. The annual cycle matches the superposition of earth and solar velocity that add and subtract each other relative to a dark matter halo at rest once per year. No background that matches this modulation as well as the WIMP hypothesis is currently known, but it is difficult to exclude that the signal might be due to the annual modulation of some environmental conditions or an unaccounted background.

Efforts to reproduce or constrain the results in a different experimental setup are actively pursued. However, the radiopurity of the NaI target crystals of the DAMA experiment has been achieved with a special patented technique and has not been reached since. Current experiments like the ANAIS [100] and DM-ICE [101] experiments are still fighting against out of equilibrium ^{210}Pb and ^{40}K contaminations, respectively.

The KIMS [102] experiment in South Korea uses CsI scintillating detectors instead. The KIMS collaboration reports that they can exclude the DAMA/LIBRA signal interpretation in spite of a low energy α surface contamination and they could set the strongest limits on the spin dependent WIMP-proton cross-section with an exposure of 24524 kg·d in 2011 [102].

Scintillation - liquid noble gas detectors

Using xenon as target, current scintillation only detectors rely absolutely on the radiopurity and shielding of the detector environment. The experiments usually use a 4π PMT instrumentation to allow an accurate position reconstruction and subsequent fiducialization. They can thus employ the self shielding properties of their target materials. Additionally pulse shape analysis techniques are being developed to allow electron to nuclear recoil

discrimination for high energy traces. Due to their simple single phase design, large setups are technically well feasible and additional physics in terms of double beta decay searches and neutrino physics are envisaged.

Current experiments include the XMASS liquid xenon experiment [103], which has been in operation since 2010. An unexpected radioactive background in the Al seals of the PMT instrumentation limited the sensitivity of the first phase such that the XMASS collaboration used the dataset up to 2013 to perform a low mass analysis of the data only. Despite the relatively large exposure of 5591 kg·d, the limit is inferior to results from Ge based experiments with more than a factor 10 less exposure and the XENON100 constraints of the time. Results of a refurbished detector are expected in 2015.

A second currently operating experiment is the DEAP3600 experiment. Using 3.6 t of liquid argon and a sophisticated pulse shape analysis technique a γ-suppression power of $3 \cdot 10^{-8}$ has been reported. Using a fiducialization from the position reconstruction and this suppression, the collaboration expects to obtain a background free data set of 3 ton years of WIMP search data within three years from now. This corresponds to a factor 23 improvement over the current best sensitivity. A first data release is expected for 2015 [104, 37]. The technique is however not adjusted for the low mass WIMP search. A threshold of 60 keVnr permits no sensitivity to probe the DAMA/LIBRA claim.

The DEAP collaboration is also involved in the MiniCLEAN prototype experiment, pursuing physics with exchangeable liquid noble gas targets. In particular, an exchange between liquid neon and liquid argon is foreseen to probe the expected A^2 dependence of spin independent WIMP nucleus scattering and to obtain sensitivity to lower mass WIMPs [105].

Phonon-ionization

Phonon ionization detectors build on the expertise of the semiconductor industry. With e^-/h^+-pair creation energies of a few eV, these detectors promise superior resolutions and lowest energy thresholds. For the case of the simultaneous phonon and ionization readout, an electron to nuclear recoil discrimination capability at the level of 1 in a few 10^5 is added. The detectors need to be cooled to mK temperatures to obtain the required low heat capacities for the calorimetric measurement of the total energy of an interaction in the usual targets with ~ 1 kg of mass. Scaling requires the installation of tens to hundreds of detectors in ever larger cryogenic facilities. This is somewhat costly and the main focus of the phonon-ionization experiments is changing towards low WIMP mass analysis. However, as the discussion of the DAMA/LIBRA claim showed, a WIMP signal in a single experiment will hardly be convincing and a second technique will be needed to cross-check a possible signal as well as to pin down the dark matter particle properties. Since phonon-ionization detectors are a robust technology with well measured ionization quenching down to lowest energies and a long standing experimental experience, this technology is well suited to explore both low and high mass WIMPs.

Results focusing on the standard scenario of WIMPs with masses of $O(100)$GeV/c^2 have been obtained by the EDELWEISS and CDMS/SuperCDMS collaborations. Results obtained with Ge as target materials exclude signal interpretations of low mass WIMPs from the DAMA/LIBRA experiment, the CoGeNT experiment (discussed in the low mass dark matter search) and the CRESST experiment. The final EDELWEISS-II [94, 93] and CDMS [106] results from 2011 were combined in a statistical analysis in [106]. Since then, the SuperCDMS-Soudan [107] prototype experiment has significantly improved their thresholds and sets the strongest limits for 5 GeV/c^2 WIMP mass with an exposure of only 577 kg·d today. Similarly the EDELWEISS-III experiment has achieved a 30% improvement in their ionization resolution and is currently taking WIMP search data with an installation of 36 800 g detectors. A further collaboration of the two experiments is expected for the

SuperCDMS SNOLAB phase where a joint operation of EDELWEISS and SuperCDMS detectors in a common infrastructure is planned.

In addition to Ge, the CDMS experiment has also employed the lighter Si as a target material. In the analysis of two separate datasets, no excess was observed in the first [108]. Contrary, a likelihood analysis of the second dataset preferred the WIMP + background hypothesis over the background only hypothesis with a p-value of 0.19% [109]. The results correspond to the observation of 3 nuclear recoil candidates not accounted for in the background model. The result is in severe tension to the SuperCDMS Soudan Ge analysis and has to face constraints from a XENON10 and LUX analysis.

Phonon-scintillation

Solid state detectors have also been used for the combined readout of phonon and scintillation. However, unlike the Ge and Si targets, no radiopure scintillating crystals are available from commercial companies. The CRESST collaboration has thus started producing their own $CaWO_4$ crystals with the Czochralski method. In contrast to most other techniques, the CRESST experiment can explore the WIMP scattering on three different target nuclei within their detectors. Similar to the phonon-ionization detectors only a few eV energies are needed to produce scintillation and experimental thresholds below the keV recoil are feasible. This translates to an extremely good sensitivity for lowest WIMP masses below $3\,\mathrm{GeV/c^2}$. Recent results include the analysis of $730\,\mathrm{kg \cdot d}$ of data in 2012 [8]. In this analysis, 63 nuclear recoil candidates were observed. A likelihood analysis of the expected backgrounds could not account for all candidates and preferred the WIMP signal hypothesis at the 4.7 σ C.L.. Nevertheless the CRESST collaboration identified the brass clamps of their detector holders as a main background source of surface events from α and ^{210}Pb recoils and revised their setup. An analysis of an improved detector in the new setup observed no significant signal excess and excluded most of the previously preferred parameter space [110]. The obtained limits make use of $29\,\mathrm{kg \cdot d}$ of exposure and represent the leading results for WIMP masses below $3\,\mathrm{GeV/c^2}$ (see fig. 1.10). A blind analysis for the data from all running detectors is expected for 2015.

Ionization-scintillation

Ionization and scintillation are used as the detection channels for the currently leading class of dual phase liquid noble gas experiments. The liquid phase is the target material, with xenon and argon being used in current experiments. The free charge carriers from an interaction are then drifted to the gaseous phase and strongly accelerated. The ionization signal is thus effectively converted into a second scintillation signal in the gas phase and can be read out by the PMT instrumentation. The scintillation yield L_{Eff} with applied electric field has been a matter of extensive research and low energy investigation of L_{Eff} are still relatively wide spread and under active investigation. The experiments employ a position reconstruction to allow a fiducialization and use the self shielding effect to reduce backgrounds. They achieve an electron to nuclear recoil discrimination of the order of 1000:1 while keeping a nuclear recoil acceptance of 50% using the dual signal readout.

Thresholds for the primary scintillation signal are at the level of $5\,\mathrm{keVnr}$ with keV resolutions. The experiments can be relatively easily scaled with mild constraints from the purity and length for the drifting of charges in the liquid phase. Ton scale experiments are currently under construction.

Recent results include the XENON100 experiment [111] which provided the world's best sensitivity in 2012, the XENON10 low(er) WIMP mass analysis [112, 113], the finished ZEPLIN experiment [114] and the current world leading results from the LUX experiment [115].

First results using Argon as a target have been published by the DarkSide50 collaboration [116], but are not at a competitive sensitivity yet. No results from the 1.1 t ArDM dual phase liquid argon experiment have been presented yet, except for results from the commissioning in 2013 [117].

Given the success of current dual phase noble liquid experiments, next generation ton scale experiments are under construction (XENON1T) or in the final stages of the conceptual design LZ [37]. Experiments using this technique to achieve an ultimate WIMP sensitivity and then measure coherent neutrino nucleus scattering are under preparation (XENONnT, DARWIN) [118, 119, 120].

Bubble chambers

An old technique that was rediscovered for dark matter search is the bubble chamber system. Dependent on the experimental conditions of pressure and temperature, a superheated liquid becomes sensitive to a certain critical energy density from the stopping power dE/dx of scattered particles. Since nuclear recoils have a much larger stopping power compared to electron recoils, bubble chambers can be operated in a regime sensitive to nuclear recoils but insensitive to γ interactions.

Currently operated targets are C_2ClF_5, CF_3I, C_4F_{10}. The experimental readout employs acoustic sensors registering the bubble formation as well as visual imaging. The setups are comparatively cheap, but for some targets the chemical stability of the target warrants further research. Due to the large amount of fluorine with its an unpaired proton and a total nuclear spin $I = \frac{1}{2}$ within the targets, bubble chambers are especially sensitive to the spin dependent WIMP-proton coupling and can set the best direct experimental limits. For the spin independent case, target masses still need to be scaled to achieve competitiveness with the large liquid noble gas experiments. It is worthy to note though, that the PICASSO experiment could set the best limit for a very small parameter space around 4.5 GeV/c^2 of WIMP mass for a short period in 2012 [121].

Current best results on the WIMP-proton coupling have been presented by the PICO-2l experiment [122]. Further results are given in detail in [123, 124]. A next generation experiment with 250 l of target mass is currently under construction by the PICO collaboration.

Direct detection - low mass WIMPs

The detection of lower mass WIMPs requires a profound understanding of detector efficiencies close to the experimental thresholds. Often large scale detectors, such as for example the LUX experiment, can set very good limits down to a few GeV/c^2 masses. In fact LUX sets the strongest experimental limits down to a mass of 6 GeV/c^2 WIMPs today (see fig. 1.10). However, the limit at 6 GeV/c^2 is about 4 orders of magnitude weaker than at 30 GeV/c^2 while the dark matter number density increased by a factor 5. In fact, LUX is mainly sensitive to upward fluctuation of the extreme tail of highest velocity backscattering events at that energy. Since the tail of the dark matter velocity distribution is especially subject to uncertainties, there are arguments for the introduction of a "WIMP safe" mass for which at least 1% of the total WIMP signal recoil spectrum is observed and which is not dominated from the upward fluctuation of sub threshold energy deposits due to poor energy resolutions [37]. Following this paradigm, the LUX limit should not be extended below 8-10 GeV/c^2 and dedicated experiments are needed to explore this region. Starting from their intrinsic good energy resolutions the phonon-ionization and phonon-scintillation solid state detectors are redeveloping their setups to experimentally achieve the theoretical resolutions. But also dedicated ionization only detectors developed for neutrino physics and new concepts are explored.

The PandaX [125] collaboration is pushing the instrumentation of PMTs for a high light yield in a liquid xenon dual phase ionization-scintillation experiment and proved that a
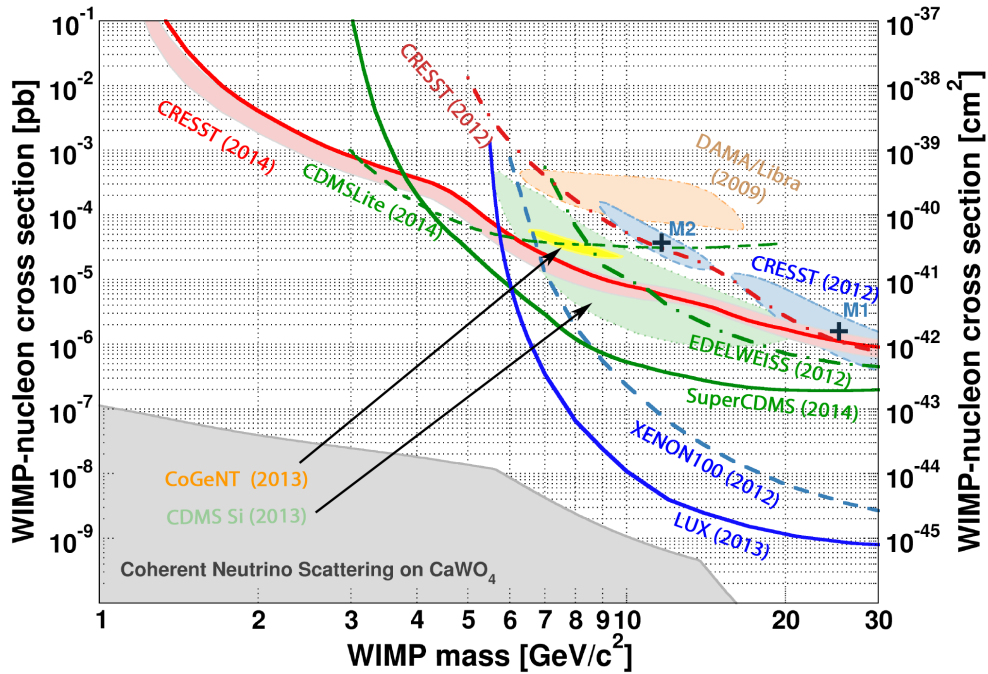
Figure 1.10.: Combination of limits and current sensitivities of direct dark matter search experiments on the spin independent WIMP-nucleon scattering cross-sections. Only experiments with a significant sensitivity on lower mass WIMPs with $m_\chi < 30\,\text{GeV}/c^2$ are shown. Figure adapted from [110]. See text for details.

significant improvement over XENON100 is feasible, but it is not competitive to dedicated low mass detectors. Instead, given its location in the deepest underground laboratory and the funding in China it might become an important contributor in the high mass WIMP search. Results with a 120 kg target stage have been reported, and a design towards 0.5 t and to multiple tons [126] has been discussed.

With a low mass target of carbon and fluorine the PICASSO experiment [121] has demonstrated that bubble chamber techniques can use the favorable kinematics for light targets and produce competitive limits even for the spin independent WIMP nucleus scattering. The PICO-250 experiment with more than a 100 times larger target is thus expected to be a strong competitor for low WIMP masses down to $\sim 3\,\text{GeV}/c^2$. (see fig. 1.9)

Ionization

As previously discussed, electron-hole pair creation in Ge requires only a few eV of initial energy deposit and Ge can be purchased with a very high intrinsic radiopurity. Ge detectors have thus been employed for a long time in high precision spectroscopy. A special type of p-type point contact diode detectors has been developed to allow the pulse shape discrimination of surface and bulk events. These detectors were designed targeting the coherent neutrino nucleus scattering, but the CoGeNT collaboration first realized their potential for the direct dark matter search [127]. By now, several experiments investigated a very similar design and publications from the Texono [128] collaboration, first dark matter search results from the CDEX experiment in China [129] and results from the MALBEK [130] experiment can be found. The technology provides no event identification in terms of nuclear or electronic recoils and results have to be interpreted in terms of an annual modulation and excess above the background. In contrast to the CoGeNT experiment, none of the latter experiments observed a signal excess.

The signal observed in the CoGeNT data is an annual modulation in three years of data in combination with an excess of low energy events above the γ background. However in

the latest analysis the signal preference is mild at best with a statistical significance of only $2.2\,\sigma$ [131]. In addition there are several investigations concluding that the modeling of surface events is crucial for the interpretation of the data from these detectors [132]. Investigating a slightly different modeling of bulk to surface events, an independent analysis of the CoGeNT data found that the signal preference is reduced to less than $1\,\sigma$ with an equally well overall fit to the data [10].

Despite the encountered difficulties with surface backgrounds the CDEX collaboration has presented an ambitious plan to implement these detectors in a ton scale experiment [133].

A novel idea is the use of Si CCDs for dark matter search. This became viable only with the development of thick fully depleted CCDs ten times more massive than conventional CCDs. Providing imaging at the μm-scale, the technique allows the discrimination between diffusion limited hits and tracks from electrons, muons and x-ray interactions. The energy resolution at the level of three charge pairs corresponds to $\sim 10\,\mathrm{eV}$ and allows thresholds below the 500 eV level. The DAMIC collaboration published results from a first prototype in a shallow underground site excluding dark matter particles with cross-sections of a few times $10^{-39}\mathrm{cm}^2$ down to 1.5 $\mathrm{GeV/c}^2$ [134].

Dual channel solid state detectors

As already discussed above, the dual channel readout of semiconductor detectors can profit from their intrinsically excellent energy resolution and provide an efficient event by event discrimination. To exploit the theoretically achievable resolutions specially adapted electronics is needed. This is most profoundly shown by the latest results from the CRESST [110] and SuperCDMS collaboration [107], that set the worlds best limits for WIMPs below $6\,\mathrm{GeV/c}^2$ mass on the spin independent WIMP nucleus scattering with exposures of $29\,\mathrm{kg{\cdot}d}$ and $577\,\mathrm{kg{\cdot}d}$, respectively.

Additionally, the CDMS collaboration showed that it is possible to use these detectors in a high voltage readout mode [11] which provides energy resolutions and thresholds competitive with pure ionization ppc-detectors as used by the CoGeNT experiment. Discrimination capability in this mode is lost and limits rely on low γ background levels as for the pure ionization detectors.

Conclusion

In the previous discussion we shortly reviewed each of the four individual signal interpretations of dark matter experiments as well as the current state of different searches. We note that all four signals have been observed in solid state detectors, two of them in experiments without electron to nuclear recoil discrimination. WIMP parameter estimates are somewhat incompatible except for the CDMS-Si and the CoGeNT result and all results are excluded by at least two independent experiments under the assumption of the standard halo model. For two experiments, an erroneous modeling of their surface backgrounds seems a likelier explanation than a dark matter interpretation in a constructed phenomenological model (e.g. [135]). The CRESST experiment significantly improved their detector concept with respect to surface backgrounds and already exclude the largest part of their previously preferred WIMP parameter region. The CoGeNT signal claim has a rather small statistical significance, which vanishes completely with a different modeling of the surface background. Results from multiple experimental techniques will help further evaluate the current situation. The CRESST and CoGeNT cases demonstrate that the surface event rejection down to lowest energies is a key requirement for the analysis of low mass dark matter searches in solid state detectors.

2. The EDELWEISS experiment

The EDELWEISS experiment is a direct dark matter search experiment pioneered by French groups from Lyon, Paris and Grenoble in 1990 and situated in the underground laboratory of Modane. As a direct dark matter search experiment it faces two major challenges: first of all to detect the energy deposit of the scattering of a dark matter particle in a detector and secondly to discriminate such an energy deposit from known radioactive backgrounds. In the following we will address these challenges and describe the solutions developed within the EDELWEISS collaboration. We will start to address the first question which encompasses the detector design and then go on to the second question which also involves the setup of active and passive shields as well as the location in an underground laboratory. The results achieved within the EDELWEISS-II setup will be reviewed and an analysis of the muon-veto system efficiency performed for EDELWEISS-II and extrapolated to EDELWEISS-III will be presented. Last the upgrades and changes to the EDELWEISS-III setup will be summarized with special emphasis on all modifications that affect the data processing and analysis and hence the work of this thesis.

2.1. Ge-bolometer detection principle

As already elucidated in section 1.3.3 the expected signal from elastic WIMP nucleus scattering is usually modeled by an exponentially decreasing energy spectrum. The WIMP mass with respect to the target nucleus mass governs the behavior of the decay parameter of that exponential. Hence, in order to gain in sensitivity and to explore the parameter space for lower WIMP masses in the range of $(1-10)\,\mathrm{GeV/c^2}$ an excellent energy resolution and threshold in the sub keV range is required. Furthermore, for the successful identification of a signal, all background sources have to be excluded. Two distinct strategies exist to achieve this goal. The dominant strategy is the use of the different properties of recoiling nuclei and electrons (see f.e. [136, 115, 110, 107, 94]) to discriminate signal and background, but also the alternative strategy of shielding an inner sensitive volume from all backgrounds f.e. [103] is actively pursued. For a more detailed overview of different techniques we refer the reader back to the discussion in section 1.3.3 and reference [137].

2.1.1. Discrimination of electron recoils versus nuclear recoils

In EDELWEISS the discrimination is achieved via a calorimetric measurement of the transferred energy in the phonon channel at $18\,\mathrm{mK}$ and a simultaneous measurement of the ionization by collection of the created free charge carriers with an applied electric field.
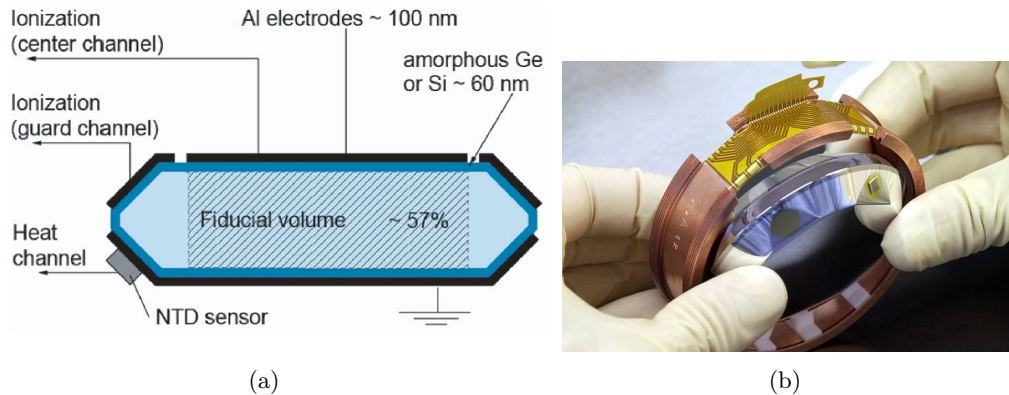
Figure 2.1.: (a) Scheme of the EDELWEISS-I detector and (b) photo of such a detector with the copper casing and the NTD-Ge thermistor glued on the surface.

The difference in ionization stems from the different stopping properties of electrons with respect to slow heavy nuclei (charged ions) within the detector. These properties have been modeled by Lindhard in order to calculate stopping ranges for charged particles [138, 139]. The same model was used to estimate the charge yield [87] from the stopping of charged ions in semiconductor detectors. The stopping of heavy ions has a large contribution from ion-nucleus scattering and these processes contribute much less to the ionization than scattering of electrons. As a result, nuclear recoils from WIMP nucleus scattering exhibit only about 1/3 of the charge of the dominant background from γ radiation. Hence these interactions can be separated on an event by event basis. This so-called ionization quenching has been proven to be very well modeled within this theory and a compilation of measurements down to 300 eV has been presented in [140].

In practice, EDELWEISS detectors are fabricated from high purity Ge monocrystals with a net density of impurities of less than 10^{10} per cm^3. For charge collection, Al electrodes are then evaporated onto the surfaces and an NTD (neutron transmutation doped) Ge-thermistor is glued onto the detector to measure the temperature via the change in resistance (fig. 2.1). These NTD sensors are produced by the irradiation of a Ge waver with the neutron flux close to a nuclear reactor. Out of this waver rectangular sensors are cut which are designed to have similar heat capacity as the Ge monocrystal and an operational resistance of a few MΩ. If fabricated correctly they are then operated close to the metal-insulator transition and show a large decrease in resistance for a small temperature increase. For the sensitivity of the measurement, the entire heat capacity of absorber and thermometer has to be as low as possible. While the Ge monocrystal is by far the largest material component its heat capacity follows the Debye law and decreases with T^3. The glue, NTD Ge-sensor and amorphous Ge also have significant contributions to the entire heat capacity at the operation temperature of 18 mK. In fact, going from an initial detector of 70 g to the current 800 g detectors the same sensitivity could be preserved by optimizing the gluing technique, NTD sensor shape and readout. For an EDELWEISS-II crystal of 400 g (70 mm diameter and 20 mm height) a typical value for the heat capacity of absorber and thermometer is C $\approx$ 2 nJ/K, which means that the temperature rise per keV is about 0.1 μK. For the current stabilized NTD sensor this translates into a $\sim$ 50 nV signal on a mV baseline [141]. The entire detector is coupled with a weak thermal link to the cryostat and returns to its equilibrium state with a time constant of (100 - 500) ms. A digitized raw pulse trace with a sampling of 500 Hz is shown in fig. 2.2.

It is worth to note that the NTD sensor is operated in a nonlinear regime. At the applied current, electron and phonon temperatures decouple inside the NTD thermometer. Additionally the temperatures of NTD sensor and absorber can decouple dependent on
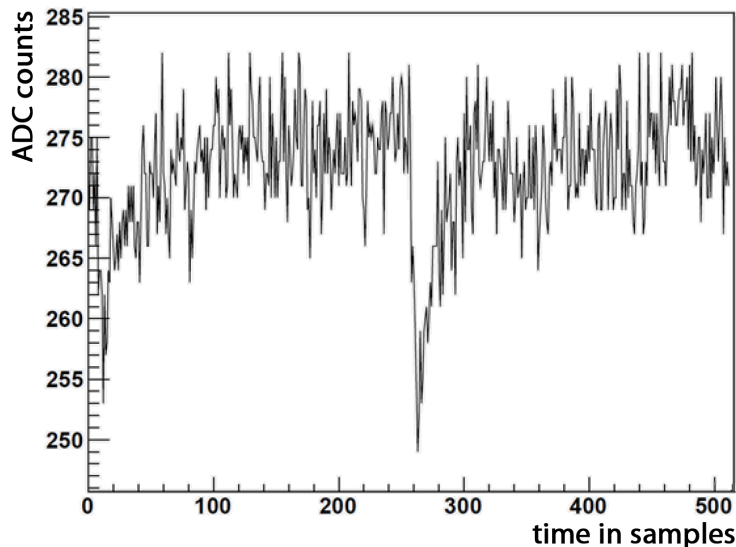
Figure 2.2.: Digitized raw data trace (500 samples per second) of a heat signal recorded by the EDELWEISS-II DAQ.

the different heat links between sensor and absorber and absorber and thermal bath. The return to equilibrium in fig. 2.2 is usually described not by a single exponential decay, but instead with two exponentials, as described in more detail in sec 3.3.1.

To read out the ionization signal, voltages of $4\,\mathrm{V}$ to $8\,\mathrm{V}$ are applied on the Al electrodes. These comparatively small voltages form a compromise between the competing requirements of complete charge collection [140] and keeping a moderate contribution of Neganov-Luke heating [142, 143, 144]. This heating is the analog to the Joule heating, but in this case for charges accelerated in a semiconductor. The band gap of Ge is only 0.735 eV and the energy required to create an electron-hole pair is $\epsilon = 2.96\,\mathrm{eV}$, which is among the smallest known pair creation energies for semiconductors [145]. This means that we expect to have about 340 e^-/h^+-pairs per keV for an electron recoil. This high statistics should lead to an extremely good intrinsic energy resolution. Furthermore, this statistics is not governed by the Poisson case of independent events. Taking into account the possible excitation levels of the individual Ge atoms, the fluctuations are further reduced by a material specific factor called Fano factor [146, 147]. For Ge a calculation has been done by Alig et al [145] and a value of $F = \frac{\sigma^2_{\mathrm{stat}}}{\epsilon \mu_E} = 0.13$ with the mean energy μ_E and the statistical fluctuations $\sigma_s tat$ has been found. The theoretical calculation is in good agreement to experimental measurements in small scale Ge detectors. For large volume Ge detectors statistical effects of trapping can play an important contribution and effective Fano factors of ~0.2 were measured for a 1.68 kg crystal at standard operation voltages [148]. For EDELWEISS detectors, the statistical effects of carrier trapping are probably even more important at the very low operation voltages. Still it is worth to note the theoretically achievable energy resolutions at low energy. With a nominal Fano factor of $F = 0.13$ an intrinsic resolution of $\sigma = 20\,\mathrm{eV}$ at $1\,\mathrm{keV}$ would be expected.

While it is tempting to extrapolate this to even lower energies one should revisit the approximations in the calculations and investigate this particular regime more thoroughly. Also one has to be aware that this argumentation has been done for the case of electromagnetic interactions with the hull electrons. If we are looking at the expected WIMP signal, which is a recoiling nucleus, a large part of the stopping process will be due to the nuclear stopping of the Ge ion. This will tend to randomize the stopping, reduce the energy transfer into ionization processes to about one third and increase the fluctuations in the ionization yield and hence the Fano factor. The reduced ionization yield allows for an
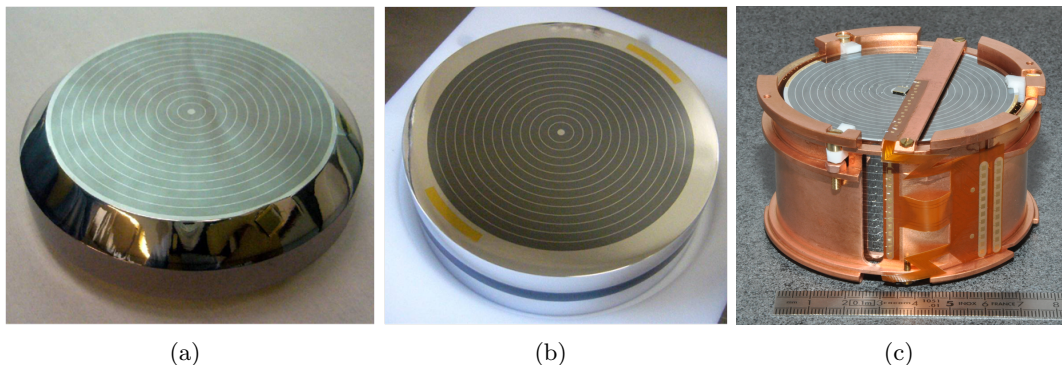
Figure 2.3.: Inter-digitized (ID) and fully inter-digitized (FID) bolometers used in EDELWEISS-II and EDELWEISS-III: (a) 360 g detector with beveled edges - 150 g fiducial (effective) volume, named ID-n; (b) 400 g detector - 170 g fiducial volume, naming convention ID-40n; (c) 800 g detector - 600 g fiducial volume, naming convention FID-80n.

event by event discrimination, when measuring both the charge yield and the calorimetric energy deposit in phonons. The reduced Fano factor, however, worsens the energy resolution and makes the discrimination of lowest energy events more challenging. A study of proton ions incident on Si showed a two times larger Fano factor than gamma particles on Si [149]. In practice, a lot of effort is spent on optimizing the individual ionization channel resolutions and we currently achieve baseline resolutions of the order of 500 eV. Hence, the noise level is still dominated by the readout and not the intrinsic Ge properties and can still be improved with better electronics and different detector designs.

Using the technique of measuring both the charge yield and the calorimetric energy deposit in phonons for an event by event discrimination, the EDELWEISS experiment was the most sensitive direct dark matter search in 2002 [150]. However, this technique still suffered from one short-coming which became limiting soon afterwards [151]. Surface events, especially β decays from ^{210}Pb in the detector holders suffer a misreconstruction of the charge signal. Charges created close to the surface can be collected by the wrong signed electrode during the Coulomb expansion immediately after the initial scattering. Hence, part of the ionization signal cancels and some of these interactions can me misinterpreted as nuclear recoils. This phenomenon can be partially mitigated by the passivation of the detector surfaces with an additional layer of amorphous Ge. However, the detailed physics of these contacts is not well understood [152].

2.1.2. Rejection of surface events

Surface events tend to be problematic in terms of charge collection. Part of the misreconstructed events mimic the ionization yield of the expected dark matter signal of nuclear recoils. Thus, different ways of surface event rejection were studied by EDELWEISS [153, 154] and CDMS [155, 156]. In fig 2.3 the EDELWEISS-solution used in EDELWEISS-II and EDELWEISS-III is shown. For these detectors the planar electrodes have been replaced by inter-digitized ring electrodes. By polarizing alternating electrodes on top with +4 V (-1.5 V) and with -4 V (+1.5 V) on bottom, an inner fiducial volume can be defined. This can be best visualized by looking at the electric field map of these detectors (fig. 2.4). While it is too simplistic to assume that the charge carriers directly follow the field lines [157], this picture still gives a basic understanding about how the surface event rejection works. Charges from surface events will be drifted to same side electrodes. Charges in the bulk however, perceive the stronger potentials from the so-called collecting electrodes at ± 4V and will be collected on these electrodes. By rejection of every event
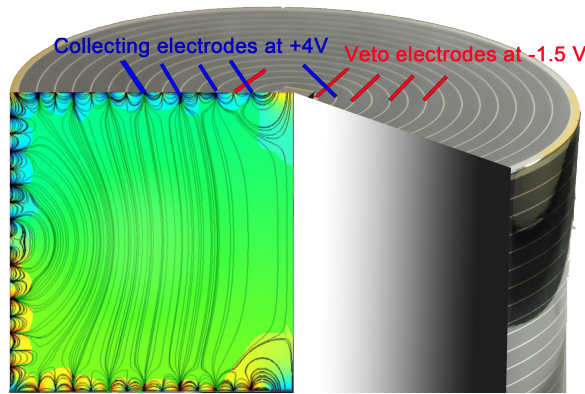
Figure 2.4.: Electric field map of a fully inter-digitized (FID) Ge-bolometer used in
EDELWEISS-III. The green shaded region corresponds to the fiducial volume
where reliable charge collection is expected. Events in the surface region (blue
and yellow), are rejected by a cut on signals on the veto electrodes.

with a signal above noise on the $\pm 1.5\,$V veto electrodes, a fiducial volume is defined, which
is then used for WIMP search. The fiducial volume in current EDELWEISS-III detecotrs
is about $600\,$g of $800\,$ g. An in depth definition and evaluation of the discrimination power
of this cut will be given in the sections 4.3.2 and 4.5.

In practice, the Al-electrodes are evaporated onto the crystal via a shadow mask with a
width of $200\,\mu$m and a spacing of $2\,$mm. The mean thickness of the electrodes is $250\,$nm.
The process was first devised for the planar surfaces of EDELWEISS-II detectors (fig. 2.3
(a) and (b)) and it could be adapted to the cylindrical surfaces for EDELWEISS-III (fig. 2.3
(c)). A problem with surface leakage currents occurring on the cylindrical sides could be
inhibited by a dedicated dry-etching procedure with XeF_2 after standard fabrication [158].
In the following, these detectors will be referred to as ID for detectors with inter-digitized
ring electrodes on top and bottom and FID for the latest detector generation with fully
inter-digitized electrode design on all surfaces. The benefit of the FID design is the much
larger fiducial volume used for the dark matter search of 75% compared to 42% for ID
detectors, together with a simpler electric field configuration. In other words, the amount
of problematic low field regions could be reduced.

In conclusion, the current FID detectors show remarkable signal discrimination powers of:

- probability for γ misreconstruction in the nuclear recoil band $R_\gamma < 6 \cdot 10^{-6}$ at
  90% C.L. [159]

- surface event misreconstruction probability per decay (^{210}Pb $\rightarrow \cdots \rightarrow {}^{206}$Pb)
  $R_{\text{surface}} < 4 \cdot 10^{-5}$ at 90% C.L.[1] [160]

Given this detector performance one can then evaluate the tolerable background levels in
the environment of the EDELWEISS detectors. While this challenge is addressed in more
detail in the following section (2.2.1) and in reference [161], here only a rough comparison
to natural radioactivity levels will be presented. Taking an average person of about $70\,$kg
for instance the intrinsic activity is about $7\,$kBq (^{40}K $\sim 4\,$kBq,^{14}C $\sim 3\,$kBq). This means
within an hour $2 \cdot 10^6$ decays occur. With a cryostat volume of $50\,$l, EDELWEISS is able to
house up to $40\,$kg of detector material, which is already within a factor of 2 with respect to
the average weight of a human body. These detectors are completely surrounded by several
$100\,$kg of material. Hence accepting a similar radioactivity as the natural radioactivity
level, such an experiment would be limited by that background within an hour. Thus,

---

[1]Both probabilities or rejection factors have been evaluated for events above 15 keV

dedicated efforts and special care need to be taken in the selection of materials and the shielding of the Ge crystals.

2.2. The EDELWEISS-II phase

After completion of the EDELWEISS physics reach in 2005 [151] a completely new setup of shields and cryostat was built to house both the EDELWEISS-II (2006 - 2012) [94, 93] phase as well as the EDELWEISS-III phase of the experiment (2013 - ongoing). Since part of this thesis has been performed on the analysis and simulation of muon-induced background in EDELWEISS-II data, we shall present the EDELWEISS-II setup and its results first. We will continue discussing the technical upgrades (sec 2.4) towards EDELWEISS-III. Special emphasis is put on the upgrades and transition in data analysis towards EDELWEISS-III. Expected performance both in terms of dark matter detection potential and in terms of surface background rejection will be reviewed. Finally, first results achieved within this thesis will be presented in chapters 4 and 5.

As discussed in section 2.1.1, special care needs to be taken to install and operate the EDELWEISS detectors in a low radioactivity environment. Especially neutrons which are produced by the spallation of heavy elements, by (α, n) reactions induced by decays in the U/Th decay chain or also importantly in interactions from cosmic rays impeding on high Z material must be avoided. Neutrons, just like the neutral WIMPs, scatter on the nuclei and are thus almost indistinguishable from the WIMP signal[2]. Hence, these experiments are built deep underground so that they are already well shielded from cosmic ray particles. EDELWEISS-II is housed in the underground laboratory of Modane (LSM), which is the deepest underground laboratory within Europe [162]. The $1800\,\mathrm{m}$ of rock on top of the laboratory add up to 4800 m w.e. (meter water equivalent) on average which reduce the cosmic ray muon flux by 6 orders of magnitude down to $5\,\mathrm{muons/m^2/day}$ [7]. Still, an active muon-veto system is used to gain another suppression factor of $\sim(1{:}100)$ on this background. Further characteristics of the underground laboratory have been summarized in reference [161]:

- Neutron flux above 1 MeV $\Phi_n \sim 10^{-6}\,\mathrm{n/cm^2/s}$ [163]

- Uranium, Thorium and Potassium contaminations of $A(^{238}\mathrm{U}) = 0.84 \pm 0.2\,\mathrm{ppm}$, $A(^{232}\mathrm{Th}) = 2.45 \pm 0.2\,\mathrm{ppm}$ and $\Gamma(\mathrm{K}) = 230 \pm 30\,\mathrm{Bq/kg}$ in rock and $A(^{238}\mathrm{U}) = 1.9 \pm 0.2\,\mathrm{ppm}$, $A(^{232}\mathrm{Th}) = 1.4 \pm 0.2\,\mathrm{ppm}$ and $\Gamma(\mathrm{K})77 \pm 13\,\mathrm{Bq/kg}$ in concrete [164]

- Radon level of $\Gamma(\mathrm{Rn}) = 20\,\mathrm{Bq/m^3}$ [161]

2.2.1. The experimental setup

In order to reduce the radioactivity in the vicinity of the detectors the following setup (fig 2.5) has been installed in a clean room environment in the underground laboratory of Modane: From outside to inside the shielding consists of 46 plastic scintillator modules with a total surface of $100\,\mathrm{m^2}$. This active muon-veto system layer almost hermetically encloses the further experimental setup. Remaining gaps in the system are due to the support structure as well as electrical and cryogenic supply lines. The efficiency of the muon-veto system for the dark matter search was evaluated to $97.7\% \pm 1.5\%$ [7]. The analysis and simulations pursued in this thesis to derive this result are given in more detail in sec. 2.3 and have been published in reference [7]. The active muon-veto system is followed by two passive shielding layers. A rectangular polyethylene castle of at least $50\,\mathrm{cm}$ thickness reduces the flux of fast neutrons (about 1-20 MeV) by five to six orders

---

[2]We note that depending on the setup a partial suppression can be realized with information from multiple scattering
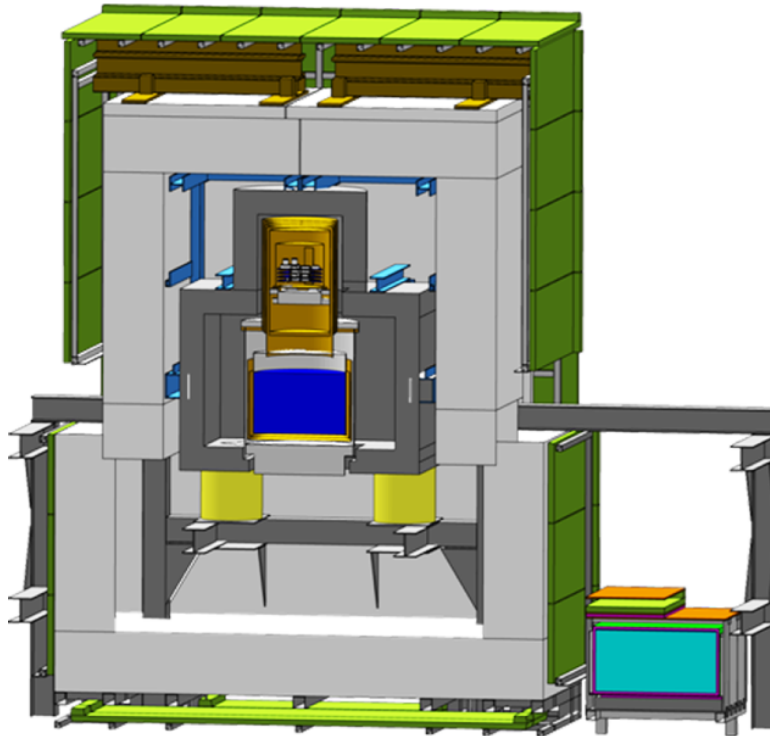
Figure 2.5.: EDELWEISS-II setup consisting of the following shielding layers (from out-side to inside): plastic scintillator modules of the muon-veto system (green); polyethylene (PE) shield to moderate neutrons (light gray); lead shield (dark gray); thermal shields from electrolytically refined copper (gold) and the detector housing (gray). A previously operated additional subdetector, a Gd-loaded liquid scintillator neutron telescope is shown in blue.

of magnitude [161]. With this attenuation a limit of $N_{NR,\,exp} < 0.1$ nuclear recoils was expected from the laboratory halls for the entire EDELWEISS-II dataset of 384 kg·d [94]. The second large passive shielding layer is an 18 cm thick lead castle which has the form of a cylinder put onto a rectangular cuboid and which encloses the cryostat beneath. This shield is very effective for the gamma ray attenuation, and the remaining gamma ray background from outside is less than 1% of the total remaining gamma ray background in the detectors [161]. However, contemporary lead has a few drawbacks: The shield itself contributes to the gamma ray background with the 46.5 keV γ-line from the ^{210}Pb decay as well as from X-rays and bremsstrahlung photons from the β^- decay of ^{210}Bi. Furthermore, its high atomic number makes it an ideal target with a huge neutron yield from incident high energy particles (e.g. cosmic ray muons). The first effect is mitigated by the installation of an additional 2 cm thick roman lead shield. For EDELWEISS this material was salvaged from a sunken roman galley [165] and in the time it passed on the bottom of the Mediterranean see, about 72 half times of ^{210}Pb passed ($T_{1/2}(^{210}$Pb) = 22.3 a). Thus, the entire lead shielding is only responsible for 3% of the gamma ray background in the detectors [161]. The second aspect, e.g. the high neutron yield from muons can be tolerated for the EDELWEISS-II and EDELWEISS-III physics reach as long as the muon-veto system is operated continuously with an efficiency of at least 98%.

In between the lead shield and the outermost cryostat screen, there is a small gap with an entire volume of 0.1 m³. Radon depleted air is constantly circulated through this volume at a rate of 0.5 m³/h. The activity is hereby reduced from $\sim 20\,Bq/m^3$ to $\sim 20\,mBq/m^3$ [161]. Still the best fit between a MC background simulation and the observed gamma ray background in the detectors could be achieved with a significant pollution around the

300 K outermost cryostat screen. Whether this was due to an unaccounted contamination in the cryogenic pipes, electronics or due to radonized air could not be discerned, but it did contribute about 27% of the gamma background in the EDELWEISS-II detectors.

The entire set of shields was constructed in two parts and is mounted on rails. Thus the shielding can slide apart to provide access to the cryostat.

2.2.2. The cryogenics system and material selection

The EDELWEISS-II cryostat is a large dilution cryostat with an experimental volume of 50 l. It is an in-house development (Institut Néel, Grenoble) where the usual orientation has been reversed and the experimental chamber has been mounted on top. This allows better access as well as an additional decoupling from the mechanics and tubes of the mixing chamber. All pumps are put several meters away and the experimental volume is put on pneumatic dampers to limit noise sources from vibrations. Its thermal layers of 300 K, 100 K, 40 K, 4.2 K and 10 mK allow to run the entire volume of the experimental chamber continuously at 18 mK with $\sim$40 kg of detective material for months and years even. Furthermore, there is a dedicated space at 1 K and 100 K to house RC- and FET- (field effect transistor)-electronics. This space below the experimental chamber is shielded by another internal lead block to limit radiation from electronics and PCBs (printed circuit board) which are one of the most radioactive parts that remain inside the cryostat. While the requirements of low noise, reliability, modularity and changeability are sometimes conflicting with low mass and low radioactivity for electronics, at least for all other components low radioactivity is essential. Better background understanding of internal components and material selection is the main reason for an expected factor 10-100 improvement from EDELWEISS-II to EDELWEISS-III in the same setup. Within EDELWEISS-II the following components were identified as the major sources of the remaining gamma background rate of $\Gamma_\gamma = 82$ events/kg/day [161].

1. Copper screens of the cryostat $\sim$ 40%

2. Unidentified pollution at 300 K (see sec. 2.2.1)$\sim$ 27%

3. Copper casings of the detectors $\sim$ 17%

For the neutron background, the dominant components of the total expectation of $N_{NR} = (1.0 - 3.1)$ events (90% C.L.) for EDELWEISS-II were:

1. PCBs of warm electronics $\sim$ 50%

2. 1 K Al connectors $\sim$ 20%

3. Coaxial signal readout cables $\sim$ 15%

It is worth noting that the U/Th contamination could only be measured for the first two items contributing to the neutron background. For the remaining items, upper limits from gamma spectroscopy measurements were used for the simulation.

2.2.3. Results of the EDELWEISS-II phase

The data collected during the WIMP search are usually presented in a scatter plot of the discriminating variable, here the ionization yield (ionization/recoil energy) versus the measured recoil energy (fig. 2.6). In contrast to experiments which measure only a single energy quantity, the recoil energy can be calculated independently of the type of the interacting particle in the crystal. Calibration is then performed such that electromagnetic interactions have an ionization yield of unity. In this calibration, the quenching for nuclear recoils follows a parametrization of $Q(E) = 0.16 \cdot E^{0.18}$ [166] which is compatible with the
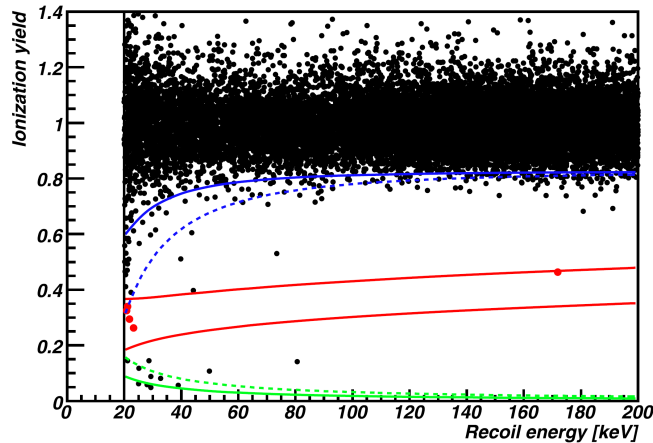
Figure 2.6.: Event distribution in ionization yield and recoil energy of the EDELWEISS-II WIMP search data (427 kg·d). The 90% signal region with 5 candidate events is marked in red. Average (worst) one-sided 99.99% rejection limits for electron recoils are drawn in solid (dashed) blue. Average (worst) ionization thresholds in solid (dashed) green. Figure from [94].

Lindhard model for the stopping of heavy ions. Additionally, it takes into account a heat quenching for the energy escape via photon emission and crystal defect creation from nuclear stopping. An individual factor for the heat quenching has been measured in extensive neutron calibrations to be $Q\iota = 0.91$ [140].

A signal region is defined by calculation of a 90% acceptance band (fig. 2.6 red) around the central Lindhard parametrization. Five nuclear recoil candidates were found in the entire measurement period of EDELWEISS-II, 325 live days (WIMP search) with 10 ID-detectors, 170 g fiducial mass each [94]. With an expected background of less than 5.1 events at 90% C.L. no significant excess was observed [161]. A limit on the spin independent WIMP nucleon cross-section was calculated using an optimum interval method [167]. This method allows to find a limit in the presence of an unknown or, as for EDELWEISS, in a case where the background is not modeled accurately enough. The resulting limit is given as red thick solid line in fig.2.7. A compilation of results from different experiments and a dedicated analysis of the EDELWEISS low WIMP mass (low recoil energy region) [93] is also shown. The EDELWEISS-II results [94] were combined with the CDMS limits [168] to extract a combined limit on dark matter scattering from Ge experiments [106] (dotted light red). This combined limit excludes a cross-section of $3.3 \cdot 10^{-44}\,\mathrm{cm}^2$ at 90% C.L. for a WIMP mass of $90\,\mathrm{GeV/c^2}$. At the time of publishing in 2011 this was the strongest limit from cryogenic experiments and 2nd only to the limit from XENON100 [169] (dashed blue). A projection for the initial EDELWEISS-III goal of 3000 kg·d with no event in the nuclear recoil band has been added in dashed red.

As assumption in this projection we took the reduction of the background from O(5) to less than one event in the ~10 times larger exposure of 3000 kg·d. Additionally, an improvement in resolution compatible with a full efficiency and 99.99% gamma discrimination above 10 keV instead of 20 keV was considered. In order to assess these assumptions, especially the background reduction, it is worth to disentangle the different background contributions. The limit of 5.1 events was calculated very conservatively from the sum of all individual 90% confidence levels. The largest component was the ambient or rather internal neutron background with $N_{\mathrm{amb-n}} < 3.1$ events [161]. This was followed by a contribution from misidentified gammas $N_\gamma < 0.9$ events [94]. Muon-induced neutrons were assessed to contribute $N_{\mu-n} < 0.7$ events[7] and misidentified surface events were expected to yield $N_{\mathrm{surface}} < 0.3$ events [94].
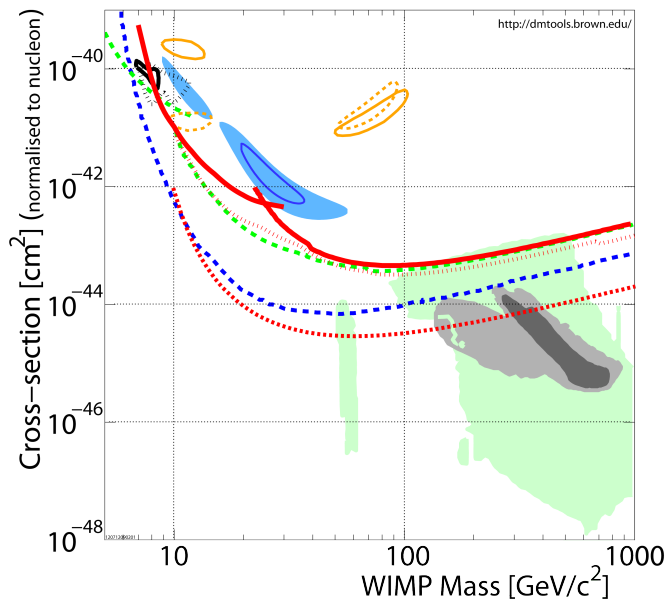
Figure 2.7.: Direct dark matter search results for the spin independent WIMP-nucleon interaction cross-section as presented at the Identification of Dark Matter conference in 2012. Event excesses interpreted in terms of a dark matter signal were reported by CRESST II [8] (shaded blue) , DAMA/LIBRA [170] (yellow contour) and CoGeNT [171] (black). The given regions correspond to their WIMP parameter regions at 2-σ C.L.. Exclusion limits in tension with a signal interpretation of the observed excesses were published by EDELWEISS-II [94] and EDELWEISS-II low mass [93] (solid red), CDMS II [168] (dashed green), CDMS-EDELWEISS [106](dotted red), XENON100 [169](dashed blue). Phenomenologically allowed regions of CMSSM parameter space were computed in [172] (shaded green) and in [173] (shaded gray). A projection for 3000 kg·d of exposure within EDELWEISS-III is shown in dashed red.

The dominant origin of ambient neutrons in EDELWEISS-II was already discussed in more detail in sec. 2.2.2. The EDELWEISS-III solution to this background is better material selection as well as additional shielding layers. The solution is summarized in sec. 2.4.1. The rejection power for electron recoil and surface events can be varied by analysis cuts as a function of the acceptance assuming that these event populations follow well behaved Gaussian models. The validity of this assumption for ID and FID detectors will be revisited in sec. 2.4.2. Furthermore, background radioactivity levels can be reduced by employing even cleaner materials. The then remaining background component is the one of muon-induced neutrons and here the limit of $N_{\mu-n} < 0.7$ events is dominated by the acceptance of data periods without running the muon-veto system and the uncertainty in the measurement of the muon-veto system efficiency. Hence I dedicated the first month of my PhD to refine my measurements of the muon-veto system efficiency from my diploma thesis [4] and to extract tighter constraints on the muon-veto system efficiency with the use of MC-simulation. The methods and results are described in sec. 2.3.

2.3. Analysis of the EDELWEISS-II muon-veto system efficiency

As summed up in the previous paragraph, the muon-induced neutron background ($N_{\mu-n} < 0.7$ events) made up a significant fraction of the entire expected background of less than 5.1 events in EDELWEISS-II. This value could be attributed to two equally large contributions. One coming from data taken without active muon-veto system and the other one being solely due to the error from a very low statistics measurement of the muon-veto

system efficiency $\epsilon = 1^{+0}_{-0.072}$ [4] during my diploma thesis. While it was clear that a factor 2-3 in exposure would be possible without any muon-induced background, it was still an open question whether the first muon-induced background event(s) would appear around the initial 3000 kg·d goal for EDELWEISS-III.

At the same time, a similar limit of $\epsilon \geq 94.9\%$[174] was obtained for the muon-veto system efficiency by derivation of the trigger efficiencies of the individual modules and subsequent application of these values to simulated muon tracks. It wasn't tried to quantify the errors since it was clear that the neglect of secondaries in the simulation led to large systematic uncertainties in the results. Interfaced with a full MC simulation, however, this method was expected to give a better quantifiable estimate of the muon-veto system efficiency. Furthermore, the method allows to extract the absolute flux of muons in the underground laboratory of Modane, which is an interesting result in its own right.

In order to pursue this work within this thesis, we could rely on an existing MC simulation code which was first developed in parallel to the construction of the EDELWEISS-II setup [5] and which was then extended and thoroughly evaluated with respect to its neutron yield in [6]. While discrepancies of more than a factor 2 have been reported in the literature between MC-simulation codes based on Geant4 [175] and Fluka [176] and the experimental results [177, 178, 179, 180, 181], the simulation code developed within EDELWEISS [6] is in agreement with experimental results within 20%. Only looking at the electromagnetic physics of the muon-veto system we expect even lower uncertainties from the MC-simulation. However, this required a more accurate modeling and calibration of the detector response of the entire muon-veto system.

In the following the details of this analysis will be presented. After introduction of a few characteristics of the muon-veto system DAQ and signals the basics of the Geant4 simulation code will be summarized. The extraction of individual detector module response functions is detailed and the validity of the detector response model is assessed in terms of a crosscheck of the angular dependent muon flux between MC-code and experiment. Finally, the main results on the characteristics of muon-induced events are given as well as the estimated muon-veto system efficiency and the muon flux underground. A first extrapolation to EDELWEISS-III is discussed.

2.3.1. Calibration of the muon-veto system

The EDELWEISS-II muon-veto system consists of modular plastic scintillator bars of 5 cm thickness, 65 cm width and 2 m to 4 m length (Bicron BC-412) which are read out by PMTs (Photo Multiplier Tubes) to record the timing and deposited energy of any interaction. In detail, the 46 individual plastic scintillator modules are read out by two groups of four 2-inch PMTs (Philips Valvo XP2262/PA). Each group has its individual HV supply and readout channel, which means in total 92 signal channels can be read out per event. An event recording is started, once both PMT groups of a module pass a certain trigger threshold within a window of 100 ns. The timing of these two PMT groups can then be used to reconstruct the position of the interaction along the module axis and the amplitude to reconstruct the energy. These two signals are often referred to as TDC (Time to Digital Converter) and ADC (Analog to Digital Converter) in the computer based analysis using the digitized signals. For the reconstruction of muon-induced bolometer events the timing from the bolometer DAQ is synchronized via an optical fiber. Apart from this synchronization, both systems operate independently and coincidences are reconstructed in an offline analysis.

A muon as minimal ionizing particle deposits on average 11.8 MeV in a horizontal module and 24 MeV in a vertical module. It is usually registered in the upper half of the muon-veto system as incoming particle and once again in the lower part of the muon-veto system
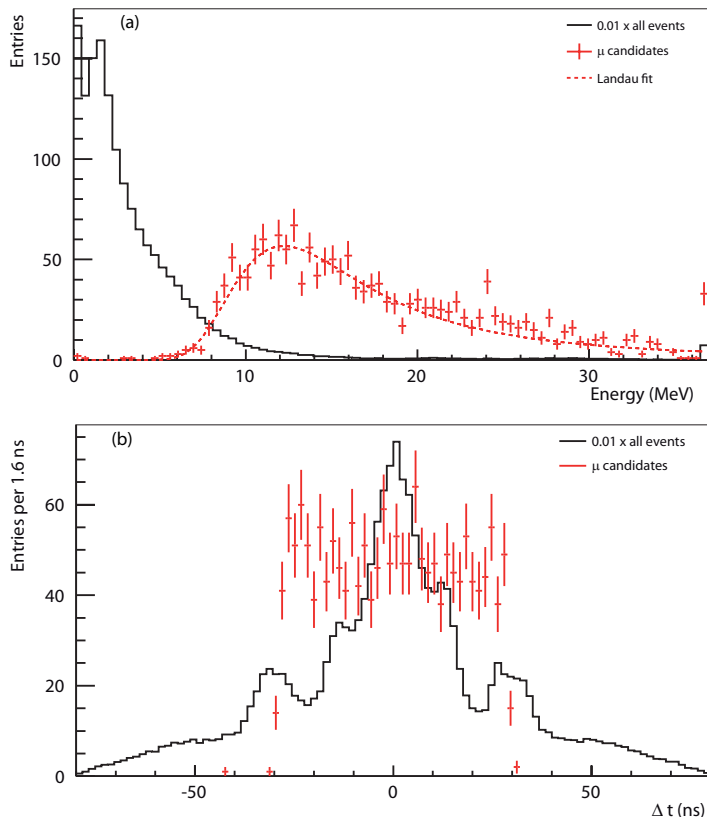
Figure 2.8.: Energy spectrum (a) and time difference (b) of all events that meet the standard
trigger condition (black line) and muon candidate events (red data points) for
a horizontal module of the muon-veto system. In order to fit both distributions
onto the same scale, the spectra for all events were scaled by 0.01. Muon can-
didate events were selected by requiring two modules that fulfilled the trigger
condition. Their energy distribution can be well described by a Landau function
(dotted red).

as outgoing particle. The energy threshold for each module is kept at a lower value of
$\sim 5\,\mathrm{MeV}$ at the center of each module in order to guarantee a high detection efficiency
even for grazing muons. In order to keep this value stable in spite of ageing effects and
transparency loss of the scintillators, the high voltage of the PMTs has to be increased
periodically. The energy threshold will still increase towards the module ends though.
This characteristic behavior is reflected by the low energy background data in fig. 2.8
b. The electromagnetic background completely dominates the data acquisition rate and
indeed the dominant part stems from interactions in the module center. The count rate
then decreases towards the module ends corresponding to values of $\Delta t = \pm 30\,\mathrm{ns}$. The two
bumps at the module edges can be attributed to the thicker scintillator layer and thus
higher detection efficiency at the module ends. In contrast, a selection of muon candidate
events reduces the count rate from $\sim 1\,\mathrm{Hz}$ down to $\sim 3.5 \cdot 10^{-4}\,\mathrm{Hz}$. A common muon
candidate cut requires energy deposits in at least one module from both lower and upper
part of the muon-veto system. These muon candidate events are typically much higher in
energy (fig. 2.8 (a)) and do not show a significant influence of the variation of the threshold
along the module axis. Hence, the position dependence of the threshold is only of minor
importance for the detection of muons and can be neglected in a first approximation.

The calibration can then be performed on such a selection of muon candidate events, where
the MPV (most probable value) of the Landau distribution is fitted once in the data and
once in the results of the MC simulation. This method is self-contained and can be applied
on the data acquired without the need of taking specific calibration data with a source or

installing additional hardware. However, it suffers a few defects. The observed Landau distribution is a convolution of the Landau distributions of all MIPs (Minimal Ionizing Particles) with all allowed different incident angles and track lengths. This broadens the Landau spectrum and increases the uncertainty in the position of the MPV from a fit. While it is in principle possible to select a combination of just a single top module and a single bottom module and thereby narrow the possible incident angles and track length, this cuts harshly into the already scarce statistics of O(1000) events for ∼1 year of data and then limits both fit convergence and accuracy. The following compromise was used in this work: For each module, negligible energy deposits in the two adjacent modules is required, together with an energy deposit above the trigger threshold on the opposite muon veto side. While this worked well for bottom and top modules, for side modules energy deposits from top (bottom) had to be allowed, too, to increase the statistics. The anti coincidence cut for adjacent modules proved useful to reduce the contribution from muon-induced secondaries and suppressed the low energy part of the spectra to get cleaner Landau peaks. Applying this cut we could achieve a reliable fit convergence and extract the individual calibration coefficients for all modules. While the fit accuracy of the MPV is of the order of 5% for most fits, it varies from module to module and a conservative overall accuracy including systematics of 20% is assumed. Calibration results for individual modules are detailed in appendix A.

The large uncertainty estimate is supposed to account for the following potential source of a systematic bias. First, the measured Landau spectra were assumed to lie entirely above threshold and could hence be extracted from the simulation independent of the individual module thresholds. Second, the coincidence selection is assumed to result in a pure muon sample that can be well reproduced in the simulation. While we believe that these assumptions are in general well met, see e.g. fig. 2.8 and the general good agreement between simulation and experiment (fig. 2.12), we have hints that we are indeed systematically overestimating the average calibration factor of 5.44 keV/ADC-value [182]. A new approach at calibrating the muon-veto system with a dedicated source and investigation of the trigger efficiency along the module axis is ongoing. First results show indeed a systematic difference between the two methods.

Further details concerning the muon-veto system DAQ are given in [7, 183] and the specifications of the plastic scintillator including measurements of the attenuation length and spectral quantum efficiencies are collected in [184].

2.3.2. Geant4 simulation of muon interactions

Modeling of muons and their interactions has been performed with Geant4 package version 4.9.2 [175, 185]. The EDELWEISS-II setup is included in considerable detail as depicted in fig. 2.5. The surroundings contain the main components of the adjacent NEMO-III experiment [186] as well as the concrete walls and the rock above the experiment. These parts have been added since they can play an important role in shower production for muons or as neutron sinks or mirrors (dependent on the material). For computing reasons muons cannot be tracked through 1800 m of rock. Instead, the muon flux underground is calculated from the muon spectrum at sea-level

$$\frac{dN_0}{dE_\mu} = \frac{0.14 \ (E_\mu/\text{GeV})^{-\gamma}}{\text{cm}^2 \ \text{s sr GeV}} \left(\frac{1}{1 + \frac{1.1E_\mu cos\Theta}{115 \ \text{GeV}}} + \frac{0.054}{1 + \frac{1.1E_\mu cos\Theta}{850 \ \text{GeV}}} \right),$$ (2.1)

[187] with the cosmic ray exponent $\gamma = 2.7$ and the elevation map of the Fréjus mountain [188]. The influence of the thickness of the atmosphere is encoded in the zenith angle dependence $cos\Theta$. The muons are then generated on a hemisphere 30 m above the EDELWEISS detectors (fig. 2.9). This ensures that these initial muons have more than
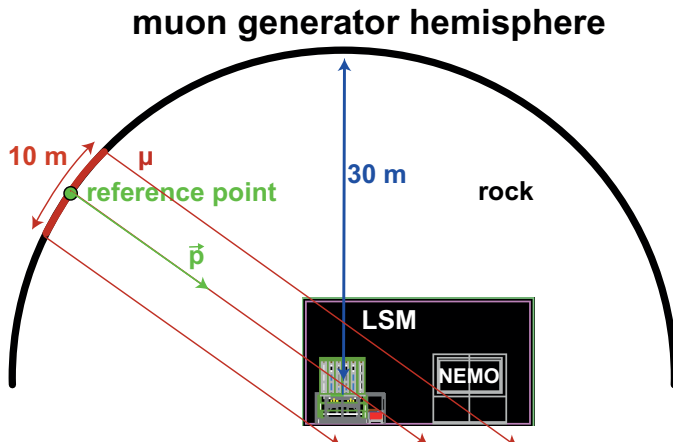
Figure 2.9.: Scheme of muon generation and LSM geometry as implemented in Geant4. The entire volume around the rectangular cuboid representing the LSM laboratory (black) is implemented as Fréjus rock. Even below the setup, 2 m of rock have been added to avoid boundary effects.

10 m of rock to develop an equilibrium of secondary shower particles before entering the laboratory. Reference starting points along the hemisphere are sampled according to the analytically calculated muon flux. Once a reference point with its specific momentum vector $\vec{p}$ has been chosen, the starting position is randomized on a disk of 5 m radius in order to ensure the complete homogeneous illumination of the muon-veto system and its close surrounding. This procedure generates a fraction of 40.9% of muons that are started with a momentum vector that geometrically penetrates the muon-veto system. The remaining 59.1% of muons illuminate the surrounding and take into account processes which create fast neutrons outside of the shielding. In very rare cases such neutrons can still reach the detectors [5]. The direction as well as the energy spectrum of simulated muons of $2\,\text{GeV} - 200\,\text{TeV}$ has been sampled with $2 \cdot 10^6$ generated muons.

The generated particles are then propagated through the entire geometry based on the QGSP_BIC_HP reference physics list of Geant4 version 4.9.2 with a few modifications as suggested in [5]. The changes include the use of the "low energy extension" packages for electron, gamma and muon interactions but mainly focus on hadronic interactions: The addition of the G4MuNuclear package is important for the neutron yield of fast neutrons, the CHIPS (chiral invariant phase space) model for gamma-nuclear processes, and the insertion of the G4PreCompoundModel and G4LENeutronInelastic are necessary for the accurate modeling of hadron physics and especially neutron scattering. The applicable energy ranges for the different models are given in fig. 2.10.

The energy deposits in the detective volumes, e.g. the plastic scintillator modules of the muon-veto system, are stored as well as position and physics information of the underlying process. Using this information we could evaluate the direct coverage of the muon flux to a value of 98% with the remaining 2% of primary muons going through gaps in the geometry. Dependent on the energy threshold of the plastic scintillator modules, the muon-veto system can also detect part of this remaining flux through the detection of secondary particles.

2.3.3. Determination of the muon-veto system response model

In order to model the detector response of the entire muon-veto system we started by modeling the response of individual plastic scintillator modules. The threshold of an individual module was approximated by an error function $\text{erf}(x) = \frac{2}{\pi} \int_0^x e^{-t^2} dt$ resembling the

charged pions						
inelastic scattering	BERT	LEP	QGSP			
photo-nuclear	CHIPS		QGSC			
electro-nuclear	CHIPS					
neutron						
elastic scattering	HP	LEP				
inelastic scattering	HP	PC	BiC	LEP	QGSP	
proton						
elastic scattering	LEP					
inelastic scattering	PC	BiC	LEP	QGSP		

10 MeV 100 MeV   1 GeV   10 GeV 100 GeV   1 TeV   10 TeV

Figure 2.10.: Physics models and application ranges for various simulated hadronic processes. The abbreviations are: data driven high precision model (HP), pre-compound model (PC), binary cascade (BiC), Bertini cascade (BERT), LEP low energy parametrized model, chiral invariant phase space model (CHIPS), quark-gluon string model (QGS) using pre-compound (QGSP) or CHIPS (QGSC) to fragment. Figure from [6].

efficiency from a step-function threshold smeared with a Gaussian resolution. In practice, a single error function model for the trigger efficiency of a plastic scintillator module can only be an approximation since we see the effect of the light attenuation and hence the position dependent threshold within a module in the trigger probability for low energy background events (fig 2.8). Furthermore, the threshold within a module does not need to be symmetric a priori. The high voltage of the PMTs is adjusted to fulfill this objective, but in principle there can be different efficiencies for the two PMT groups at the module ends. Still, the simple error function model can be fit to the data with very good agreement and little systematic uncertainty. In order to extract the trigger probability from the data we rely on the storage of all nonzero ADC and TDC values once a single module had an internal coincidence (TDC data of both ends above threshold within 100 ns). This allows to use a dataset where always a second module apart from the module under investigation produced the trigger. In this dataset the fraction of events which had an internal coincidence of the TDC values, or in other words which met the trigger requirement can be plotted versus the deposited energy. An example of the resulting efficiency curve $\epsilon_i(E)$ for a module i is given in fig. 2.11 (a). For the entire set of modules an average threshold energy of $\langle E(\epsilon_i = 0.5)\rangle = 7\,\text{MeV}$ and an average standard deviation of $\sigma(E) = 1.9\,\text{MeV}$ was found. The individual results for all modules are given in appendix A.1 in table A.1.

Using this detection efficiency one can calculate an integrated muon detection efficiency for a single module by weighting the muon spectrum with the measured trigger efficiency.

$$\epsilon_i^\mu = \frac{\int_{6\text{MeV}}^{\infty} \epsilon_i(E) N_{\mu,i}(E) dE}{\int_{6\text{MeV}}^{\infty} N_{\mu,i}(E) dE}. \tag{2.2}$$

The effect of this efficiency decrease is shown in fig. 2.11 (b) as the correction of the black Landau spectrum for the trigger inefficiency resulting in the red spectrum. There is good agreement of a Landau fit with data for large energy deposits but at low energies additional contributions from secondaries are expected in the data. This can be seen for the lowest energy bins of fig. 2.11. After correction of the data for the inefficiency, the Landau fit (solid red) and corrected data points (red) begin to diverge at energies below $\sim 6\,\text{MeV}$. Hence, a threshold of $6\,\text{MeV}$ was used for the evaluation of the individual muon module detection efficiencies. This ensures that only a negligible part of the Landau spectra is omitted while keeping uncertainties due to secondary particles at the level of a
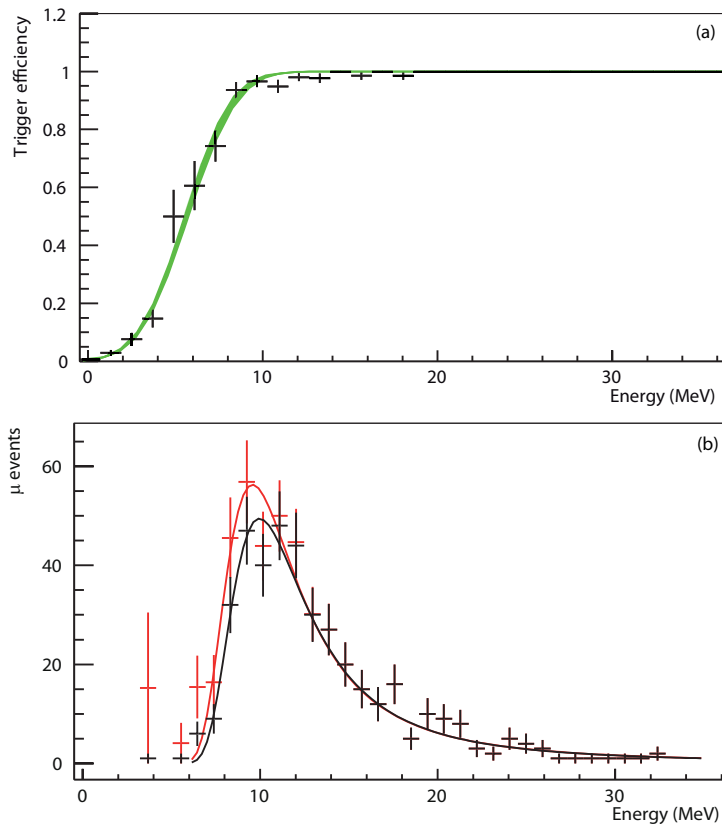
Figure 2.11.: Trigger efficiency $\epsilon_i(E)$ for a single module (a) and effect of this efficiency on the measured Landau spectrum from muon candidate events in this module (b). The original data is shown in black. In red, the data has been scaled to account for the measured trigger (in)efficiency of this module. Solid lines represent Landau fits through the data points. The green band in (a) is the 1 σ confidence band of an error function fit where $\epsilon_i(E)$ has been fixed to unity at the highest energy.

few percent. In conclusion, an average integrated muon detection efficiency of $\langle \epsilon_i^\mu \rangle = 95\%$ with $\sigma(\epsilon_i^\mu) = 4\%$ per module could be deduced.

While this result is not directly applicable to the dark matter search, it is a very interesting result in order to find individual modules which can be optimized in terms of high voltage and consequent muon detection efficiency.

2.3.4. Validation of MC-code and detector response model

In order to find the muon-veto system efficiency which is applicable for the dark matter search, we interfaced the above detector response model with the MC simulation results. In addition to the trigger efficiency this incorporates a modeling of the position reconstruction which allows to directly test and compare the muon simulation together with the detector response model in terms of the measurement of the derivate of the muon flux with respect to azimuth and zenith angles.

This measurement yields a negative imprint of the shielding provided by the mountain profile convoluted with the acceptance of the specific experimental setup. It allows hence to evaluate our understanding of both muon generation in the MC simulation and the detector response model. In order to disentangle these two different sources we also used the acceptance map of the Fréjus experiment and tested our simulation and muon generation versus its data [189].
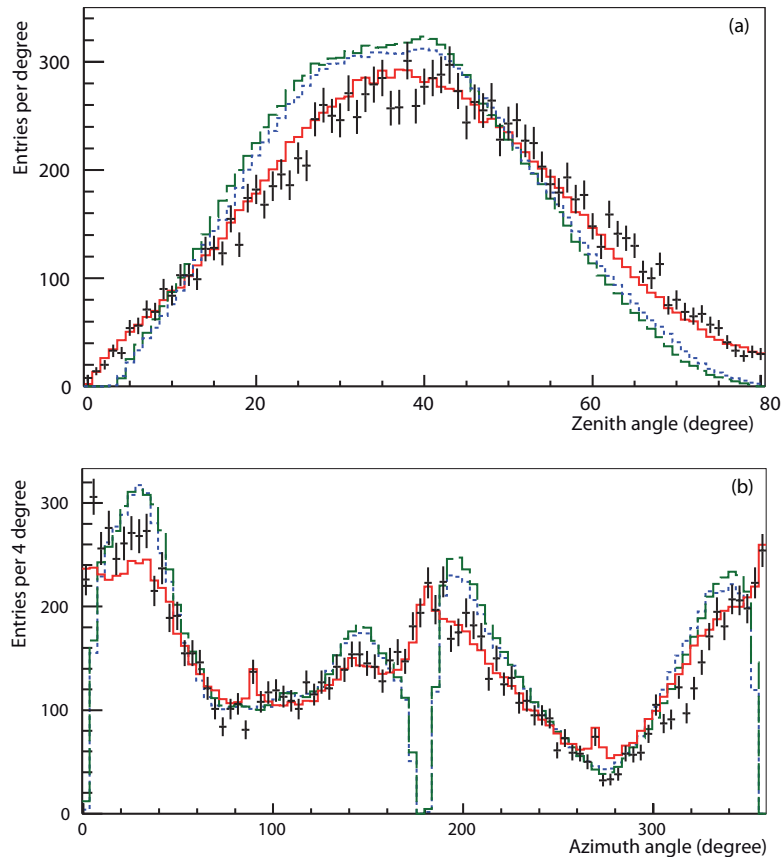
Figure 2.12.: Reconstructed zenith (a) and azimuth (b) angle distributions of muon candidate events in the EDELWEISS-II muon-veto system (black data points) and in the Fréjus proton decay detector (dotted blue). In our MC simulation we can achieve good agreement both with the Fréjus data [189] (dashed green) as well as with the EDELWEISS-II data (solid red) dependent on the detector acceptance model. Fréjus data and the two simulation data sets were normalized to the EDELWEISS-II data set.

The resulting zenith and azimuth angle spectra are displayed in fig. 2.12. Black data points are results obtained from the EDELWEISS-II muon-veto system data. The simulation has been normalized to match the integrated EDELWEISS-II statistics. Simulation results are obtained from the EDELWEISS-II simulation applying the EDELWEISS-II muon-veto system detector response model in solid red and applying the acceptance map obtained from the Fréjus collaboration in dashed green. The good agreement between MC-simulation and experimental data both for EDELWEISS-II as well as for Fréjus data [189] (normalized to the EDELWEISS-II dataset) gives confidence that first of all muons are generated with correct energy and angular dependence and that secondly also the detector response models are consistent. The difference between the Fréjus and EDELWEISS-II datasets show the importance of the detector response and give a feeling for the possible deviations that one can expect from different acceptance and resolutions and hence also from errors in the modeling of the detector response.

The observed spectra can be well understood with the knowledge of the actual mountain profile as displayed in fig. 2.13. The Fréjus tunnel cuts through the Alps almost directly from north to south. The smallest rock overburden is not found in the vertical direction as for the case of mines but in the direction to the mountain flanks. The highest muon flux resulting from the combination of low rock overburden and large angular acceptance is thus observed at a zenith angle of $35°$. These flanks show up again in the azimuth profile

Figure 2.13.: Geographic map of the Fréjus mountain with the highway tunnel crossing the
Alps from north to south (red). The laboratory is located at the middle of the
tunnel just before the border between France and Italy (yellow) with the largest
possible rock overburden of $\sim 1800\,\text{m}$. An elevation map along the length of
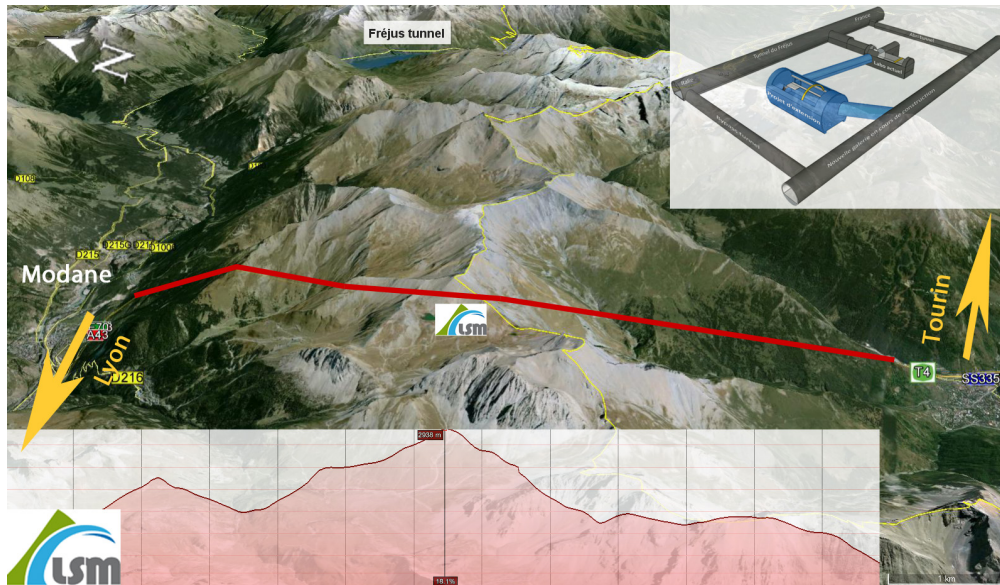the tunnel is shown in the lower left corner. The overlay in the top right shows
the current laboratory halls of LSM in gray and a planned extension in blue.
Figure adapted from [190].

at angles of 20° and 180°. Note that the reference frame used in fig. 2.12(b) is oriented at
the laboratory walls which have an offset of 16° to the north direction. Along the mountain
ridge from east to the west (100° and 280°) the smallest muon flux is observed.

Some peculiarities in the azimuth spectra like the two gaps at 0° and 180° for the Fréjus
experiment require a more detailed knowledge of the experimental setup and the position
reconstruction. For the Fréjus experiment these directions correspond to the orienta-
tion of the detector planes where the experiment has negligible detection efficiency. For
EDELWEISS-II the specific modeling of the position reconstruction includes a Gaussian
randomization along the module axis with an uncertainty of $\sigma_l = 15\,\text{cm}$ which reflects
the accuracy of our TDC measurements. Furthermore, both simulation and experimental
data are randomized according to a uniform distribution across the module width of 65 cm.
This ensures that no artificial steps are introduced to the geometrical distributions. The
module thickness of 5 cm has been neglected. This reconstruction produces two bumps at
90° and 270°, where a particle is reconstructed at the end of a top module which is then
in perfect alignment with a module from the side and can only give 90° or 270° azimuthal
orientation.

In the data a unique track could only be calculated for events where exactly two modules
on opposite sides had a full TDC recording. This means that there is a bias towards single
muon events without the presence of secondary muons in the data. This is also included
in the detector response model of the MC simulation.

An important variable for muon-induced events is the minimal distance of the recon-
structed muon track to the center of the cryostat and hence the detectors [4]. The agree-
ment between data and simulation for this variable is plotted in fig. 2.14. Compared to the
azimuth angle spectrum which shows a slight discrepancy between Geant4 simulation and
EDELWEISS-II data for the 0° to 40° region the agreement is even better in this variable.
This is understood in the sense that some imperfections of the individual detector response
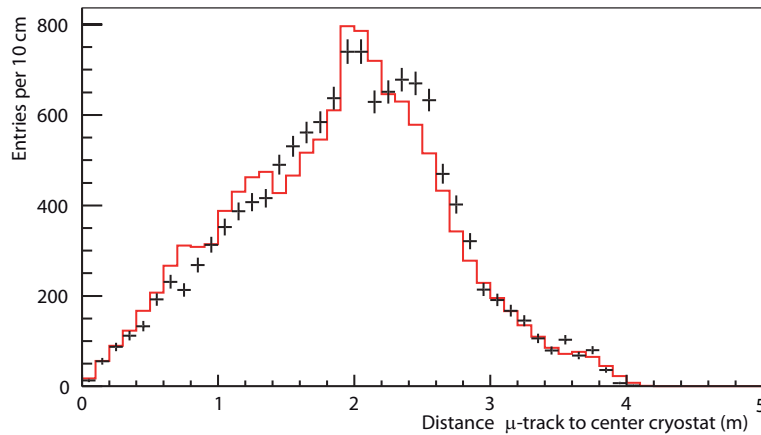
Figure 2.14.: Distance of reconstructed muon tracks to the center of the cryostat (black data points). For comparison, the MC simulation is given in red.

model average out when looking at global variables of the muon-veto system. We expect a similar effect for the overall muon detection efficiency.

2.3.5. The muon-veto system efficiency and measured muon flux

For the overall efficiency of the muon-veto system two distinct results were derived from the MC simulation. The first value represents the efficiency to detect any muon which enters anywhere into the experimental setup, even if it just passes through the outermost corner and is thus not very likely to produce secondaries which can reach the cryostat. Taking into account the detailed geometry, the individual muon-veto system module trigger probabilities as presented in sec. 2.3.3 and primary and secondary particles as modeled by Geant4, a detection efficiency of $\epsilon_{tot,\ MC\ veto-volume} = (93.6 \pm 1.5)\%$ was obtained. The uncertainty in this efficiency is dominated by the uncertainty in the individual muon-veto system module response. In order to account for a systematic bias in this determination the MC simulation has been evaluated by the conservative approach of scaling the entire set of individual module thresholds by $\pm 20\%$.

Out of the undetected 6.4% of muons which enter the veto volume, a third (2.4% of all) pass through geometrical gaps. Further 0.9% of all muons passed through a single plastic scintillator module which had a technical defect in its readout for parts of the 2009-2010 data taking and which was hence deactivated for the appropriate amount of simulated time. The remaining 3.1% were missed due to the inefficiencies of the individual modules. It is worthy to note that there is quite some variation in the detection efficiency among the μ-veto modules and that even though some modules started missing a small fraction of muons there was also a significant sensitivity for the detection of secondaries. Additional events with muons passing outside of the geometry could be detected through secondaries, adding 25% on top of the throughgoing μ-events.

The second efficiency $\epsilon_{tot,\ MC\ central\ sphere}$ derived from the MC-simulation is the efficiency to detect muons passing within a distance of 1 m from the center of the cryostat. This efficiency

$$\epsilon_{tot,\ MC\ central\ sphere} = (97.7 \pm 1.5)\% \tag{2.3}$$

is the most realistic estimate for the actual efficiency to veto muon-induced bolometer events within the WIMP search, which we can obtain with the current accuracy of our detector response model and without dedicated simulation and processing of energy deposits
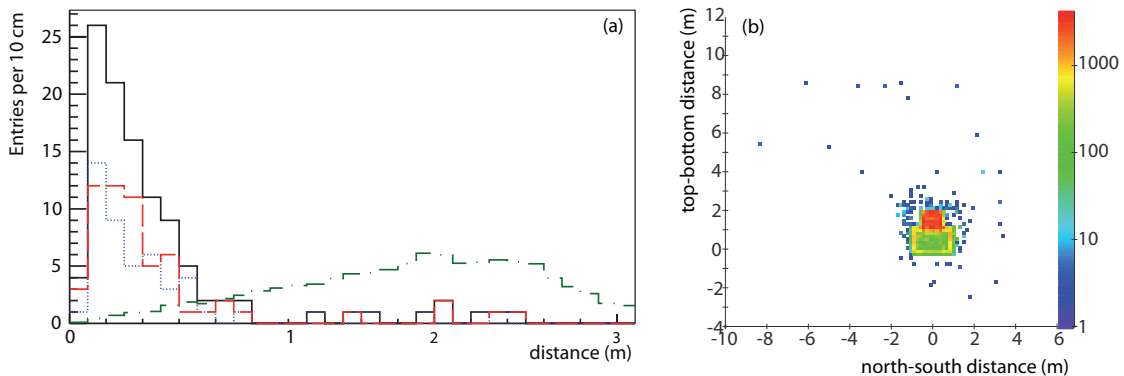
Figure 2.15.: (a) Distance of reconstructed muon tracks to the center of the cryostat, in black 109 events with energy deposit in the bolometers, in dashed red the events with energy deposit larger than 1 MeV, in dotted blue the events below 1 MeV in the bolometers. For comparison the distribution of muon tracks without requirement of an energy deposit in the bolometers is shown in dash-dotted green. (b) Production vertices of neutrons which scatter in the bolometers [5]. Only a tiny fraction of neutrons which scatter in the bolometers are produced outside of the lead shield.

in the bolometers. This claim is confirmed by results achieved within the analysis of coincident events in my diploma thesis and from earlier simulations of the neutron production vertices in coincidence with energy deposits in Ge crystals (fig. 2.15 a and b, respectively).

From the data analysis in 2009-2010 we could identify 234 coincidences between the bolometers and the muon-veto system. For 109 out of these events, a unique track could be reconstructed from full spatial information in exactly two of the veto modules (fig 2.15 (a) black). These tracks show a clear clustering with more than 90% of the events being produced by muons passing within a radius of 1 m around the center of the cryostat and hence passing through either the lead or even the copper shield of the cryostat. We subdivided this data sample into two datasets, one with energies above 1 MeV and one below 1 MeV. The first dataset is dominated by primary muon interactions and shower like events in the bolometers (dashed red) for which a passing of the muon through the lead and cryostat is expected. The second should be due to the scattering of secondary particles which could eventually mimic a WIMP signal in the bolometers (dotted blue). Both datasets show the same distance distribution. Hence, also for secondaries the dominant part of muons that need to be tagged pass within a radius of 1 m around the cryostat. However, one could still argue that the ultimate background which needs to be suppressed is not just from any secondary but from muon-induced neutrons which have a higher penetration than all other particles. In conclusion one needs to look at the production vertices of neutrons which scatter in the detectors. This has been done in [5] (fig 2.15 (b)), and the lead castle has been identified as the overwhelming place of neutron production with negligible contribution of at most 0.05% from outside of the EDELWEISS-II setup.

We conclude that the obtained efficiency $\epsilon_{tot, \, MC \, central \, sphere} = (97.7 \pm 1.5)\%$ appropriately reflects the efficiency to veto muon-induced background in the dark matter search. Deficiencies due to the non-detection of muon-induced events with muon tracks far from the cryostat are by far outweighed by the uncertainties and the inefficiency of individual veto modules.

Finally, with the help of the developed Geant4 code and the detector response model as described in sec. 2.3.3 we could translate the measured muon flux in the EDELWEISS-II muon-veto system to an integral muon flux through a horizontal surface. In total, we acquired 18503 muon candidates with at least a single module on two different sides of

the muon-veto system being hit. The resulting rate of $\Gamma_{\mu-cand.} = (108.7 \pm 0.8)/\text{d}$ was transferred into a flux through a horizontal surface

$$\Phi_\mu^{\text{horizontal}} = \Gamma_{\mu-\text{cand.}}/a_{\text{MC}} = 5.4 \pm 0.2(\text{stat})^{+0.5}_{-0.9}(\text{syst.})\,\mu/\text{m}^2/\text{d} \qquad (2.4)$$

with the acceptance $a_{\text{MC}} = 20.0 \pm 0.4\,\text{candidates}/(\mu/\text{m}^2)$. The systematic uncertainty of the muon flux is made up of three contributions: There is a 10% uncertainty from a possible contamination of secondaries in our data. Electromagnetic background occurring at the edges of the experiment could fulfill the requirement of triggering two modules on different sides, but are not included in the MC simulation. This source of error was assessed varying the chosen cut both in simulation and data. Rejection of adjacent geometrical sides diminished the estimated flux by 10% at most. A second contribution comes from the uncertainty in the modular detection efficiencies ϵ_i^μ. A common variation of these by $\pm 20\%$ led to another 10% uncertainty.

A remaining source of uncertainty comes from the generated muon flux. We only simulated single primary muons while the Fréjus experiment measured the distribution of muon bundles and found an overall contribution of about 5% to the total muon flux [189]. Measured as the flux through a sphere as recommended in [191] the above result changes to the most probable value of

$$\Phi_\mu^{\text{sphere}} = 6.6\,\mu/\text{m}^2/\text{d}. \qquad (2.5)$$

The muon flux as measured in this work eq. 2.4 was compared to the only preexisting measurement of the muon flux in the laboratory of Modane. However, it was unclear whether the muon flux given in [189] was obtained as the flux through a horizontal area or through a sphere. Hence the comparison for both interpretations is given. The result of [189] scaled for an estimated inefficiency of a 60° zenith angle cut which was applied in their analysis is $\Phi_{\text{Fréjus}}^{\text{horizontal}} = (5.2 \pm 0.1_{\text{stat}})\,\mu/\text{m}^2/\text{d}$. The alternative interpretation of a flux through a sphere after transferring into the flux through the horizontal yields $\Phi_{\text{Frjus sphere}}^{\text{horizontal}} = (4.2 \pm 0.1_{\text{stat}})\,\mu/\text{m}^2/\text{d}$. While the first interpretation results in a better agreement of the two measurements the second interpretation is statistically compatible, too. We tried to disentangle the ambiguity in discussions with former Fréjus collaboration members and V. Kudryavtsev. A summary of these communications together with an attempt to reverse engineer the most likely interpretation is given in the appendix in [5].

2.3.6. Projections for EDELWEISS-III

The initial goal for EDELWEISS-III is the acquisition of 3000 kg·d of exposure in 6 months time. Assuming a simple scaling from EDELWEISS-II to EDELWEISS-III and taking the measured rate of muon-induced WIMP-like events $\Gamma^{\mu-\text{n}} = (0.008^{+0.005}_{-0.004})\,\text{events}/\text{kg/d}$ [4] one can hence calculate the expected number of events after tagging with the muon-veto system.

$$N^{\mu-\text{n}} = \Gamma^{\mu-\text{n}} \cdot 3000\,\text{kg} \cdot \text{d} \cdot (1 - \epsilon_{\text{tot, MC central sphere}}) = (0.6^{+0.7}_{-0.6})\,\text{events} \qquad (2.6)$$

This is however, an overly pessimistic estimate where multiple changes from EDELWEISS-II to EDELWEISS-III were disregarded. First, the muon-veto system has been upgraded with 4 additional plastic scintillator modules (fig. 2.17). The readout problem for the non-working module has been fixed and high voltage values to individual PMT groups have been increased. First dedicated calibration measurements yield lower single module thresholds than determined in sec. 2.3.3.

Secondly, muon-induced bolometer events have a much higher average multiplicity in the bolometers than normal events. The multiplicity distribution for the EDELWEISS-II setup
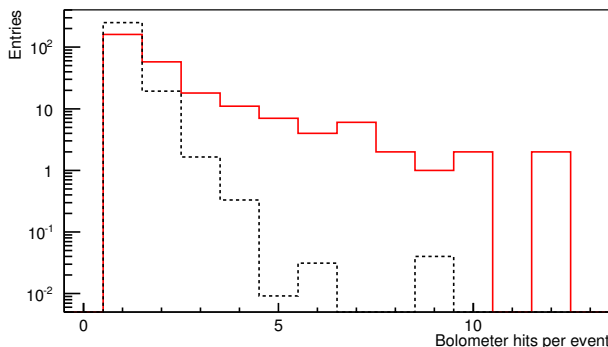
Figure 2.16.: Distribution of the number of bolometers which are hit within muon-induced
events (red histogram). For comparison, a scaled distribution of bolometer
multiplicity is given for the entire DM search event sample (dotted black).

has been measured in [4] and is shown in fig. 2.16. Since only single scatter events are
expected from WIMPs this is an additional criterion for rejection. From a preexisting
simulation it is known that the fraction of single scatter events could be lowered by more
than a factor of 3 going from 10 detectors in EDELWEISS-II to an extremely dense con-
figuration of 120 detectors [5]. This leaves a fraction of only 16% single scatter events.
In EDELWEISS-III the density and granularity was increased from the 10 detectors with
400 g to 36 bolometers with 800 g. Last, but certainly not least a newly installed internal
PE shield below the lead (see sec.2.4.1) will be able to attenuate the fast neutron flux.

In conclusion, we don't expect any muon-induced background event within the signal region
during the first 3000 kg·d of EDELWEISS-III. However, in order to be able to extrapolate
the muon-induced neutron backround to a possible extension of EDELWEISS-III data
taking towards 12000 kg·d , this needs to be better quantified. New simulations in the
complete EDELWEISS-III setup and a dedicated measurement campaign to extract the
individual μ-veto module response functions with better accuracy are ongoing [182].

2.4. The EDELWEISS-III configuration

EDELWEISS-III is the largest running cryogenic dark matter search, with a projected
sensitivity reach for spin independent WIMP nucleon scattering of $\sigma \geq 2 \cdot 10^{-9}$ pb [192].
This is more than a factor 10 improvement with respect to EDELWEISS-II. Still, all the
necessary detectors can be mounted in the same cryostat and the same general setup as
EDELWEISS-II. This could be achieved through an innovation in detector technology, the
identification and subsequent replacement of remaining radioactive materials in cables and
connectors, the deployment of cleaner copper shields and the consequent improvement of
cryogenics and electronics to achieve a low noise environment and readout.

The only change in the outer setup of the shielding layers (see fig. 2.17) is the addition of
4 plastic scintillator modules (green) to the muon-veto system. Due to an exchange of the
EDELWEISS-II pulse tube with a cryoline with a slightly larger diameter it was unclear
whether the two movable wagons of the EDELWEISS-III shielding setup could close as
tightly as before. Hence in order to cover this possible central gap and in order to boost the
detection performance for central muons, these additional modules were installed. In order
to better monitor the stability of the scintillator over time these modules were equipped
with LED pulsers and a continuous quality monitoring is performed with this data.

The polyethylene and lead shield were kept unchanged. However, the gasket between the
two parts of the lead shield had to be redesigned to ensure that the space between lead
shield and cryostat which is flushed with deradonized air is still leak tight and no contam-
ination from an inflow of laboratory air can occur. The changes which have been done
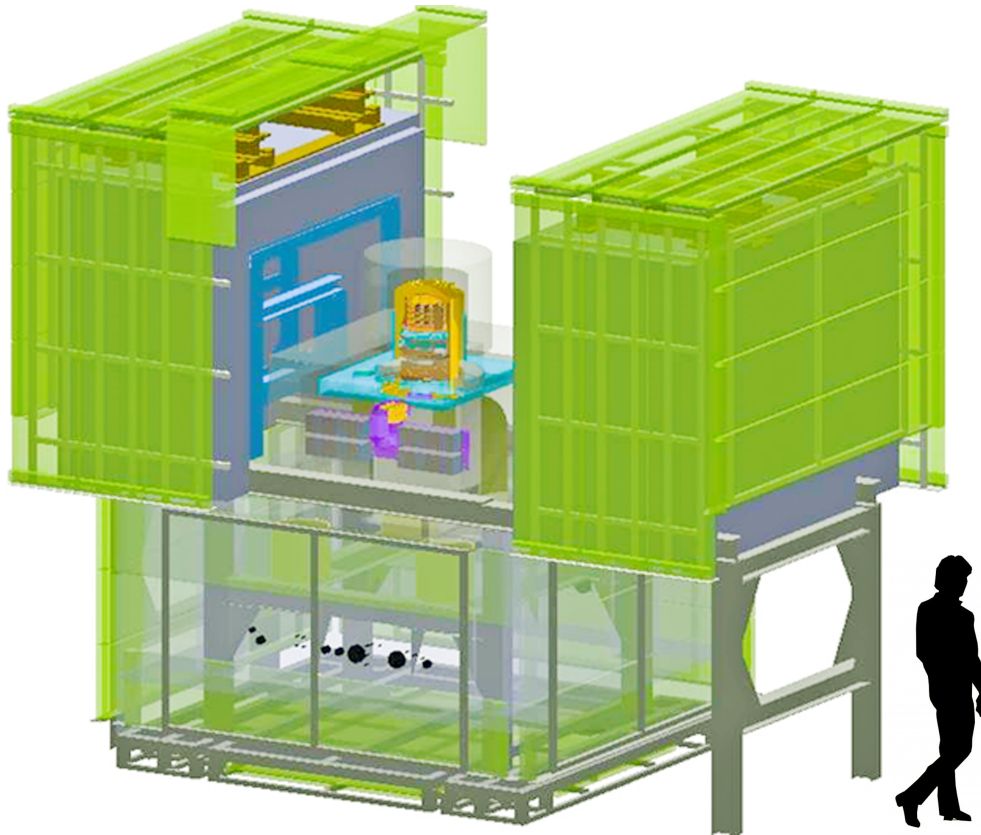
Figure 2.17.: 3D scheme of the EDELWEISS-III setup, the only visible difference to the EDELWEISS-II setup (fig. 2.5) are the additional μ-veto modules above the intersection of the two movable parts of the shields.

on individual intrinsic components will be discussed in the following. First, the actions to improve the neutron and gamma background will be reviewed both in terms of shielding and radiopurity and in terms of detector improvement and discrimination for electromagnetic background events. Then the changes to achieve lower readout noise and thus gain sensitivity for low mass WIMPs will be discussed. Last, a new software framework [3] will be introduced which allows for a paradigm change from single developer/analyst towards a distributed analysis in the future. The design of the high level data analysis layer as well as a first complete implementation of a data processing solution from amplitude extraction, over calibration towards a surface background analysis is the central part of this thesis.

2.4.1. Internal shielding and EDELWEISS-III material selection

Since a detailed MC-study of the EDELWEISS-II setup identified a few of the internal components as dominant sources of neutron and gamma backgrounds, a large improvement could be achieved with relatively few changes. For the reduction of the gamma backgrounds the thermal screens as well as some further parts inside of the EDELWEISS-II cryostat could be replaced with extremely pure NOSV quality copper versions from Norddeutsche Affinerie (now AURUBIS AG) [193]. For this kind of copper an extensive measurement of its radioactivity was performed on a large sample in LNGS (Laboratori Nazionali di Gran Sasso) [194], ascertaining that the remaining contaminations in this material are about two orders of magnitude lower than in the material used in EDELWEISS-II [161]. At the same time these new thermal screens were designed to allow the insertion of an additional internal PE shield into the cryostat as shown in fig. 2.18. While lead, germanium and copper mostly acted as neutron reflector, this PE shield can really attenuate the internal neutron flux. The most important piece is the 10 cm thick PE block (light gray) above

(a)   (b)
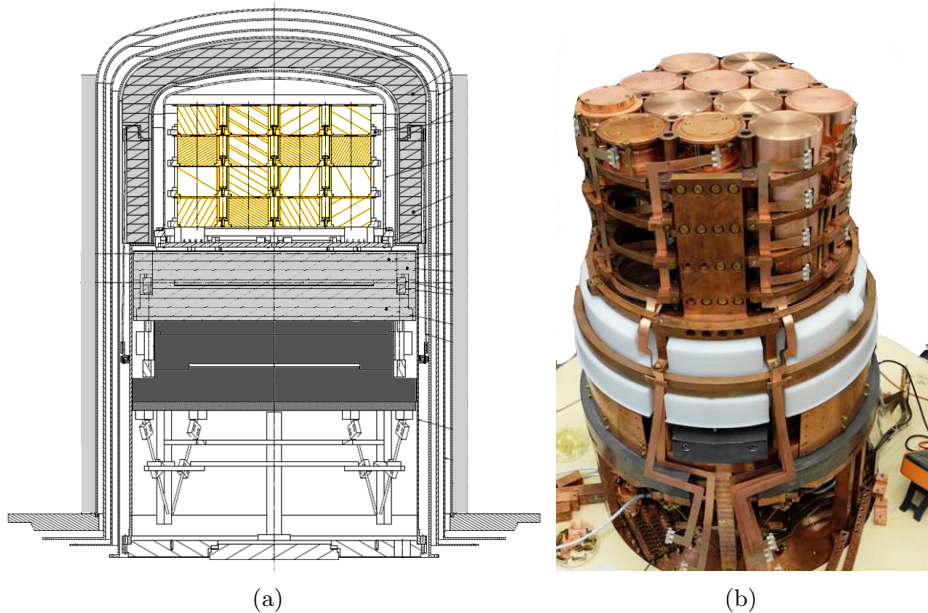
Figure 2.18.: (a) Scheme of the modified EDELWEISS-II cryostat. The new radiopure cop-
per shields allow the installation of an internal PE shielding (light gray) on
the sides of the shields and internally on top of the roman lead (dark gray).
This lead was already shielding the EDELWEISS-II detectors from the cold
electronics. (b) Photo of the mounting of FID detectors in EDELWEISS-III.
Previously installed Axon cables with Al connectors were replaced by an in-
house production of radiopure copper-Kapton cables.

the roman lead (dark gray) which shields the detectors from the cold electronics at 1 K.
Furthermore, the Al connectors and coaxial cables inside the cryostat were replaced by
an in-house production of copper-Kapton cables [195] with brass Delrin connectors shown
in the photograph in fig. 2.18 b. These cables are suitable for operation in an extreme
environment at 18 mK. They are robust against thermal stress, rigid and do not pick up
microphonics easily. But most importantly, their contribution to the neutron background
via (α-n) or from fission of contaminants is almost two orders of magnitude lower than in
the commercial axon [196] cables used in EDELWEISS-II.

The effectiveness of the entire set of measures was evaluated in a modified version of the
EDELWEISS-II MC-simulations [161]. In conclusion, we expect to reduce the γ back-
ground from 82 events/kg/d (20 keV-200 keV) to (14-44) events/kg/d at 90% C.L.. Fur-
thermore, ambient neutron background is expected to decrease from $\Gamma_{\mathrm{amb-n}}^{\mathrm{Edw2}} = (2.6 - 8.1) \cdot 10^{-3}$ events/kg/d to

$$\Gamma_{\mathrm{amb-n}} = (0.8 - 1.9) \cdot 10^{-4} \text{ events/kg/d.} \tag{2.7}$$

The two values given in eq. 2.7 refer to the 90% confidence bounds. The expected reduced
neutron rate allows for a data taking of more than 3000 kg·d before a single background
event from ambient neutrons is expected. For the gamma rate, the improvement of a factor
of 2-6 over EDELWEISS-II would not be sufficient using the EDELWEISS-II ID detector
technology. However, progress in detector design and treatment allowed to further improve
the ID detector performance.

2.4.2. Detector upgrades

The largest background contribution for EDELWEISS-II was understood as misidentified
gamma events. The contribution was quantified from a large statistics of gamma calibra-
tion events acquired with a ^{133}Ba source. Six misidentified gamma events were observed
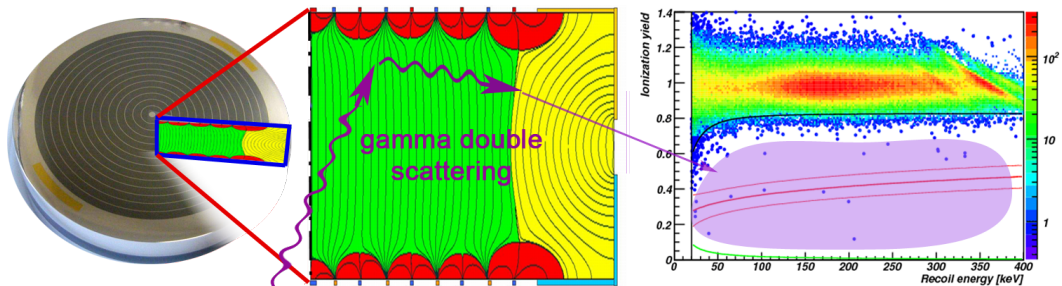
Figure 2.19.: EDELWEISS-II ID detector (left) and electric field map (middle) with large non fiducial regions (red and yellow). In simulation it was shown that the charge yield of double Compton scatter events can be misreconstruced for some fiducial - non-fiducial double scatter events. Such events fall into the purple shaded region in the scatter plot (right) and can mimic WIMP signal events.

in the nuclear recoil band of the ID detectors (fig. 2.19 (right)). A misidentification probability of $R_{\mathrm{ID}} = 3 \cdot 10^{-5}$ was measured which corresponds to a limit of the discrimination of $R_{\mathrm{ID}} < 5 \cdot 10^{-5}$ at 90% C.L.. This would have been insufficient for EDELWEISS-III. It was also clear that these events could not be understood as a tail of a Gaussian distribution leaking into the signal region. As can be seen in (fig.2.19 (right)) they do not follow the tail of the distribution of gamma events indicated by the lower blue 99.99% electron recoil band. In contrast, they are spread over the entire energy range and show charge yields from 10% to 60% or more. These charge yields require a significant recombination of (e^-/h^+)-pairs. A possible explanation was obtained from simulations where a double compton scattering between fiducial and guard region could reproduce a lower charge yield for some low electric field regions (see fig. 2.19). However, the simulations were not detailed enough to take into account all effects from crystal defects and electron propagation, scattering and space charge buildup [197, 152, 198, 157] and hence a quantitative comparison could not be made.
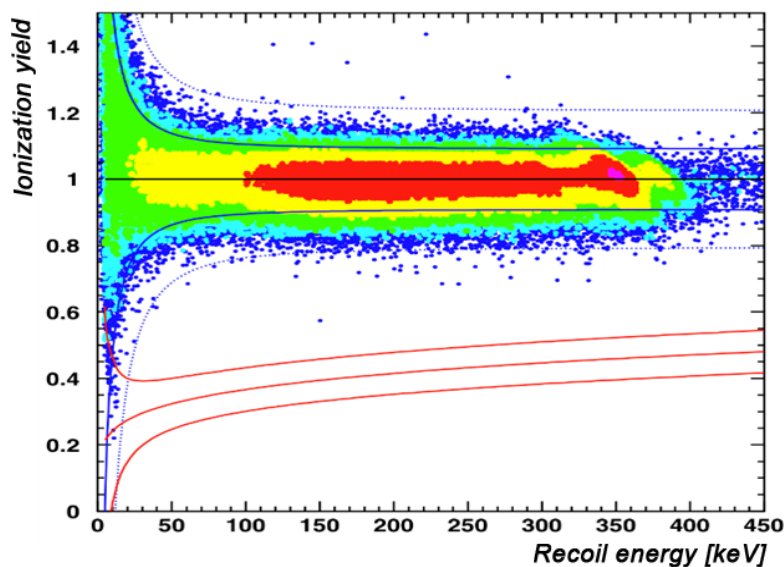
Figure 2.20.: Event distribution in ionization yield versus recoil energy for a large statistics ^{133}Ba gamma calibration measurement with EDELWEISS-III FID detectors. Since no misreconstructed event was found in the signal region (red band, $E_{\mathrm{Rec}} > 15\,\mathrm{keV}$) this is clear confirmation that the EDELWEISS-II problem of misreconstructed gamma events has been solved. A gamma discrimination of $R^{\gamma}_{\mathrm{FID}} < 6 \cdot 10^{-6}$ was demonstrated, only limited by statistics [159].
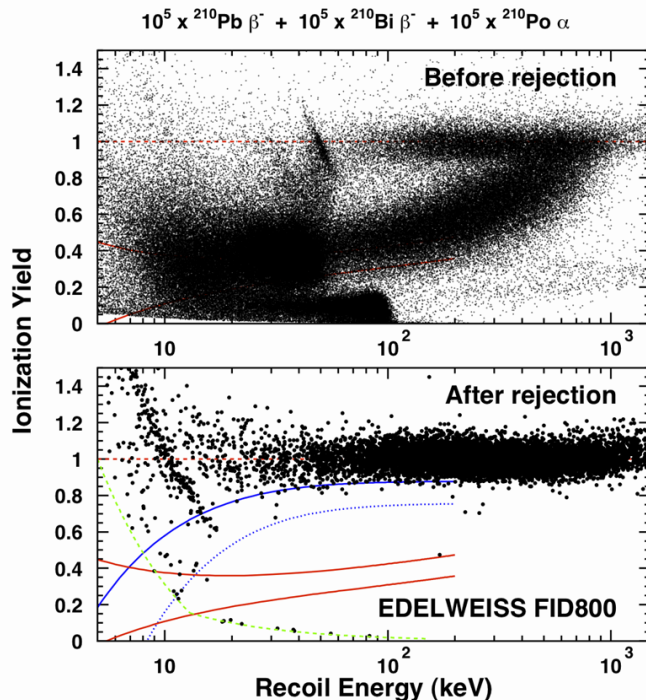
Figure 2.21.: Event distribution in ionization yield versus recoil energy for a surface β rejection measurement with EDELWEISS-III FID detectors. For a statistics of roughly 100000 high and low energy β's a single event above 15 keV was observed in the region of interest (red band) after application of the fiducial cut. The event was found in the signal region close to the 99.99% gamma rejection line.

For EDELWEISS-III, the fabrication process of the interleaved electrode design could be adapted to the planar sides. Hereby, a simpler electric field configuration and a larger fiducial volume as indicated in fig. 2.4 could be achieved. A gamma calibration of 411633 events (15 keV - 200 keV) did not show a single anomalous event with significantly reduced charge yield (fig. 2.20). Hence, the 90% Poisson limit of 2.3 events was used to extract a limit for the remaining misidentification probability

$$R_{\text{FID}}^{\gamma} < 6 \cdot 10^{-6} \, \text{WIMP-candidates/gamma-event.} \tag{2.8}$$

This translates into a factor of more than 8 improvement in gamma discrimination while simultaneously enlarging the fiducial volume fraction from $\sim 40\%$ to $\sim 75\%$ for these new 800 g crystals. The entire gain in gamma background including a factor 2-6 in the background rate due to the cleaner radiopure copper shields sums up to a factor larger than 16 for EDELWEISS-III. In turn the expected background contribution for an initial dataset of 3000 kg·d can be quantified to be $N_{\gamma} < 0.8$ at 90% C.L.. The value is entirely dominated by the uncertainty of the rejection factor of FID detectors. Through periodic calibration runs during EDELWEISS-III data taking, the measurement of the rejection factor R_{FID}^{γ} will be refined with higher statistics. Also the achieved gamma background rate will be extracted during WIMP data taking. Unless both the discrimination capability as well as the gamma background rate turn out to lie close to their respective upper bounds an extension of data taking beyond 3000 kg·d will not be limited by the gamma background.

The expected background from surface events might be a more delicate subject as discussed for various experiments in sec 1.3.3. For the EDELWEISS FID detectors, a surface event rejection measurement has been performed with a dedicated calibration exposing

two detectors to the α and β radiation from a ^{210}Pb source (fig. 2.21). The source was fabricated from copper adhesive tape exposed to the flux of ^{222}Rn and glued to the detector holders [2]. Afterwards, the copper surface has been cleaned to remove dust and improperly implanted ions. Placed in the detector holder of a crystal the subsequent decays of the long lived ^{210}Pb (T$_{1/2}$ = 22.3 y) $\rightarrow$ ^{210}Bi $\rightarrow$ ^{210}Po $\rightarrow$ ^{206}Pb can be used to probe the surface event rejection capabilities of these detectors for the relevant species of surface events. The measurements performed for EDELWEISS-III found a single interaction inside of the nuclear recoil band above 15 keV out of 100000 low energy surface β's. This is equivalent to a rejection

$$R_{\text{FID}}^{\text{surface}} < 4 \cdot 10^{-5} \text{ WIMP-candidates/surface-event.} \tag{2.9}$$

Furthermore, the ratio of fiducial to surface area was increased by a factor $\sim$3 for the FID detectors. In addition to an improvement in surface contaminations this leads to a measured α-rate of $\sim$ 4 events/kg/d for the ^{210}Po to ^{206}Pb decay rate [199]. Assuming secular equilibrium in the decay chain one can calculate an expected contribution of this background during the WIMP search. The number of low energy βs from the ^{210}Pb decay to ^{210}Bi which need to be rejected in the WIMP search is then the same as the α-rate from the subsequent ^{210}Po decay and

$$N_{Edw3}^{\text{surface}} = \Gamma_\alpha \cdot E \cdot R_{\text{FID}}^{\text{surface}} < 0.5, \tag{2.10}$$

where E is the expected exposure of $E = 3000 \, \text{kg} \cdot \text{d}$. This limit is still smaller than the expected misidentified gamma background and the extrapolated background contribution from muon-induced neutrons. However, the gamma discrimination factor is only limited by the statistics of the calibration measurement and can be much better. For the β rejection the limit comes from an observed event a the border of the 99.99% γ discrimination band. In addition we cannot claim that this extrapolation is overly pessimistic as we do for the muon-induced background. In fact, in EDELWEISS-II we observed an additional low energy surface background with a component from ^{109}Cd contaminations for a few detectors [199]. Hence, it is especially important to further investigate this background and the detector performance.

Potential background from α decays from ^{210}Po $\rightarrow$ ^{206}Pb exhibit energies outside of the region of interest of the order of 5.4 MeV and quenching values that lie even below the nuclear recoil band. Nevertheless potential backgrounds from degraded α's are included in the surface event rejection measurement and the extrapolated background of surface events.

2.4.3. New cold electronics and upgrades to the cryogenic system

Proving that large exposures can be acquired in cryogenic experiments without background limitation is certainly important in order to have two separate technologies to assess a possible WIMP signal. However, the primary focus of cryogenic experiments has shifted away from competing with liquid noble gas detectors in scaling and exposure. Instead, the main focus is utilizing their intrinsic strength of energy resolution and low threshold to assess the parameter space of low mass WIMPs. Thus, they can expand the experimental sensitivity to additional low mass WIMP models and at the same time technology development towards larger exposures is continued. In case evidence for a heavier WIMP of the order of $m_\chi \sim 100 \, \text{GeV/c}^2$ should be discovered, a follow up search with much better energy resolution and a different target to pinpoint the dark matter parameters will be available.

For EDELWEISS-III, this paradigm change is reflected in its aim to improve the ionization resolution by 30% with respect to EDELWEISS-II. This goal is approached on several

(a)   (b)
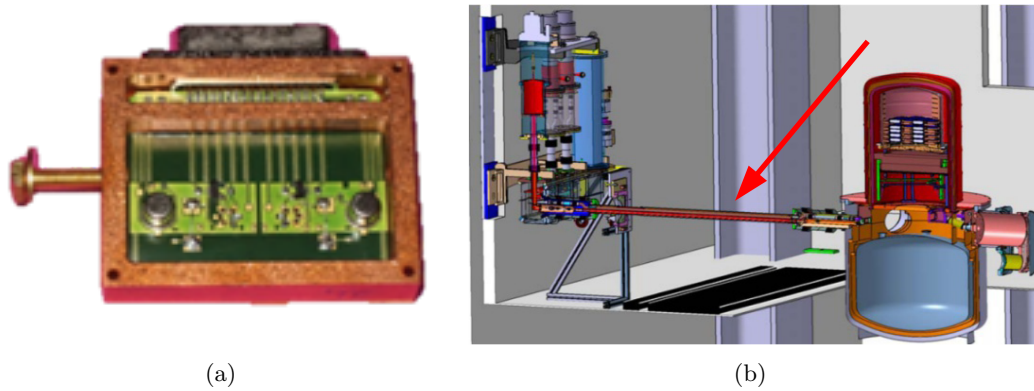
Figure 2.22.: (a) New cold electronics boxes for EDELWEISS-III with improved low noise ionization readout. (b) Scheme of the EDELWEISS-III cryogenic line and thermal machines (mounted on the wall). This system replaced the EDELWEISS-II pulse tube and allows a much better decoupling from vibrations.

levels: New cold electronics has been designed for EDELWEISS-III. By a modification of the $1\,\mathrm{K}$ RC electronics and $100\,\mathrm{K}$ FET amplifier scheme, feedback resistances could be replaced with an FPGA controlled relay switch [200]. Hereby the frequency range of the ionization signal could be extended towards higher frequency, which allows faster sampling of the ionization signal including the resolution of charge propagation effects on a sub μs scale [197]. Furthermore, the signal shaping has been altered to a step function and allows to use long integration times O($1\,\mathrm{s}$) to extract signal information at low frequencies where a better signal over noise ratio can be achieved. Additional Johnson noise from the feedback resistors could be reduced and the radioactivity of the device as shown in fig. 2.22 (a) is lower than before.

Mechanical vibrations, coupling to the readout cables and production of microphonics both on heat and ionization signals were reduced by modification of the EDELWEISS-II cryogenic system. A scheme of the new setup is shown in fig. 2.22 (b). The pulse tube cryogenerators cooling the $50\,\mathrm{K}$ and $100\,\mathrm{K}$ thermal shields were exchanged by a system of thermal machines outside of the lead and polyethylene shields together with a cryoline. The heat conduction is ensured by the circulation of a cryogenic fluid in this $\sim 2\,\mathrm{m}$ long tube which allows to reduce microphonics from this source. Also the cryostat position and damping level can be slightly adjusted in order to best decouple from the pumps and active machines needed to achieve the vacua or for example needed for the He reliquifier.

Finally, also on the data analysis and software level new algorithms have been tested and data management and backup tasks have been automated to free up time for the exploration of improved data analysis techniques. In particular, for individual ionization channels a significant additional improvement of 22% could be achieved in baseline resolution. This is especially beneficial for the reduction of low energy near surface background which exhibit a charge sharing between fiducial collecting and veto electrodes. The specific data analysis algorithms implemented and used during this thesis will be discussed in chapter 3. Their performance is assessed in chapter 4. They are embedded into a data analysis framework featuring a new versatile data structure that allows the analysis of different detector subsystem in the same ROOT tree [201, 202]. The design of the final high level analysis part of this framework is subject of this thesis and is discussed in section 2.4.5.

2.4.4. EDELWEISS-III data acquisition

The EDELWEISS DAQ scheme was guided by two major design choices. In order to limit radioactivity, all electronic parts should be placed as far as reasonably possible from the detectors. At the same time an early digitization should be achieved to minimize electromagnetic noise and allow intensive offline processing. The resulting setup employs minimal RC-electronics at $1\,\mathrm{K}$ and FET amplifiers at $100\,\mathrm{K}$ [200]. The signals are then guided outside of the cryostat into dedicated boxes and amplified and digitized at $300\,\mathrm{K}$. These boxes also control the cold electronics. This includes a generation of a square modulation to read out a contact potential free signal for the heat channel and the reset of accumulated charge on the ionization channels by controlling some relays.

After digitization with $100\,\mathrm{kHz}$ at $16\,\mathrm{bit}$ precision, the data are further distributed on a network of P2P connections on optical fibers. Clock signals are attached and the data is redistributed to several acquisition Macs. In EDELWEISS-II this was done trough a set of dozens of individual embedded computers which converted the data stream from the optical fiber network onto a UDP-packet conform data stream that was sent via $1\,\mathrm{Gb}$ Ethernet [203]. These embedded computers, based on a design from the OPERA experiment, were seen as individual machines from the network side and created a huge work load for network management and time synchronization. They introduced a large complexity and instability into the DAQ system.

For EDELWEISS-III this redistribution step was solved by employing a single crate based solution developed at the IPE in Karlsruhe [204]. Adapted versions of this crate have been successfully employed in other experiments like the Auger experiment [205] and the KATRIN experiment [206]. It has even been used in the design and evaluation of a medical prototype for early breast cancer detection via ultra sound computer tomography (USCT) [207, 208]. It is a scalable solution that allows the integration of additional subdetectors like the EDELWEISS muon-veto system and the potential readout of hundreds up to thousands of detectors even, as proposed for EURECA [209]. Its FPGAs can perform signal shaping and triggering operations, and its data management and event building capabilities are required for the testing and evaluation of a time resolved ionization readout with a $40\,\mathrm{MHz}$ sampling at $16\,\mathrm{bit}$ resolution. At the same time it can still stream all data at a slower sampling rate of $100\,\mathrm{kHz}$ over a 1 GBit ethernet to the following acquisition computers which can perform a more intensive processing and subsequent triggering for the standard analysis. For EDELWEISS-III the typical trigger is applied on the best of the two heat channels of a detector. The trigger algorithms include an IIR (infinite impulse response) filter designed with coefficients corresponding to a 1st order Butterworth type [210]. The cutoff frequencies are optimized from an offline analysis. Finally, a trigger threshold is applied to the correlation of filtered signal and template. This threshold is set at a very low value to record lowest energy events hidden in the noise level. It is adapted according to variations in the noise level during WIMP data taking to acquire data at a constant rate of $\sim 10\,\mathrm{mHz}$ per detector. The acquisition software called SAMBA is run on up to 3 Macs simultaneously. It is an in-house solution that manages the electronics, triggers and saves data to disk.

2.4.5. New data structure and analysis framework

As dark matter search experiments are increasing their sensitivity and hence their target mass, experiments grow in size, grow in complexity and especially grow in their computing aspects. With the advent of cheap data storage and faster digitization the storage of digitized pulses increases as well as the storage of environmental slowly varying parameters. With pulse shape analysis detailed pulse characteristics are extracted in an offline
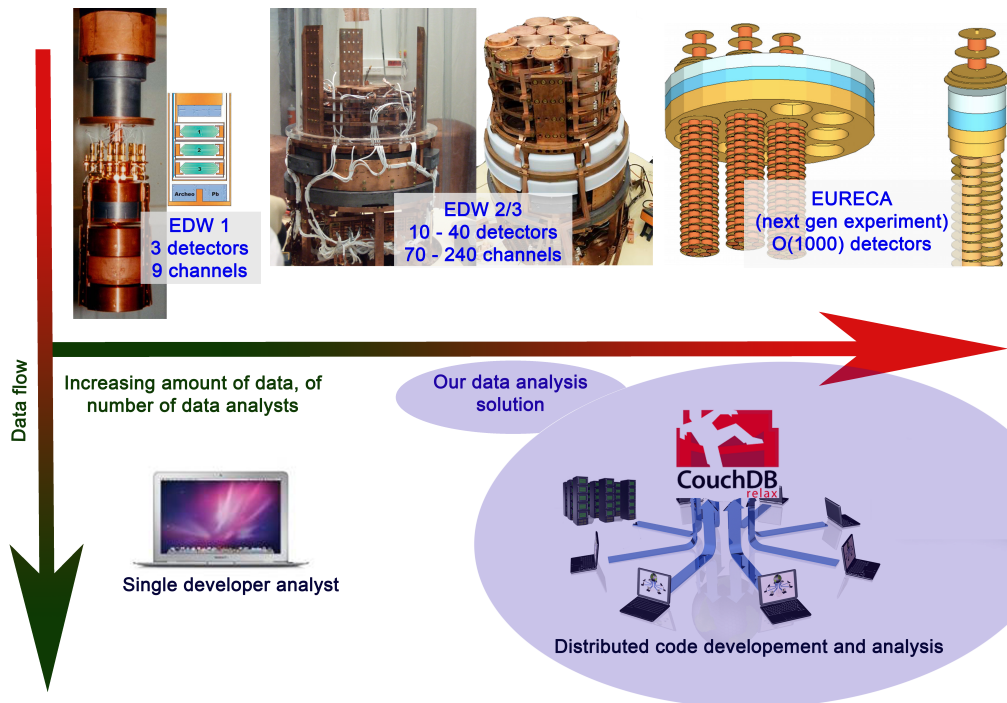
Figure 2.23.: Visualization of the EDELWEISS detector configuration and experimental size over time. From the original experiment with 3 detectors in a commercial cryostat in the underground laboratory of Modane a scaling towards the operation of O(1000) detectors in a EURECA type experiment is envisaged. The amount and complexity of data is further increased by an increasing number of channels per detector, faster sampling and different detector types, as foreseen for EURECA. Similarly the collaboration has grown in size and a coordinated analysis strategy and a common data analysis framework is needed to fully exploit the data from a future experiment.

analysis and multivariate techniques are often used to mine the subsequent datasets, to find correlations and to do event classifications on a subset of the available variables.

For the EDELWEISS collaboration this situation of growing analysis needs is summarized in fig. 2.23 by the detector and channel configuration which is shown for different experimental stages from EDELWEISS to the proposed EURECA experiment. At the same time collaborations grow in size and several institutes want to contribute to the data analysis effort. This situation prompted the development of a data analysis framework called KData to collect common analysis code for the EDELWEISS collaboration, to automate data management tasks and to build it flexible enough to create an analysis and development environment, which can be extended to a EURECA size experiment. A prime target to make the project independent of a single developer was documentation and accessability. The design guidelines as well as the implementation of the raw data tier and amplitude estimation libraries have been published in reference [3] and an html documentation of the KData project including reference pages, installation guidelines and coding paradigms for contributors is available at [211]. The code itself is maintained on a self-administrated subversion [212, 213](version control) server at KIT.

The framework consists of two separate organizational layers. The first is a schema-free CouchDB [214] based database (DB) solution that collects all metadata of the DAQ, environmental variables like the Radon level, HV values from the muon-veto system and other slowly varying data. Furthermore, it controls certain data processing and management tasks dependent on the metadata in the DB. A set of regularly executed, automated queries starts and stops different analysis and backup routines. Success and failure of in-

dividual processes is documented on the database so that there is a single accessable place to document all processing done on a certain data set. It was found that existing libraries provided in Python (e.g. Couchdbkit [215]) are very practical tools for the realization of this interface. However, no programming language is needed to view the metadata stored on the database since a powerful web interface is provided by CouchDB. It has a replication feature that allows to host local databases with lower network latency, which we do behind a firewall at LSM and then replicate the changes to another database. Performance measurements published in [3] show that a document throughput of about 7 EDELWEISS DAQ documents/s is realistic for single write and DB update times in LSM. Our current DAQ produces only 3 documents per hour. The second database location, which is our main analysis database, is hosted by the commercial provider Cloudant, now IBM. This choice allows to rely on a highly available, fast accessible and scalable solution of a commercial company without the overhead of server administration. For immediate visualization of slow control variables JavaScript and HTML5 based web applications (CouchApps) can be added directly into the database. Additionally the "Advanced data extraction infrastructure" (ADEI) [216] is currently being expanded with an interface to EDELWEISS CouchDB based data. This will provide an alternative data extraction interface and additional data monitoring with the same interface as used in TOSKA (ToroidalSpulen Testanlage Karlsruhe), KATRIN and several other experiments. Another implementation of a CouchDB based data management solution was explored by the Majorana experiment and is detailed in [217].

In the context of this thesis the layout of analysis and calibration specific databases were designed. They collect metadata from the data processing like baseline resolutions, live time, rate of events and calibration specific parameters. An example document is given in the appendix listing 6.1. The main DAQ-specific database and how it manages the data processing will be detailed in sec. 3.1.

For EDELWEISS the data we want to store has the following properties. The recorded pulse traces are digitized over long times to feature both pretrace information as well as maximal signal shape information. Hence, the traces make up about 90% of the original event data as extracted from the DAQ. For data portability and analysis reasons it was decided to design three data tiers, the raw data level which holds the entire event information as converted from the DAQ, an amplitude (Amp) level layer which omits the pulse traces but saves a set of extracted parameters like the rise-time and amplitude and finally a high level analysis (HLA) layer that stores the calibrated amplitudes and additional variables like the estimated recoil energy of an event.

In addition to the data structure, the second part of the KData framework consists of a set of C++ libraries providing a complete data encapsulation, a rather generic set of pulse processing routines, EDELWEISS specific analysis implementations and some plotting and fitting utilities. Specific examples for data analysis algorithms developed and applied within this PhD thesis will be presented in chapter 3. We will outline the design of data encapsulation here. Data encapsulation itself is a key feature for a data framework designed to last over time. It retains the flexibility of exchanging the actual data storage and adapting to new experimental requirements while keeping the same data access interface and keeping alive all analysis code on top .

For the implementation of the data encapsulation a few general goals were defined based on perpetuity considerations as well as by the specific requirements of the EDELWEISS experiment. Likely these considerations apply to other rare event searches as well. For EDELWEISS-III we want to store a set of global experimental conditions, data from an arbitrary number of Ge - bolometers, each of which can be configured with a different number of readout channels and data from additional subdetector systems like the muon-
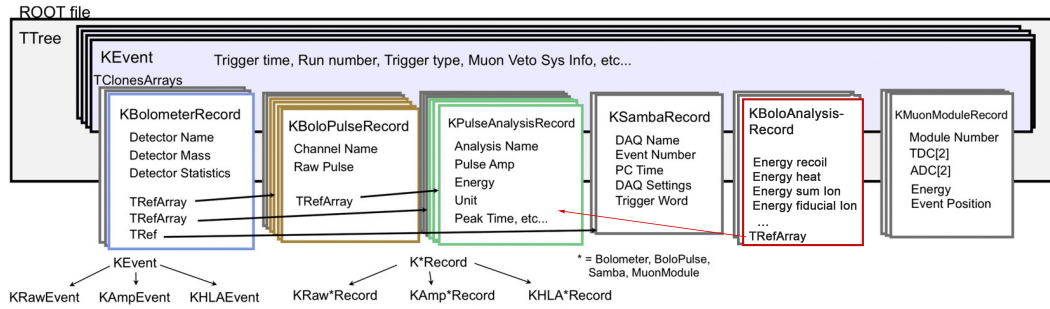
Figure 2.24.: Layout of data storage in the KData data structure library libkds, exemplified for the high level analysis data tier. Data of recurring objects has been encapsulated in the classes KBolometerRecord, KBoloPulseRecords and KMuon-ModuleRecord. Analysis dependent data, which can vary depending on algorithms as for example pulse amplitudes, are stored in KPulseAnalysisRecord and KBoloAnalysisRecord. For the creation of a logic structure, e.g. which pulse belongs to which bolometer and which analysis record to which pulse, pointer like objects called TRefs are used.

veto system. For FID detectors the configuration of a varying number of readout channels can account for broken channels. Furthermore, it should allow to store data from different detectors like the EDELWEISS-II ID-detectors with 6 ionization channels and a single heat channel in exactly the same data structure. These requirements can be well fulfilled with the ROOT framework within a single primary event tree. ROOT [201, 202] itself was chosen due to its guaranteed continued development during LHC live time, its dominant spreading in the high energy physics community and its already existing libraries ranging from data compression to plotting. For perpetuity we required our data to be readable with standard ROOT. This ensures that data can be read even without access to the KData libraries.

The idea of storing a variable number of bolometers with a variable number of channels inside of one event calls for a nesting of variably sized arrays. However, this is a conflicting requirement to the independence on any library other than the ROOT ones. In order to achieve this one needs to contain a so-called fully split tree which is composed entirely of branches of primitive data types. The solution which was found for the EDELWEISS data structure is shown in fig. 2.24 for the example of the HLA data tier designed and coded during this PhD thesis. Data associated to recurring objects like pulses is encapsulated in specific C++ classes for this example in the class KHLABoloPulseRecord. Reconstructed data which are dependent on analysis algorithms like an extracted pulse amplitude and peak position are stored in separate classes, for example KPulseAnalysis-Record. Objects of these types in turn are stored in variable sized TClonesArrays directly at the event level. This allows to add individual numbers of analysis results per channel or an individual number of channels per bolometer and linking between those objects can be ensured through the storage of pointer like objects called TRefs. Storing of multiple analysis results in the same event facilitates comparison of different analysis algorithms or parameters and is a key feature for the EDELWEISS-III data analysis detailed in this thesis. The subdivision into HLA, Amp and Raw data tiers has been realized designing a base class for each physics object for example the class KBoloPulseRecord and subsequent inheritance to the three subclasses KRawBoloPulseRecord, KAmpBoloPulseRecord, KHLABoloPulseRecord. This design allows to write a subset of analysis code that can run on all data types independent of the specific data level.

3. Calibration of raw data

As direct dark matter searches are progressing towards the ultimate sensitivity limit for spin independent elastic WIMP-nucleus scattering of $\sigma_{SI} \sim 10^{-48} \, \text{cm}^2$, two distinct search strategies have emerged. Dual phase noble liquid detectors have shown an unmatched capability and speed of scaling up their target mass and reducing their background from ambient radioactivity (f.e. [111, 115]). Bolometric searches on the other hand have pushed their resolution and thresholds to the level of a few 100 eV (f.e. [110, 131, 218, 107, 11]). This allows the bolometer based experiments to target dark matter scenarios with WIMP-masses as low as $m_\chi \sim 1 \, \frac{\text{GeV}}{\text{c}^2}$. These scenarios can be characterized by a very steep exponential energy spectrum of nuclear recoils. Large WIMP-masses in contrast should result in a flatter detectable energy spectrum extending to higher energies. For the latter scenarios the liquid noble gas experiments seem to be the best adapted technology to probe the WIMP-nucleus scattering cross-section down to the limit of coherent neutrino nucleus scattering.

This situation has evident implications on the raw data processing and calibration of a Ge-bolometer based experiment. For a rare event search where signal and noise overlap the trigger rate is usually set in the noise level. As a trade off in order not to induce too much dead-time the targeted trigger rate is of the order of 10 mHz per detector. Since this is still a low rate it is possible to optimize and maximize the offline signal treatment in order to further improve the energy resolution and decrease the energy threshold. The following chapter will detail the data processing and calibration scheme which was developed during this PhD thesis to improve the existing data analysis. The analysis was adapted to a change in signal shape caused by the deployment of new electronics for EDELWEISS-III. This work is embedded into the initial design for a collaboration wide and scalable data analysis toolkit developed by A. Cox [3]. It completes the envisaged database driven processing and analysis chain by incorporating a full processing, calibration and analysis of EDELWEISS data for the very first time.

3.1. Database-driven processing

Going from EDELWEISS-II to EDELWEISS-III the number of detectors was increased from 10 detectors for the standard WIMP-search to 36 detectors. Planning for a future experiment, like EURECA [209] or within an EU-US collaboration one expects to run hundreds of detectors at the same time. While the analysis of the 10 crystals was still done by a single developer/analyst within EDELWEISS-II this certainly won't be practical
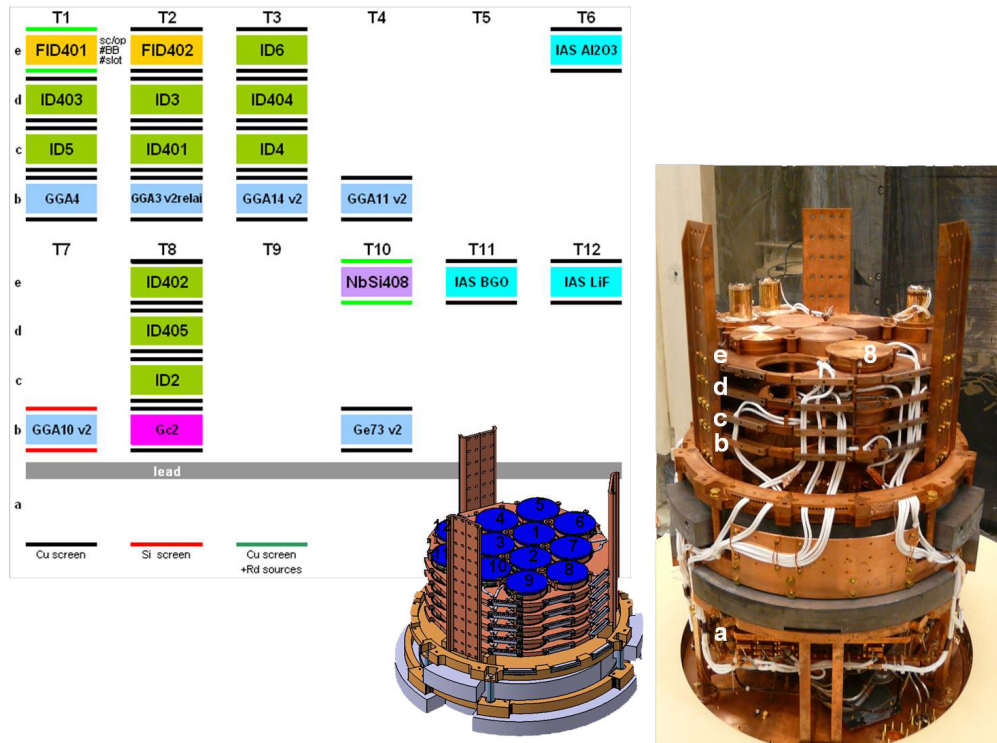
Figure 3.1.: Overview over the detector setup in the last long-term data taking 2009-2010 in the EDELWEISS-II setup. Detector types and casings are indicated by a color scheme with ID type detectors in green and standard copper casing in black.

any more for the future. As one of the principles to adapt to this different situation a database driven processing scheme was devised that acts as a central point to document and automate the data processing. For an overview on design guidelines and general considerations for the realization of this setup we refer the reader to section 2.4.1 as well as reference [3]. In the following we want to show how the system is used in the specific detector configuration on which the current data processing was evaluated (fig. 3.3) and on which it is running at the moment (fig. 3.2). Since the processing will be compared to the data processing for EDELWEISS-II we will also quickly revise the EDELWEISS-II detector configuration (fig. 3.1).

3.1.1. From EDELWEISS-II to EDELWEISS-III detector configuration

In EDELWEISS-II a total of ten ID detectors were run for the dark matter search. Additional detectors include R&D for low mass WIMP search and studies of the FID detector design with two 400 g Ge-crystals (fig. 3.1). For the dark matter search this meant 10 detectors with 6 ionization and a single heat channel each. That sums up to 70 channels in total which had to be stored and tracked throughout a data acquisition of 330 live days. Furthermore, additional meta data like voltage configuration of detectors and data type (Ba calibration, neutron calibration, WIMP data, test measurement) had to be noted. During analysis, event data needs to be correlated with parameters such as the radon level [219], closed shielding [4] and cryostat conditions.

These data tracking tasks have to be performed in parallel to daily shifts needed to recover the detectors from a slow space charge build-up during data taking [198]. To remove space charges all electrodes are grounded typically once per day for about one hour and an intense ^{60}Co source is used to irradiate the crystals. After the procedure a new data run has to be initialized and proper detector configuration and data taking has to be ensured. In special circumstances swapping of the voltage configuration of top and bottom electrodes

Figure 3.2.: Current detector setup in the EDELWEISS-III WIMP search. The color scheme encodes the distribution of detectors to the readout Macs. Additional information includes an identification of the NTD heat sensors per detector, the cabling type and data distribution system. Data taking in this configuration with three EDELWEISS acquisition Macs started July 2014.

was found useful to recover a specific Ge-detector. Finally, also data distribution and back up has to be ensured. All of these tasks require manpower and in case multiple institutes are sharing the data analysis a lot of communication, data transfer and documentation. Traditionally, a Word document was edited locally in LSM and is still used as logbook to track ongoing operations and communications about planned interventions and cryostat maintenance.

For EDELWEISS-III the complexity of the experiment and the amount of data scales up by a factor of two to four. In total 36 FID detectors are installed in the cryostat. However, due to an unfortunate material defect in cabling, only 24 are read out in the current configuration (fig. 3.2). Additionally three more crystals of the Lumineu [220] neutrino-less double beta decay search are installed in the same setup. This can already be seen as an example for a EURECA type shared cryogenic infrastructure with different detectors operated in a single cryostat. However, for the EURECA experiment another factor 10 to 20 increase in the number of detectors is expected.

On such scales manually keeping track of all individual detector conditions and subsequent spreading to analysis groups becomes unrealizable. Also the amount of not yet automatized or semi-automatized calibration and analysis tasks e.g. the production of heat templates and calibration procedures won't be feasible for an individual alone. The KData framework was invented to serve as a basis in which data tracking is automated and where data is automatically distributed and shared. It facilitates bringing together slow control meta data or sub-detector data that needs to be correlated to the WIMP search data.

For the last and major EDELWEISS-III commissioning run (cryogenic Run 305, fig. 3.3) this worked the following way: Data from in total 15 FID Ge-detectors was recorded by a single acquisition Mac. This Mac would store a single data partition per hour in order to prevent data loss and to allow a near-time data monitoring on closed data files. Data were then copied via an automated script to a dedicated monitoring and processing Mac, which
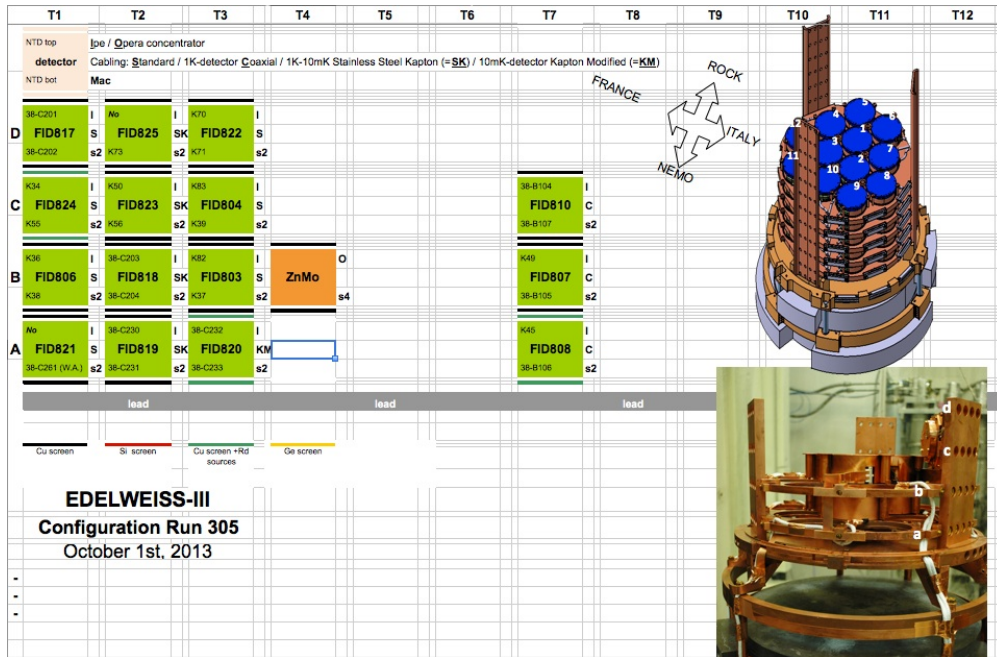
Figure 3.3.: Detector setup in the calibration and commissioning phase in the EDELWEISS-
III environment for the data investigated in this thesis (October 2013 to January
2014). FID detectors are read out by a single acquisition Mac and thus are all
colored in green. Additional information includes an identification of the NTD
heat sensors per detector, the cabling type and data distribution system.

took care of the further data management steps in Modane. This setup allows to have a
central Mac for data management and processing. At the same multiple acquisition Macs
can be used to run the DAQ-software SAMBA in parallel. This ensures that the DAQ
software which performs time-critical trigger decisions doesn't have to share resources with
other processes.

A set of python scripts has been configured on the analysis Mac to run as LaunchDaemons
and schedule the further data management. The first job triggers the scanning of the
SAMBA raw data directory for new files. In case a new data partition appears, it extracts
the header information and creates a new document on a DAQ specific database called
datadb (listing 3.1).

Listing 3.1: Excerpt of the JSON (Java Scrip Object Notation) code of a datadb document
created for the corresponding SAMBA data partition.

```
1   {
2      "_id": "run_oj24c002_005_kdatascript",
3      "_rev": "6-b4bfab3b8c375960b9b27767c95bcf2e",
4
5      "type": "daqdocument",
6      "date_uploaded": 1414142211.624394,
7      "status": "good",
8      ...
9
10     "Intitule": "Edelweiss3, run 308",
11     "Fichier": "/Volumes/DonneesEDWh3/events/oj24c002",
12     "Condition": "fond chateau ferme",
13     "Date": {
14         "month": 10,
```

```
15          "day": 24,
16          "year": 2014
17      },
18      "file_number": 5,
19      "Detecteurs": [ ...
20      ],
21      "Source.2.calib": "absente",
22      "Byte-order": "little",
23      "Tubes-pulses": "arretes",
24          ...
25  }
```

These JSON documents feature a set of key-value pairs, which can be sorted into three groups. A CouchDB specific part of the two keys "_id" and "_rev", which are a unique ID and a version control identifier. This allows to automatically keep track of all updates to a specific document.

The second part of the document is created by the python code that scans the data partition and consists in the meta information from processing e.g. the document type, the current date given as the unix time in seconds since 1970, the status of reading the file and further information including some machine specific variables. The last part of the document beginning at line 10 (listing 3.1) is the extracted DAQ specific header information of the data partition. Using a schema free database has the nice advantage that the information inside of this part can change without influence on the database itself.

The solution of reading in the header information from the data file and storage on datadb (listing 3.1) has been proven viable during EDELWEISS-III commissioning. Nevertheless, it is intended to replace this step via a direct communication of the DAQ software and the database. This will allow the storage of additional information from data taking like the total number of events and the rate of events, which is not available during writing of the header of a data file. Furthermore, errors can be tracked and documented. A separate database has been created to test the communication between SAMBA and CouchDB and a migration to this database is imminent.

A second job is run continuously and listens to the "changes feed" of the CouchDB server [214] hosted on the same analysis Mac in Modane. Whenever a a new document is registered on datadb, an sftp copy of the raw data to the computing center of Lyon (ccin2p3) is triggered. After successful completion the datadb document is updated with a key-value pair that documents this processing (listing 3.2 lines 0-6) and the next process can be launched. This following process named "proc1" is the rootification on the analysis Mac in Modane and subsequent copy of the ROOT file to the computing center in Lyon.

Listing 3.2: Excerpt of the JSON (Java Scrip Object Notation) code after automatic processing. Processing specific information has been appended to DAQ documents.

```
1   "proc0": {
2       "transfer_method": "sftp",
3       "file": "/sps/edelweis/kdata/data/raw/oj24c002_005",
4       "file_size": 375779911,
5       "date": "2014-10-24 09:23:18.035898"
6       "log": ...,
7       ...
8   },
9   "proc1": {
10      "date": "2014-10-24 09:24:49.643948",
```

```
11        "file": "/sps/edelweis/kdata/data/raw/oj24c002_005.root
             ",
12        "processname": "samba2kdata",
13        "file_size_mb": 163.8764238357544,
14        ...
15    },
```

Further tasks scheduled and documented in the same way are the amplitude extraction performed at the LHC (Large Hadron Collider) Tier2 (it's also a Tier1) computing cluster in Lyon [221] and the backup of the original raw data from disk to the HPSS (High Performance Storage System) tape drive system [222] of the ccin2p3 computing center.

During my time of responsability of this system (2013-2014) 7.5 TB of raw data have been processed consisting in a total of 23000 files. Several routines were modified to account for changes of the DAQ and the entire system was migrated to a new analysis Mac.

3.2. Signal processing in EDELWEISS-II

In order to discuss and motivate the data processing algorithm used in this thesis we will quickly review previously tested algorithms within EDELWEISS-II. Hence, we will summarize the detailed pulse characteristics here, before discussing the different algorithms that were applied. In EDELWEISS-II both heat and ionization signal had a very similar signal shape of exponential decays (fig 2.2 and 3.5). The decay of the ionization signal was shaped by the RC feedback in the electronics and was designed with a decay time constant of the order of 10 ms. The heat signal, in contrast, shows two exponential decays which are due to the thermalization processes and the weak thermal links of the bolometer. They have much slower time constants ranging from 100-500 ms.

The trigger was applied on the single heat channel, as the heat channel is affected far less by the ionization quenching from nuclear recoils. It is still affected due to the smaller Neganov Luke heating, but at least a similar sensitivity and trigger threshold for electron and nuclear recoils is retained. In addition, the heat signal readout is performed after a so-called demodulation procedure (fig. 3.4). The heat sensors are biased with a constant current, but alternating polarity. This enables a contact potential free absolute measurement of the operation point of the NTD.

The consequently required demodulation procedure has another positive benefit. The procedure consists in taking the difference between first and second half of a square wave period and it allows the suppression of slowly varying crosstalk components. Since some microphonics at a few Hz can be present in the EDELWEISS setup varying with time or the exact setting of the cryostat damping and positioning, this modulation facilitates a stable triggering. The further trigger algorithm implemented in SAMBA is visualized in the remaining sub-figures in fig. 3.4. It consists of a 1st order digital Butterworth filtering and cross-correlation of filtered pulse and template. A simple threshold is then applied
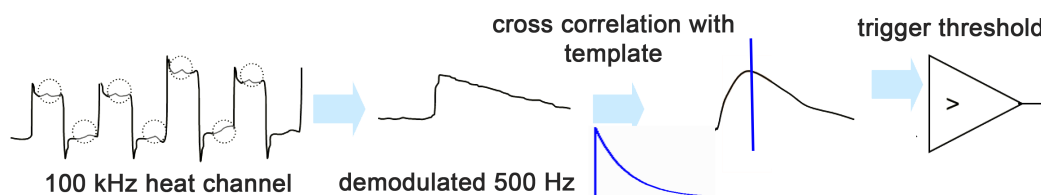
Figure 3.4.: Trigger scheme of EDELWEISS-II heat channels.
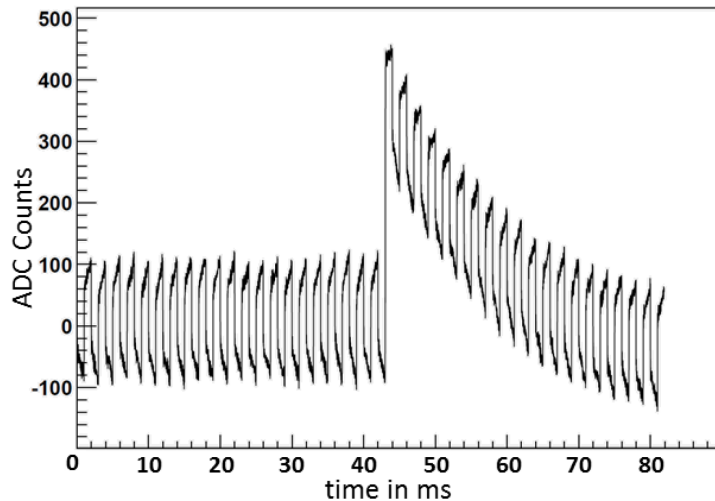
Figure 3.5.: Digitized pulse trace of an EDELWEISS-II ionization signal. A large cross-talk from the heat modulation is superimposed on the signal.

on the output of the cross-correlation. The template was usually defined through careful selection of an event with $E = 356 \, \text{keV}$ from Ba calibration and a parametrization of the rise and two exponential decays with

$$f(x) = p[1] \cdot (1 - e^{\frac{x-p[0]}{p[2]}}) \cdot (e^{-\frac{x-p[0]}{p[3]}} + p[5] \cdot e^{-\frac{x-p[0]}{p[4]}}). \tag{3.1}$$

The five parameters are p[0] - position of the pulse inside the trace, p[1] - overall amplitude, p[2] - rise time parameter, p[3] - fast decay parameter, p[4] - slow decay parameter and p[5] - amplitude ratio between fast and slow decay. When the threshold on the amplitude was surpassed, event building was started and in total seven traces were recorded to disk. The heat signal was stored at a sampling of $500 \, \text{Hz}$ with 512 sample points. The signal of the 6 physical electrodes of the ID detectors were stored at the original sampling of $100 \, \text{kHz}$ with 8192 sample points. A single ionization trace within its $82 \, \text{ms}$ time window is shown in fig. 3.5.

The heat modulation has significant side-effects for the ionization channels. The square pattern couples to the ionization channels via capacitive and inductive cross-talk. Some extra processing is thus required to remove this spurious noise again. The data trace, which is shown here corresponds to an $O(100 \,)\text{keV}$ event. Half of the trace was recorded as pretrigger information. This has to be done not only to account for the jitter in the position of the faster ionization trace with respect to the heat trigger, but more importantly to be able to extract the heat modulation pattern from the pretrace.

3.2.1. Common data preprocessing

For the data analysis, a common set of operations was performed on the extracted pulses before applying different filter algorithms. For the heat channel this consists of a baseline subtraction only. The recorded data contains an equal amount of pretrigger and post trigger data. Hence, the first 50% of each trace should correspond to pure baseline data. Including the signal rise time and a possible jitter in the trigger position, especially for the ionization channel, this value is reduced. In order to define a conservative pretrace length, only the first 40% of each trace were regarded. From these samples the mean baseline amplitude was calculated and subtracted from the entire trace.

For the ionization channel it is obvious to remove the crosstalk from the heat modulation pattern before parameterizing the signal accurately. Hence, the pretrace was used to

extract the crosstalk from the heat modulation pattern. In practice the first 40% of the trace (32 ms) contain 16 full heat modulation patterns. The observed pattern was averaged based on these 16 cycles and subtracted from the entire trace. While this removes most of the heat modulation, it proved useful to also extract a pattern at half of the heat modulation frequency (250 Hz) and remove that as well. Afterwards the remaining baseline was subtracted and the ionization signal could be parameterized by a single exponential decay

$$f(x) = p[1] \cdot e^{-\frac{x-p[0]}{p[2]}} . \tag{3.2}$$

p[0] denotes the pulse position in the pulse, with the additional constraint that $f(x) = 0$ for $x < p[0]$. p[1] is the absolute amplitude and p[2] the decay parameter of the template.

After this pretreatment four different types of pulse shape analysis algorithms were applied within the KData framework.

A computationally fast amplitude extraction based on a trapezoidal filter [223] was implemented and adapted to the double exponential decay of the heat signals [224]. However, as a single analysis it was not competitive to other algorithms. Also a wavelet transformation based approach was studied within a Bachelor thesis [225]. It was implemented along a design employed by the CDMS experiment [226]. During the limited amount of time very good accuracy for some parameters like signal rise-time and start time could be achieved. Also, the algorithm is computationally fast. But for the most important parameter, the amplitude estimate, the algorithm could not compete to either an optimized bandpass with consecutive time domain template fit or to an amplitude estimate from an optimal Wiener filter. Since these two analysis algorithms were hence the obvious choice for the implementation of a first full processing of EDELWEISS-III data, they are discussed in more detail in the following two sections.

3.2.2. Bandpass filter

The goal of signal processing is in general to increase the signal-to-noise ratio and hence recognize even very small signal pulses among the existing noise. As a common practice this optimization is often designed and sometimes also performed in the frequency domain instead of the time domain. A standard way to tackle this problem is the attenuation of low and high frequencies outside of the signal's main frequency range, while amplifying or keeping a set of middle frequencies. These types of filters are then called bandpass filters. A particular analog implementation with maximal smoothness in the pass band of highpass and lowpass filter was developed in 1930 by S. Butterworth [227]. The simplest 1st order filter has a very smooth transition from passband to attenuation. Higher attenuation and sharper cutoffs can be reached with higher order implementations. An example of the frequency response of this filter is shown for the frequency range of the EDELWEISS-II ionization signals with a highpass cutoff frequency of 50 Hz in fig. 3.6.

A digital version has been implemented as IIR (infinite impulse response) filter in KData. The filter operation

$$y[n] = \Sigma_{i=0}^{P} b_i \cdot x[n-i] - \Sigma_{j=1}^{Q} a_j \cdot y[n-j] \tag{3.3}$$

is performed in the time domain. Notation and parameter conventions follow the filter implementation of the scipy scientific computing library for python [228]: b and a are the numerator and denominator polynomials of the IIR filter. P and Q are related to the number of polynomials used in the filter. y denotes the filtered sample points and x the unfiltered sample points. Using existing algorithms included in the scientific python
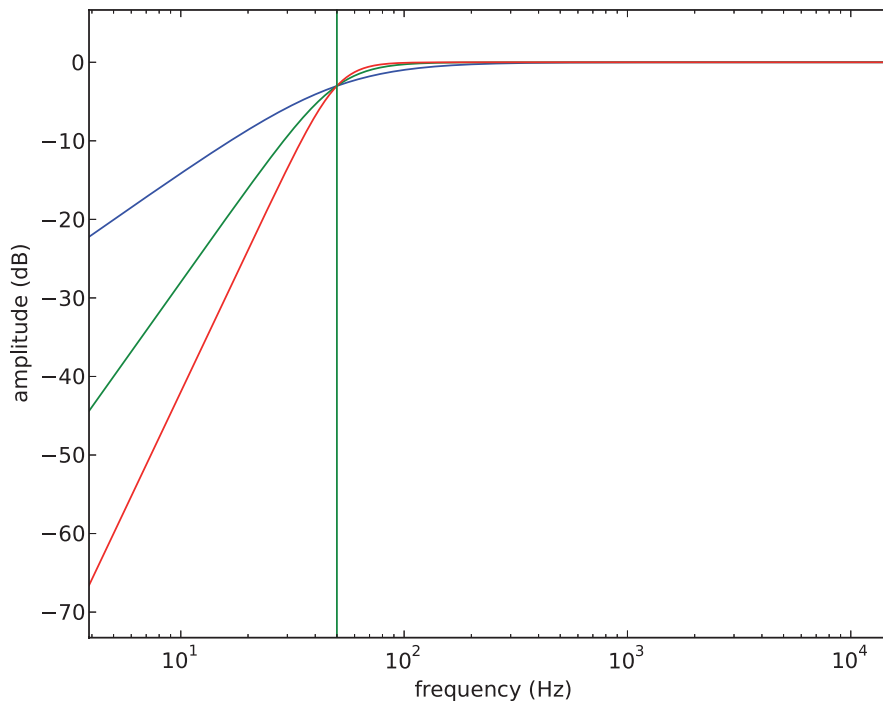
Figure 3.6.: Frequency response of a 50 Hz highpass Butterworth filter implemented in KData. Blue corresponds to the 1st order filter, green to the 2nd and red to the 3rd order filter. The cutoff frequency is marked by the vertical green line.

libraries [229] the numerator and denominator polynomials are calculated once for a specific filter and a set of parameters and are then stored on the CouchDB database.

A specific example of the use of both a highpass Butterworth filter and an additional lowpass filter for the data analysis in EDELWEISS-II is shown in fig. 3.7. In (a) a raw heat trace of an $O(100\,\text{keV})$ event is plotted. First the baseline is removed from the trace (b). Then the trace is filtered with a Butterworth low and high pass filter (c). The filtered trace is cross-correlated to a filtered heat template (d). From the point of maximal correlation, timing and amplitude are extracted as start parameters of a template fit with two free parameters. The position is allowed to vary within ± 5 bins of the point of maximal correlation and the amplitude is the second free parameter.

An additional fixed time fit with the signal rise at a position of $\sim 600\,\text{ms}$ is performed to obtain a baseline estimate. The position was chosen to be free from a potential bias of the pulse preprocessing which is performed on the pretrace. Instead, it has to be ensured that the contamination of real pulses which lead to a one sided tail is not too large. In general this will not be too difficult in a rare event search. Either a specific noise sample can be taken or in our case the trigger itself is set at a level such that most traces are pure noise. Additionally in EDELWEISS-II an entire tower of detectors was read out simultaneously if a single one of them had a signal above the trigger threshold. In any case the resulting estimate of the baseline width is conservative.

The influence of specific filter parameters, e.g. order and cutoff frequencies on the achieved resolution was studied on a single detector (ID3) and single data set of several hours from June 7th, 2009. As a measure of the performance, the FWHM of the heat channel baseline has been plotted versus the highpass cutoff frequency for 1st (blue) 2nd (green) and 3rd (red) order Butterworth filters in fig. 3.8.

For each of the seven channels an optimal set of parameters was defined. For example for the heat channel from fig. 3.8 a 2nd order Butterworth filter with 8 Hz highpass and an
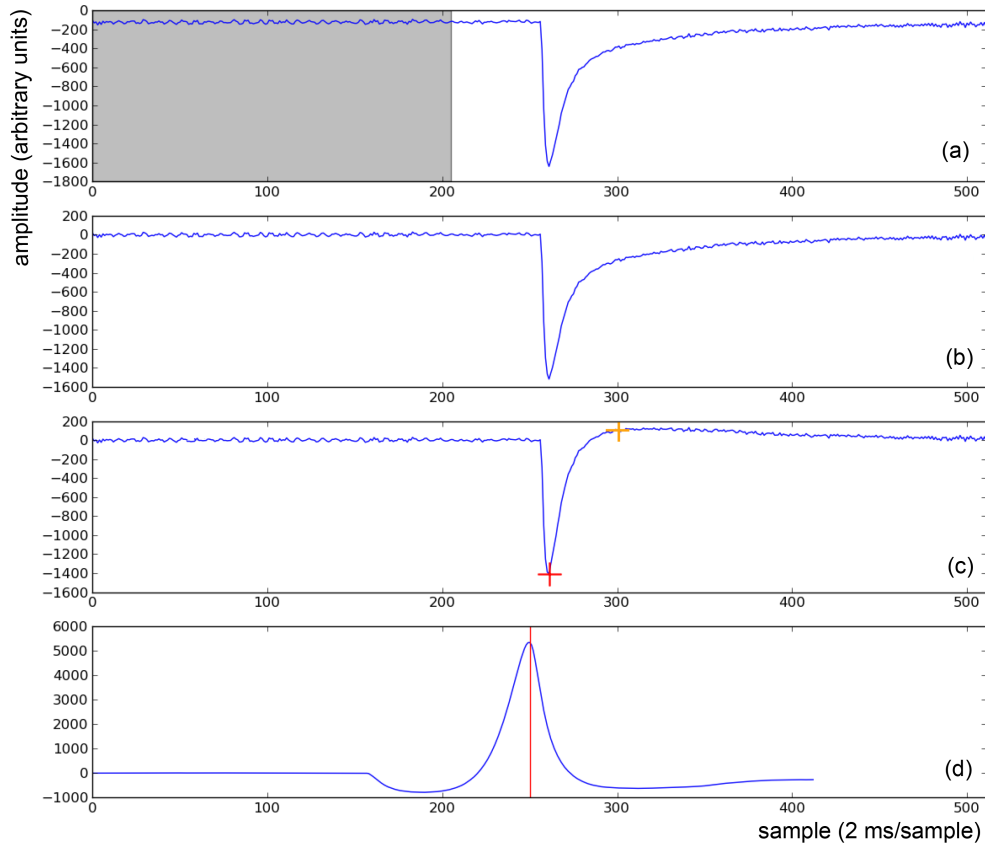
Figure 3.7.: Overview of the standard procedure to estimate the heat amplitude in EDELWEISS-II. (a) raw trace, the first 40% (gray shaded area) was used to estimate the baseline; (b) trace after baseline subtraction; (c) trace after bandpass processing with the position of the amplitude estimation (red cross) and a fixed position to estimate the baseline resolution (yellow cross) (d) result of the correlation of the filtered heat template with the filtered pulse. The position and amplitude of maximum correlation are used as start values for the fitting of the template. Figure from [224].

additional 100 Hz lowpass was used. The performance proved almost independent of the lowpass filter, which can be understood in the sense that the template fitting in the time domain is implicitly doing a lowpass operation and is rather insensitive to high frequency noise.

Using the selected filter parameters a data set of 2 month was processed for this single detector to compare the performance to the main EDELWEISS-II analysis, which employed an optimal Wiener filter.

3.2.3. Optimal filter

The idea of the optimal filter or Wiener filter [230] is to go beyond the performance of a bandpass filter by designing a very specific frequency dependent filter for a well known stationary signal and noise power spectrum. It was developed independently by Kolmogorov and Wiener in the early 1940s and is often referred to as optimal filter. It is optimal in the sense of minimizing the mean-square error of the measured data with respect to a desired noiseless signal. Assumptions are the absolute knowledge of both signal and noise power spectrum.

In EDELWEISS-II the original implementation with Wiener-Hopf equations is computationally not well feasible due to the long pulse traces of up to 8192 samples. Instead, an
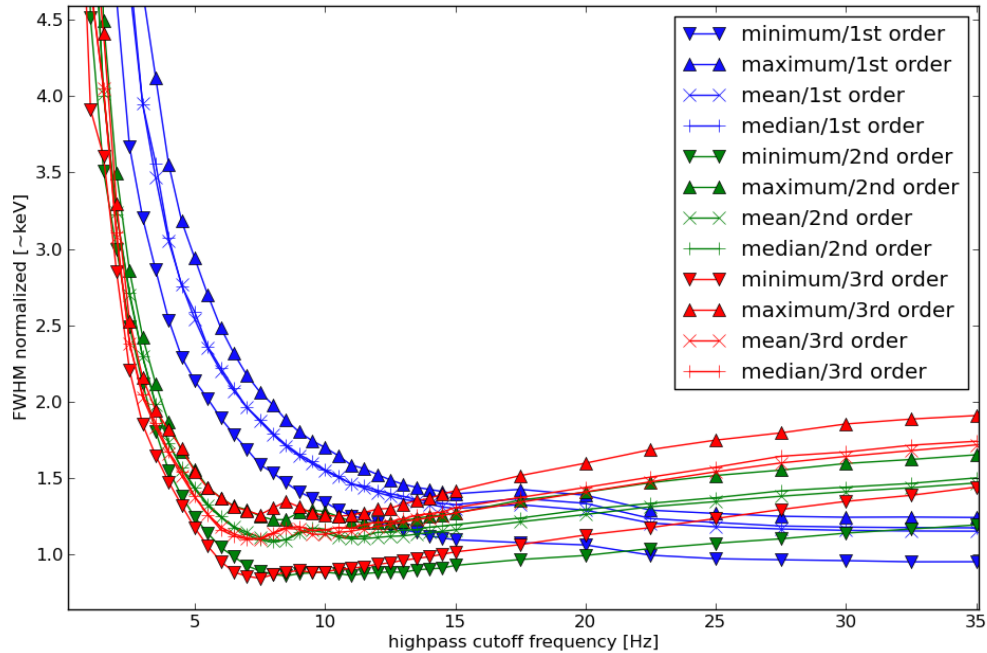
Figure 3.8.: Baseline resolution (FWHM) as a function of the Butterworth filter parameters for the heat channel of ID3. The study has been performed on a single data set from June 7th 2009. Figure from [224]

implementation in the frequency domain along a design used by the CDMS experiment [231] has been realized in KData. As an additional assumption in this process, the noise was taken as stationary, Gaussian distributed noise without correlations inbetween individual frequencies. A review of the most important equations has been presented in [224] and will not be repeated here. It is worth to note however, that in the current implementation the position of maximal amplitude and minimal χ^2 don't line up perfectly. This could hint at a problem with the assumption of stationary Gaussian noise that is uncorrelated in the frequency domain or at an unidentified problem in the code.

Nevertheless the implemented Wiener filter has been tested in [224] on a data sample from 23rd January 2012. In fig. 3.9 the signal power of a heat template is shown in green. A noise power spectrum obtained from the same data set is shown in blue. The frequency response of the optimal filter is shown in red. It can be nicely seen how frequencies with a bad signal to noise power are attenuated by the optimal filter. Dependent on the supplied noise spectrum the implemented filter could yield comparable and in some cases superior resolutions with respect to the bandpass analysis, as one would expect.

However, the optimal filter is very sensitive to inaccuracies in describing the noise power spectrum, and it proved a non-trivial task to extract an accurate noise power spectrum. For the EDELWEISS experiment there are two challenges for obtaining an accurate noise estimate: The 1st is the fact that the noise power spectrum is not stable over time. Instead, the noise level and spectrum can vary significantly over time. Whether this is due to microphonics from mechanical parts which are only working part time, from slow drifts in cryostat temperature or positions or from other sources is unknown. As a solution to that challenge one can try changing the noise power spectrum over certain time periods or using a time weighted average of the noise power of adjacent noise pulses. In order to keep the time window small and the statistics high one needs to build the noise from as many pulses as one can. In the EDELWEISS-II trigger scheme with its very low threshold most traces contain no real pulse but noise only. Hence one is tempted to use these pulses to
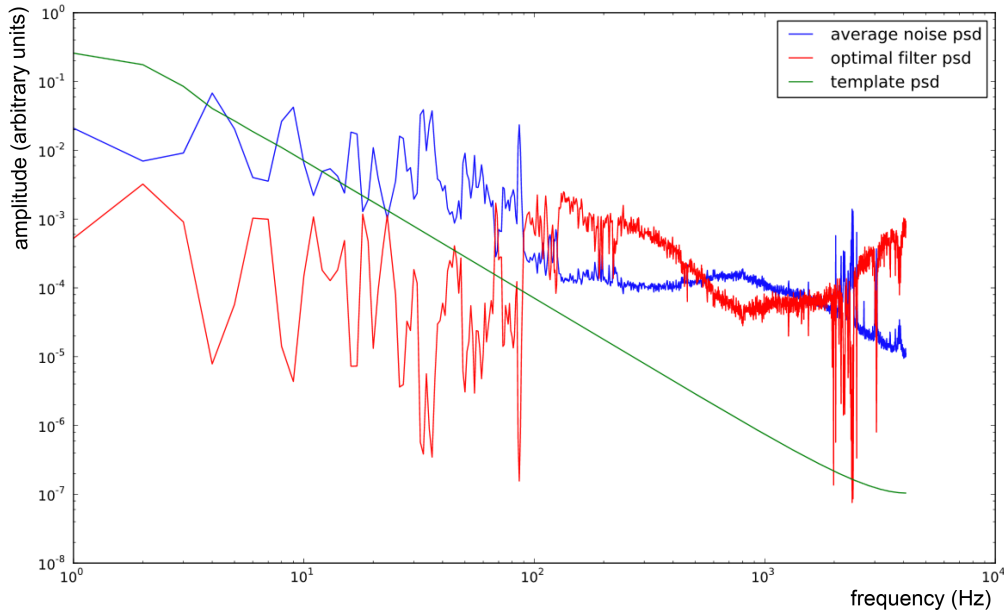
Figure 3.9.: Normalized power spectral densities for signal template (green), noise (blue) and frequency response of an optimal filter (red). Example data from January 23rd 2012 for the heat channel of an FID detector operated in the EDELWEISS-II setup. Figure from [224].

build the noise spectrum. Consequently, the second challenge is acquiring a representative noise power spectrum without polluting the noise power spectrum with signal events. This in turn requires an analysis on its own.

The task of finding an algorithm to reliably extract an accurate noise power spectrum which results in a better performance than the simple bandpass analysis was further complicated by the nature of the data taken in early 2012. In the transition to EDELWEISS-III the first FID detectors had severe leakage problems resulting in additional low frequency components in the pulses. The change of cryostat shields and the replacement of the pulse tube required readjustments of the optimal running conditions. Also optimal values of the voltages on the electrodes or for the heat modulation were not known for FID detectors.

Thus none of the initially tested methods to extract the noise power spectrum was as stable and reliable as the bandpass analysis discussed before. Further approaches at determining the noise including the acquisition of multiple noise power spectra instead of a single one and checking which one is optimal on a trace by trace basis were discussed, but not vigorously studied. A decomposition of signal and noise as it is inherent to the wavelet transformation method might be another well suited approach for extracting a better noise power spectrum.

3.3. Signal processing in EDELWEISS-III

In EDELWEISS-III the FID Ge detectors are equipped with 2 NTD heat sensors instead of one, and the number of physical ionization channels was reduced from six (ID detectors in EDELWEISS-II) to four. At the same time the modification of the ionization readout altered the signal from an exponential decay to a step function. Thereby signal power has been shifted to much lower frequency components. The precision of the signal amplitude can hence be increased with integration over long times. At the same time one wants to keep the original time resolution for the correlation of events with the muon-veto system and subsequent rejection of muon-induced events. To address both of these requirements,
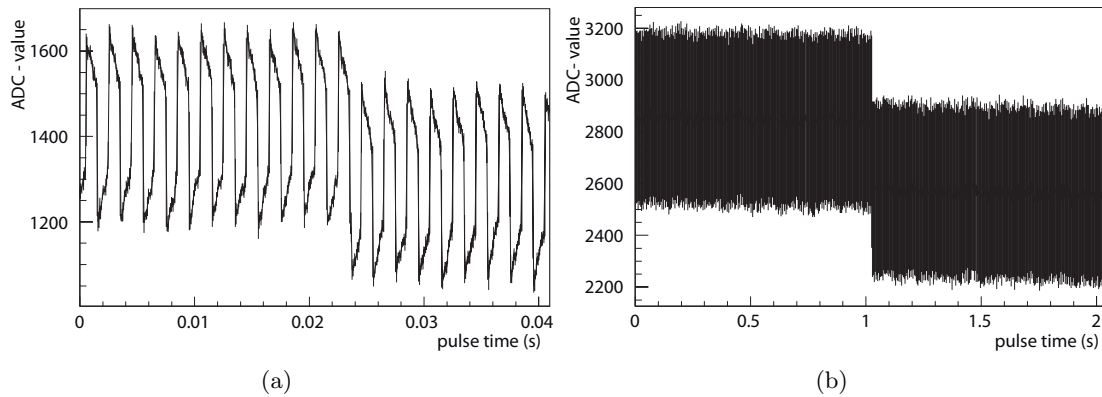
Figure 3.10.: Ionization traces recorded in the EDELWEISS-III setup. Due to the large signal power at low frequencies, a down sampled slower ionization trace (b) has been added to the event storage in addition the original trace (a). The signal in the above traces corresponds to an O(50 keV) event.

the DAQ software SAMBA has been modified to store an additional set of 4 more ionization channels with lower sampling. For the commissioning run discussed in the following analysis this data was stored at a sampling of 2 kHz with a length of 4096 sample points ($\sim 2\,\mathrm{s}$). Each of the sample points in such a trace is calculated from the average of 50 sample points at the original physical digitization of 100 kHz. Examples for the altered ionization raw data, showing the trace at its original sampling and after down-sampling are given in fig. 3.10.

This altered ionization trace has some implications on the analysis. For one thing it opens up the possibility to try an entire set of algorithms which were designed to find steps in piecewise constant signals. On the other hand it also produces a new problem for the existing optimal filter. The Fourier transform of the step function can be calculated analytically for the continuous case and results in a $1/\omega$ spectrum. The finite window and sampling recorded by the DAQ on the other hand introduces discontinuities to the data. A solution to this problem can be designed using windowing techniques which restrict the
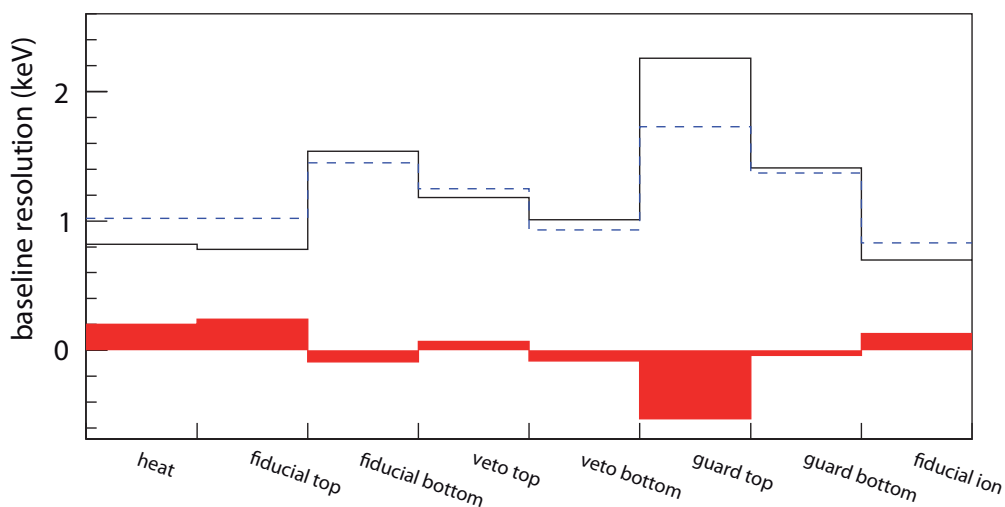
Figure 3.11.: Results from the comparison of baseline resolutions for an optimized IIR Butterworth filtering in KData (dashed blue) versus the Wiener filtering used in the main EDELWEISS-II analysis [94] (solid black). The absolute difference in the energy resolution (KData - optimal filter) is plotted in red. Figure based on data from [224].
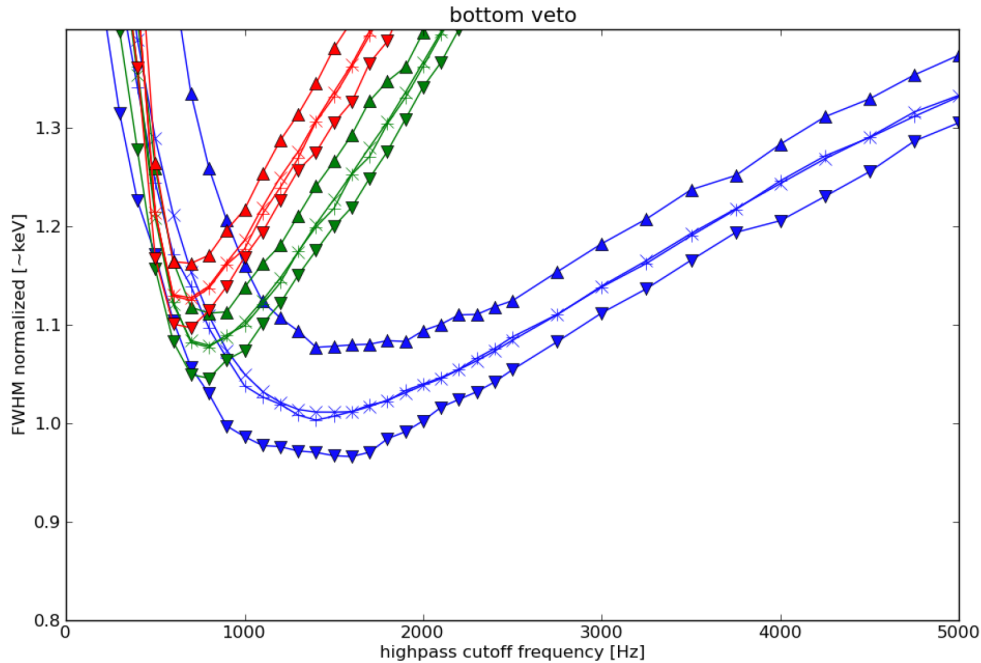
Figure 3.12.: Study of the optimal cutoff frequency in terms of baseline resolution for an ionization channel of detector ID3. Color coding as in fig. 3.8

frequency space of the signal.

However, given the experience we had about the reliability of the optimal filter during commissioning it was difficult to find a robust solution. The competitive performance of the Butterworth filter, observed in a comparison over stable EDELWEISS-II data taking (fig. 3.11), led to the implementation of a full processing on the basis of an improved bandpass analysis, before attempting to find a better noise detection algorithm for the Wiener filter. The subsequent implementation and analysis is the main part of this thesis.

The analysis is designed as a general analysis for all data from our detectors. In contrast to the specialized analysis of a single detector in [224] we could thus not afford to scan different filter parameters for individual detectors and data sets manually. Instead the processing is designed to select the optimal filter parameters automatically and continuously on a run by run basis adapting to current running conditions. As a viable compromise on the number of tested bandpass filters and computing time the method of choice was a continuous analysis with a set of 12 different lowpass filter configurations. The highpass filter showed a very limited influence of the performance of filtering was thus skipped entirely.

The choice of filters was motivated by the results from [224]. Within first to third order filters the third order filters showed a very similar performance to the second order filters. Since the second order filters had typically a smoother behavior with respect to the cutoff frequency, the third order filters were dropped. An example for the baseline resolution (FWHM) versus filter parameters is shown for one of the ionization channels investigated in EDELWEISS-II in fig. 3.12.

The analysis was thus run with six different cutoff frequencies both at first and second order of the Butterworth filter. The selection of the best filter parameters was studied in terms of both the best baseline resolution and also in terms of reliability and uniformity of the data period reflected in the χ^2 of the Gauss fit to the baseline estimates. The algorithm selecting the best parameters was determined in a dedicated study [232] and will be detailed in sec. 3.3.3. The results of this study could be used in the current WIMP data taking to select the best first order filter that can be applied in the DAQ software
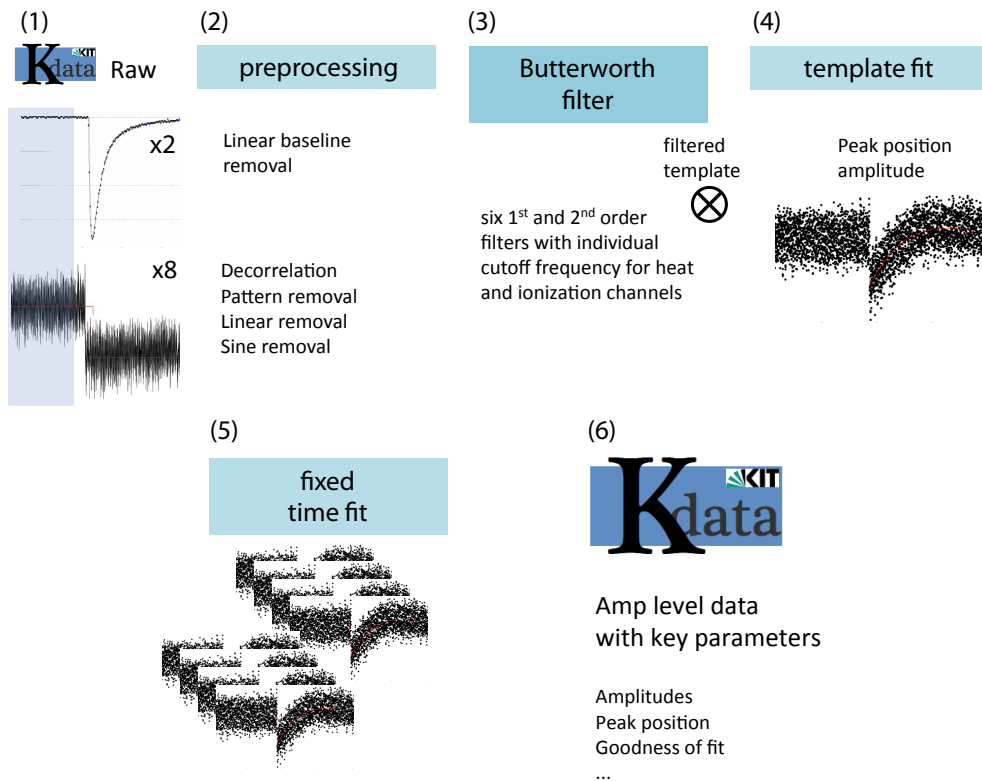
Figure 3.13.: Scheme of the bandpass analysis implemented in KData. The preprocessing uses the first 40% of the trace (shaded blue) to remove a baseline offset and to improve the signal to noise for the entire trace. After preprocessing, the data are filtered with 12 different highpass Butterworth filters. A template fit is initialized with amplitude and peak position estimated from the cross-correlation of filtered pulse and template. In addition to this two parameter fit, the results of a fit with a common timing derived from the largest ionization amplitude is stored in the amplitude level.

to achieve better trigger thresholds. A new tool to extract more reliable heat templates from averaging of several pulses has been added for the same purpose. It has been used for the main analysis both in the commissioning data under investigation and in the currently ongoing WIMP search.

Special emphasis of this thesis has been put on the improvement of the ionization channel analysis. Not only did we need to adapt to the different template and sampling for the EDELWEISS-III DAQ, but the ionization channel resolution was the limiting factor in the EDELWEISS-II low WIMP mass analysis [93]. A significant improvement in the resolution of individual ionization channels was achieved in this work through the introduction of two more techniques to suppress noise in the ionization signals. The first employs the fact that the sum of the net charge (electrons and holes) of real and induced ionization signal is always zero. This allows for a decorrelation of the four ionization channels by the removal of common noise. The second method uses the pretrace to fit the phase and amplitude of especially strong noise components and removes those from the entire trace.

At the moment all channels are analyzed independently within KData. But it can be beneficial to employ a second analysis stage and fix the timing of the individual channels to a common time for a second fitting. In that way, a better position of the heat and slow ionization channel fits can be achieved. All ionization amplitudes can be compared directly, too. This mode is already foreseen for the processing discussed herein and the
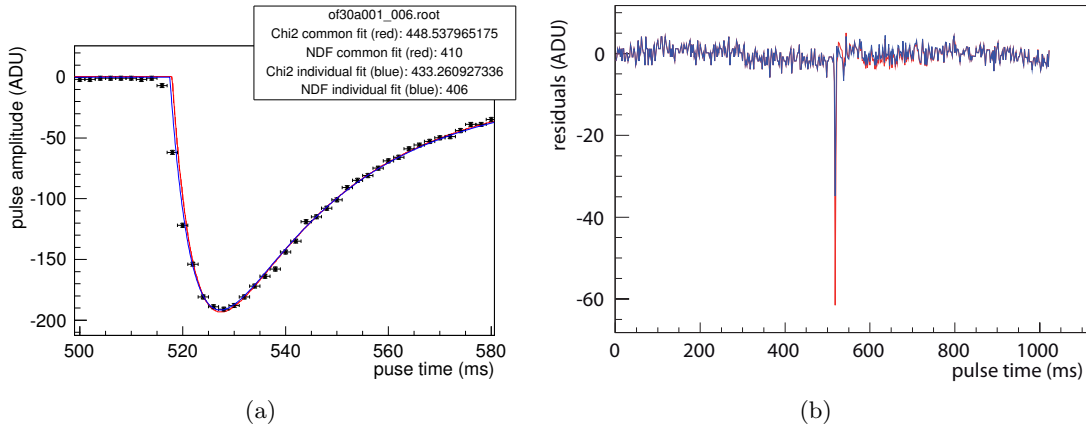
Figure 3.14.: (a) Zoom to the central region of the heat template fit for the first of the two NTD heat sensors of detector FID827. Both fit results, the individual template creation (5 parameter fit) in blue and the averaged template fit with 2 free parameters (amplitude and position) in red are displayed. (b) Residuals between fit and data. Except for the signal rise very good agreement is observed in both fits. The template has been computed on data from 30th June 2014 for the ongoing data taking.

time of the common fit has been fixed to the time of the fit to the largest ionization excursion in a first prototype analysis. This could potentially be improved by fitting the timing in the channel or combination of channels with best signal to noise ratio first, and then restricting the time window for the fit in the fast channels from which the common time is extracted.

A summary of the KData processing scheme has been visualized in fig. 3.13. In the following, inidividual algorithms introduced in this thesis and their physical and mathematical basis will be discussed.

3.3.1. Definition of a template pulse for heat signals

In KData the parameters of the function approximating the heat signal shape (eq. 3.1) is estimated at the beginning of data taking from a set of five to ten pulses. With this method a possible bias from the selection of a single high energy pulse can be avoided. The semi automatic tool developed during this thesis preselects high amplitude pulses and fits the 5 different parameters (eq. 3.1) of the heat template signal to the pulse. For better fit convergence a set of average decay and rise-time parameters are used and position and amplitude values are extracted from a correlation to an average template and set as initial fit parameters. In case the user does not decide otherwise the fit parameters are subsequently added to an averaging procedure.

Once the specified number of pulses has been fit, averages of the rise and decay parameters are computed. In a second round of fitting the results of the free fit with 5 different parameters and a constrained 2 parameter (amplitude and pulse position) template fit, where all shape parameters are fixed to their averages are compared. In case a strong deviation of a single pulse fit is observed this pulse can be excluded and a new template can be computed. Otherwise the fit results are automatically stored as a graphics file (fig. 3.14) in a specific folder documenting the processing steps. The resulting average template parameters as well as the template formula are stored directly on one of the CouchDB databases, so that they are available for all analyses. During the definition of the templates a certain energy dependence of the pulse shape was noted, which is especially pronounced for the rise of the signals (see fig. 3.14 (b)). It is expected that

the documentation and accessibility of template parameters in a well organized storage scheme, will help to find different dependencies of the template parameters as well as provide the possibility to monitor the long term stability of the template parameters.

3.3.2. Additional ionization channel preprocessing

The motivation to pay special attention to the ionization channels comes from a background population of heat-only events (e.g. without measurable ionization signal), which limit the sensitivity to low mass WIMPs. An improvement in ionization resolution allows the better separation of signals with small ionization component with respect to this background population. An example of this background population is given later in this thesis in fig. 5.2, where low energy background data from this commissioning run has been plotted. Any gain in the fiducial ionization resolution translates directly into a narrowing of this population. Since they have zero charge their spectrum follows the Gaussian of the ionization baseline distribution. The rate of these heat only events can hence be reduced by a factor 10 at an energy $E_i = 4 \cdot \sigma$ by a mere 15% improvement in the ionization resolution [233].

3.3.2.1. Removal of single frequency noise

One possible way to improve the signal to noise is to make further use of the pretrace data and not only extract and remove the pattern from the heat modulation, but also to filter out further noise components. One common class of noise that can be superimposed onto the data trace are sinusoidal components which can be due to crosstalk from microphonics or even from the 50 Hz AC power supply. Such specific noise frequencies become visible in the power spectrum of noise traces.

The noise power spectrum shown in fig. 3.15 shows signal and noise power for the entire available frequency range in the digitized slow ionization pulses. While the noise usually may be described by three components, a 1/f, $1/\sqrt{f}$ and a white noise component [200], the signal power only has a $1/f^2$ dependence. Hence, the dominant contribution in signal to noise should be gained at low signal frequencies. In addition to the specified noise components the actual noise power spectrum shows a forest of single frequency noise superimposed to the smooth model. Dominant peaks above 1.25 Hz show up in the displayed spectrum at 8 Hz, 50 Hz, 125 Hz and 800 Hz. There is a huge dip at 500 Hz which corresponds to the frequency of our heat modulation. This dip is interpreted as an overcompensation due to the pattern removal algorithm.

A zoom to the low frequency region, which is of interest for the optimization of the signal to noise ratio is shown in fig. 3.15(b). After identification of certain noise frequencies the phase and amplitude of these sines can be fit within the pretrace of each event and afterwards removed from the entire trace. The implementation adapted here avoids the time intensive process of the χ^2 minimization procedure inherent to most fitting algorithms. Contrary, it uses the properties that sine and cosine are building an orthogonal basis and extracts the amplitudes of sine and cosine of a set of given frequencies via a much faster cross-correlation. It has been ensured that the cross-correlation is applied on full periods to avoid bias. A resulting noise power spectrum after application of 4 Hz, 8 Hz and 50 Hz noise removal is shown in dashed blue in fig. 3.15. For 8 Hz and 50 Hz an attenuation (plotted in green) of a factor ~20 has been achieved. For 4 Hz where no additional sinusoidal noise was present in the particular channel and data period shown, the algorithm introduced a slight worsening of the signal to noise ratio.

For the current processing, the sine removal processor is set to three dominantly occurring fixed frequencies (4 Hz, 8 Hz, and 50 Hz). However, these noise frequencies can vary over
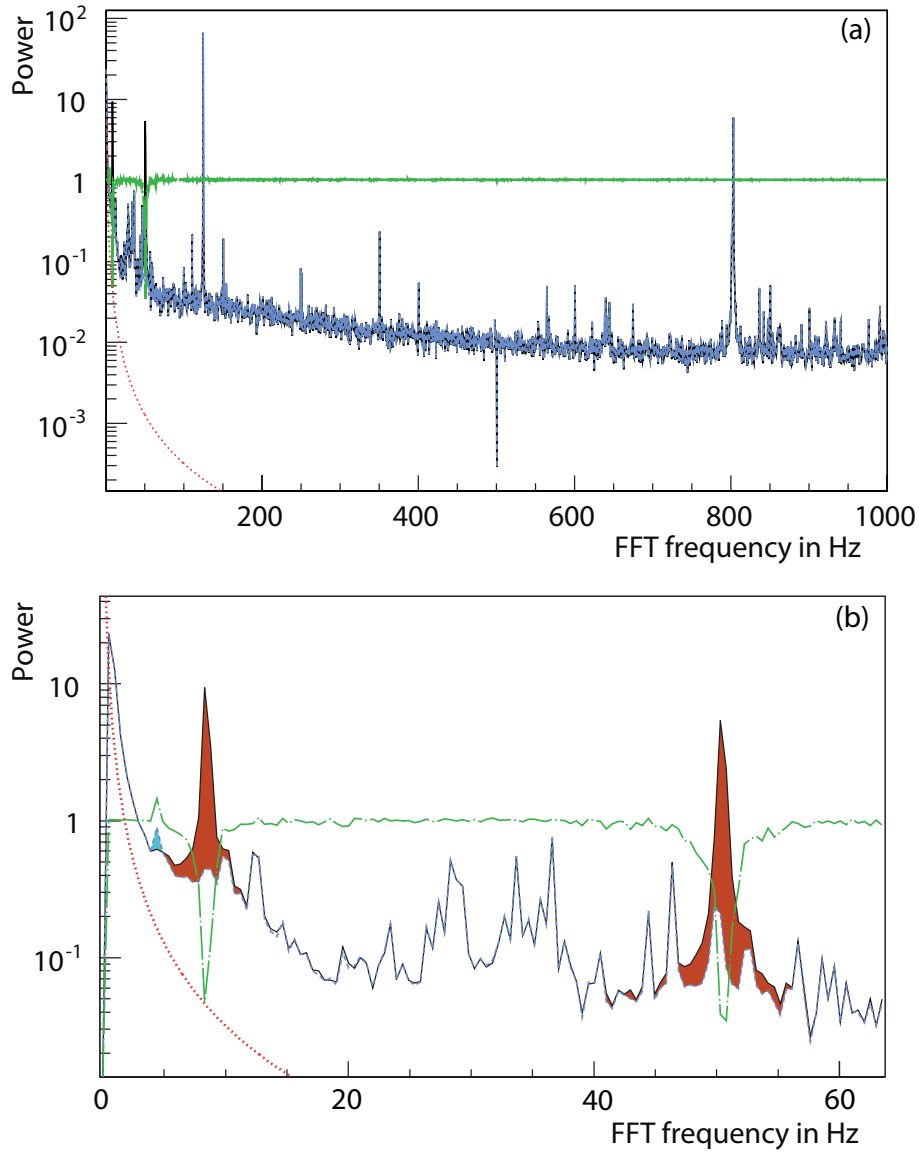
Figure 3.15.: Power spectral density for signal and noise for the veto channel of FID808 (a) and zoom (b) in the frequency domain. An analytical calculation of the power spectrum of the signal (step function) is plotted in dotted red. The power spectrum for noise events after pattern and linear removal has been averaged from 5 traces and is shown in black. The power spectrum after sine removal which is only different at the given frequencies of 4 Hz, 8 Hz and 50 Hz is shown in dashed blue. The brown and cyan area show the positive (negative) improvement (change) through the sine removal processor. Additionally, the noise attenuation factor achieved with this operation is given as attenuation factor per frequency bin in green.

time, and individual channels can show additional or different noise contributions. As a further improvement one could tune these frequencies over detectors and over time. Similarly one could try to build an automatic noise detection tool which could be used for a better single frequency noise removal together with an optimal filter afterwards.
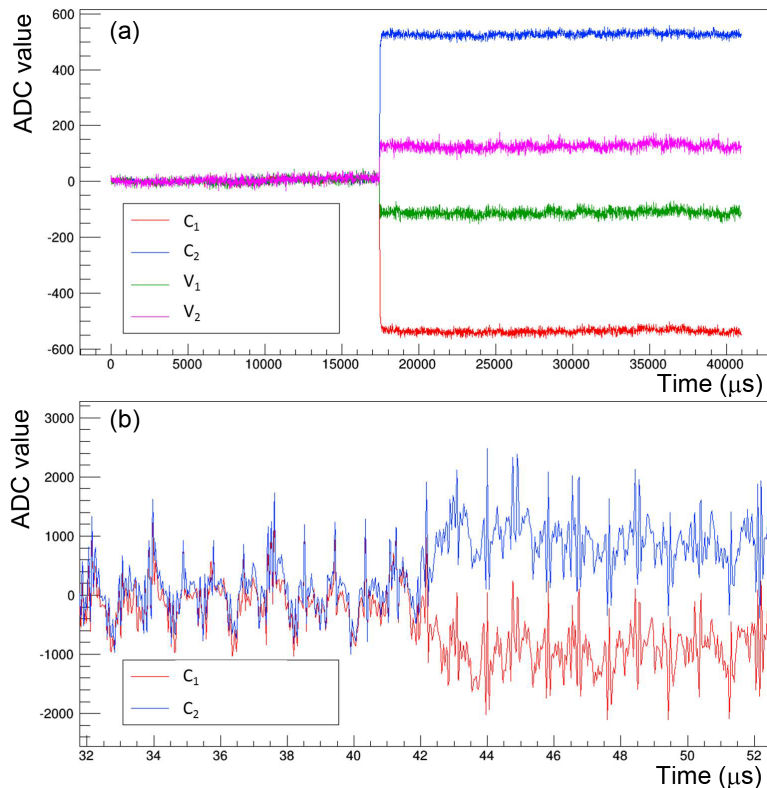
Figure 3.16.: (a) All four ionization traces of a bulk event at 100 kHz sampling (after pattern removal); (b) digitized pulse traces of the collecting electrodes for the same signal at 40 MHz sampling. Figure from [234].

3.3.2.2. Decorrelation

Another technique that can be used to improve the quality of individual traces is the removal of common noise. The operation

$$A_i[t] = A_i[t] - \frac{1}{4} \cdot \Sigma_j^{\text{ionization channels}} A_j[t] \tag{3.4}$$

removes the average noise of all ionization channels from the trace $A_i[t]$. Hereby i stands for a specific ionization channel, one of the collecting electrodes or a veto electrode and the sum is carried out over all ionization channels. This operation only works since the sum of all signals is zero. Charges are always created in electron-hole pairs and hence this requirement is obviously fulfilled assuming a complete charge collection without trapping and keeping in mind that charge propagation effects are not resolved at the sampling of 100 kHz (fig. 3.16 (a)).

The sum of all signals at a given sampling time is zero even for the more general case when taking into account trapping, charge propagation effects in time-resolved signals (fig. 3.16 (b)) and Ramo-induced signals on all electrodes. This could be especially helpful to clean the highly sampled ionization traces which are polluted with an overwhelming noise from the DC-DC converters in the warm electronics boxes used in EDELWEISS-III.

The underlying effect and ways to calculate potentials induced by moving charges were originally described by Shockley and Ramo [235, 236]. A discussion and application of this effect to study the trapping properties of FID Ge detectors and optimize the EDELWEISS-III high energy calibration is given in [237].
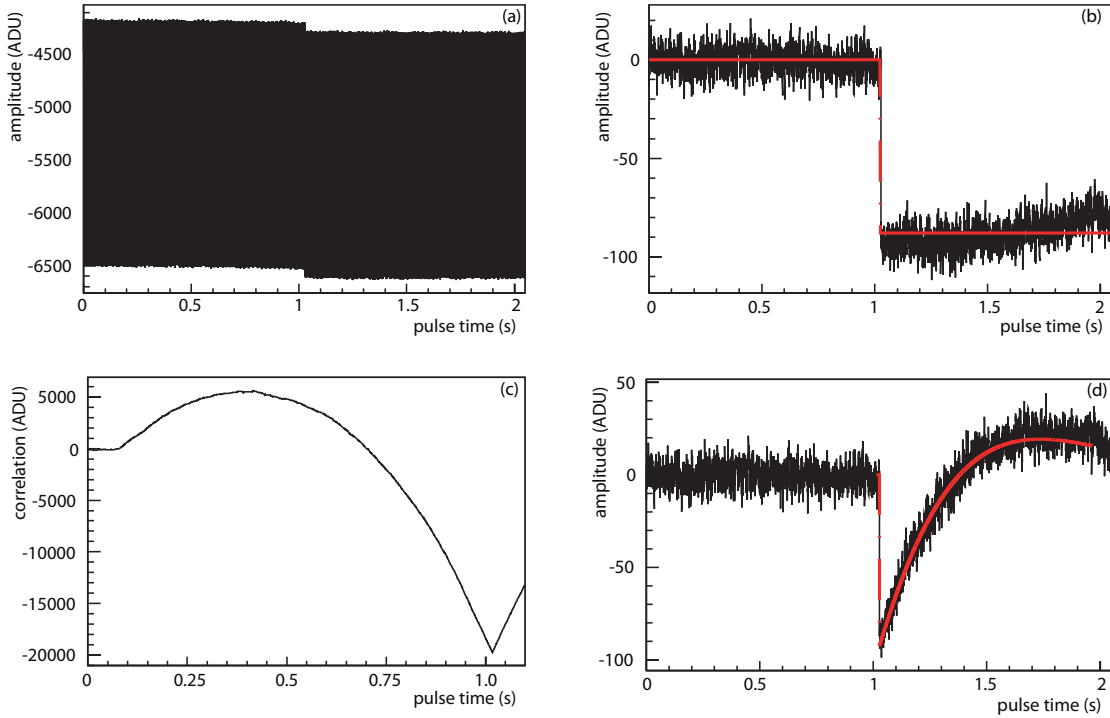
Figure 3.17.: EDELWEISS-III pulse processing scheme exemplified for the ionization channel at reduced 2 kHz sampling. The raw pulse trace (a) is preprocessed through decorrelation, pattern removal, linear removal and sine frequency removal (b). Then both template (red) and pulse are filtered with a Butterworth highpass filter and the cross-correlation of template and pulse is computed (c). From the point of maximal correlation pulse position and amplitude are extracted as starting parameters for the χ^2 minimization of the template fit (d).

3.3.3. Optimal Butterworth parameter selection

The amplitude extraction as summarized in fig. 3.17 is performed with 12 different filter parameter sets. This has implications on the portability and analysis speed of these files. Hence it was decided to implement a data quality analysis as early as possible and to select an optimal set of filter parameters. Calibration and further analysis tasks can then be carried out on a factor $\sim$10 smaller skimmed data files. The files containing all analysis records are kept and can be used for special analyses. Different filtering techniques and parameters might perform better or worse for different variables like pulse timing and amplitude.

For this analysis the selection of the best set of filter parameters i is performed requiring the minimum of a weighted combination of both the baseline resolution σ_i and the reduced $\chi^2_{red\,i}$ of the Gauss fit. Both parameters are estimated from the fit to the baseline distribution applying only a minimal noise selection algorithm. Events where the free pulse fit went to its boundaries or where there is an obvious signal of more than 5 keV on the sum of the electrodes are discarded. This allows to minimize non Gaussian tails from crosstalks and gives a better estimate of the baseline distribution. The best set of parameters i is then determined according to the minimal value of

$$f(\sigma_i, \chi^2_{red\,i}) = \sqrt{0.9 \cdot \sigma_i^2 + 0.1 \cdot \frac{\langle\sigma_i\rangle^2}{(\frac{1}{12}\Sigma_{i=1}^{12}\chi^2_{red\,i})^2} \cdot (\chi^2_{red\,i})^2}. \tag{3.5}$$

This selection is optimized to find a set of filter parameters which are rather aggressive in terms of resolution with a high weight of 0.9 on the energy resolution, e.g. the width
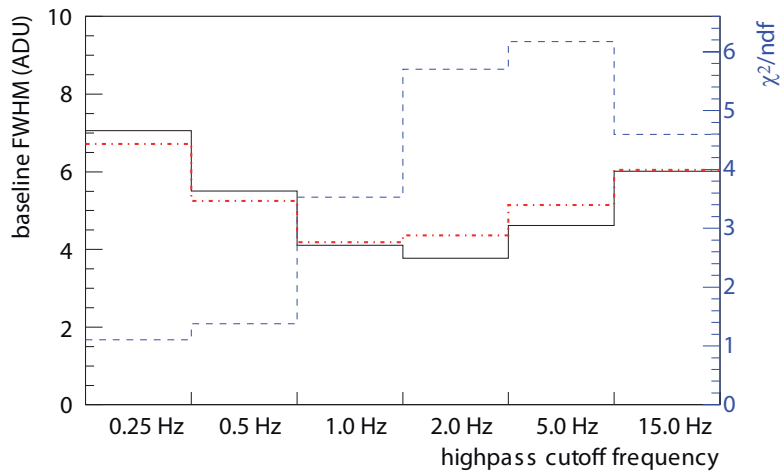
Figure 3.18.: Selection of the optimal filter parameters, e.g. the cutoff frequency and order from the reduced χ^2 and baseline resolution (FWHM) from a Gauss fit to the amplitude distribution of noise events. This is exemplified for the hole collecting electrode of FID808 for a tpycial one day data set, here a gamma calibration data set from the 5th November 2013. In this example only a comparison of 1st order results is shown, but the 2nd order filters follow the same qualitative behavior. Measured baseline resolutions of the Gauss fits are given in solid black, χ^2-values in dashed blue, and the result of the selection formula in dash-dotted red. For this example a 1 Hz highpass cutoff frequency has been chosen as best cutoff frequency.

of the Gauss fit. The weight of 10% on the goodness of the fit to the baseline seems low in comparison, but any serious deviation of the data from a Gauss distribution drastically effects the χ^2 and 10% was found as a sufficient weight to ensure the robustness of the fit result. An example of the measured baseline resolution values, χ^2 values and subsequently calculated weights is shown for detector FID808 for a large statistics gamma calibration (fig. 3.18). A similar analysis could be used to find the average best filter parameters to be used in our trigger algorithm in SAMBA.

While the selection function applied here is tuned to gain in resolution, the selected low corner frequencies of the Butterworth filters show a side effect for Ba calibration data. Due to pile-up events the Butterworth highpass filters show an event population of spurious technically mis-reconstructed noise events at negative energies. It is possible to suppress these events requiring a sensible pulse timing of ± 2.5 ms around the trigger or by putting a cut on the goodness of the template pulse fit to the data. The event-rate is much lower during WIMP search data taking and only a negligible amount of pile-up events is expected. No such problem was observed in the data. Nevertheless, dependent on the analysis purpose, a filter with higher cutoff frequency might be better suited for some analysis tasks of the Ba calibration data. The issue is discussed in more detail in appendix C.

3.3.4. Outlook: linear versus non-linear filtering techniques

The analysis described in sec. 3.3 is in some sense a very classical analysis, based on conventional filtering techniques developed in 1930. This makes it a very robust analysis and at the same time, the automatic cutoff frequency selection of the highpass filter may even outperform more aggessive techniques like Wiener filtering for given time intervals. Solving the challenge of determining an accurate time varying noise spectrum this should change, however. Further optimizations of the bandpass analysis are still possible. This includes the tweaking of implemented procedures as suggested in the description of in-

dividual processors and the implementation of additional algorithms. E.g. an adaptive detection of sinusoidal noise frequencies in the pretrace, an optimization of the ordering of different preprocessors and a variation of the overall processing scheme with the amplitude estimation at a common event time leave room for further improvement.

Furthermore, one could try to optimize the energy determination for fiducial events by using the crosstalk from collecting electrodes to veto electrodes of about 20-30% as an additional input to improve the signal to noise ratio. This could be especially beneficial for detectors with better baseline resolution on the veto channels than on the collecting electrodes.

For the optimal filter, one could study whether it is possible to disentangle stationary and time dependent noise frequencies. It might be possible to construct a stationary noise power spectrum and additionally use the pretrace information to find time dependent changes.

Apart from the optimization of the existing analysis algorithms there is also a complete class of filtering techniques specifically designed to detect steps in piecewise constant signals [238], which has not been touched. Since both step function and noise overlap in the frequency domain, it is potentially feasible to achieve better results through nonlinear techniques. Since the objective of step detection has a wide range of application from image denoising to biophysics it is well studied and receives a lot of attention even today. Specific proposed implementations of non linear algorithms have been reported in [239] or [240] for example.

3.4. Energy calibration

In order to understand the response of the Ge bolometers to different signals, the extracted amplitudes need to be calibrated, and both electromagnetic scattering and neutron scattering are used to verify the response model of the detectors. The energy calibration is performed using a set of two ^{133}Ba sources to irradiate the crystals. Photopeaks in the captured spectra are then used to identify certain energies and to linearly scale the measured ionization amplitudes. Ba calibrations are regularly repeated to check the detector behavior and stability of the calibration.

Neutron calibrations with an AmBe source are performed once per WIMP search data set. They are used to check the parametrization of the ionization quenching for nuclear recoils and to directly extract efficiencies for the low mass WIMP search. Furthermore (n,γ) reactions with the natural Ge isotopes (^{70}Ge - ^{76}Ge) lead to the homogeneous production of short-lived (less than a two weeks) isotopes that can be used for the analysis of the fiducial volume of the crystals after the neutron calibration. In the data, under investigation in this thesis, extensive Ba calibrations were carried out to optimize voltage configurations, but no neutron calibration was performed.

The decay scheme of ^{133}Ba and a reference spectrum obtained with a commercial Ge detector are shown in fig. 3.19. The dominant γ transition line is the 356 keV γ line which occurs in 62.05% of all decays. The second strongest line is at 81 keV with a probability of 34%. However, due the γ-ray attenuation of the copper shields and the Ge detectors themselves (fig. 3.20) this line disappears in the continuum of the compton scattering of all higher energy transition lines.

From the five strongest transition lines summarized in table 3.1, at most the four high energy lines are visible dependent on the position of the detector within the cryostat and the length of the gamma calibration. Even for the two high energetic lines at 356 and 384 keV the attenuation of 1/e for every 2 cm of Ge starts to be problematic for the calibration of the innermost crystals, which are shielded by another tower of detectors.
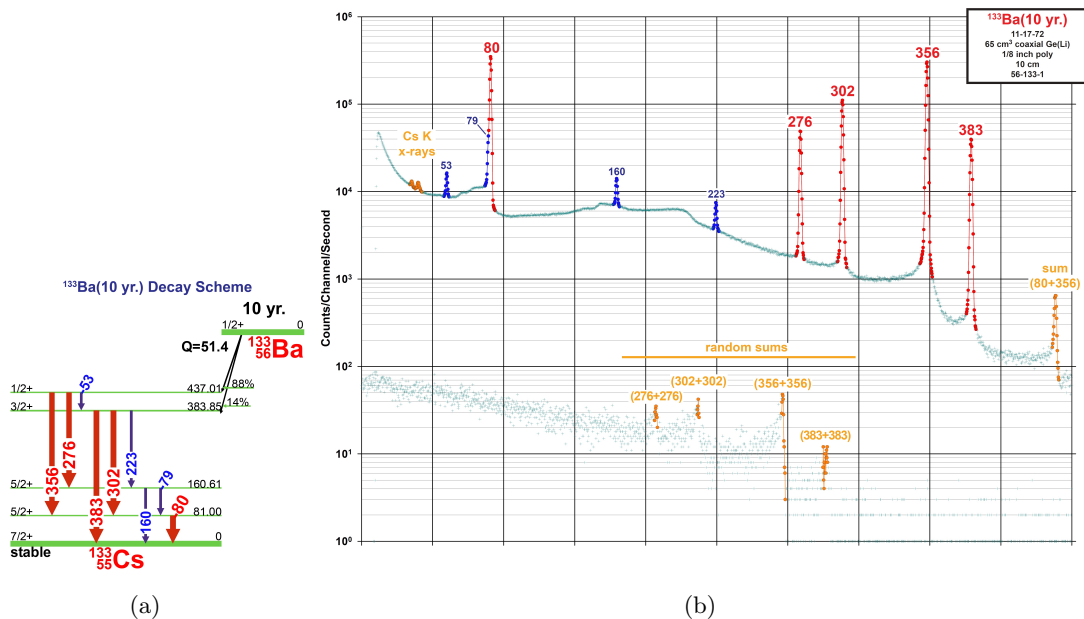
Figure 3.19.: Decay scheme (a) and reference spectrum (b) of a ^{133}Ba calibration source as used in the EDELWEISS experiment. Spectrum from the online version of the gamma-ray spectrum catalog published in [241]. Strong photopeaks with a large relative intensity and good signal to noise ratio for the photopeaks over the compton background are colored in red, smaller ones in blue.

Table 3.1.: Energy and intensities of the dominant γ-ray lines (relative to the strongest line and relative to the decay probability) in the ^{133}Ba decay. Data from the online version of [241]. Measurement uncertainties are 1 eV for the energy of the decay lines and $\leq 0.3\%$ for the intensity of the γ line relative to the decay probability.

$\mathbf{E_\gamma}$ **(keV)**	I_γ (rel)	$I_\gamma(\%)$
80.997	52.0	34.06
276.400	11.69	7.16
302.851	29.78	18.33
356.013	100	62.05
383.848	14.43	8.94

In general an initial calibration is performed on an early γ calibration data set during data taking. Afterwards the stability of the calibration is monitored to ensure compatibility, and a corrected calibration is calculated from a summed data set including all compatible γ calibration data sets. Since no long term drifts of the ionization calibration have been encountered, in principle all data sets can be added for the ionization calibration. For the heat channel, biweekly helium refills and cryostat maintenance induce long term drifts and the calibration has to be performed on a short term basis.

3.4.1. Calibration of ionization signals

In general it is most convenient to start calibrating the collecting electrodes of the Ge detectors since these have the largest statistics. The veto channels can subsequently be calibrated from all events using a charge consistency requirement for a surface event population. This leads to the calibration, with the total recoil energy E_{Rec} being set tot the ionization signal E_{I} from γ calibration,

$$E_{\text{Rec}} = E_{\text{I}}^\gamma, \tag{3.6}$$

and the subsequent energy scale is referred to as keV$_{ee}$ (electron equivalent). It is a measure of the true recoil energy for electron recoils only. In fig. 3.21, the ionization calibration performed on a single data set is summarized. A semi-automatic tool has been implemented in a joint effort of the Saclay and KIT analysis groups to determine the 4 linear gain coefficients and the two major cross-talk coefficients. These are then saved on a CouchDB document and read back by a program developed in this thesis to apply these coefficients and calculate a set of detector based variables e.g. the total ionization energy and the recoil energy. Dependent on the analysis, especially to make use of the Ramo-induced signals from trapping, a more detailed determination of all 12 cross-talk coefficients can be necessary [237].

In the first step of the calibration, the cross-talk coefficient from collecting electrode to adjacent veto electrode is extracted. Fig. 3.21 (a) and (b) shows the corresponding scatter plot for the upper and lower set of electrodes. For real events in the surface region, signals should have opposite signs on the two electrodes, corresponding to the opposite charges. For cross talk however, real signal on a collecting electrode and crosstalk have the same sign. The population of events marked in green is hence the population of real bulk events showing cross-talk. A line fit is automatically calculated, but can be corrected by hand if there is a large population of events which exhibit a charge sharing between multiple electrodes and do not fall into the green shaded region. On average, a cross-talk of 25% with an overall variation from channel to channel of ±3% was found for the twelve detectors which had fully working ionization channels.

The next step is the determination of the linear gain for the collecting electrodes as in fig. 3.21 (c) and (d). In this first calibration, the position of the 356 keV peak is estimated by eye with the help of the red bar which can be moved interactively along the spectra.

Finally, the linear gain for the two veto channels is determined from the scatter plot of veto to collecting electrode, see fig. 3.21 (e) and (f). Three distinct event populations have been marked with different colors. In the green shaded region, bulk events after cross talk correction can be found. In the red region pure surface events can be found. In between in the orange shaded regions, events which exhibit a charge sharing between the veto electrode and the two collecting electrodes can be found. Since an automatic fit
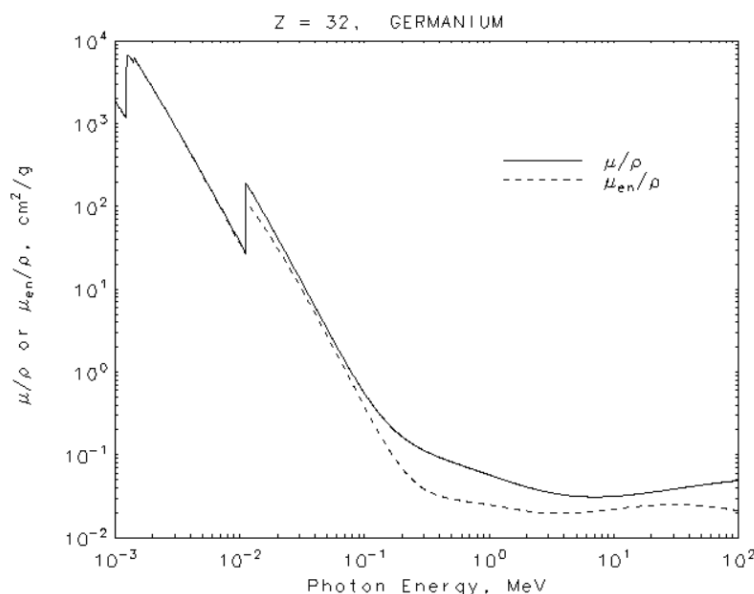
Figure 3.20.: Photon mass attenuation coefficient for Ge. For the main calibration line at 356 keV an attenuation to 1/e is reached after ∼2 cm of Ge. Figure from [242].
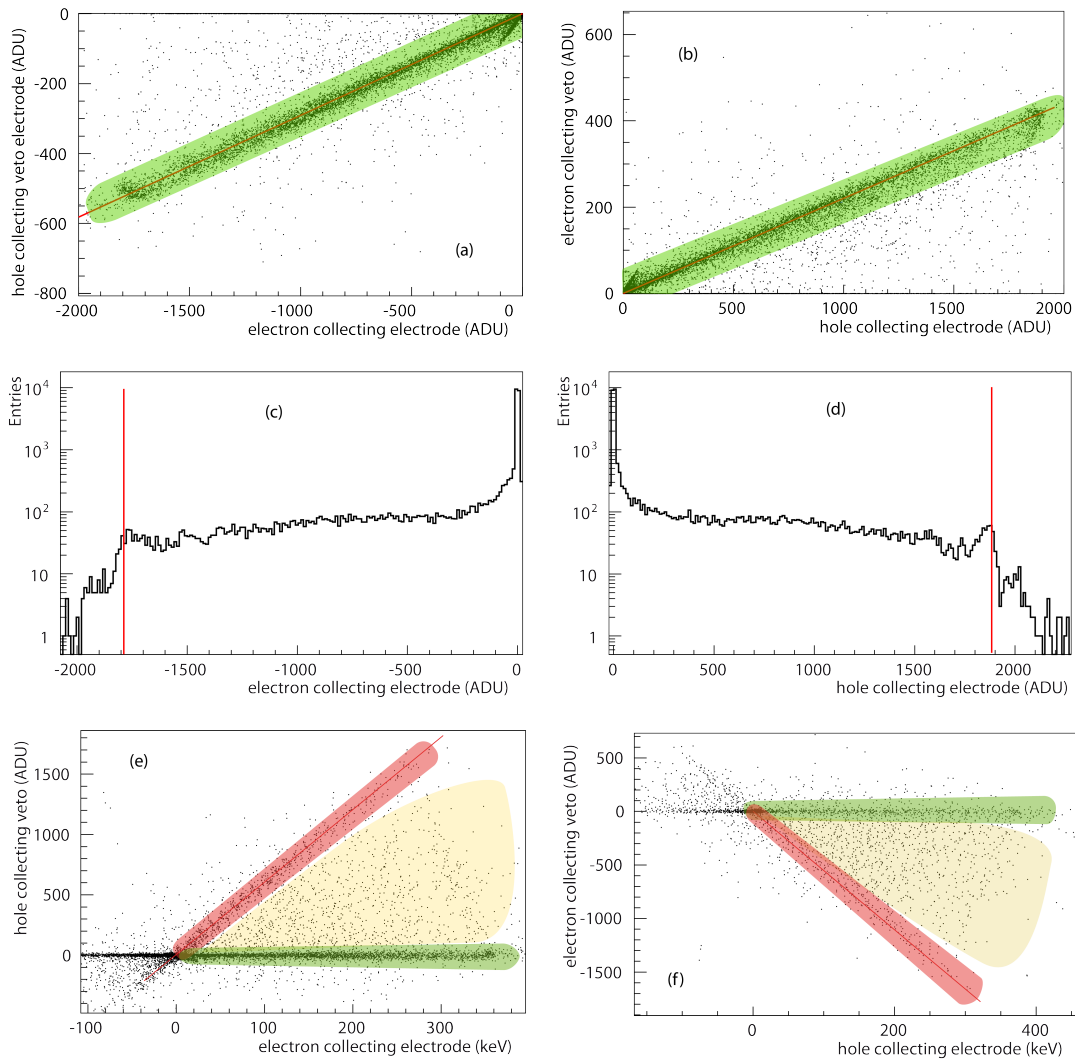
Figure 3.21.: Calibration procedure for an initial calibration from a single large γ calibration data set. Exemplified for data from FID823 from 5th November 2013. (a), (b): cross talk correction from collecting electrode to adjacent veto electrodes. (c), (d): linear gain calibration of collecting electrodes on the main photopeak of the ^{133}Ba source at 356 keV. (e), (f): linear gain calibration of surface electrodes with respect to collecting electrodes. For details see text.

convergence is difficult to achieve in this scatter plot, the line fit for these events is done by eye. In total an average linear gain of $g_{\mathrm{ion}} = 0.204 \, \mathrm{keV/ADU}$ and a variation from channel to channel of $\sigma_g = 0.028 \, \mathrm{keV/ADU}$ was observed.

In order to monitor the stability of the calibration of the collecting electrodes all Ba calibration spectra are plotted into a 2 dimensional histogram. In fig. 3.22 the histogram for the hole collecting electrode of FID823 is shown. On a long term scale no indication of a change of linear gain could be observed. There is, however, a remaining correlation of the linear gain with the applied cutoff frequency. The induced variation is below the % level for all except the highest cutoff frequency. It was checked that this variation can be corrected, but it was found that it was not limiting the current analysis and does not need to be done for all detectors.

From all of these γ calibration data sets an improved calibration could be performed finding the 356 keV Ba peak not only on the collecting electrodes, but also on most of the veto electrodes. Furthermore, the statistics is then good enough to fit the major photopeak of the collecting electrodes with a Gaussian and extract the resolution at 356 keV. Dependent
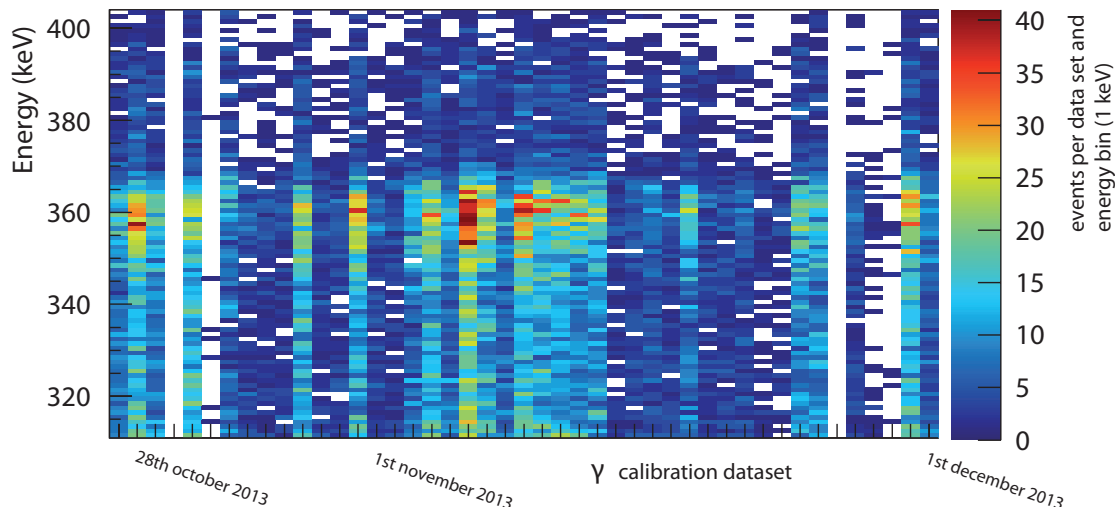
Figure 3.22.: Monitoring of the stability of the gamma calibration for the hole collecting electrode of FID823 over all data sets with the same collecting voltage of $\pm 4\,$V setting. The data sets are distributed over a ~ 1 month period where intermittent data sets with different voltage settings have been omitted.

on the detector, also the other three high energy photopeaks from the γ-ray transitions at $276\,$keV, $303\,$keV and $384\,$keV can be seen. An example is given for the hole collecting electrode of FID823 in fig. 3.23 (a). Hole collecting electrodes usually have superior resolution at high energies compared to their electron collecting counterparts. This is understood in the context of different trapping and charge propagation dynamics [243]. Veto electrodes in turn have even better charge collection properties at high energy due to the stronger electric field gradients and shorter path for charges. The $356\,$keV peak of the adjacent veto electrode to the presented collecting electrode was fit with a Gauss of width $\sigma = 2\,$keV (fig. 3.23 (b)).

Having determined the ionization calibration one can proceed to the calibration of the heat channels. In order to perform a consistent calibration both during WIMP search data taking and from gamma calibration data the heat signals are calibrated versus the ionization energy and not on the spectral features of the calibration source. This requires however, that one can separate clean bulk electron recoils from surface events and from pile-up events during γ calibration. Within this work this is achieved using a goodness
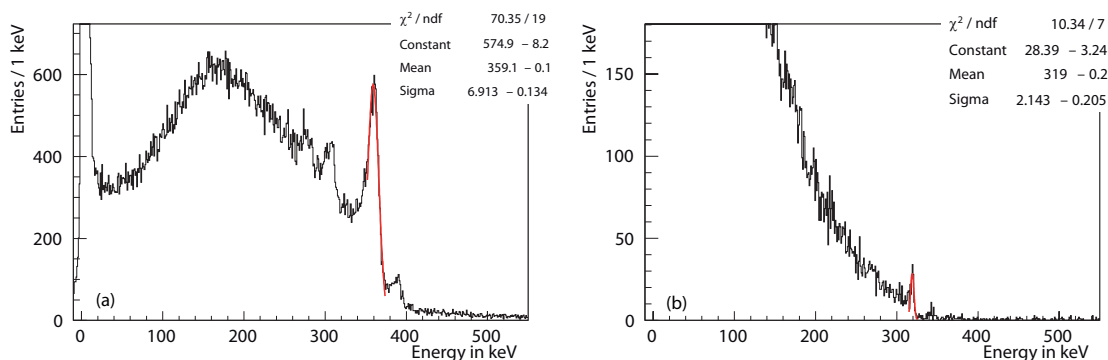
Figure 3.23.: Evaluation of the energy resolution at $356\,$keV and correction of the ionization calibration gain via a Gauss-function fit to the main photopeak of the ^{133}Ba calibration source with high statistics. All calibration data sets at $8\,$V bias have been used to plot (a) the hole collecting electrode of FID823 and (b) the adjacent veto electrode.
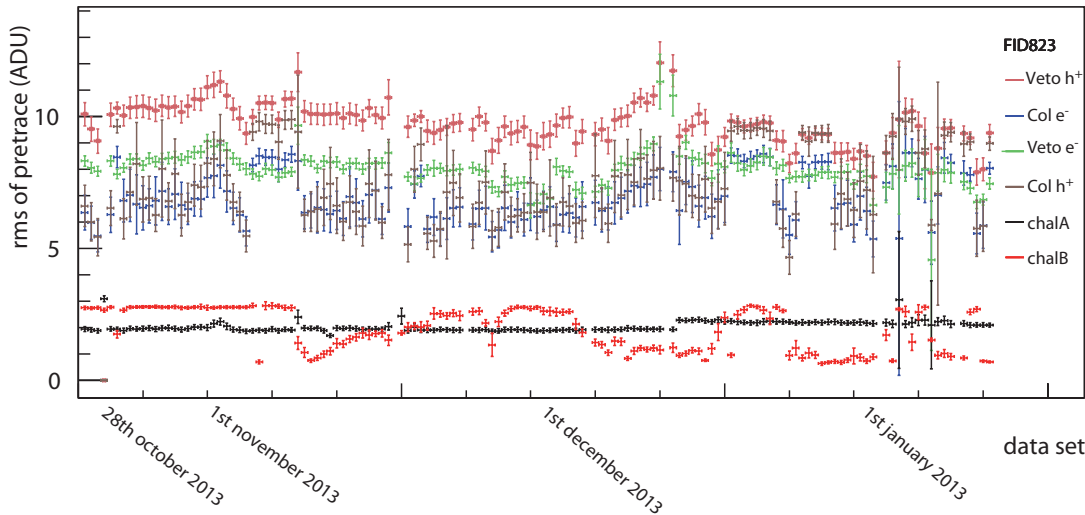
Figure 3.24.: Mean values μ_{RMS} of the Gauss fits to the distribution of the RMS values of the first 40% of the processed trace (pretrace) per data set. The results for all ionization channels (2 kHz sampling) and the heat channels is presented for the 8 V bias data sets here. Data sets are defined by the DAQ software SAMBA. The typical length of a data set is 20 h, but it can be much shorter for maintenance and other reasons (See introduction to chapter 4 for details).

of fit test from the χ^2 of the template fit. Additionally a set of loose cuts on the veto electrodes is applied to reject surface events.

3.4.2. Data quality monitoring - RMS and χ^2

In order to be able to apply a reliable goodness of fit cut on the template fits to data and thus reject pile-up events, the errors intrinsic to the data samples which are fit have to be known or have to be stable at least. In the EDELWEISS-III setup the noise is not stable. Hence, either the cut has to be varied over time or the baseline variation of the data samples has to be monitored over time and can then be used to achieve a pseudo normalization of the χ^2 values. This can only be a pseudo normalization since it does not take into account any errors due to the real pulses like the statistics of electron hole pairs, current fluctuations in the NTD or correlation of the errors of adjacent points in the template. A remaining energy dependence within the χ^2 values of the template fits is thus expected.

As a measure of the standard deviation of each sample in a pulse we monitor the RMS of each processed pretrace, plot the distribution of RMS-values of a data set and fit a Gauss function to this distribution. The resulting mean value of the fit μ_{RMS} can be used to monitor the data quality as it is done in fig. 3.24, and it can be used to normalize the χ^2 values of the template pulse fit via

$$\chi^2_{red} = \frac{\chi^2}{(\mu_{\text{RMS}})^2 \cdot \text{ndf}}. \tag{3.7}$$

The number of degrees of freedom (ndf) are the template length (1900 samples for the 2 kHz ionization; 900 samples for the 100 kHz ionization; 100 samples for the 500 Hz heat channels) minus the number of free fit parameters, which is two for the amplitude and position of the pulse.

After this normalization a common goodness of fit or χ^2 cut can be defined on the ensemble of all data sets, for which a reliable RMS estimate was achieved. In order to assess the
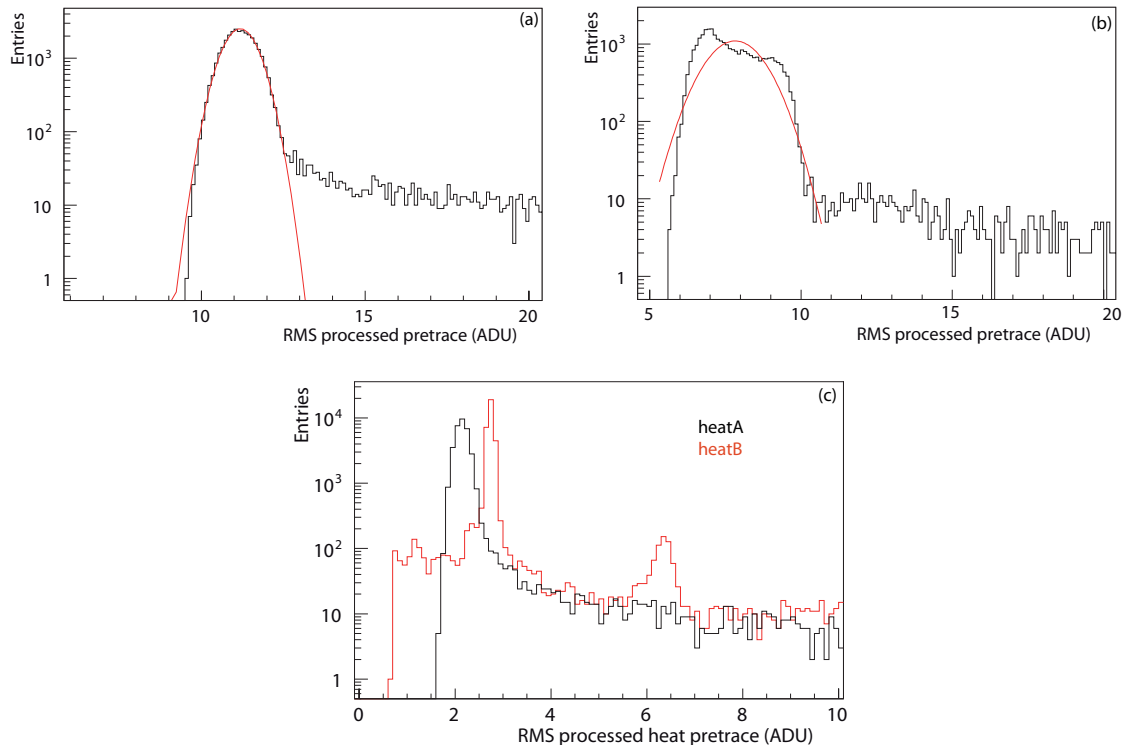
Figure 3.25.: Distribution of the RMS values of the first 40% of the processed pulse trace for the hole collecting veto electrode of FID823 (a), the adjacent collecting electrode (b) and the two heat channels (c). For each channel a Gauss function is fitted automatically with initial parameters put to the position of the largest bin. Resulting fits are shown in red in (a) and (b). Data from 5th November 2013. For details see text.

reliability of the RMS estimate it is useful to discuss a few examples of the Gauss fits to the RMS distributions. The distributions for several channels of FID823 are given for the 1 day γ calibration data set from the 5th of November 2013 in fig. 3.25. This data set falls into a period when the collecting electrodes labeled as slowB and slowD in fig. 3.24 have a rather high RMS, thus it is a rather noisy period. Within this period a large difference in the behavior of noise is observed on the different channels. In this particular case both hole collecting electrodes (bulk and veto) show an RMS distribution that can be well described with a Gaussian (fig. 3.25 (a)) and an additional tail to higher RMS values that is expected from events with a signal contribution contaminating the pretrace. The Gaussian RMS distribution is expected in the case of a stable noise spectrum. The events with higher RMS values can be pile-up events with a trigger on the second of the two pulses or for example a trigger in an adjacent bolometer close to a real event in the current bolometer. While this RMS distribution is an indicator that the noise power spectrum could be stable, it is no proof. The amplitude of the noise could vary at different frequencies and thereby keep the RMS of the pretrace stable. In contrast, the RMS distribution of the pretrace in fig. 3.25 (b), shows clear signs of a variation of the noise power over time. The RMS distribution is broadened and not well described by the Gaussian fit. Finally, also the RMS distributions for the two heat channels exhibit large deviations in their RMS distributions fig. 3.25 (c). While the black distribution from heatA has the well behaved structure already seen for the hole collecting electrodes, the 2nd heat channel (red) has a double peak spectrum. This could hint to a noise source only running part time, like crosstalk from a machine which is operated in intervals.

For the assessment of good periods from fig. 3.24, very loose requirements have been applied

in order not to cut too much on the statistics. Any data set with an RMS-value within]0,20] (ADU) and a reasonable statistics of at least 300 traces has been accepted for the further processing. For FID823 this cuts a single data set at the end of October which has an RMS estimate of zero for the ionization channels and a couple of data sets in November and January with very little statistics. The RMS estimate of zero was obtained for a single data set due to an error in data taking. The accumulated charge on the ionization channels was not reset properly and the ADCs were stuck in saturation.

3.4.3. Calibration of heat signals

Analog to the ionization calibration, one generally calibrates the heat signal on bulk γ events according to

$$E_{\mathrm{H}}^{\gamma} = E_{\mathrm{Rec}}. \tag{3.8}$$

Unlike the ionization signal the heat signal is affected by long term temperature drifts encountered around He refills and needs to be correctly calibrated over time with an automatic procedure. The starting point to this procedure is the estimate of the linear heat gain both for calibration and WIMP data, taken from a clean sample of bulk gamma events with a constant heat to ionization ratio.

First, the RMS monitoring is used to remove data sets where the ionization signals are untrustworthy. Furthermore on an event by event basis surface events need to be excluded and events where the template and pulse shape disagree, e.g. pile-up events, need to be rejected. The latter is achieved with a cut on the χ_{red}^2 of the template fit to the ionization pulses of the events.

An automatic procedure of the definition of a χ^2-cut has been implemented in this work. It takes the entire γ calibration data and produces a scatter plot of the χ_{red}^2 vs the energy for each single channel (fig. 3.26 (d)). It then takes the events within three energy ranges [10,30] keV, [150,170] keV and [340,360] keV and plots the distribution of χ_{red}^2 values into a one dimensional histogram (fig. 3.26 (a), (b) and (c)). A Gauss function is automatically fitted and a one sided 99.9% C.L. limit is extracted from this Gauss function. Finally, a second order polynomial (with positive curvature) is calculated through these points and defines the cut for each ionization channel. The parameters of the parabola are stored on CouchDB and can subsequently be used as input for a cut in calibration and analysis.

While the tool is automatic in principle, it was found that the distribution of χ_{red}^2 values varies a lot from channel to channel and from detector to detector. Subsequently it was found useful to supervise the extraction of cuts and adjust the Gaussian acceptance level to account for non Gaussian tails and not to cut too harshly. It was considered to cut on the distribution directly, but given the unknown level of signal and pile-up in the distribution it seemed more conservative to use the Gauss function as pure signal approximation, even in cases when it turned out to be a very bad signal approximation. The real acceptance has to be evaluated separately as it is done for FID808 in sec. 4.5.3.

A χ^2-cut can similarly be used to identify different pulse characteristics in the heat channel. With such a cut, intrinsic physical NTD events can be separated from Ge bolometer events. This can be beneficial to reduce the amount of heat-only events in an analysis. However, one might consider estimating the RMS over shorter time periods or to normalize the χ^2 with the RMS of each individual pretrace and use an additional cut on the RMS value of the pretrace instead of the procedure developed for the calibration within this work. On the other hand, it is also possible to see the RMS of the pretrace as an indicator of the current noise level and try to use this information to cut noisy periods on an event by event basis.
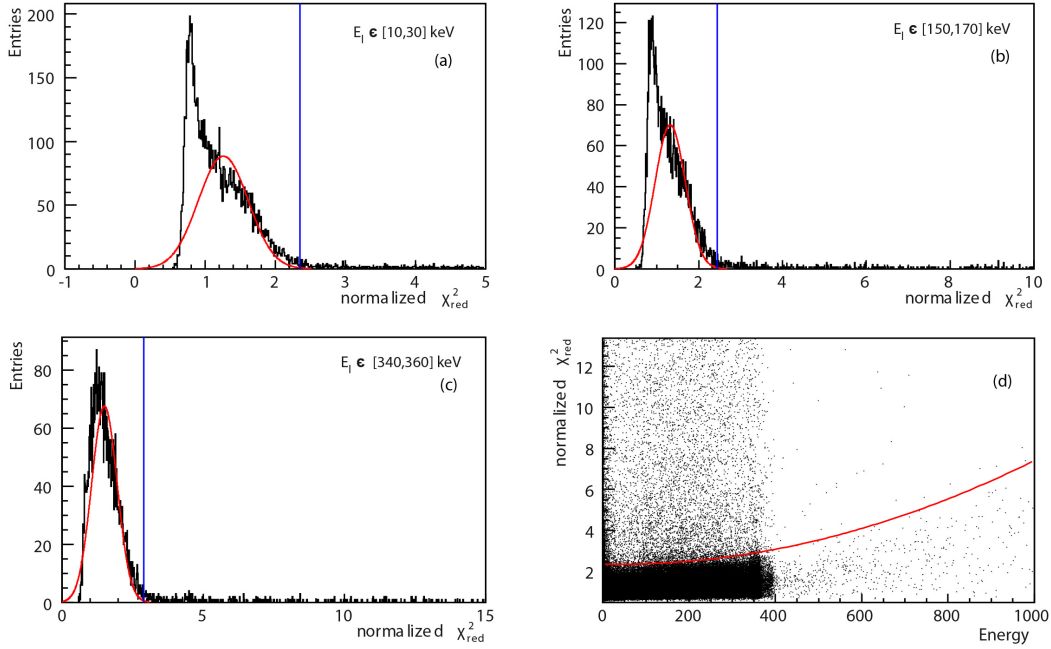
Figure 3.26.: Example of the χ^2 cut definition (electron collecting ionization channel of FID823) on the goodness of the template pulse fits from the entire gamma calibration statistics. A Gauss function is fit to the projection of the distribution in three distinct energy regions (a), (b) and (c) onto the χ^2 axis. A parabola at the one-sided 99.9% acceptance level of the gauss fit (blue lines) defines the χ^2 cut (d). The previously discussed cut on the peak position of $\pm 2.5\,\mathrm{ms}$ around the trigger position has been applied to remove pile-ups and for better visualization.

Further event quality cuts for the heat calibration include the rejection of low and highest energy events below $20\,\mathrm{keV}$ and above $1000\,\mathrm{keV}$ on the average ionization energy $\langle E_{\mathrm{Col}}^{\mathrm{avg}} \rangle = (E_{\mathrm{Col1}} + E_{\mathrm{Col2}})/2.0$: low energy events suffer from poor signal to noise ratio and a large subsequent spread in their ionization to heat ratio. Highest energy events on the other hand tend to suffer from saturation and subsequent misreconstruction effects. Furthermore, a requirement of a positive heat signal on the NTDs with a threshold of $5\,\mathrm{ADU}$ was used as an additional assuration that both NTDs observe a sensible signal. $5\,\mathrm{ADU}$ corresponds to a $10\,\mathrm{keV}$ threshold on average, but varies a lot from $2.5\,\mathrm{keV}$ as minimal value to $40\,\mathrm{keV}$ at maximum, dependent of the linear gain of the NTDs used. An additional periodic cut is used to reject pulses that can be generated from the adjusting of DAC voltages to compensate for the accumulated charge on the ionization channels. For details see sec. 4.2.1.

Finally, the removal of surface events is achieved with a generic fiducial cut common to all detectors. It consists of two individual requirements on the amplitude of individual channels.

$$E_{\mathrm{Veto}}^{i} < 2.0\,\mathrm{keV} + 2.25\% \cdot \mathrm{E}_{\mathrm{Col}}^{\mathrm{avg}} \tag{3.9}$$

$$\Delta E_{\mathrm{Col}}^{\mathrm{avg}} < 2.0\,\mathrm{keV} + 5.6\% \cdot \mathrm{E}_{\mathrm{Col}}^{\mathrm{avg}} \tag{3.10}$$

The index i runs over the two top and bottom veto electrodes. Parameters were adopted from the EDELWEISS-II experiment. These parameters have to be chosen as a trade off between data quality and statistics. Since the statistics of all calibration data sets is in general much higher than during WIMP data taking it is likely that these values can
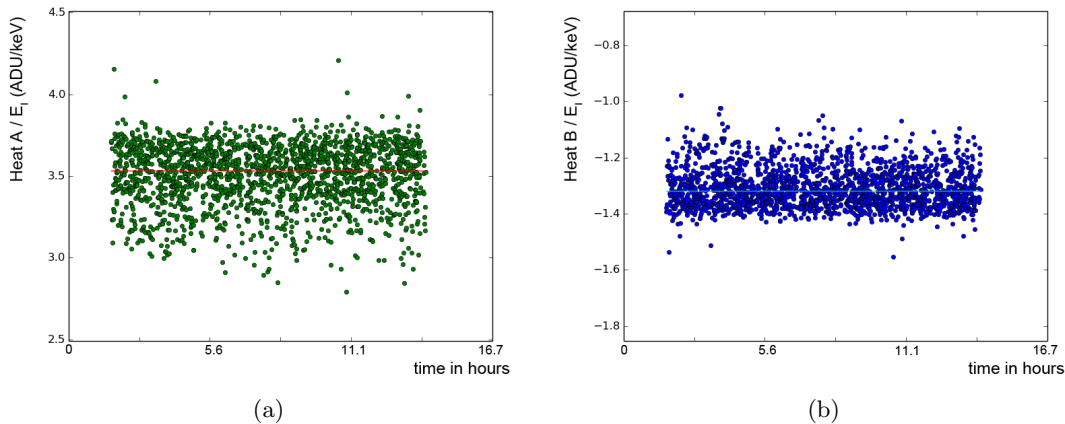
Figure 3.27.: Linear heat calibration procedure. The ratio of the heat amplitude over fiducial ionization (keV) is plotted for a selection of clean bulk events for the two heat channels of FID823 (a) and (b). The linear gain of the heat channel is extracted from the mean of the distributions and automatically stored on our CouchDB database.

still be optimized for the calibration of pure background data during the ongoing WIMP search.

After application of this cut the ratio of the individual heat amplitude over the ionization energy $\langle E_{\text{Col}}^{\text{avg}} \rangle$ is plotted (fig. 3.27) versus the time for each individual data set. Typical duration of these data sets, defined by the DAQ software SAMBA, are 20 hours for each data set. They can be much shorter, however, in case of manual interventions or for example during optimization procedures. The mean of the plotted distribution is uploaded as the linear heat gain onto the CouchDB run documents.

After determination of the linear heat gain values, all γ calibration data sets are combined to measure and subsequently correct the nonlinearity of the response of the NTD sensors. The function used to describe the nonlinearity is defined on the $\log_{10}$ of the calibrated heat energy of a given channel. An example for the first of the two heat channels of FID823 is given in fig. 3.28. Note that the event based cuts have been slightly altered. The lower energy threshold was set to a value between 1 - 10 keV to extract the nonlinearity also at low energy. In addition a cut on the ionization quenching with a lower value of 0.6 was introduced. The function is defined piecewise for three energy ranges with a constant, first and second order polynomial part. The transition points denoted as $x0$ and $x1$ are varied freely in energy but a smooth continuation of the function is required. Hence four free parameters $p0$, $p1$, $p2$ and $p3$ remain. The function is mathematically implemented with the following parametrization

$$x0 = \frac{p2/p1 - 1}{p1} \tag{3.11}$$

$$x1 = x0 + p3 \tag{3.12}$$

$$\text{if } x < x0: \quad f(x) = p2 \tag{3.13}$$

$$\text{if } x0 < x < x1: \quad f(x) = p2 \cdot (x0 - x + p3) + p0 \cdot (x + p3 - x0) \tag{3.14}$$

$$+ 0.5 \cdot p0 \cdot p1 \frac{(x + p3)^2 - x0^2}{2 \cdot p3}$$

$$\text{if } x > x1: \quad f(x) = p0 \cdot (1 + x \cdot p1) \tag{3.15}$$

The set of parameters obtained from the χ^2 minimization during a fitting procedure for
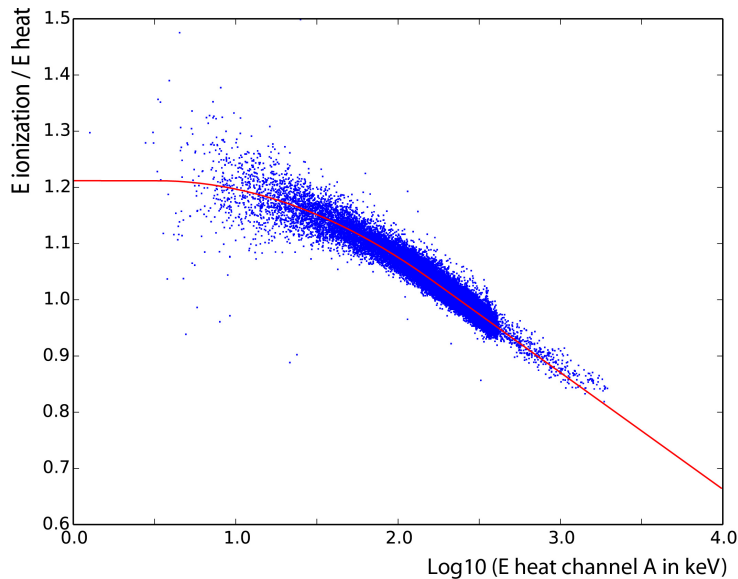
Figure 3.28.: Logarithmic correction of the energy calibration in the heat channels. A four parameter function consisting of a constant, linear and quadratic regime is used to model the nonlinearity of the heat axis in $\log_{10}(E_{Heat})$. The results of the fit are automatically stored in the CouchDB database and applied when calculating calibrated energy variables.

the data set in fig.3.28 is $p0 = 1.46$, $p1 = -0.13$, $p2 = 1.19$ and $p3 = 0.75$.

During application of these parameters to the background data taken in the last commissioning run it was noticed that the ionization yield for the distribution of bulk γ events showed a deviation from unity. The investigation of this deviation revealed that the shape of the nonlinearity is generally compatible in calibration data and background data. But the estimation of the linear gain produces a different bias for the energy distribution of background events and gamma events. Hence, either the linear gain has to be corrected or the logarithmic correction which compensates an offset of the linear gain in its parameters has to be performed separately. This effect is discussed in more detail in the appendix D.

From the calibrated individual signals subsequent combined variables like the recoil energy are calculated. While this procedure of the heat calibration is performed with a great deal of automatization it showed a large dependence on different parameters. Also the accuracy of the estimated parameters is bound to be limited to the same accuracy as the ionization signals which suffer from carrier trapping effects. Any change in cuts or in the ionization calibration directly propagates into the heat calibration and can produce a bias. For a EURECA sized experiment, a different means of calibration like the injection of heater pulses (as in CRESST [244]) seems highly appropriate to break some of the correlations encountered during this procedure.

3.4.4. Calculation of the "true" recoil energy

"True" recoil energies can be calculated from the knowledge of all individual ionization and heat energies, independent of the ionization quenching. This "true" recoil energy together with the ionization yield is the most wide spread variable in order to present results in an easily understandable way. However, it is not a very useful variable for a statistical analysis. Hence, multiple combined energies are calculated and stored for visualization and data analysis.

In the following discussion the calculation of the "true" recoil energy and Q-value for fiducial events will be presented. Also, the calculation of variables usually used in a low mass analysis [93] will be given. The extension from fiducial to non-fiducial events taking into account different Neganov-Luke heating from different voltage settings on the veto channels is straight forward, but will be omitted for brevity reason. Within this restriction averaged quantities of ionization and heat are generally used to obtain a better signal-to-noise ratio. The best variable for ionization is the resolution weighted average of the amplitudes of bottom and top collecting electrodes, subsequently called E_{Col}. Similarly the phonon signal can be averaged with the weights of the heat channel resolutions from the two heat channels and is further referred to as E_{Heat}. The energy resolution for a channel i at a given energy E is hereby calculated from the measured resolutions σ at $356\,\text{keV}$ and the baseline

$$\sigma_{\text{i}}(E_{\text{i}}) = \sqrt{\left(\sigma_{\text{base}}^{\text{i}}\right)^2 + \frac{\left(\sigma_{356\text{keV}}^{\text{i}}\right)^2 - \left(\sigma_{\text{base}}^{\text{i}}\right)^2}{356^2} \cdot E_{\text{i}}^2}. \tag{3.16}$$

The weighted average is subsequently calculated using the energy dependent resolution from eq.3.16, e.g.

$$E_{\text{Heat}} = \frac{\sigma_{\text{heatB}}^2(E_B)}{\sigma_{\text{heatA}}^2(E_A) + \sigma_{\text{heatB}}^2(E_B)} \cdot E_{\text{heatA}} + \frac{\sigma_{\text{heatA}}^2(E_A)}{\sigma_{\text{heatA}}^2(E_A) + \sigma_{\text{heatB}}^2(E_B)} \cdot E_{\text{heatB}}. \tag{3.17}$$

For the overall energy budget measured in the heat channel, the energy E_{tot} is then given by the original energy of the scattering E_{Rec} plus an additional part E_{L} due to the Neganov-Luke heating from the drifted charges.

$$E_{\text{tot}} = E_{\text{Rec}} + E_{\text{L}} \qquad \text{with} \qquad E_{\text{L}} = qN_IV = \frac{E_{\text{Rec}}}{\epsilon}V. \tag{3.18}$$

Herein, N_I is the number of charge carriers created and V is the applied drift voltage, which is $8\,\text{V}$ for bulk events under the standard operation conditions of FID detectors. $\epsilon = 3\,\text{V}$ is the required ionization potential for gamma interactions to create an electron hole pair. The lower ionization yield of nuclear recoils or any other interaction with lower charge yield can be expressed in terms of the charge quenching factor Q. Thus the total energy splits up into the following two equations for gamma interactions and for charge quenched interactions

$$E_{\text{tot}}^{\gamma} = E_{\text{Rec}}\left(1 + \frac{V}{\epsilon_{\gamma}}\right), \tag{3.19}$$

$$E_{\text{tot}}^{\text{n}} = E_{\text{Rec}}\left(Q\prime + Q\frac{V}{\epsilon_{\gamma}}\right). \tag{3.20}$$

Hereby, the quenching factor $Q\prime$ is a heat quenching factor from photon-emission and crystal defect creation during nuclear stopping. Historically this factor was unknown, but early data were compatible with a non-existent heat quenching, i.e. $Q\prime = 1$. Hence only the ionization quenching was taken into account In practice the signals are calibrated with the data from a ^{133}Ba source such that

$$E_{\text{Col}}^{\gamma} = E_{\text{Rec}} \qquad\qquad E_{\text{Heat}}^{\gamma} = E_{\text{Rec}}. \tag{3.21}$$

From the comparison it can be seen that this calibration is equivalent to the scaling of the total heat energy with the factor

$$\frac{1}{1 + V/\epsilon_{\gamma}}. \tag{3.22}$$

Application of the same factor to the quenched signals from nuclear recoils yields the calibrated energy

$$E_{\text{Heat}}^{\text{n}} = E_{\text{Rec}} \frac{Q\prime + QV/\epsilon_\gamma}{1 + V/\epsilon_\gamma}. \tag{3.23}$$

Neglecting the heat quenching factor $Q\prime$ taking the ionization yield

$$Q = \frac{E_{\text{Col}}}{E_{\text{Rec}}}. \tag{3.24}$$

a true recoil energy can be calculated independent of the interaction type.

$$E_{\text{Rec}} = \left(1 + \frac{V}{\epsilon_\gamma}\right) E_{\text{Heat}} - \frac{V}{\epsilon_\gamma} E_{\text{Col}}, \tag{3.25}$$

More recent measurements of the EDELWEISS experiment combined their precise measurement of both heat and ionization signals with measurements of the pure ionization quenching from neutron beam experiments to measure the heat quenching factor. The same determination of the recoil energy i.e. eq. 3.25 was kept, but note that the meaning changed. It is no longer the true recoil energy, instead the calculated quantity turns out to be $Q\prime E_{\text{Rec}}$. Subsequently the parametrization of the quenching of nuclear recoils which is performed from neutron calibration data in these coordinates is not $E_{\text{Col}}/E_{\text{Rec}}$ but $E_{\text{Col}}/(Q\prime \cdot E_{\text{Rec}})$ or $Q/Q\prime$. Combination of the Lindhard parametrization of $Q/Q\prime = 0.16 \cdot E^{0.18}$ and the direct measurements of the pure ionization quenching gave $Q\prime = 0.91 \pm 0.03 \pm 0.04$ [140]. Negelction of $Q\prime$ corresponds to a systematic bias of a about 10% in the recoil energy scale of such plots (see for example fig. 3.29). However, since this measurement is only barely more than a 1σ observation of $Q\prime \neq 1$, the measurement can also be taken and interpreted as the uncertainty in the calculated recoil energy scale.

Statistical errors in the $Q_{\text{Edw}} = Q/Q\prime$ vs E_{Rec} plain can be calculated for each individual event, however it is common practice to calculate an error of $Q_{\text{Edw}}(E)$ and draw respective bands for both electron and nuclear recoils. Specifically these bands are calculated under the assumption of uncorrelated errors in heat and ionization by Gaussian error propagation from the equation $Q_{\text{Edw}} = \frac{E_{\text{Col}}}{E_{\text{Rec}}}$. Uncertainties in heat and ionization are measured continuously for the baseline and once from the overall gauss fit to the 356 keV Ba-peak and are then inter- and extrapolated according to

$$\sigma_{\text{Col,Heat}}(E_{\text{Rec}}) = \sqrt{\left(\sigma_{\text{base}}^{\text{Col,Heat}}\right)^2 + \frac{\left(\sigma_{356\text{keV}}^{\text{Col,Heat}}\right)^2 - \left(\sigma_{\text{base}}^{\text{Col,Heat}}\right)^2}{356^2} \cdot E_{\text{Col,Heat}}^2}. \tag{3.26}$$

For the nuclear recoils and gamma events the error propagation results in the following expressions

$$\sigma_{Q_{\text{Edw}}^n}(E_{\text{Rec}}) = \sqrt{\frac{1}{E_{\text{Rec}}^2} \cdot \left[\left(1 + \frac{\text{V}}{\epsilon_\gamma} Q_n\right)^2 \cdot \sigma_{\text{ion}}^2 + \left(1 + \frac{V}{\epsilon_\gamma}\right)^2 Q_n^2 \cdot \sigma_{\text{Heat}}^2\right]}, \tag{3.27}$$

$$\sigma_{Q_{\text{Edw}}^\gamma}(E_{\text{Rec}}) = \sqrt{\sigma_{\text{Col}}^2 + \sigma_{\text{Heat}}^2} \cdot \frac{1 + \frac{\text{V}}{\epsilon_\gamma}}{E_{\text{Rec}}}. \tag{3.28}$$

Resulting bands for the time averaged energy resolutions are superimposed on the calibrated data of FID823 (γ calibration data sets) in fig. 3.29. The bands are drawn at 90% C.L. for nuclear recoils in red and at 99% C.L. for electron recoils in blue (99.99% C.L. only lower band in dashed blue). For clarity, quality and fiducial cuts have already been
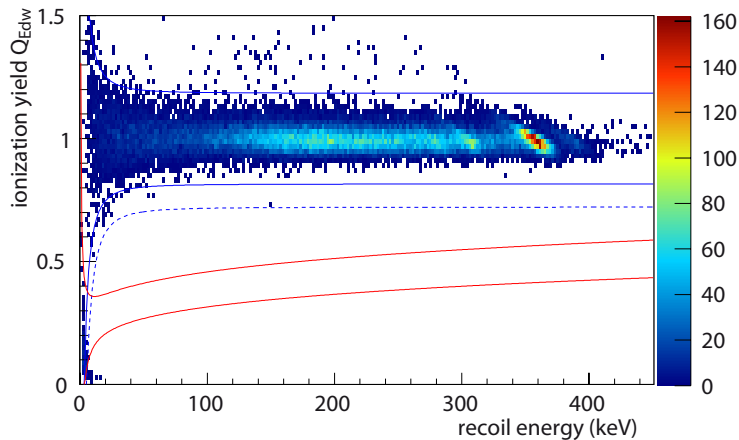
Figure 3.29.: Event distribution in the ionization yield versus recoil energy plane for the entire 8 V γ calibration data set (11.75 days) for FID823. The 99% C.L. (lower 99.99% C.L.) electron recoil band is indicated in solid (dashed) blue. The 90% C.L. signal region for nuclear recoil is visualized by the red bands.

applied to the data. The entire 8 V γ calibration data sets from this commissioning run correspond to a period of 11.75 days. The intersection of the lower 99.99% C.L. electron recoil band with the signal region represented by the 90% C.L. nuclear recoil band is often taken as a lower analysis threshold. This threshold is also referred to as magic point in the terminology within the EDELWEISS collaboration.

For analysis purposes it can be useful to analyze the data from heat and ionization signals without the loss in resolution from the calculation of the true recoil energy. For this purpose a nuclear recoil energy scale (keV_{nr}) can be calculated from eq. 3.23 relating E_{Heat} with E_{Rec}. Together with the Lindhard parametrization $Q/Q\prime(E) = 0.16 \cdot E^{0.18}$ and the heat quenching factor $Q\prime(E) = 0.91$ this scale could be corrected for the heat quenching bias. However, since the low energy behavior of the heat quenching is not well studied we conservatively set $Q\prime = 1$ and accept a bias at higher energy. The resulting energy scale does not correlate the measurements of ionization and heat. Technically, the calculation of E_{Rec} from E_{Heat} is performed numerically since the inversion of eq. 3.23 is not straight forward. A resulting plot of the gamma calibration data in the E_{Col} vs $E_{\text{Rec}}^{\text{nr}}$ plain is shown in fig. 5.2.

4. Background rejection of FID detectors in EDELWEISS-III

After the implementation of a fully working data processing chain within a new data management and analysis framework (KData) the last important step is the evaluation of its performance and the validation of its physics results. The evaluation of the performance is discussed both as a comparison against the results of an existing analysis chain on the same data set and in comparison to the average EDELWEISS-II baseline resolutions. The validation of physics results includes a cross check of the discrimination power in terms of γ-events with respect to nuclear recoils. Also, γ event rates during WIMP search data taking have been measured and compared to the results of an existing analysis chain. Peak identification and consistency of pulse timing has been verified within a study of muon-induced events. Finally, one detector equipped with a ^{210}Pb source has been analyzed with special care to quantify the acceptance of several cuts and to extend the measurement of the surface event rejection of FID detectors to lower energies than before.

The data used for this comparison is the last commissioning run of the EDELWEISS-III experiment which lasted from the 28th of October 2013 to the 6th of January 2014. The data taking was used to evaluate detector performances under several different voltage bias configurations. Both collecting and veto bias were changed to explore a set of different possibilities. Configurations of high bias for collecting and low bias for veto electrodes were of special interest to test possible configurations for CDMSlite-like [11] data taking. Hereby the heat signal is strongly enhanced by the Neganov-Luke effect of the drifted charges and can be approximated as a pure ionization measurement. The threshold and resolution are enhanced in this mode to allow resolutions close to the statistical limit (see sec. 2.1.1). While event by event discrimination for bulk γ events is lost a surface event discrimination might be retained. Due to electronics limitations, all tests were restricted to 20 V difference on the collecting electrodes.

Finally, values of ± 4 V on collecting and ∓ 1.5 V on the veto electrodes were selected as optimal configuration for the standard analysis. A summary of all available data sets including a classification into γ-calibration and WIMP search data as well as a specification of the bias difference of the collecting electrodes is given in fig. 4.1. The run type is indicated by the gray and black bar on top and the bias by the yellow, cyan and red bars standing for the main configurations at 8 V, 12 V and 20 V collecting voltage. For each data set, the ionization spectrum of the hole collecting electrode of FID823 is given on the y-axis. The length of a data set is specified during operation of the experiment within our
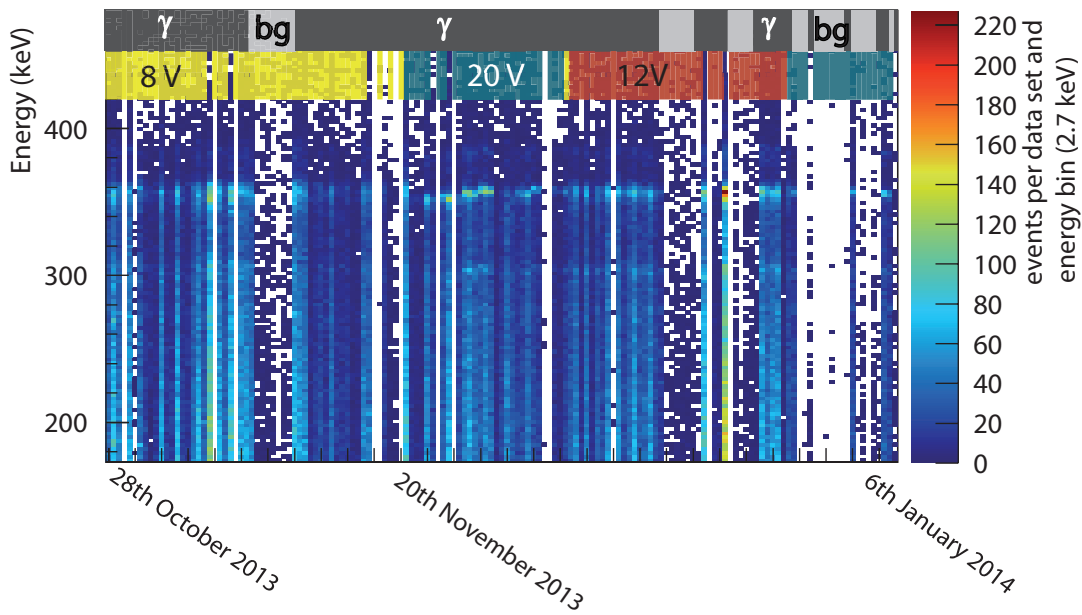
Figure 4.1.: Ionization energy spectra (y-axis) for individual data sets (x-axis) of the entire period from the last EDELWEISS-III comissioning run. Datasets are taken as defined during operation of the DAQ software SAMBA. During stable operation a typical length of a data set is about 20h. However, in case of cryogenic problems or in order to recover a misconfigured electronics box or to recover from a software crash much shorter periods are possible. On the top of the diagram, the type of data taking, e.g. γ calibration or low background/WIMP search (bg) data taking is indicated. Just below that bar, a second bar shows the absolute bias applied between the collecting electrodes of the FID detectors.

DAQ software SAMBA. A typical length of a data set is 20 hours, but shorter periods are possible. Some examples can be found just at the beginning of data taking after the 28th of October where some γ calibration data sets with extremely small statistics have been taken. Such small data sets are often correlated with a change of settings or optimization of running parameters. One of these parameters that was optimized at the beginning of the run was the frequency of the voltage reset or rather compensation pulses that counterbalance the build up of charge on the ionization electrodes and maintain the DACs in their linear range. Other statistically small data sets can be related to cryogenic maintenance operations, inefficient space charge removal, or misconfigured running conditions.

Within this thesis, one of the detectors, FID823, was calibrated for each of the voltage configurations to ensure that there is no principle problem for the combination of such data sets. The resulting energy spectrum for the hole collecting electrode of FID823 is shown in fig. 4.2. In the comparison with the 8 V bias data, the energy resolution of the dominant 356 keV photopeak width is significantly reduced from σ_{356}=6.9 keV to σ_{356} = 4.35 keV. Also, the remaining peaks are sharper.

However, for the WIMP search higher bias voltages lead to an additional Neganov-Luke heating and make it more difficult to reconstruct the real recoil energy. Therefore, it was decided to further operate the detectors at ± 4 V bias on the collecting electrodes. For the purpose of the validation of the above mentioned processing and for the measurement of the rejection performance of FID detectors, only the data at this bias is considered. Each different operation voltage requires to account for different charge trapping and different Neganov-Luke heating effects. Thus, rejection performances cannot be easily combined. Furthermore, each operation voltage requires an independent calibration and analysis. This includes not only the recalibration of heat but in fact a complete study of ionization
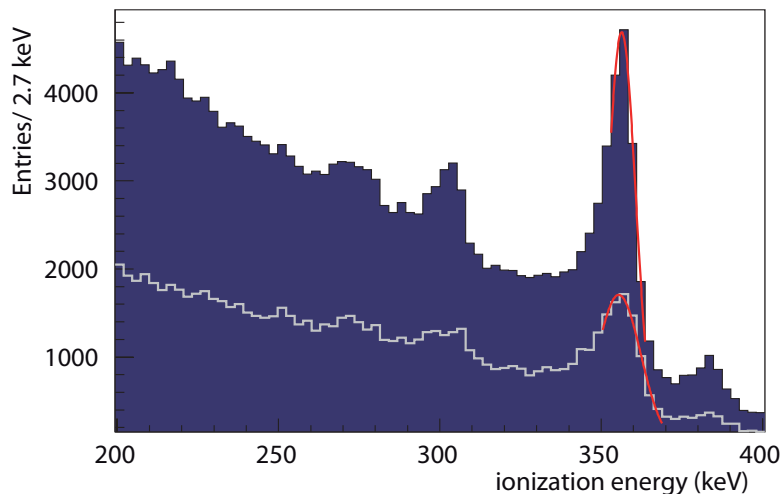
Figure 4.2.: Energy spectrum of the hole collecting electrode of FID823 after stacking all calibration data sets at different collecting voltages. For comparison, the energy spectrum from the 8 V data sets is drawn in gray (see fig. 3.23). Higher bias voltages reduce charge trapping effects and improve the charge collection of high energy events. This is reflected in the width of the 356 keV Ba peak, $\sigma = 4.35$ keV in comparison to $\sigma = 6.9$ keV for the 8 V data sets. The structure of additional photopeaks at 276 keV, 303 keV and 384 keV is also much clearer in the stacked spectrum.

with different trapping properties and all subsequent event quality cuts.

Three of the 15 FID detectors, FID803, FID819 and FID824, (see fig. 3.3) had broken or unusable ionization channels and were disregarded entirely within this analysis. Two detectors, FID806 and FID817, had a surface leakage problem and were biased with ± 2.67 V collecting bias and ∓ 1 V on the veto electrodes. These detectors have been kept for the comparison of the performance of the processing and have been used within the search for coincident muon-induced events, but were not investigated further in the analysis of FID rejection performances.

Out of the remaining 10 detectors, FID808 and FID820 were equipped with ^{210}Pb-β sources. However, FID820 had a severe problem in its heat read-out. One heat channel was dead and the other heat channel had an excessive noise pollution leading to a large FWHM heat baseline resolution of a few keV. Hence, this detector is not competitive in γ event discrimination and was not suited to explore the surface event rejection at low energy.

Thus, to sum up: The comparison of the performance of processing is based on all 12 FID detectors. Also muon-induced events have been investigated using this set of 12 detectors. Consistency checks of the γ background count rate and γ discrimination capabilities have been performed on a subset of two (three) detectors. Finally, the low energy surface rejection measurement was performed on the data from FID808.

4.1. Performance of data processing

The performance of the raw data processing can be estimated in multiple ways, and dependent on the objective of the processing one or the other is better suited. Within this work, a processing chain for the offline data analysis has been developed and is validated against an existing analysis chain. The low energy analysis threshold is the most important parameter to optimize for a low mass WIMP search. This threshold is best represented by the achieved baseline resolutions on the individual and combined energy variables. Hence,
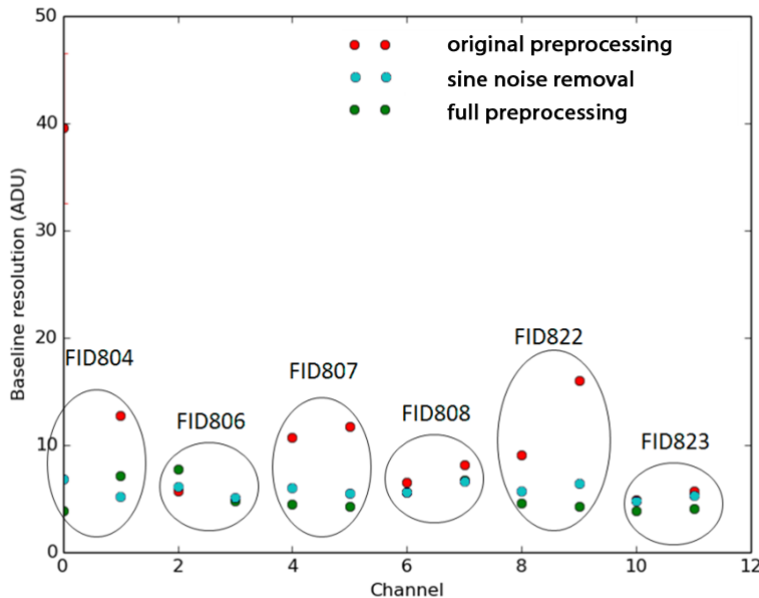
Figure 4.3.: FWHM of the baseline amplitudes of the collecting electrodes for a selection of 6
FID detectors with 8 V bias and reliable performance for a large statistics γ cali-
bration data set (16th November 2013). Three different processing versions have
been evaluated. The processing with original preprocessing including pattern re-
moval and linear removal is represented by red points, an additional removal of
sinusoidal noise at 4 Hz, 8 Hz and 50 Hz gives the cyan performance and start-
ing the preprocessing with the additional decorrelation processors provides the
green resolutions. Figure adapted from a dedicated study [232].

the FWHM of the Gauss fit to the baseline distributions was chosen as an estimator of
the performance of the processing. In order to demonstrate the improvement besides the
adaptation to the new pulse shape and the implementation of the high level data analysis
layer and calibration routines, baseline resolutions are compared within KData to evaluate
the new pulse processors used in this thesis. A separate comparison is made to judge the
performance against the alternative, previously existing analysis chain.

4.1.1. Relative improvement of the implemented processors

The performance of the newly implemented pulse processors e.g. the sine noise removal
and the decorrelation (sec. 3.3.2.1 and 3.3.2.2) was evaluated during a dedicated study
in 2014. For a subset of six of the 12 detectors, the baseline resolution was compared
for a standard preprocessing (pattern removal of the heat modulation and linear removal)
versus the resolution achieved after adding the sine noise removal versus the performance
after using both sine noise removal and decorrelation.

A comparison of the performance of the three different processings is given in fig. 4.3 for
a one day γ calibration data set. In general, a large improvement is achieved by applying
the single frequency noise removal (from red to cyan). Some resolutions are improved
by a factor 2 to 7 (collecting electrodes of FID822, FID807 and FID804) while others
were improved only a little bit (one of the electrodes of FID806, FID808 and FID823). An
additional smaller gain was observed from the addition of the decorrelation procedure (cyan
to green). Two exceptions to this general trend were observed: While one of the channels
of FID804 was improved drastically by the decorrelation, it seems that at the same time
some noise was injected into the other channel and the resolution was slightly worsened.
The other exception is FID806 where the new processing did not proof better, but instead
even produced slightly worse results on one of the two collecting channels. After special
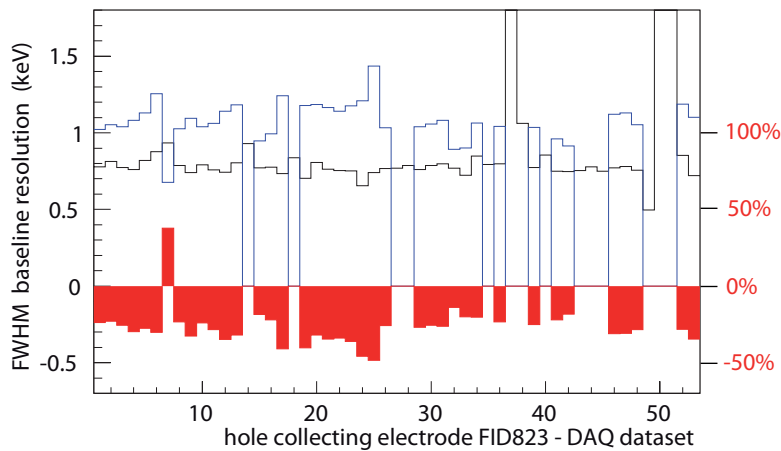
Figure 4.4.: Improvement in the energy resolution of the baseline for the hole collecting electrode of FID823. The processing developed in this work is shown in black. An existing bandpass analysis run by the Lyon analysis group which was optimized on a single data set is shown in blue. The relative improvement ((KData-Lyon)/Lyon) is shown in % in red.

inspection the reason could be identified: First of all, the sine noise removal was futile, since the noise structure looked slightly different. And the worsening of the resolution in the decorrelation seems to be correlated to a veto electrode where an extremely bad heat channel has been mounted on top.

Nevertheless, in the overall comparison it was clear that the implemented processors provided superior resolution to the previous processing. After an additional check that a consistent improvement could be observed for all data sets these processors were implemented as the standard version of the processing.

4.1.2. Baseline resolution compared to existing analyses

In this section the results of the KData pulse processing chain will be compared to an existing PAW (Physics Analysis Workstation), Fortran and C++ based analysis chain. Since PAW development stopped several years ago and newer operating systems and libraries have compatibility problems, the long term future of this processing chain would probably need some major adaptations. Hence, the validation of the processing chain within this thesis is of special importance. Both processing chains use very similar techniques. The PAW based analysis is maintained by the Lyon-analysis group [245] and has been used for the data analysis since the beginning of the EDELWEISS experiment. It uses a Butterworth filtering with fixed parameters and a subsequent template fitting routine. It includes sinusoidal noise removal and a set of different preprocessors, but no decorrelation. Optimization of filter parameters and sine noise removals is performed once, and special attention is paid to the calibration of all cross-talk coefficients. In the following this analysis will be referred to as the processing from the Lyon analysis group or the Lyon analysis.

For the comparison the following data quality selection was made. For each data set, a baseline estimate was performed on the set of events with a signal on the sum of ionization below $5\,keV$ and the free ionization fits converging within the fitting range and not at the boundary. Each data set, where the subsequent Gauss fit to the baseline distribution converged in a fitting range of $0 \pm 5\,keV$ with a width of $\sigma \in]0,3]\,keV$ was assumed as a valid estimate of the baseline. Larger energy estimates are probably not fit correctly or correspond to data sets with insufficient performance for the discrimination of low energy
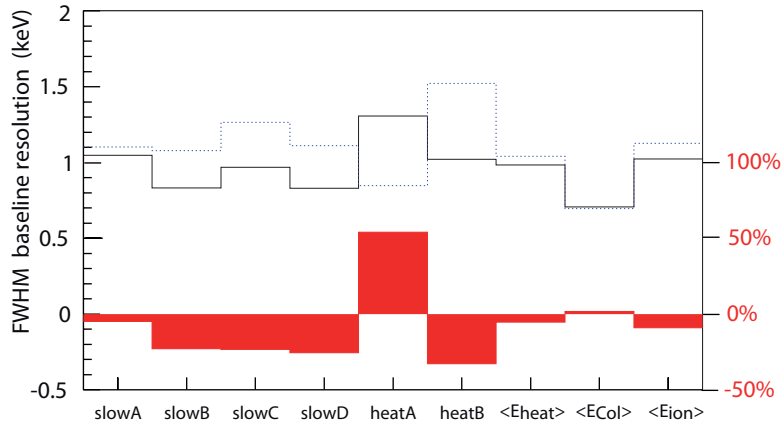
Figure 4.5.: Performance in terms of the FWHM of the baseline energy resolution for the implemented analysis in this work shown in (black), compared to an existing band pass analysis (dotted blue). The improvement or relative change ((KData-Lyon)/Lyon) between the processing chains is given in red. The performance has been averaged over all 12 FID detectors and all data sets with a statistics of at least 300 traces and a resolution (FWHM) in between]0,3.0] keV. Individual electrodes are numbered alphabetically according to SAMBA terminology. The total ionization signal $\langle E_{\mathrm{ion}} \rangle$ as well as weighted averages of of the bulk ionization signal on the collecting electrodes $\langle E_{\mathrm{Col}} \rangle$ and of the heat channels $\langle E_{\mathrm{Heat}} \rangle$ has also been compared.

(O(10) keV) electron and nuclear recoils. The energy cut at 5 keV is in fact a cut at $\sim$5 times the FWHM of the total ionization signal $\langle \mathrm{E}_{\mathrm{ion}} \rangle = \langle \Sigma_i \mathrm{E}_i / 2.0 \rangle = 1.02 \pm 0.17$ keV.

The resulting comparison is shown in fig. 4.4 for the hole collecting electrode for all of the 8 V bias data sets for FID823. The absolute baseline resolution achieved from this processing is given in black, and it is compared to the processing from the Lyon analysis group in blue. The relative change in percent is drawn in solid red. The detector and the channel shown is a typical result on a single channel.

The achieved baseline resolution is about 20% better and the adaptive selection of filter parameters keeps the overall performance more uniform (see fig. 4.4). Individual data sets were excluded from one or the other analysis and hence omitted from the comparison. An average of the baseline resolutions of the different channels has been computed, averaging over all 12 detectors and all compatible data sets. The results are shown in in fig. 4.5.

The mean resolution of all ionization channels, achieved with the processing developed in this thesis and averaged over all data sets, is $\langle \mathrm{FWHM} \rangle_{\mathrm{ion}} = 920$ eV with a spread of $\sigma(\mathrm{FWHM}) = 210$ eV. In total, this corresponds to a 22% improvement over the Lyon analysis. Looking at the individual channels and data sets, 1490 out of 1810 data sets were found, where KData performed better. An unexpected feature is the possible dependence of the performance on the ionization channel, in particular that the new processing did not improve as much on the veto electrode slowA as it did on the other channels. However, there is a possible correlation to the noise of the heat channels. In the current EDELWEISS readout, all channels, except for one of the heat channels (chalB), are read out by the same electronics box. Since the heat channels are glued onto the veto electrodes, an especially large cross-talk between the heat and veto signals exists. Hence, this could be a source to change the ratio of common noise versus individual noise components.

No special emphasis has been put on the optimization of the heat pulse analysis within this thesis. Only the adaptive Butterworth parameter selection has been implemented. Straight forward optimizations include the tuning of the template length and an additional sine noise removal as preprocessing. In the comparison to the Lyon analysis (fig.4.5) there
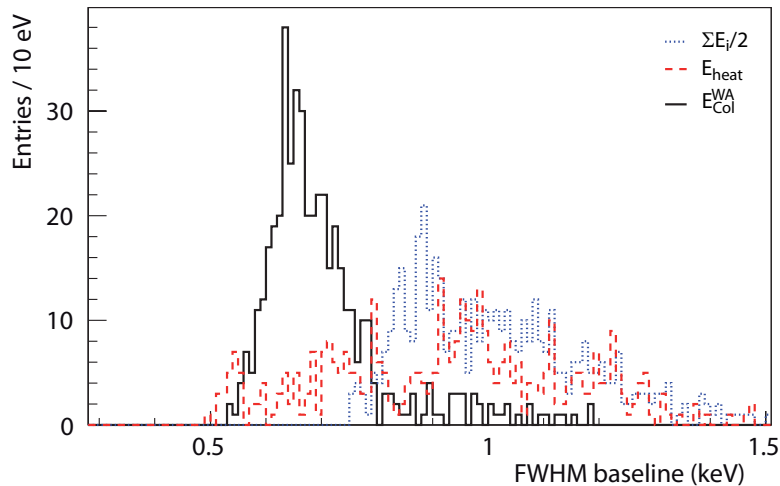
Figure 4.6.: Distribution of the FWHM of the baseline energy resolutions of all 12 FID detectors and all 8 V data sets for the main combined energy variables.

is an obvious inconsistency between either heat channel A or heat channel B being better in terms of baseline resolution. A possible explanation is the application of the sine removal on a few selected heat channels within the Lyon analysis. Since, there is more variation among noise frequencies in the heat channels, the application of the sine noise removal becomes more difficult. A better tuning for individual channels is required.

A further discrepancy is found when comparing the weighted average of the heat signal. In the Lyon analysis, the weighted average is computed from the overall time averaged resolutions of the individual channels and the weighted average can hence be worse than the better of the individual resolutions. Within the KData analysis, the weighted average is computed from the resolutions of each run and is then slightly better for the given data set and in the overall comparison.

The energy resolution of the total measured ionization signal on all four electrodes i ($E_{ion} = \Sigma_{i=1}^{4} E_i / 2.0$) is improved by an average of 9.7%. This somewhat smaller improvement with respect to the individual ionization channels is expected, since the summing of all ionization channels implicitly carries out the decorrelation procedure. Thus, no additional gain from this processor is expected in the total ionization variable. The same argument is valid, approximately, for the weighted average of the collecting electrodes $\langle E_{Col} \rangle$. However, it turned out that the energy resolution in this variable is not improved. Both analyses show a very similar performance concerning the bulk ionization $\langle E_{Col} \rangle$. From the entire 8 V bias data a 1.2% broader baseline resolution has been measured within KData. From the WIMP search data alone, which has less signal contamination in the baseline distribution, a 1.6% improved resolution has been found. The difference between the improvement of the sum of ionization and the weighted average of ionization hints at a compensation of the positive effect of the removal of common noise with a surplus contamination of individual noise from the veto channels. For a future processing it is foreseen to test a different ordering of pulse processors, e.g. to remove the heat pattern and clean up some noise induced by cross-talk on the individual traces before applying the decorrelation procedure.

The analysis presented here shows improved or at least compatible baseline resolutions to the alternative processing chain. Especially for the case of the individual ionization signals, which affect the surface event rejection at low energy, a 22% improvement has been demonstrated. Many optimizations, such as the adaptation of the single frequency noise removal for each channel (heat and ionization), as they are partially done in the alternative analysis for the heat channels, can easily be implemented and will further

improve the performance of this processing chain.

The distribution of baseline resolutions for the ensemble of all detectors is given in fig. 4.6 for the weighted average of ionization E_{Col} (solid black line) and heat signals E_{Heat} (dashed red line) and for the total ionization signal $\Sigma_{i=1}^{4} \frac{E_i}{2.0}$ (dotted blue line). Mean values and their standard deviation are $707 \pm 140\,\text{eV}$, $984 \pm 327\,\text{eV}$ and $1023 \pm 173\,\text{eV}$, respectively. In comparison to the averaged EDELWEISS-II performance of $899\,\text{eV}$ (with the same selection criteria) for the weighted average of the ionization signals, this is an improvement of 21%. Individual resolutions for EDELWEISS-II were provided from the Wiener filtering analysis on an hour-by-hour basis [246]. One systematic source of uncertainty from this extraction is the fact that the resolution for the weighted average ionization resolution for EDELWEISS-II has been computed via Gaussian error propagation. Hence, correlations and cross-talk noise components are not considered correctly. For the individual ionization channels, no such bias exists and the improvement is even stronger. The reduction of the baseline resolution at FWHM from $1.47\,\text{keV}$ to $0.92\,\text{keV}$ corresponds to an improvement of 37%.

Furthermore, it should be kept in mind that the improvement presented in this section was measured during a commissioning run to test different voltage settings. It is expected that the stability of a long term WIMP data taking in the same configuration will help in the optimization of the running conditions and hence improve on the achieved resolutions. An additional bonus can be achieved selecting only the best detectors and periods. Within this commissioning run this is represented by the best resolution of $\sim 500\,\text{eV}$ on heat and $\sim 530\,\text{eV}$ on the weighted average ionization. The readout of 24 detectors in the current ongoing WIMP search data taking makes it more likely to find detectors, where such excellent resolutions on both heat and ionization are measured on the same detector.

4.2. Data consistency

The consistency check of the data processing in a more detailed analysis has been performed on a subset of three detectors. FID818 and FID823 were kept as standard reference detectors and FID808 was analyzed in order to perform the measurement of the surface event rejection. For all of these detectors the logarithmic calibration correction for the heat signals was performed on WIMP search and γ calibration data sets independently. Datasets were selected more carefully based on the consistency of the calibration and the current noise level and subsequent baseline resolutions. For the WIMP search data, two data sets labeled nk14b001 and nk15b000 were found which were falsely labeled WIMP search, but were indeed γ calibration data sets. The cut on the baseline resolutions was not performed on individual resolutions but on the so-called magic point, i.e. the energy at which the lower 99.99% C.L. γ band intersects with the 90% C.L. signal region. A common value of $E_{MP} = 12\,\text{keV}$ could be used for all three detectors inducing only minimal loss in live-time of less than 10% for each detector.

As described in the following we performed both a very robust estimate and a comparison of the γ event rate during WIMP search data taking between the Lyon analysis and the analysis of this thesis. In addition a consistency check of the gamma event rejection on a sample of 116000 γ events has been done.

4.2.1. Selection of good quality time intervals

In order to compare both the Lyon processing [2] and the data processing developed within this thesis, the γ event rate is compared with a minimal selection of cuts. This includes a period cut requiring that both baseline and RMS estimate converged with a sensible baseline resolution estimate in the range $]0,3]\,\text{keV}$ (see also sec. 3.4.2). Furthermore, the
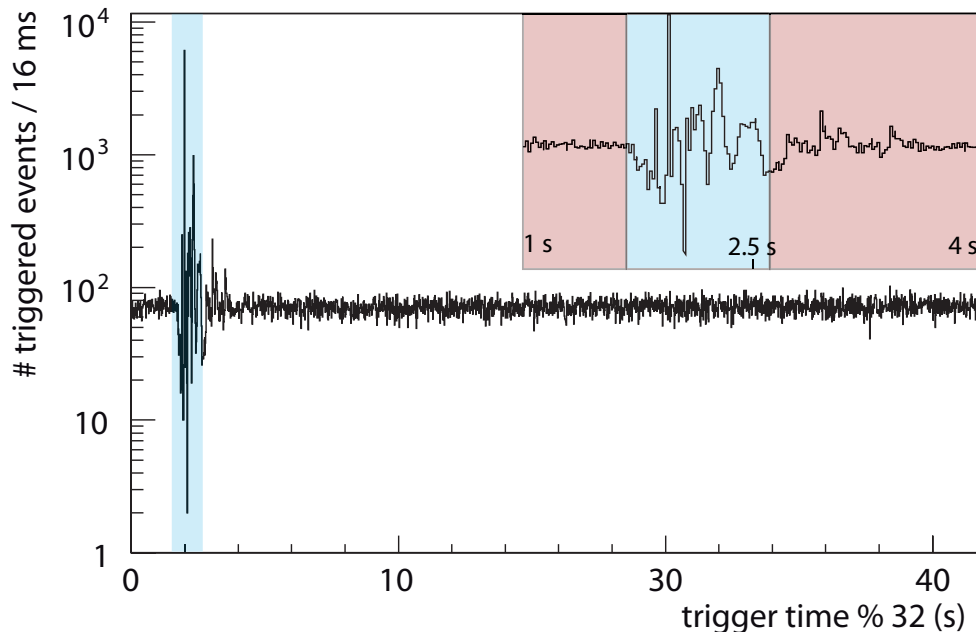
Figure 4.7.: Remainder of the trigger time modulo 32 for the entire WIMP search data of FID808. The so-called reset pulse cut, which removes technically introduced compensation pulses is exemplified by the blue shaded region. All events triggered with a remainder in between (1.6 - 2.6) s are rejected.

combined resolutions on the weighted average of ionization and heat need to be good enough to allow a discrimination of γ events above $12\,\text{keV}$ at 99.99% C.L.. The resulting data sets include a period of 5.06, 5.05 and 5.1 days for FID818, FID823 and FID808, respectively, and are comprised of 6 individual DAQ data sets each. In principle, the 2nd cut could be relaxed or removed entirely for the comparison of γ event rates, since only events with $\text{E}_{\text{ion}} > 100\,\text{keV}$ are taken into account. However, the cut allows to work with a more uniform data set both for the γ event rate comparison and later for the γ event discrimination.

One further periodic cut is applied on the trigger time to remove artificial pulses that compensate the build up of charge on the ionization channels and keep the DACs in their linear range. These artificial pulses are only applied to the ionization channels, however, they trigger the bolometer readout due to a higher noise level and cross-talk to the heat channels at the time of this operation. The pulses are injected at a known frequency every 32 seconds and last for about half a second. Thus it is possible to cut these periods with a small loss in live time. In fig. 4.7, the remainder of the trigger time in seconds modulo 32 is plotted for FID808. While these pulses can in principle be removed with a χ^2-cut due to their pulse shape and their higher noise level, the sheer amount of these events favors the more vigorous approach of treating these events with a periodic cut. For the $8\,\text{V}$ bias data, one single cut removing any event within a period of $[1.6 - 2.6]\,\text{s}$ could be used. However, it is worthy to note that both of the parameters of the reset pulses, the frequency and time within the remainder changed multiple times within the data sets with other biases of the commissioning run. They have been varied also within the 2014/2015 WIMP data taking.

The cut corresponds to 1/32 acceptance loss, which is 3.1% data loss. It is a conservative cut that removes all compensation pulses and allows for the count rate to come back to a flat stable level. The remaining wiggling of the count rate is understood as an interplay of the trigger dead time e.g. the time it takes a pulse to decay, before the next one can be registered.

A last periodic cut is intrinsically carried out by the DAQ. With the above procedure

Figure 4.8.: Event distribution in ionization yield versus recoil energy for 5.05 days of WIMP search data for detector FID823. Only periodic cuts, but no event based cuts have been applied.

of reset pulses the accumulated charge on the ionization electrodes is only compensated at the level of the ADCs. Hence, every 6000 s, a so-called maintenance procedure has been performed to put the ionization channels back to their nominal voltages and to reset the charge on the channel. After this large reset, the voltage on the DAC needs to be set correctly again and several rounds of adjustment are performed to eliviate the offset. Dependent on the parameters of this procedure an additional dead time of 4% to 8% was induced.

4.2.2. Rate of γ background events

In fig. 4.8 the ionization yield is plotted versus the recoil energy for all events in the entire WIMP search data set of 5.05 days for detector FID823 after applying the periodic cuts described in sec. 4.2.1. Note, that unlike for the WIMP search analysis, the total ionization signal and not the signal of the collecting electrodes is used for the determination of the recoil energy and ionization yield. Two dominant and two subdominant event populations become visible within this plot:

The first is comprised of the physical γ background at LSM. The events are calibrated to an ionization yield of one and lie dominantly in between the blue bands with recoil energies of $\sim 10 \, \mathrm{keV} \leq \mathrm{E}_{\mathrm{Rec}} \leq 3000 \, \mathrm{keV}$. The second is a population of events with a signal compatible with noise on the ionization channel and a small heat signal. Some of these events are likely to be triggered on noise excursions of the heat signal, but also energy deposits within the NTDs with different heat pulse shape and heat only events are known.

Without the application of a fiducial cut there is another widely spread sub dominant population with an ionization yield of 0.1 - 0.8 which can be associated to physical charge-quenched events of both γ and β particles. These events contaminate the signal region in between the red bands already at this low statistics of $\sim 4 \, \mathrm{kg \cdot d}$. These events can be rejected by a fiducialization as discussed for the heat signal calibration or as discussed in more detail in sec. 4.3.2. In fact all of these events above $\sim 10 \, \mathrm{keV}$ could be removed with the application of a fiducial cut, see fig. 4.9.

The fourth population of events can be identified in the lower right corner of fig. 4.8 at a quenching of 0.2 and about $\mathrm{E}_{\mathrm{Rec}} \approx 5 \, \mathrm{MeV}$. These events can be associated to the 5.3 MeV α decay of $^{210}\mathrm{Po}$ to $^{206}\mathrm{Pb}$. They occur in the decay chain of $^{210}\mathrm{Pb}$, one of the long lived

daughter nuclei of ^{222}Rn which is easily implanted in copper surfaces. A tail both in recoil energy and ionization yield is observed. During the study of the surface event rejection capabilities of FID detectors, the tail in charge yield could be associated to an unusual broadening in the relative position of ionization and heat pulses. This points towards a technical misreconstruction due to saturation effects. The tail in recoil energy can be explained most likely by an implantation depth and subsequent energy loss in the escape of the α's from the copper surfaces.

For the comparison of the γ event rate we refrained from intricate cuts and took the robust selection of $Q \in [0.5, 2.0]$ and a total ionization energy of $E_{\mathrm{ion}} \in [100, 3000]$ keV. 1621 events were observed in this analysis compared to 1625 events within the Lyon analysis [2] in the same range of quenching, and ionization energy. The live time as measured by the Lyon analysis group was 5.2 days.

Gamma event rates with statistical uncertainties of $\Gamma_\gamma = 13.0 \pm 0.3$ evts/h (Lyon analysis) and $\Gamma_\gamma = 13.3 \pm 0.3$ evts/h (this analysis) were subsequently calculated. The agreement in between the analyses is, however, not limited by the statistical error of the underlying Poisson process but by several systematic uncertainties. A systematic bias in the determination of the live time for example can fully explain this remaining difference. In this analysis, the live time was calculated from the time span in between the first and last event in each 1 h DAQ data partition. In the Lyon analysis each half hour period which has at least a single event was counted as live time. Hence, this analysis might underestimate the live time, while the Lyon analysis might overestimate the live time. Taking an average live time of 20 hours per DAQ data set and an uncertainty of the half hour binning, a bias of about 2.5% is expected. The bias due to the underestimation of the live time in this analysis was estimated from the trigger rate of about 50 mHz for FID823. For a 1 h period a typical bias of 1.1% is expected from this method. Thus the total calculated bias of 3.6% in between the live time estimates brings both measurements back into better agreement and can even slightly overcompensate and lead to a higher measured rate in the Lyon analysis. However, one additional source of bias in between the two analyses is expected from the reset cut. While the reset cut in this work is more conservative and cuts an entire second, a more aggressive one has been used in the Lyon analysis. The acceptance loss was estimated at a level of 0.5% only, compared to 3.1% within this work. Thus, all in all accounting for the different live times the results come into close agreement and remaining differences can be accounted for by less than 3% of difference in the calibration.

The same study has been performed for FID818, and 1570 events were counted in this study versus 1605 events by the Lyon analysis. Live times are again very similar: 5.06 days within the KData analysis and 5.19 days within the Lyon analysis. Allowing for the systematic bias in the live time of the analysis, a similar level of agreement is observed for FID818 as for FID823.

Hence, no hint at a disagreement or any problematic issue in either the amplitude estimation, event building or the calibration was observed in this comparison. Thus, the data processing from this work is assumed to produce reliable results, and rejection factors for both γ and surface events as measured during this thesis are assumed to be trustworthy.

The overall estimate of the γ rate can be transferred to a rate per kg·d using the nominal weight of 800 g per detector. Hence, it is possible to compare this rate to previous measurements and to the MC expectation discussed in sec. 2.4.1. For the two detectors analyzed herein the total rate in [100, 3000] keV is about 400 evts/ kg · d and 160 evts in [20, 200] keV. The MC expectation on the other hand was evaluated to yield 14-44 evts/ kg·d within [20,200] keV at 90% C.L. [161]. This large discrepancy can only be partially reduced by several systematic effects. The above measurement is a measurement of both surface and bulk events, in contrast to the simulation of bulk γ events only. The individual weight
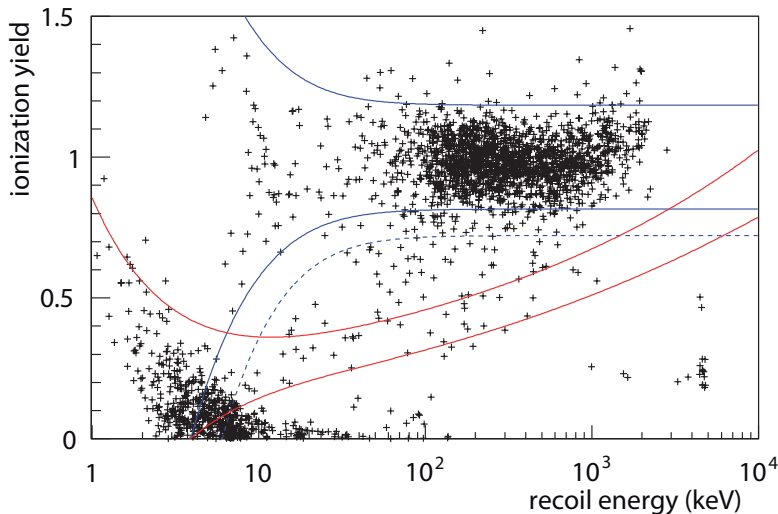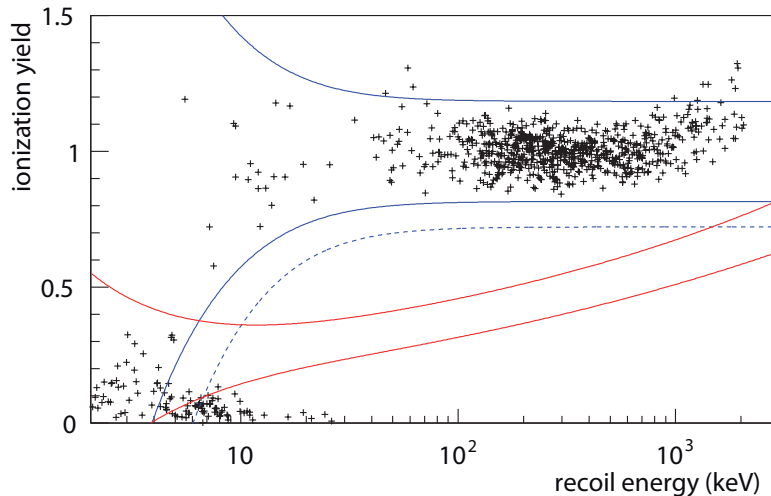
Figure 4.9.: Event distribution in ionization yield versus recoil energy for 5.05 days of WIMP search data for detector FID823 (as in fig. 4.8) after application of the fiducial cut.

of crystals ranges from 800 g up to 870 g, which also reduces the rate/kg·d. But most of the systematic biases discussed for the calculation of the live time tend to overestimate the live time by up to 20% and hence increase the measured rate.

A clear excess is observed also in the comparison of the total rate to previous measurements with similar selection cuts and less systematics. Within EDELWEISS-II a detailed study of the γ-background has been performed in [247] and a rate of about 200 evts/ kg·d was measured.

Higher material contaminations of the copper shields and other possible sources like an increased event rate from an additional contribution of radon could be excluded. Radon was measured continuously and did not exceed a level of 100 mBq/m^3 in between the lead castle and the cryostat. Instead, a correlation between the observed event rate of detectors and their position was found in [2]. Detectors on the top level showed a factor two to three higher rates than detectors beneath like FID818 or FID823. The main hypothesis that the increased rate came from the incomplete closing of the lead castle is currently under investigation. Due to the new EDELWEISS-III cryogenic line, a remaining gap of a few cm could have persisted at the intersection of the two movable wagons. Additional lead was placed at this position in 2015 and the improvement is currently being investigated. Preliminary results indicate that the total γ event rate in [100, 3000] keV as measured above reduced from 400 evts/ kg·d to 250-300 evts/ kg·d [248]. This is consistent with measurements obtained with the first FID detectors in the EDELWEISS-II setup [249] and it is much closer to the observed background in Ge-NTD detectors in Run 8. Remaining differences may be explained by the age of the Ge detectors or the radioactivity of the NTDs.

However, a somewhat reduced discrepancy to the expected γ rate from MC seems to persist. In the light of the excellent discrimination capabilities of FID detectors such a higher γ event rate might be tolerated, but at the same time additional larger γ statistics are being taken with the current setup to confirm this.

4.3. Discrimination of γ events

The γ event discrimination capabilities of FID detectors were evaluated already in 2012, with an extensive γ calibration data set of 411633 events [250]. With less than two weeks

of γ calibration data with the operation conditions of the current WIMP search, and with less than ten fully trustworthy detectors, this statistics can hardly be superceeded. But the analysis threshold can be reduced significantly, thereby providing both a further crosscheck of the processing developed in this thesis and adding valuable insight in the discrimination capabilities of the FID detectors at low recoil energies.

In the sense of providing a crosscheck, the analysis was carried out on FID808, FID818 and FID823 only, and the additional work of adjusting the calibration and cuts for the other detectors was skipped. The data was selected with the same quality criteria as for the background data given in sec. 4.2.1. Live times of 11.98 days, 10.93 days and 11.75 days after selection of high quality time intervals were obtained. In contrast to the estimate of the γ event rate, multiple further event based quality cuts are necessary which are described in the following.

4.3.1. Event quality cuts

In this analysis, pile-up events have to be taken into account due to the higher event rate in Ba calibration runs and the long integration times of 2 s for the ionization signal. For a pulse with pile-up, the template function cannot be fit correctly and individual ionization or heat amplitudes are misreconstructed. This can lead to events where the ratio of ionization and heat varies significantly, and in case the ratio is lower than 1.0, these events can mimic nuclear recoils.

To reject these events, the same goodness-of-fit cut on the template pulse fit, namely a χ^2 cut, was used as for the heat channel calibration procedure (sec. 3.4.3). Since the ionization channels sampled at 2 kHz have the largest pulse window and still finer sampling than the heat channels, the χ^2 cut was applied on the ionization channels only. This should still be sufficient to remove pile-up events with misreconstructed signals but avoids putting a goodness-of-fit cut on the less stable heat channels. A particular example underlining this argument can be seen in fig. 3.25 (c) where the difference in the RMS of the pretrace and hence in noise for the second heat channel of FID823 is shown.

Additionally a consistency requirement on the amplitudes of the two heat channels was introduced.

$$abs(\Delta E_{\text{Heat}}) = abs(E_{\text{heatA}} - E_{\text{heatB}}) < C_1 + C_2 \cdot E_{\text{Heat}} \tag{4.1}$$

The values $C_1 = 2\,\text{keV}$ and $C_2 = 5\%$ were chosen from previous experience. They are optimized for acceptance and allow for a significant miscalibration between the two heat channels rather than obtaining optimal rejection.

Finally, generic thresholds of $E_{\text{Col}} > 0.1\,\text{keV}$ on ionization and $E_{\text{Heat}} > 1\,\text{keV}$ on heat were introduced to remove a vast population of noise only events. These thresholds do not follow the measured baseline resolutions and are only introduced to allow better visualization when the dominant event populations are in fact physical event populations and not noise. They are set low enough to still see where noise events start appearing.

4.3.2. Selection of bulk events with a fiducial cut

In order not to be limited by surface events as in the 5 days of WIMP search data in fig. 4.8, the γ event discrimination has to be studied after fiducialization. For this purpose, a tool to develop a fiducial cut based on a given acceptance has been implemented in KData.

In principle, every event within the bulk fiducial volume should be accepted, because charges are collected only at the top and bottom electrodes at $\pm 4\,\text{V}$. In contrast any event at the surface where charges are drifted to one collecting electrode and an adjacent veto
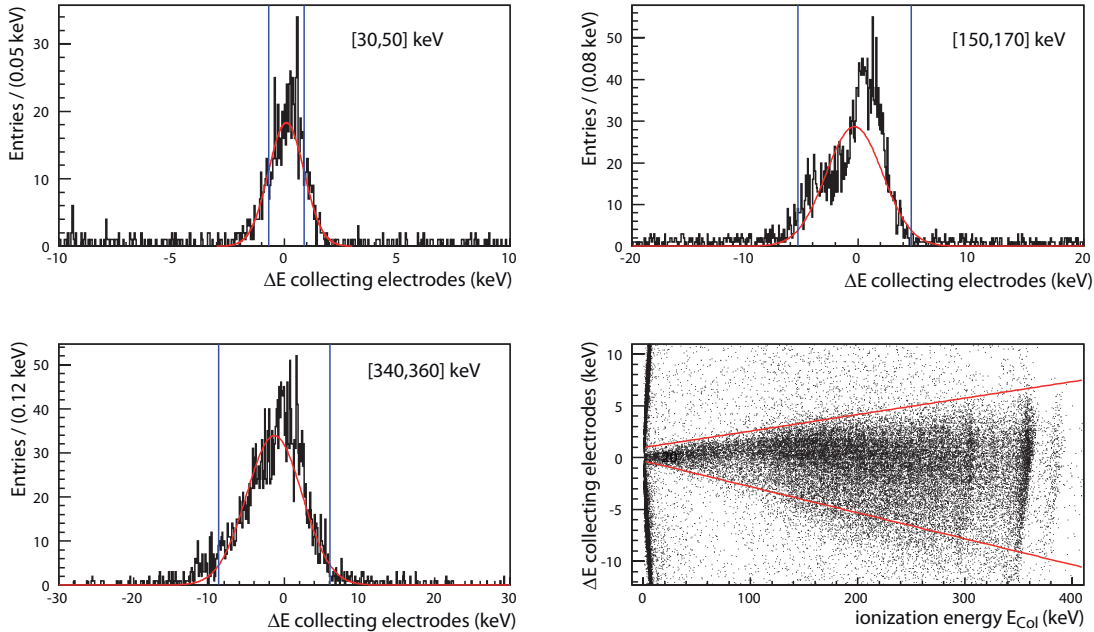
Figure 4.10.: Definition of the fiducial cut, based on the energy difference of the collecting
electrodes. A Gauss function is fitted to the distribution of the energy difference
of all events from the ^{133}Ba γ calibration data sets. To account for the energy
dependence, three energy ranges ([30,50] keV, [150,170] keV, [340,360] keV) are
fitted independently from one another. A red line for the resulting energy
dependent cut is shown in the lower right plot. For details see text.

electrode at ∓ 1.5 V bias should be rejected. Hence, for bulk events zero charge is expected
on the veto channels and the energy difference on the collecting channels has to be zero
since it contains all charges. Furthermore, since channels are first analyzed independently,
it is useful to add additional cuts on the estimated pulse timing. A bulk event should have
the same peak position on heat and collecting ionization channels, while surface events
can have different timing on the collecting electrodes.

In practice, neither timing nor amplitude estimates are ideal and the cuts have to be
designed allowing for energy dependent resolutions, uncorrected cross-talks and trapping
effects. For the cuts on the veto channels and the energy difference of the collecting
electrodes the acceptance of the cut is defined from γ calibration data. An example of the
cut definition for the energy difference ΔE_{Col} for FID808 is given in fig. 4.10. A scatter
plot (d) shows the energy difference ΔE_{Col} versus the estimated ionization energy E_{Col}.
Projections of this distribution in the energy ranges [30,50], [150, 170] and [340,360] keV on
the ΔE_{Col} axis are shown in (a), (b) and (c). Gauss functions are fitted to the individual
distributions. 1 σ limits at [30,50] keV and 2 σ limits at [150, 170] keV and [340,360] keV,
indicated by the blue lines are extracted and a linear regression algorithm is used to define
a positive and, independently, a negative line fit. The slopes are kept and a symmetric
constant term according to current or average resolutions is added. In this work, a single
constant term has been used and set to 900 eV for both the energy difference of the
collecting electrodes and for the individual veto channels. 900 eV corresponds to a ~ 2 σ
acceptance level with respect to the overall average resolution of 920 eV FWHM. This also
holds approximately for the energy difference of collecting electrodes since they generally
have 10-20% better individual resolutions.

In spite of the energy dependence of the estimate of the pulse position, a fixed cut of 10
samples is used for the time difference of the peak position in the two collecting ionization
channels. This does not account for all of the possible jitter in the peak position of
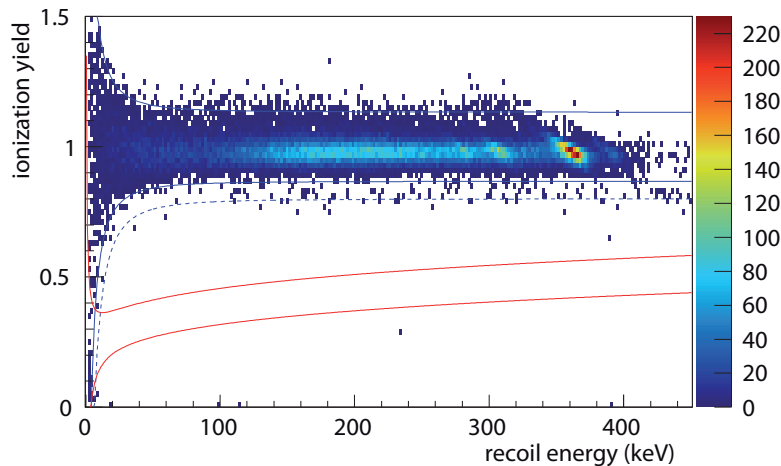
Figure 4.11.: Event distribution in ionization yield versus recoil energy for 10.9 days of γ calibration data for detector FID818 after application of the fiducial cut. Out of 48331 events in the 99.99% gamma band (dashed blue) none falls into the signal region (red band with $E_{Rec} > 10\,keV$).

low energy events. However, a difference in pulse position will necessarily reflect in an inaccurate estimate of the amplitude. Hence, this is a conservative choice.

This timing requirement is applied on both the ionization signals sampled at 2 kHz and at 100 kHz. The latter is not strictly necessary but ascertains that the bolometer timing is good enough for a precise correlation with event data from the muon-veto system. At the same time it acts similar to a threshold cut for large noise excursions. Since the smaller integration times at this faster sampling only allow for significantly worse energy resolutions, it can be useful to relax or remove this cut for low energy analyses.

To summarize, the fiducial cut for each detector consists off the following four requirements

$$(-900\,eV + p1 \cdot E_{Col}) < E_{Veto1} < (900\,eV + p2 \cdot E_{Col}) \tag{4.2}$$

$$(-900\,eV + p3 \cdot E_{Col}) < E_{Veto2} < (900\,eV + p4 \cdot E_{Col}) \tag{4.3}$$

$$(-900\,eV + p5 \cdot E_{Col}) < \Delta E_{Col} < (900\,eV + p6 \cdot E_{Col}) \tag{4.4}$$

$$\mathrm{abs}\,(\Delta t_{Col}) < 10\,\mathrm{samples}, \tag{4.5}$$

where $p1, \ldots, p6$ are individual parameters defined as visualized in fig. 4.10.

After application of these cuts, no event with $E_{Rec} > E_{MP}$, the energy of the 99.99% C.L. gamma discrimination thresholds (magic point), remains within the signal region. Fig. 4.11 shows the event distribution in ionization yield versus recoil energy for FID818. Similarly, no event remains in the nuclear recoil band of FID823 (fig. 3.29) and FID808 (fig. 4.20 (b)). Hence, out of in total 115642 γ events, not a single one was observed in the signal region above $E_{Rec}=$ 11 keV, the worst of the gamma discrimination thresholds. The rejection performance has thus been probed with 27% percent lower threshold with a remaining misidentification probability of

$$R_\gamma^{11\ keV} < 2.0 \cdot 10^{-5} \quad (90\%\,\mathrm{C.L.}) \tag{4.6}$$

per γ event. Individual gamma discrimination thresholds calculated from the average resolution of the entire data sets are $E_{MP} = 9.1\,keV$, $E_{MP} = 9.9\,keV$ and $E_{MP} = 11.0\,keV$ for FID823, FID808 and FID818 respectively. The γ event statistics was counted in the 99.99% C.L. gamma band in the energy range $E_{Rec} \in [10, 450]\,keV$ and yielded 42453, 25483 and 47706 events, respectively.

However, 3 anomalous events were observed which could be neither associated to the nuclear recoil nor the electron recoil band or their tails. Two of these events were observed in FID818 with a quenching of $Q \approx 0.25$ and $Q \approx 0.7$ and recoil energies of $E_{\text{Rec}} \approx 230 \, \text{keV}$ and $E_{\text{Rec}} \approx 400 \, \text{keV}$. In contrast to FID808 and FID823, FID818 only has a single heat channel, and no heat consistency cut could be applied. Taking a closer look at the individual events, they could be correlated to misreconstructed heat amplitude estimates. The χ^2_{red} of the fit of the heat pulse template to the trace had values of 80 and 270, which is more than a factor 4 above a 99.9% acceptance cut as defined on the ionization channels. The last obviously anomalous event was observed in FID808 at $E_{\text{Rec}} \approx 100 \, \text{keV}$ with a quenching of $Q \approx 0.6$. Again, the χ^2_{red} had significantly larger than average values of 18 and 10 on the two heat channels. The values are more than a factor of 2 above a potential χ^2-cut. All of these events can hence be easily removed with a χ^2-cut. However, the optimization of this χ^2-cut in terms of rejection and acceptance is not trivial. It might also require a higher accuracy in the time resolution of the determination of the RMS (see sec. 3.4.2). Since it is likely that this cut will be required for a blind WIMP search analysis, this is an important study to undertake.

The fiducial cut used in this work is not identical to the fiducial cut used for the initial determination of the γ discrimination capabilities of FID detectors [250]. Nevertheless, especially at high energy, the performance of the cut is insensitive to changes of the parameters. Since the initial measurement was performed above $15 \, \text{keV}$, which is a 27% lower higher threshold compared to this analysis, no significant impact of the different cuts is expected. Thus it is possible to use the statistics of this analysis to improve the original measurement of the γ rejection of FID detectors by 22% and calculate a combined rejection of

$$R_\gamma^{15 \, \text{keV}} < 4.4 \cdot 10^{-6} \quad (90\% \, \text{C.L.}) \tag{4.7}$$

above $15 \, \text{keV}$.

4.4. Background rejection of muon-induced events

The investigation of muon-induced events provides an excellent target to cross-check the event time estimate of the processing and to check the reliability of the DAQ operation of both the muon-veto system and the bolometer data acquisition. In addition, muon-induced events are an interesting event species to test the effectiveness of the new EDELWEISS-III internal PE shielding for the case of muon-induced neutrons. This data sample can also be used for the training and validation of the EDELWEISS-III MC simulation, from which the ambient neutron background is then estimated. Unfortunately, the WIMP search data set of this commissioning run has not enough statistics to really address these question. But it serves as testbed to prove the feasibility of this analysis. With the new DAQ (see sec. 2.4.4), a potentially more robust and faster way of performing this coincidence study was introduced. The muon-veto system readout was integrated into the bolometer DAQ sending and receiving restricted event information. The bolometer DAQ can hence tag coincidences and also trigger the bolometer data acquisition from signals in the muon-veto system. This method was evaluated in dedicated test runs at the end of March 2013. The data has been analyzed within a bachelor thesis [251], and both a validation of this method and an additional direct measurement of the dead time of the muon-veto system could be performed.

With the installation of further detectors the existing DAQ software SAMBA reached its limit in terms of CPU consumption on a MAC. Consequently, the muon-veto system readout was disabled in the commissioning run investigated in this thesis and in the first part of the current data taking. Hence, we need to rely on an offline analysis for the
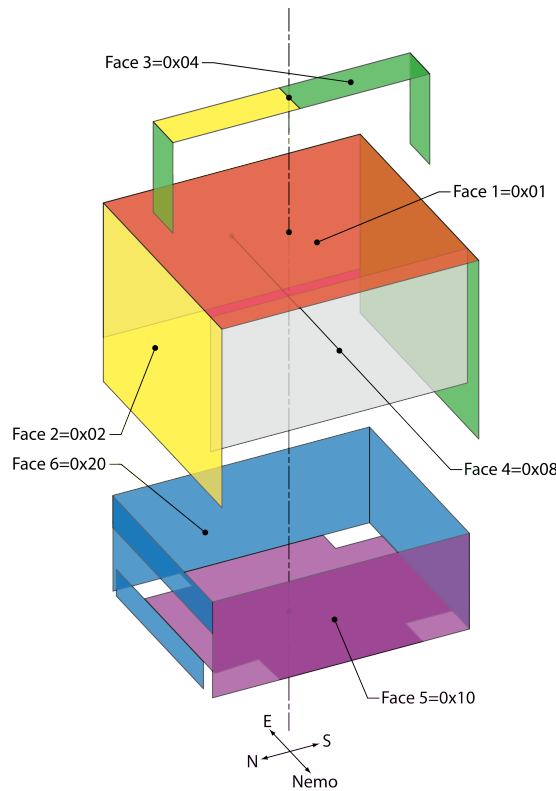
Figure 4.12.: Scheme of the EDELWEISS-III muon-veto system with geometry face bits in color coding.

identification of coincident events. The adaptation of the software from the coincidence analysis in EDELWEISS-II to the analysis of the data of this commissioning run is subject of another bachelor thesis [252]. Due to this work, several minor bugs in the timing parameters of the processing could be fixed. The results give confidence that both the 10-20 year old hardware of the muon-veto system DAQ as well as the new processing produce reliable output.

4.4.1. Study of the muon-veto system dead time with the bolometer DAQ

In March 2013 several data sets were taken to test triggering of the bolometer DAQ with events recorded by the muon-veto system. The information sent to the bolometer DAQ consisted of a continuous stream of the so-called geometry bit in combination with the time stamp from the common clock. The geometry bit is already constructed in the muon-veto electronics to allow low level consistency checks of event rates with different geometrical signatures. Hereby, the entire muon-veto system system is divided into 6 faces, see (fig. 4.12). Whenever an event above threshold is registered in any of the modules of one face, the corresponding geometry bit is activated. Only when data readout of the muon-veto system is complete, a reset command is sent and the geometry bit is set to zero again. Thus, the dead time of the muon-veto system is encoded in the number of samples with an activated face bit and can be extracted directly from the bolometer data. Since the muon-veto system information was read out for the very first time by the bolometer DAQ, all results were cross checked with the information stored by the muon-veto DAQ.

Within the bolometer data, this information was stored into a pulse array, and for each event a pulse trace of 8192 $10\,\mu$s samples was stored, see fig. 4.13 (a) for a partial trace. For the relevant physics of light propagation in the up to 4 m long modules, and taking into account shower like events a physical event length of tens of ns is expected. Adding
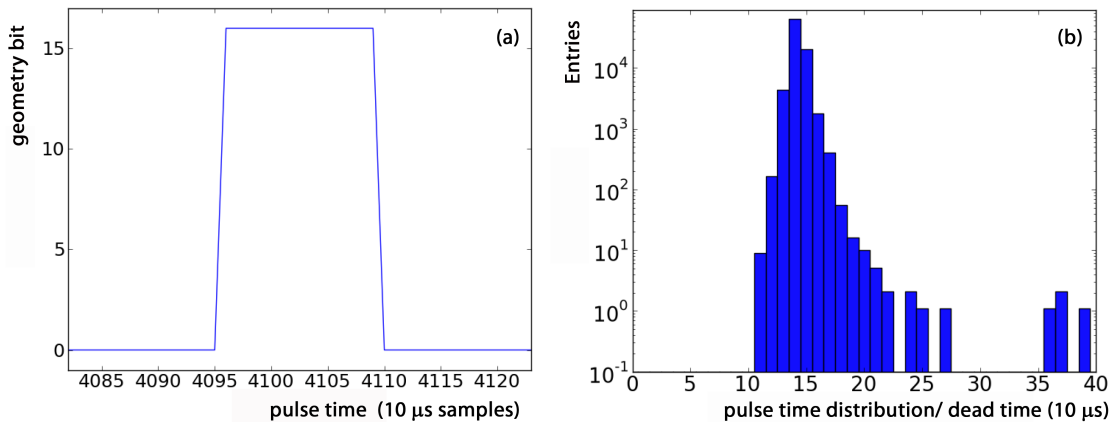
Figure 4.13.: First analysis of the muon-veto system information integrated into the bolometer DAQ. In this run (18th March 2013, 11.75h) the DAQ triggered on information from the muon-veto system. The so-called geometry bit relating to different sets of modules was stored into a pulse array (a). The length of a pulse corresponds to the time it takes for the muon-veto system DAQ to trigger, process the event information and reset the electronics. Hence it is a direct measure of the dead time. A distribution of the length of these pulses is given in (b). Figure from [251]

the readout electronics and event building, the dead time was determined in an original laboratory measurement to $\tau = 48.7 \pm 5.7 \mu s$. Hence, 8192 samples is an excessively large value and is only motivated by keeping a bolometer-like trace structure. However, since an unknown elongation of the dead time had occurred in a previous period and in order to have maximal information for the first test measurements, such long traces proved beneficial. Especially, a minor issue with an incomplete reset of the geometry bit after event readout could be detected [251]. In contrast, for the majority of all registered muon-veto system events the pulses were nicely centered and no anomalous event with a pulse duration of more than 40 samples was observed. The distribution of pulse durations for these events is given in fig. 4.13 (b). The mean of this distribution and hence the muon-veto system dead time is

$$\langle t_{\mathrm{P}} \rangle = (0.143 \pm 0.001)\,\mathrm{ms}. \tag{4.8}$$

This value has been cross-checked with a statistical approach at measuring the muon-veto system dead time independently from the muon-veto system data. The time difference between consecutive events for a typical one month DAQ period has been plotted in fig. 4.14 (a). As a Poisson process, the resulting spectra can usually be well fit by a single exponential. However, several influences like light and ventilation in the clean room strongly affect the count rate in the muon-veto system. Hence, not a single but a double exponential fit was introduced, which can describe the data very well. The fit was truncated at 0.01 s and at 0.99 s just before a time difference of 1 s. Thus, no influence of several calibration and monitoring LEDs is observed, which are operated at a frequency of 1 Hz every 8 hours. In order to measure the dead time, the residuals between fit and data have been plotted in fig. 4.14 (b). They were fit with an error function in the range 0 - 800 μs.

This scheme has been applied on the same data period investigated in the bolometer data. A dead time of

$$\tau = (0.145 \pm 0.008)\,\mathrm{ms} \tag{4.9}$$

consistent with eq. 4.8 has been measured. Furthermore, all muon-veto system data sets between May 2011 and April 2013 were investigated. The analysis helped understand
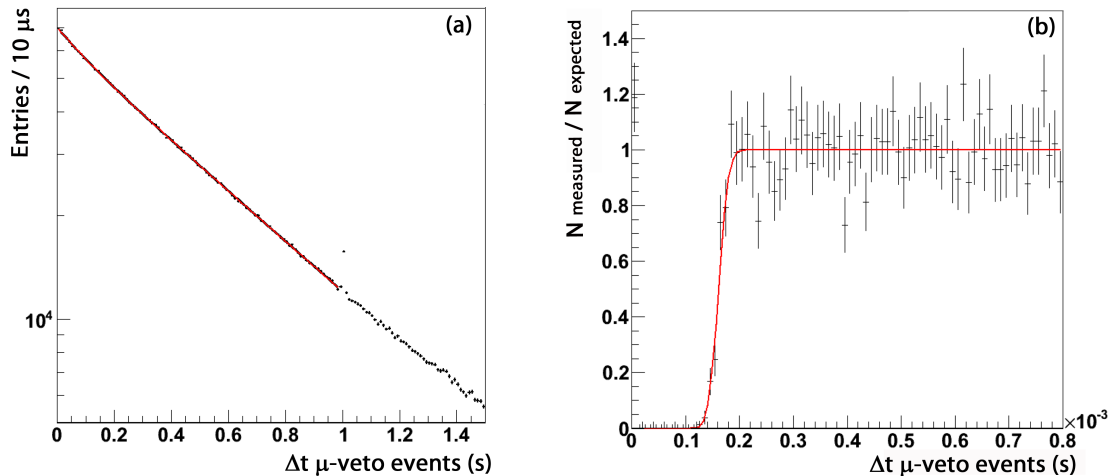
Figure 4.14.: (a): Δt distribution between consecutive events of the muon-veto system for a 1 month period. An increased rate of events is observed at 1 Hz due to the operation of a set of LEDs for calibration and monitoring purposes. (b): residuals between data and double exponential fit for small Δt values. The dead time was extracted via an error function fit. Figure from [251].

the previously noticed problem of the elongation of the muon-veto system dead time and confirmed that this was solved with the installation of a new Linux kernel on the data acquisition computer. An overall dead time of

$$\langle \tau \rangle = (0.156 \pm 0.001)\,\mathrm{ms} \tag{4.10}$$

was obtained for the 2011-2013 data taking. This value somewhat contrasts to the original laboratory measurement of $\tau = 48.7 \pm 5.7\mu s$. However, already with the installation and integration of another sub-detector, the neutron counter in 2007, there were measurements of the dead time of $\tau = 100 \pm 30\mu s$ [253]. Since then, hardware and operating system of the DAQ computer changed and the remaining discrepancy is possibly caused by such systematic differences.

In the course of this work, single event information stored in both the bolometer data and muon-veto system data were thoroughly checked. The events were correlated and, except for a now solved technical delay of 100001 samples in the bolometer DAQ, no reason was found prohibiting the use of this data for muon tagging and event rejection in a WIMP search.

4.4.2. Offline coincidence study

In a bachelor thesis an offline investigation of coincident events was performed using WIMP search data from this commissioning data set [252]. In contrast to the remainder of this chapter, this includes not only 5 days of data at 8 V bias, but also 6 days of data at 20 V bias. A few more WIMP search data sets at 12 V bias exist, but were excluded from the analysis. The DAQ was reset during that time leading to a restart of the common clock, which requires some extra effort for the synchronization. The data at 12 V bias cannot significantly increase statistics and thus do not alter the scope of this analysis.

The 20 V bias data has been calibrated in much less detail, and only for ionization, thus far larger uncertainties are expected in the pulse energy estimates. They can be tolerated since the identification of muon-induced events predominantly relies on the timing. A noise removal with threshold cuts of 2 keV on heat and ionization in the bolometer data
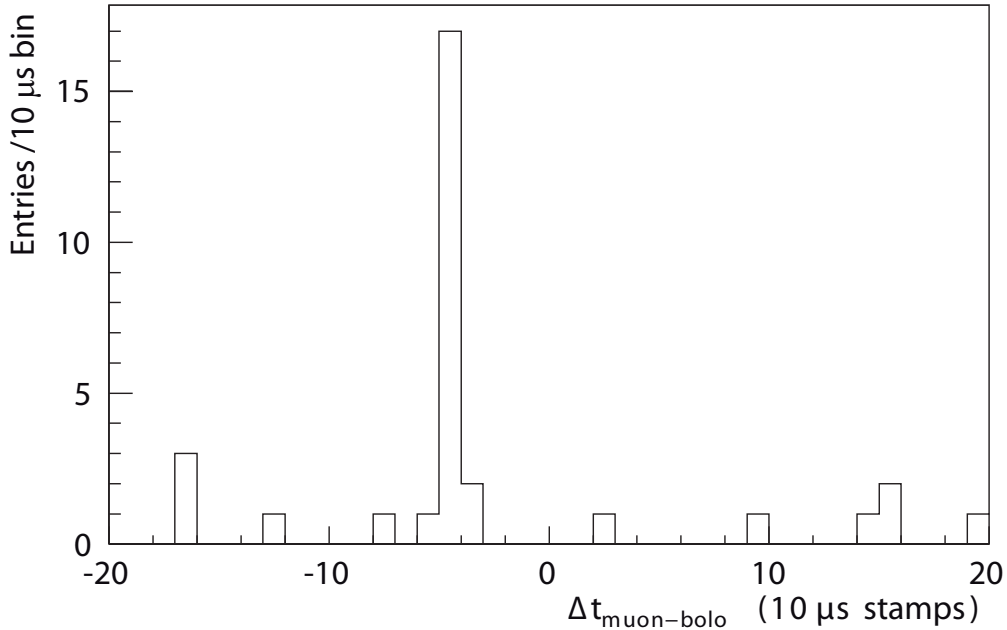
Figure 4.15.: Δt distribution between muon-veto system and bolometer hits. A clear signal of muon-induced events is observed with 17 hits over an average background of 0.2 accidental coincidences per bin. The distribution has been corrected for a known offset of 1,00001 s from a bug in the DAQ firmware and an additional shift of 0.02 s corresponding to the pretrace length of the ionization template.

together with a selection of muon candidates requiring an energy deposit in at least two modules is enough to obtain an almost background free identification of coincident events (fig. 4.15).

For the calculation of the combined live time, muon-veto system and bolometer event rates have been plotted in 10 minute bins in fig. 4.16. The values are combined rates for the entire muon-veto system without cuts and for the 12 bolometers with reasonable ionization signals applying the 2 keV threshold. Note that the 8 V bias and 12 V bias data sets have been analyzed separately and that only the time span of the 8 V bias data is shown. Both the muon-veto system and bolometer event rate show some characteristic features. The muon-veto system count rate (in blue) shows a pattern of spikes every 8 hours. They are introduced by the firing of calibration and monitoring LEDs. Then there are two periods after November 14 where the muon-veto system count rate increased by a factor ∼10 and exceeds the scale. The periods coincide with a stopping of the bolometer data acquisition. The large muon-veto system count rate is typical for periods correlated to light, ventilation and work within the clean room.

The bolometer count rate on the other hand shows a pattern of low count rate with a spacing of 6000 s. This drop in count rate is associated to a so-called maintenance procedure of the bolometer DAQ. During normal data taking, charges accumulate on the electrodes and they are regularly compensated by the so-called reset pulses. This build up of charge cannot be compensated indefinitely. Instead, every 6000 s all electrodes are set to the nominal biases and given some time to discharge. Then the DAC voltages are adjusted to bring the ADCs back to zero. The bolometer event rate increases from 0.4 Hz to 2.6 Hz after November 14 . From the ionization energy spectrum, clear indications were found that these last two data sets were mislabeled as WIMP search data, while in reality they were γ calibration data with the ^{133}Ba source. These data sets lead to a slightly higher rate of accidental coincidences, but do not limit this analysis and hence were kept.

For the remaining data the $\Delta t = t_\mu - t_{bolo}$ of all coincident hits with abs(Δt) < 200 μs
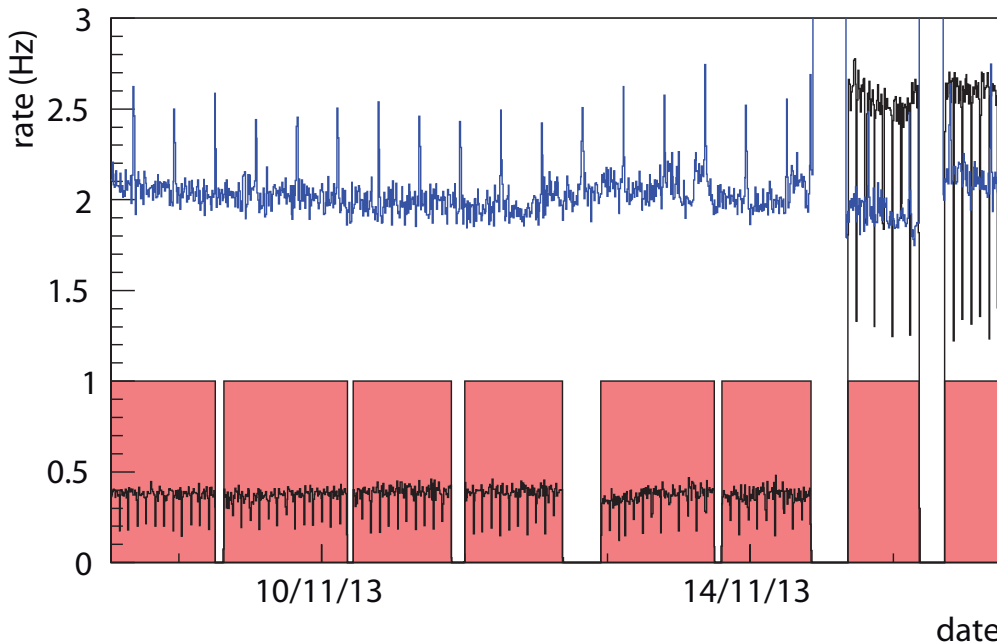
Figure 4.16.: Calculation of the combined live time of muon-veto system and bolometer DAQ (shaded red) for the first of the two 1-week data sets used in this coincidence study. The bolometer count rate is displayed in black, the muon-veto system count rate in blue. An 8 hour pattern from the consequent firing of monitoring LEDs at 1 Hz is observed in the muon-veto data. Similarly, each 6000 s a drop of the count rate in the bolometer system can be observed, where a maintenance procedure is started for a couple of minutes and no trigger can be observed. The two rises in count rate in the muon-veto system exceeding the range of the plot is a typical phenomenon associated to work and light in the clean room. The rise in the bolometer count rate is a change from WIMP search data taking to gamma calibration.

is plotted in fig. 4.15. The timings are the trigger time stamp t_μ and the reconstructed peak position in the 100 kHz ionization channel with the largest amplitude estimate of a bolometer. Since the timing accuracy of the ionization fits is needed for this analysis, it is natural to analyze individual bolometers in coincidence with the muon-veto system and to build coincidence events after this first analysis.

A dominant peak of 17 bolometer hits is visible at a timing of $\Delta t_{\mu-\text{bolo}} = -50\,\mu s$ above the background expectation of ~ 0.2 accidental coincidences per bin calculated from the live time of 11.2 days. The timing difference of 50 μs is not understood in terms of physics, but is consistent with previous results [4]. The 17 hits could be grouped into 10 coincidence events with 5 single and 5 multiple hit events. The total rate of muon-induced events was estimated with the assumption of an average FID detector mass of 820 g to

$$\Gamma_{\mu-\text{ind}} = (0.09 \pm 0.03)\,\text{evts/ kg} \cdot \text{d.} \tag{4.11}$$

This is slightly lower with respect to the estimate of the EDELWEISS-II analysis of $\Gamma_{\mu-\text{ind}} = (0.15 \pm 0.01)$ [4]. However, considering the systematic effects that have been neglected in the calculation of the live time, which include the maintenance procedures and the analysis of all bolometers with a common live time and common weight, no significant difference remains. Hence, no statement on a possible effect of the internal PE shied is possible within the limited statistics and considering the systematic effects of this analysis.

Instead, the analysis helped to correct the pretrigger length parameters for the KData

processing and demonstrated an excellent time resolution between bolometers and muon-veto system. The results are again consistent with previous data and instill confidence in the processing.

4.5. Background rejection of surface events

Surface events are a very dangerous background for dark matter searches, especially if crystals are employed as target. Various effects reduce the charge yield or scintillation yield of electron recoils such as an altered band structure at the surface, surface defects and trapping or charge recombination within the electrodes. The reduced charge yield can lead to the misidentification of electron recoils as nuclear recoils. Both for CRESST [8] and CoGeNT [9, 131], an observed signal excess might be due to the modeling of surface events. The signal preference dropped below the 1σ level in an independent analysis of the CoGeNT data [10] with different bulk to surface population modeling. New data from the CRESST dark matter search [110] with an improved detector design with fully scintillating housing and thus better surface event discrimination exclude most of the previously preferred dark matter parameter space. The study of these event is thus of special importance.

4.5.1. Surface background in EDELWEISS

In the EDELWEISS experiment, surface events are generally identified as an event with a significant contribution of charge on one of the veto electrodes. With a fiducial volume within the FID detectors of roughly 75%, this translates to an average thickness of the surface of the order of 3 mm. This definition is a very inclusive one, where a surface event can be any charged particle impinging on the surface and penetrating into the crystal or it can be a gamma interaction close to the surface with a part of the charges drifted to the veto electrodes. Particles of the first category are electrons from β decays in the natural radioactive decay chains and charged ions. These are dominantly α particles, but also recoiling nuclei from high energy α decays. Typical stopping lengths of such particles range from less than 100 nm for heavy charged ions up to the order of mm for MeV electrons in germanium.

In comparison, a typical dimension associated with the surface effect of leakage currents between electrodes is at the (sub) μm level. All surface leakage problems encountered on FID Ge detectors could be cured with a XeF_2 etching, that affects the surface in a very nonuniform way up to the scale of a few μm [158]. The Al electrodes, which have been deposited with a thickness of the order 250 nm, can also affect the charge yield of surface events. Any particle stopped within the Al electrode will not produce a charge signal and even for penetrating particles, a part of the charge will be lost.

Considering these length scales one could be tempted to further reduce the surface region, which would be possible by a change of the bias configuration of the detectors. However, in practice the cut on the ionization signal of the veto channels leads to a nonuniform thickness of vetoed surface events. Additionally the 3 mm of Ge provide the benefit of attenuating the γ-rate below 30 keV by a factor $\sim$50 (see fig. 3.20). Given these different aspects and the difficulties in modeling of the intricate details of surface effects, an optimization of the bias configuration is a very nontrivial task which usually requires large statistics of near-surface events. Within this analysis, only data at the standard operating conditions of ± 4 V and ∓ 1.5 V is used.

While many potential α and β sources exist in the natural decay chains, the dominant surface background in the EDELWEISS experiment can be associated to the single isotope ^{210}Pb and its daughters. The reason for this is its long livety of 22.2 years and its position
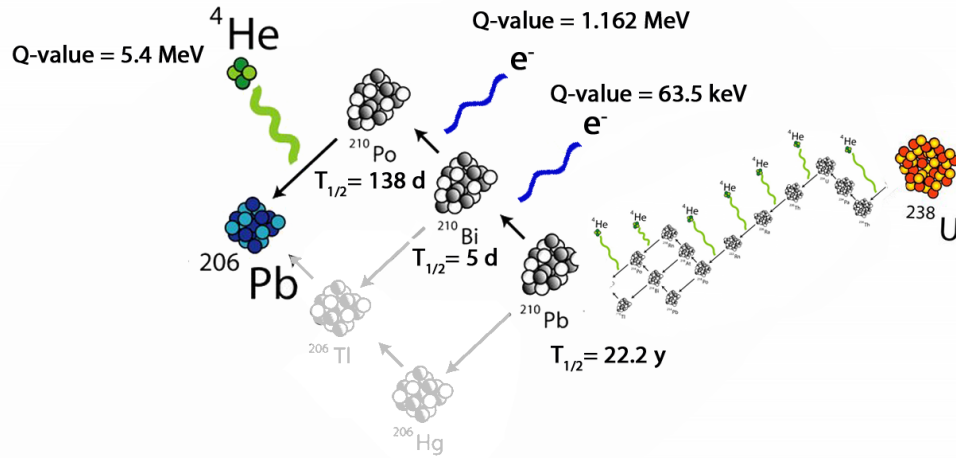
Figure 4.17.: Decay scheme of part of the ^{238}U decay chain. The long lived ^{210}Pb isotope is the dominant source of subsequent surface background in EDELWEISS. Figure adapted from [256] with data from [257].

in the natural decay chain after ^{222}Rn. ^{222}Rn itself is a gas, which is soluble in water and aqueous solutions. It is hence realistic to assume that along with U and Th with their natural abundance in copper ore, also at least an equilibrium amount of ^{222}Rn and its decay products will be present in the copper salt solutions used for electrolytic refinement of the copper. In contrast to U and Th, Pb isotopes seem to have an affinity for codeposition in the electrolytic refinement of copper [254]. Thus, much higher contamination of ^{210}Pb in contrast to other unstable elements can be expected in copper and have indeed been measured [255]. No other characteristic energy signatures of surface background have been observed on multiple detectors within the EDELWEISS-II measurements, and since copper is by far the dominant material in direct sight of the Ge crystals, this source of contamination is assumed to be the dominant source.

This argument leads to the conclusion that the measurement of the surface event rejection should be done with a similar source. Such a source can be produced simply enough by the exposure of copper, or copper adhesive tape to an enriched Rn flux. Via the $5.5\,\mathrm{MeV}$ α decays, ^{218}Po daughter nuclei can be implanted on the Cu surface. The following α and β decays release a total energy of $\sim 18\,\mathrm{MeV}$ and transfer a few $100\,\mathrm{keV}$ into kinetic energy of the nuclei. This will distribute the nuclei even deeper into the material until the long lived ^{210}Pb is reached. After cleaning of the surface the copper tape can be glued into the detector holders and can hence be used for the surface event calibration.

All of the observable decays of the remaining decay chain up to the stable ^{206}Pb are summarized in fig. 4.17.

^{210}Pb decays almost entirely (BR $= 1 : 10^{-8}$) under emission of an electron to ^{210}Bi. The energy is released either in a single decay with a Q-value of $63.5\,\mathrm{keV}$ or a 17 keV β decay is followed by x-rays or conversion and auger electrons. The measurable kinetic energies of the electrons thus fall perfectly into the region of interest of the WIMP search. ^{210}Bi undergoes another β decay with $Q = 1.2\,\mathrm{MeV}$ to ^{210}Po which in turn decays under emission of an α with $Q = 5.4\,\mathrm{MeV}$. From the last decay one can either observe an α particle with $E_{\mathrm{Rec}} = 5.3\,\mathrm{MeV}$ or a recoiling ^{206}Pb nucleus with $E_{\mathrm{Rec}} = 103\,\mathrm{keV}$.

For both the Pb nuclei and the α particles one usually registers the total energy deposit diminished by a potential energy loss in the escape from the copper source. For the β decays one expects the continuous energy spectra from the energy division between $\bar{\nu}_e$
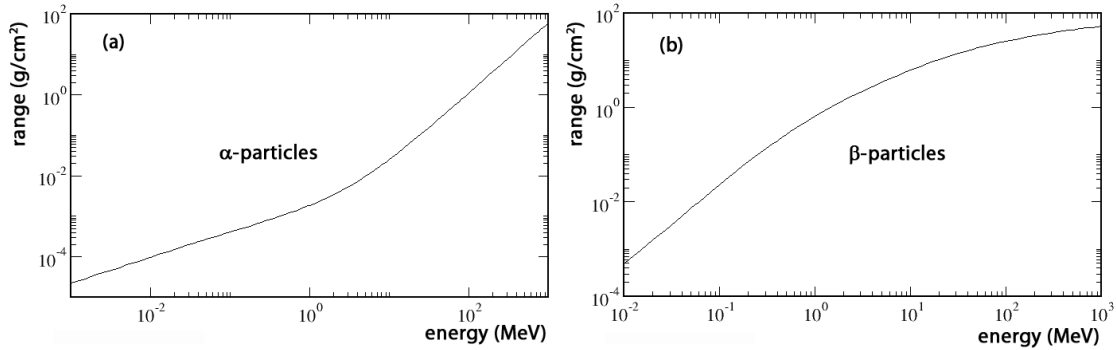
Figure 4.18.: Stopping range of α (a) and β (b) particles incident on Germanium. Figure adapted from the NIST (National Institute of Standards and Technology) ESTAR and ASTAR database access system with data from [258, 259].

and e$^-$. Dependent on their energy, α and β particles have a different stopping range as indicated in fig. 4.18. For high energy β's, a combination of surface charge quenching and unquenched charge collection is expected. An additional sharing of charge between same-side veto and opposite side collecting electrode occurs when particles tracks cross from surface electric field to bulk electric field regions within their stopping process.

In practice, a charge quenching of $Q \sim 0.3$ is seen in fig. 4.19 for low energy surface electrons. In this data set which spans a period of 5.1 days, 19795 low energy β's in the range [10,60] keV were observed. The high energy electrons from the ^{210}Bi decay form a band from the low energy region up to 1 MeV. Within this band a transition from dominating surface effects with a charge quenching of 0.3 to a dominant bulk stopping with a quenching approaching unity around 800 keV can be seen. Beyond 800 keV an additional effect from the imperfection of the logarithmic heat correction becomes apparent. The heat amplitude is over corrected and the γ band population starts bending upwards, to an ionization yield beyond unity. This effect could already be seen in the logarithmic heat correction where parametrization and data do not agree very well at such high energies (fig. 3.28). But 800 keV is far beyond the signal region of the WIMP search, and this imperfection can hence be tolerated for this analysis. Finally, there are the two well defined surface event populations of α particles with E ≈ 5.3 MeV and $Q \approx 0.2$ and the recoiling Pb nuclei at E ≈ 100 keV and $Q \sim 0.1$. These lower quenching ratios can be understood as a combination of surface and nuclear recoil like quenching for the stopping of different heavy ions.

Statistics of these event populations including low and high energy β particles are summarized in table 4.1. In principle the statistics of the observed decay products can be used to

Table 4.1.: Event statistics for 5.122 days of surface event calibration data of FID808 at 8 V. The data set is plotted in fig. 4.19. All data selected with a magic point smaller than 12 keV. The average is 10.5 keV

event population	energy range in keV	ionization yield	# events	ratio Po α
Po α	[900, 10000]	[0.0, 0.9]	17723	1.00
high energy β	[50, 900]	[0.25, 0.85]	17485	0.99
low energy β	[10, 60]	[0.2, 0.7]	19795	1.12
Pb recoils	[20, 120]	[0.0, 0.2]	12577	0.71
γ evts	[60, 10000]	90% C.L. γ-band	1302	-

Figure 4.19.: Event distribution in ionization yield versus recoil energy for 5.112 days of surface event calibration (WIMP search) data for FID 808 at 8 V bias. Only very basic event-based cuts are applied. A threshold cut of 0.1 keV on ionization and 1 keV on heat has been used together with a requirement on the consistency of the two heat channels ($|\Delta E_{\text{Heat}}| < 2\,\text{keV} + 5\% \cdot E_{\text{Heat}}$). 90% C.L. signal region (red lines) and gamma band (blue lines) parameterizing bulk nuclear and electron recoil distributions are shown as an eye guide. Note, that in contrast to a standard WIMP search analysis, the ionization yield and recoil energy are calculated from the sum of ionization E_{ion} instead of from the weighted average of the signal on the two collecting electrodes E_{Col}.

check whether the radioactive source has reached equilibrium so that $A_{\text{Pb}}(t) = A_{\text{Bi}}(t) = A_{\text{Po}}(t)$. However, different stopping ranges, the energy overlap of the two β decays and detector thresholds that reduce the detection efficiency for lowest energy β's makes this analysis quite intricate. Energy loss within the source might also require the comparison of data with MC simulation to correctly account for source implantation depth. An indication of this effect is seen in the comparison of Pb recoils and Po α's (see table 4.1). While both the 5.3 MeV α's and 100 keV Pb recoils come from the same decay, 28% less Pb recoils have been observed. The surface of the detectors, which is covered by Al electrodes, can account for about 10% of the difference, by completely stopping the Pb within the Al electrodes. Thus, a significant discrepancy remains, which requires a more detailed study of the geometries and source implantation depth with simulations.

A thorough analysis of these effects is beyond the scope this thesis which features a first analysis and validation within a new data analysis framework. But the observed ratio between high energy β's from the ^{210}Bi decay and the α events from ^{210}Po is indeed close to unity (ratio of 0.99). The ^{210}Bi will come into equilibrium very quickly due to its relatively short half live of only 5 days. For ^{210}Po this time scale is significantly longer. With a half live of 138 days, a state close to equilibrium is reached after many months only. Since about three half lives of ^{210}Po passed since the production of the source, this state should be closely reached for the source employed in this thesis. This is reflected in the measurement in table 4.1 where the remaining differences in the abundance of the different decay products is less than 15%, which is well within the systematic uncertainties. In the following we will thus assume that the source reached equilibrium and measure the rejection factor for surface events as the number of rejected decays including all possible background from low energy β events, from the ^{210}Pb recoils and from α events that can be

rejected by the fiducial cut introduced in sec. 4.3.2. For equilibrium the number of decays from ^{210}Pb $\to^{210}$Bi $\to^{210}$Po $\to^{210}$Pb is best measured as the number of ^{210}Po α's. This number is going to give a conservative estimate, as contaminations in the detector holders in the WIMP run will typically be closer to equilibrium than the ^{210}Pb source used in the calibration. Calibration data will thus have additional low and high energy β's from the ^{210}Pb and ^{210}Bi decays, if equilibrium is not reached yet. This definition is consistent to previous analyses [2].

4.5.2. Surface event rejection applying the fiducial cut

Applying the fiducial cut (sec. 4.3.2), two factors need to be considered: the rejection power that quantifies the ability to remove unwanted surface events and the acceptance that quantifies the amount of wrongly rejected physical bulk events. In this work the rejection factor includes both effects and is defined as the number of rejected surface events diminished by the acceptance of the fiducial cut for real bulk events. As the acceptance of the fiducial cut (see fig. 4.20) is flat in energy down to ~ 5 keV the acceptance is accounted for by a simple scaling with the plateau value.

In principle the acceptance of the fiducial cut has been already defined by the construction of the energy dependent cuts on both of the ionization veto channels and on the energy difference between the collecting electrodes (see sec. 4.3.2). The individual cut values were extracted to give a $\sim 2\,\sigma$ acceptance (95.5%) cut. Nevertheless, the individual cut acceptances need to be combined to yield the complete acceptance. Assuming no correlation between the variables a combined cut acceptance of 87% is calculated. However, this assumption is certainly not perfectly true. Uncorrected cross-talk coefficients as well as

Figure 4.20.: Event distribution in ionization yield versus recoil energy for 11.98 days of γ calibration data before (a) and after (b) application of the fiducial cut. The acceptance of the fiducial cut (c) is evaluated from the upper half of the 90% C.L. γ-band (blue) in (a) and (b). The cut is evaluated on γ-calibration data to ensure that only a small contamination of surface events is present in the data sample. A χ^2 cut has been applied in order to remove pile-up events. Ionization yield and recoil energy are computed from the weighted average ionization E_{Col} and weighted average of heat.
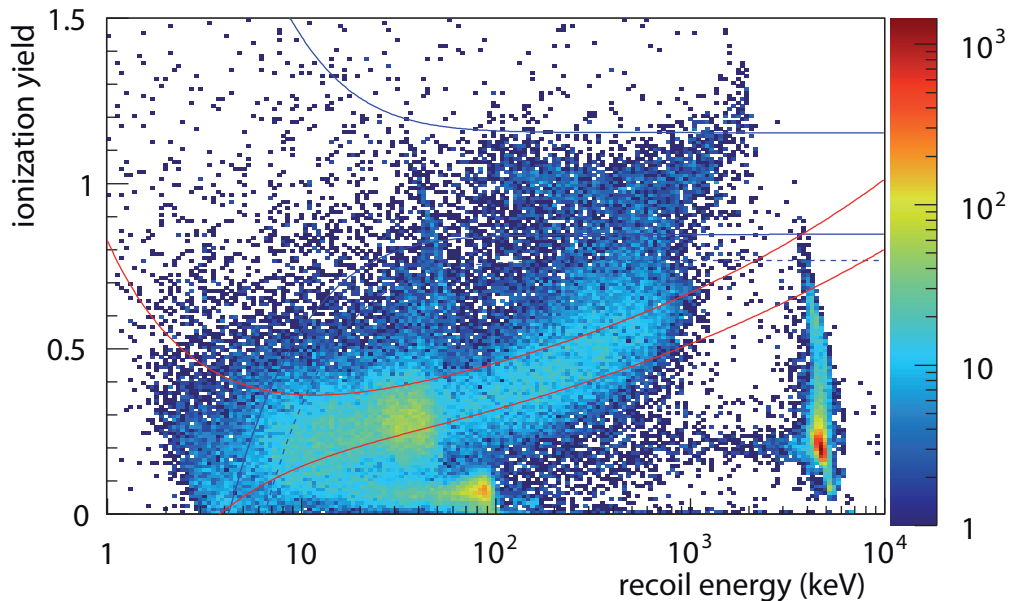
Figure 4.21.: Event distribution in ionization yield versus recoil energy for the 5.122 days of surface event calibration (WIMP search) data of FID 808 at 8 V bias after application of the fiducial cut (eq. 4.5). Additional event based cuts are the same as in fig. 4.19.

charge trapping and induced signals correlate and distort the division of signals on the veto electrodes and the energy difference of the collecting electrodes (see fig. 4.10). In addition, a single value of 900 eV was used to define the width of the cut at zero ionization energy. While this value corresponds to the average $2.35\,\sigma$ baseline resolution of all channels, it does not account for the variation among channels. Finally, also the timing consistency cut between the collecting electrodes introduces an energy dependency. At lowest energy the position of the pulse fit will be modified by large noise excursions and reduce the acceptance. This is especially important for the 100 kHz ionization channels, which have worse signal to noise ratio than the 2 kHz traces. Hence, it is necessary to confirm and measure the acceptance of the combined fiducial cut from data. This has been done on the ^{133}Ba calibration data as demonstrated in fig. 4.20. In contrast to fig. 4.19, ionization yield and recoil energy are calculated from the weighted average of the ionization signal on the collecting electrodes and the heat signals. Thus, a better resolution is reached in these quantities, and surface events show a lower ionization yield (event population at $Q \leq 0.2$ in fig. 4.20 (a)) due to the fact, that the part of the signal on a veto electrode is discarded. These effects are also used in the WIMP search analysis. In this plot of ionization yield versus recoil energy comprising 11.98 days of data, the upper half of the 99.99% electron recoil band is treated as a quasi background free region of real bulk γ events. By comparison of the number of events before and after fiducial cut in each 2 keV bin, an acceptance efficiency has been derived (fig. 4.20 (c)). This efficiency could be characterized by an error function fit with an energy threshold of 4.1 ± 0.6 keV and a width of 1.1 ± 1.1 keV on the ionization energy E_{Col}. The acceptance saturates at $(90.6 \pm 0.3)\%$ with a remaining energy dependence of 2-3%.

Applying the fiducial cut (eq. 4.5) to the surface event calibration (WIMP search) data, no surface event remains within the 90%C.L. signal region (fig. 4.21 and fig. 4.22 for a zoomed view at low energies). This corresponds to a rejection of
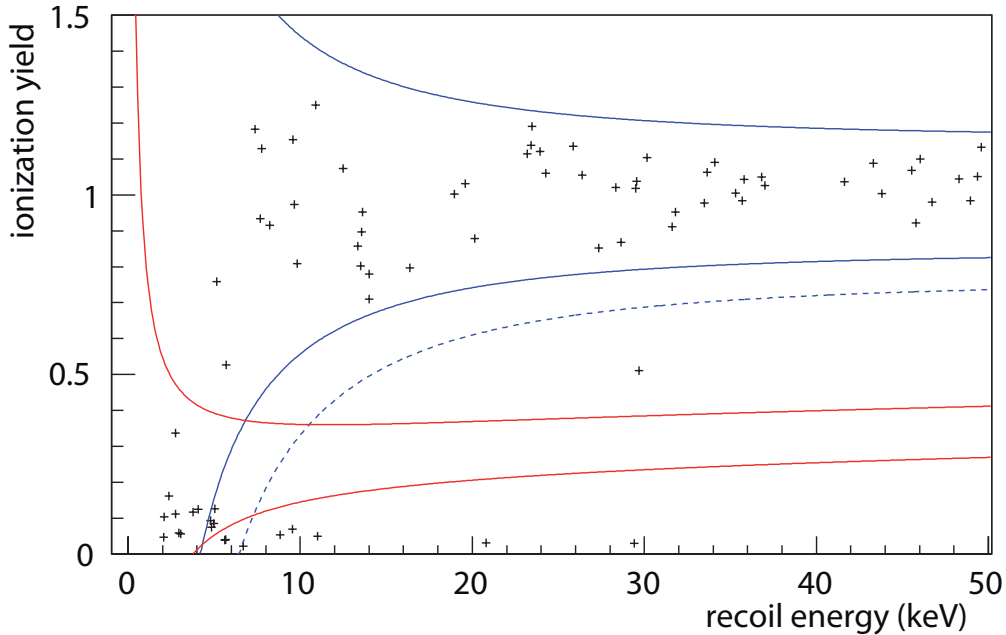
Figure 4.22.: As fig. 4.21,but zoomed to the low energy region $E_{\mathrm{Rec}} \leq 50\,\mathrm{keV}$.

$$R_{\mathrm{surface}}^{10.5\,\mathrm{keV}} < \frac{2.3}{17723\ \alpha\ \mathrm{evts} \cdot 0.906} = 1.5 \cdot 10^{-4} \quad \mathrm{at}\ 90\%\mathrm{C.L.} \tag{4.12}$$

above the average gamma discrimination threshold ("magic point") of $E_{\mathrm{MP}} = 10.5\,\mathrm{keV}$. A zoom of the low energy region of the data after the fiducial cut is given in fig. 4.22. Two distinct event populations can be identified: The bulk electron recoils within the blue bands and a population of noise and heat only events creeping in from the lower left corner which follow a hyperbola in the plane of ionization yield versus recoil energy. The border of this hyperbolic shape corresponds to an ionization threshold above which ionization noise events spill into the data sample.

Finally, there is a single anomalous event at an ionization yield of $Q \sim 0.5$ and a recoil energy of $E_{\mathrm{Rec}} \approx 30\,\mathrm{keV}$. This event has normalized χ^2 values of 4 and 5 for the pulse fit of the collecting ionization channels at an ionization energy of $E_{\mathrm{Col}} \approx 15$ keV. This is more than a factor 3 above the ionization χ^2 cut defined for the pile-up rejection on Ba calibration data (see sec. 3.4.3 for details on the definition of this cut). Thus, it is another indication that a goodness of fit cut will be needed for a blind WIMP analysis.

4.5.3. Additional statistics from γ calibration data

It is principally feasible to add data from γ calibration statistics to determine the surface event rejection from higher statistics. However, one has to be careful in the interpretation of the results. The higher event rate during runs of γ calibration leads to a significant fraction of pile-up events with misreconstructed charge and heat signals. Compton scattering in the surface volume add bulk-like surface events to the data set, which additionally need to be rejected. Both effects tend to worsen the estimate of the rejection performance. The first can be counteracted with an additional χ^2 cut on the ionization pulse fits. Herein the same cut as obtained for the ionization calibration is used. The acceptance of the cut has been tailored at the 99.9% acceptance level for individual channels not accounting for non-Gaussianities due to time variations of noise conditions (see sec. 3.4.3). Since the rejection power of this cut is, however, unknown, remaining events after fiducial cut need not be
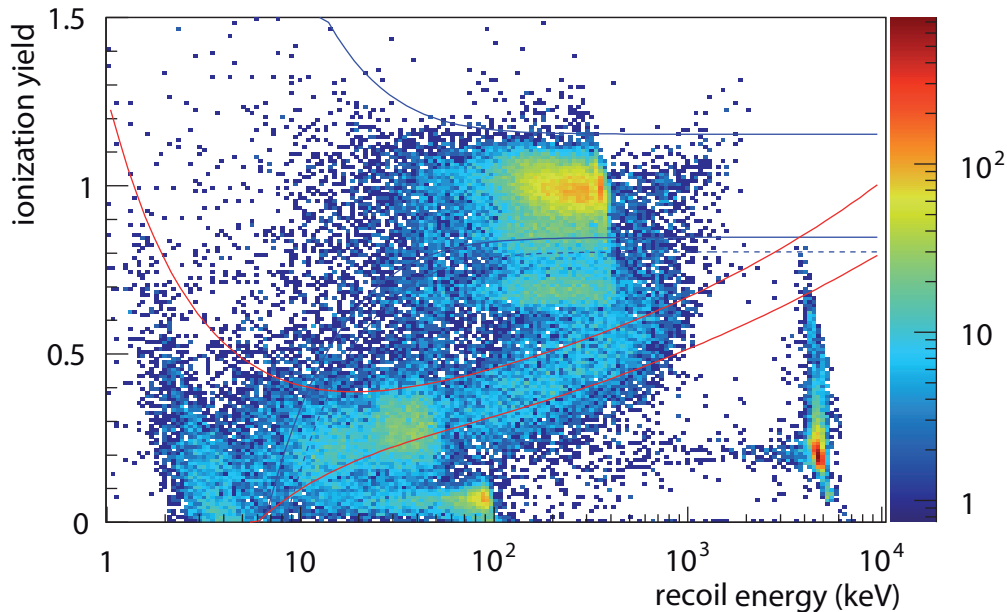
Figure 4.23.: Event distribution in ionization yield versus recoil energy for 11.98 days of γ calibration data of FID 808 at 8 V bias. In addition to the cuts on the surface event calibration data set (fig. 4.19) a χ^2 cut is applied on the goodness of the pulse fit for all ionization channels. This removes pile-up of pulses and hence events with misreconstructed energies.

due to the performance of the fiducial cut. Hence this data set can only be interpreted unambiguously if no misidentified event remains after the application of both goodness of fit and fiducial cut. Furthermore, it needs to be verified that the goodness of fit cut has a constant acceptance in energy and that the ratio of registered α and β particles is similar to the surface event calibration data. For this purpose the γ calibration data of FID808 is plotted in fig. 4.23. In addition to the thresholds of 0.1 keV on ionization, 1 keV on heat, and the heat consistency cut at $abs(\Delta E_{Heat}) < 2\,keV + 5\% \cdot E_{Heat}$, the ionization χ^2 cuts are applied on the 2 kHz ionization signals.

In the resulting plot of the ionization yield versus the recoil energy the same event populations as discussed for the surface event calibration data set (fig. 4.19) become visible. Additionally, a much larger population of γ events up to an energy of 350-400 keV from the ^{133}Ba calibration source can be seen. However, it seems that this distribution extends below the 99.99% electron recoil band (dashed blue) down to a charge yield of 0.7. This might be explained by a population of bulk-like γ interactions in the surface regions. Due to the larger errors on the ionization calibration of the veto channels and the uncorrected cross-talk from veto to collecting electrodes, a bias in the reconstruction of Q and E_{Rec} is expected for surface interactions. Assuming a similar cross-talk from veto to collecting as from collecting to veto electrode, this can easily explain the discrepancy. With respect to the surface event populations no significant energy dependence of the χ^2_{red} cut could be seen. The ratio of ^{210}Pb and ^{210}Bi low energy β's over the Po α's is 1.15 compared to 1.12 for the surface event calibration data. Also the ratio of ^{206}Pb recoils versus Po α is almost constant with a value of 0.74 compared to 0.71 for the surface event calibration data. Thus the energy dependence of the χ^2_{red} cut is constrained to below the 5% level. The large discrepancy in the ratio of high energy β particles to Po α is obviously due to a leaking of the misreconstructed γ event population with a charge yield down to 0.7. The statistics of all populations is summarized in table 4.2.

Additionally, the energy dependence of the χ^2 cut has been investigated over surface event calibration data. Due to the much smaller trigger rate (significantly below 1 Hz even with
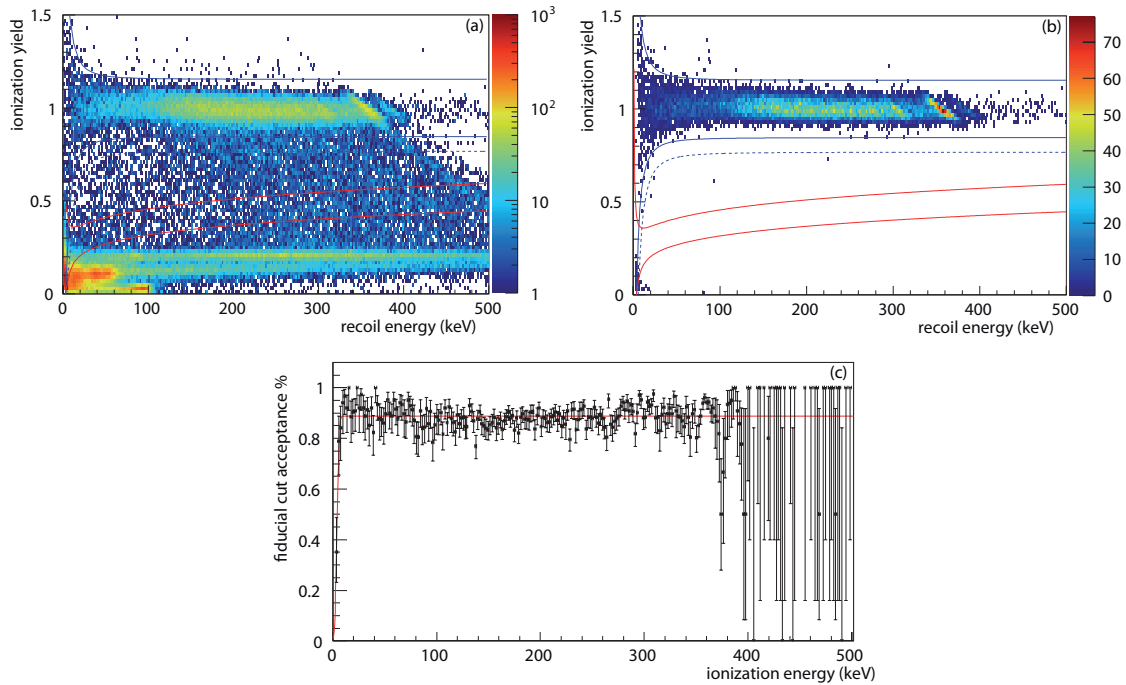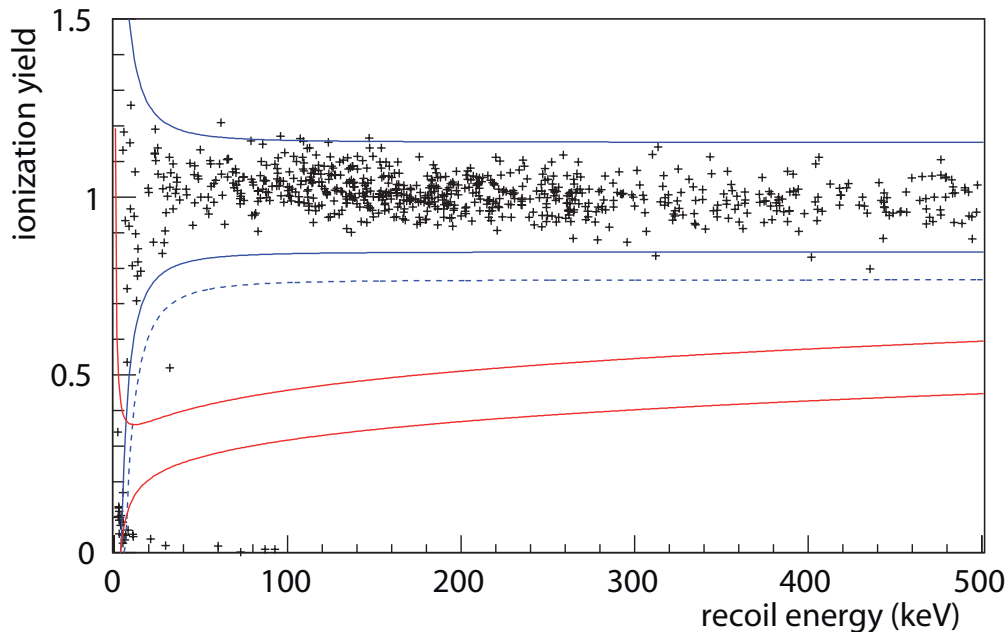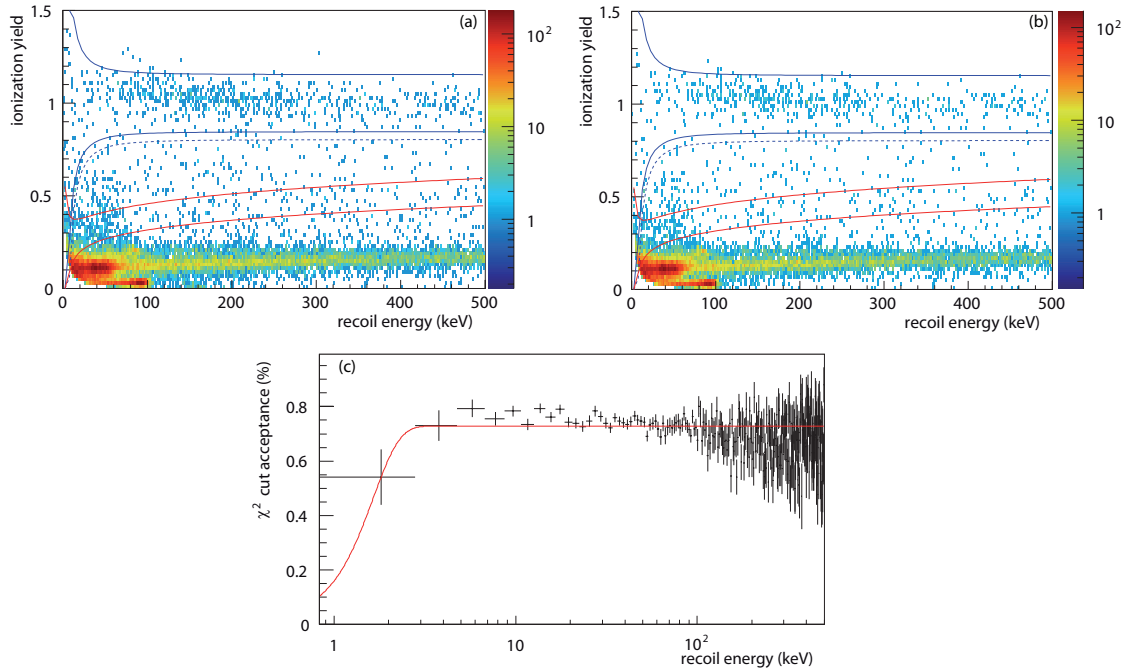
Figure 4.24.: Event distribution in ionization yield versus recoil energy for 5.122 days of surface event calibration data before (a) and after (b) application of the χ^2 cut. The acceptance of the χ^2 cut (c) is evaluated from the number of accepted events per energy bin (b) over (a). Since the WIMP search (surface event) calibration data is taken with a low trigger rate only negligible contamination with pile-up events is expected, the reduced acceptance is thus supposed to be due to variations of noise in time. A fiducial ionization threshold of $E_{\text{Col}} <$ 0.1 keV, a heat threshold of $E_{\text{Heat}} > 1$ keV and a heat consistency cut are applied as basic quality cuts.

the ^{210}Pb source), only a minor contribution of pile-up events is expected in this data. In fig. 4.24 the surface event calibration data is shown before (a) and after the goodness of fit cut (b). The energy dependent survival probability of events is given in (c). The cut is stable with an acceptance at the level of 75%. Only the lowest energy bin shows a discrepancy but with low statistics. Hence the already observed energy stability of the cut between the number of low energy β's or Pb recoils to the Po α's at 5 MeV, can be confirmed for the region of 0 - 500 keV. Remaining energy dependencies are constrained below the 5% level. Above 500 keV, statistics becomes gradually more scarce, but there is no indication for a change at higher energy.

The acceptance of the cut is surprisingly low for a cut which has been designed to be 99.9% for each of the four individual cuts on the different ionization channels. However, the normalization of the χ^2 estimation (sec. 3.4.2) depends quadratically on the exact

Table 4.2.: Event statistics for the gamma calibration data of FID808 at 8 V.

| event population	energy range in keV	ionization yield	# events	ratio /Po α
Po α	[900, 10000]	[0.0, 0.9]	16078	1.00
high energy β	[60, 900]	[0.25, 0.85]	29534	1.83
low energy β	[10, 60]	[0.2, 0.7]	18553	1.15
Pb recoils	[20, 120]	[0.0, 0.2]	11865	0.74
γ evts	[60, 10000]	90% C.L. γ-band	42142	-
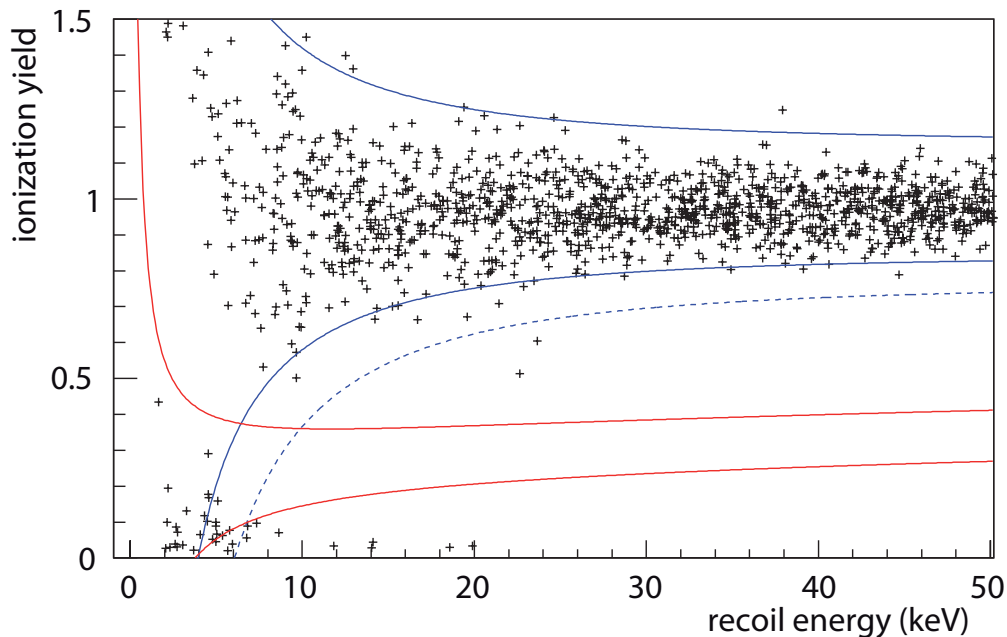
Figure 4.25.: Event distribution in ionization yield versus recoil energy for 11.98 days of γ calibration data of FID 808 at 8 V bias after application of the fiducial cut. In addition to the cuts on the surface event calibration data set (fig. 4.19) a χ^2 cuts is applied on the goodness of the pulse fit for all ionization electrodes. This removes pile-up of pulses and hence events with misreconstructed energies.

knowledge of the current noise in the data sampling. This knowledge on the other side has been extracted from the average of a SAMBA run period that can last up to a day. Thus the discrepancy is interpreted as a combination of the following two factors: a remaining contamination of the initial data sample with pile-up events that should be rejected; and the time dependence of the noise that is not accounted for in enough detail to follow short term drifts at and below the level of one hour.

Given the potential time dependence of the χ^2 cut it's not obvious to transfer the measured acceptance directly to the γ calibration data. But the measured number of 16078 Po α events in 11.98 days of data compared to 17723 in only 5.12 days of data taking can be well explained with a reduction of the live time due to the χ^2 cut and an additional dead time due to pile-up of $25\% \pm 5\%$. This level of pile-up has been observed manually on a short data period, and should be valid for the entire data set.

Since no significant energy dependence has been found in the χ^2 cut, the energy spectra of the α, β and Pb recoils that constitute the surface background in EDELWEISS are assumed to be the same as during WIMP search. Thus, a combined rejection is estimated from both γ calibration and surface event calibration data set. No event has been observed in the signal region of both data sets (fig. 4.25 and 4.21), hence a combined limit of

$$R_{\text{surface (bg}+\gamma)}^{10.5\,\text{keV}} < \frac{2.3}{33801\,\alpha\,\text{evts} \cdot 0.906} = 7 \cdot 10^{-5} \quad (90\%\,\text{C.L.}) \tag{4.13}$$

for a surface background event to be reconstructed as potential WIMP signal can be extracted. The γ discrimination threshold ("magic point") of 10.5 keV was kept as the larger of the two γ discrimination thresholds of the two individual data sets (10.5 keV and 9.9 keV).

4.6. Combined surface event rejection factor of FID detectors

The measured surface event rejection in this thesis improves on previous analyses by testing the rejection for lower energies, i.e. down to a γ discrimination threshold of 10.5 keV. However, one has to note that the fiducial cut used in this work introduces an energy dependent acceptance due to the cut on the timing of the peak position on the collecting ionization channels. This cut applies on the ionization variables and thus influences charge-quenched signal events differently from unquenched electron recoils.

For the WIMP signal, this translates to a very low acceptance of 20% just above the γ discrimination threshold at 12 keV rising to 50% efficiency at 15 keV and full efficiency for $E_{\mathrm{Rec}} \geq 20\,\mathrm{keV}$. It is possible to improve this acceptance by relaxing the timing consistency cut on the ionization channels. Dropping the timing consistency of the 100 kHz sampling ionization channel and only keeping the consistency requirement on the 2 kHz ionization channels, one can improve the acceptance to give full efficiency below $E_{\mathrm{Rec}} = 15\,\mathrm{keV}$. However, an accurate timing is important for the correlation and rejection of muon-induced events, without too much dead time. Additionally, the sampling of the 2 kHz ionization channels has been further reduced to 500 Hz in the current WIMP search data taking. With a muon-veto system event rate of a few Hz and a timing accuracy of a few samples in the reconstruction of the pulse position in the bolometers this is at the limit of what can be accepted for the correlation and rejection of muon-induced events. Otherwise the induced dead time becomes important. In order to be conservative in this first analysis we thus keep the timing consistency cut on the ionization channels sampled with 100 kHz. For the future it is foreseen to improve both the timing and acceptance of the analysis by the use of the combined signal to noise power of the two collecting ionization channels in a simultaneous fit. By restricting the peak position from an initial pulse fit on the 2 kHz ionization channels, the fitting range can be limited for the fit in the 100 kHz ionization channel to further improve the convergence of the pulse fitting.

Part of this procedure has been used in an earlier analysis of the surface event rejection of FID detectors on an independent data set within the PAW based processing chain of the Lyon analysis group. Within this analysis one event was observed among a sample of at least 100000 low energy β surface events with a γ discrimination threshold of 15 keV [232]. Due to the amplitude extraction from a common pulse time, for this analysis an almost full efficiency is expected above 15 keV.

Both analyses use slightly different definitions of cuts. Within the Lyon analysis, in general stricter quality cuts also cutting on the χ^2 of the pulse fit on all individual heat and ionization channels were used. However, the fiducial cut within this work requires additional cuts on the ionization timing. Hence, it introduces an additional energy dependence. To account for that, both measurements are combined with a reduced acceptance of only 50% for the data analyzed in this work.

$$R_{\mathrm{surface}}^{15\,\mathrm{keV}} < \frac{3.9}{(100000 + 33801 \cdot 0.5 \cdot 0.906)\,\alpha\,\mathrm{evts}} = 3.4 \cdot 10^{-5} \quad (90\%\,\mathrm{C.L.}) \qquad (4.14)$$

The combined result thus improves the previous limit, adding 15% of additional statistics.

To better assess the demonstrated performance, the rejection power of the EDELWEISS FID detector can be compared to the SuperCDMS iZIP detector [11]. In their analysis, the SuperCDMS collaboration used a slightly different definition of the rejection, measuring the rejection performance as the performance to reject all kinds of low energy surface events within 8-115 keV recoil energy. Thus to compare the data, a region of the (Q, E_{Rec})-plane was defined to measure the number of rejected events. Within [8,115] keV recoil energy and $Q \in [0.15, 0.75]$, 28828 events were measured for the 17723 Po α events of the surface

event calibration data sample. The entire statistics of the EDELWEISS-III experiment is hence scaled by this ratio and the contribution of ^{210}Pb recoils has been added to the data to yield

$$R_{\text{surface}}^{\text{FID}} < \frac{3.9}{115000 \cdot \frac{28828}{17723} + 115000 \cdot 0.71} = 1.5 \cdot 10^{-5} \quad (90\% \text{ C.L.}) \tag{4.15}$$

In comparison, the SuperCDMS collaboration has analyzed the surface event discrimination with a statistics of $(71525+38178)$ β's and $(16258+7007)$ Pb recoils [11] above a recoil threshold of 8 keV. No misidentified event in the region of interest was observed leading to a rejection of

$$R_{\text{surface}}^{\text{iZIP}} < 1.7 \cdot 10^{-5} \quad \text{at } 90\% \text{C.L.} \tag{4.16}$$

Hence the demonstrated surface event rejection capability of FID detectors is even slightly higher than that of the SuperCDMS iZIP detectors. The misidentification ratio of $R_{\text{surface}}^{\text{iZIP}} < 1.7 \cdot 10^{-5}$ has been shown to be sufficient for the next generation of SuperCDMS at SNO-LAB with an anticipated exposure of 0.3 ton·years. The energy threshold achieved with the SQUID readout on the iZIP detectors is still superior to the EDELWEISS offline threshold achieved in this analysis of the commissioning data set. Still the EDELWEISS FID detector surface discrimination is the best measured surface event discrimination for cryogenic dark matter search experiments and is thus compatible in terms of surface background suppression with the science goals for operation in a combined setup of CRESST, EDELWEISS and SuperCDMS detectors in the SuperCDMS SNOLAB framework.

5. Expected Wimp search sensitivity

In this chapter, the anticipated sensitivity of the EDELWEISS-III experiment is revisited including all results from the commissioning data set analyzed in this thesis. Improved rejection performance and better resolutions as well as the unexpectedly higher γ background are considered to give a more realistic expectation of the experimental sensitivity. For the initial data taking with an exposure of $t_{\text{Exp}} = 3000\,\text{kg·d}$, which is expected to be background-free, the experimental sensitivity is compared using three different scenarios of ionization and heat resolutions and their corresponding γ discrimination thresholds.

For the γ event rate, the expected improvement from the installation of better, electrolytically refined copper shields (see sec. 2.4.1) has not been observed. Instead in this commissioning data set an even worse background rate compared to EDELWEISS-II has been measured (sec. 4.2.2) in the high energy region. The dominant source of this surplus γ background was traced to a gap in the closing of the lead shield after the installation of the new cryogenic supply line for EDELWEISS-III. In the current WIMP data taking this gap could be closed with additional lead, reducing the γ-rate by a factor ~ 2 to roughly the level of EDELWEISS-II. This is still short from the expected improvement. Thus, assuming no improvement at all, but the same event rate of $\Gamma_\gamma = 82\,\text{events/kg/d}$ (20 keV-200 keV), the expected background from gamma events can be quantified to

$$N_\gamma = \Gamma_\gamma \cdot R_\gamma^{15\,\text{keV}} \cdot t_{\text{Exp}} < 1.08 \text{ evts} \quad (90\%\,\text{C.L.}) \tag{5.1}$$

for the initial 3000 kg·d data set for EDELWEISS-III. Since the discrimination power $R_\gamma^{15\,\text{keV}}$ is only limited by calibration statistics, it can be a factor of a few better and has to be validated with higher statistics. Hence, a background free exposure of $\sim 12000\,\text{kg·d}$ could be possible, even with the higher γ-rate Γ_γ.

The surface event misidentification could be probed to a value of $R_{\text{surface}}^{15\,\text{keV}} < 3.4 \cdot 10^{-5}$ within this thesis. In contrast to the γ event rate, the surface event rate is not affected by the problem of not closing the lead castle completely. Hence taking the expected rate of (sec. 2.4.1), $\Gamma_{\text{surface}} = 4\,\text{evts/kg/d}$, the possible remaining background is reduced to $N_{\text{surface}} < 0.4 \text{ evts}$ for the initial 3000 kg·d exposure.

The last remaining background component is the background from neutron scattering. The neutron background can be divided into a muon-induced component and the neutron flux from ambient radioactivity. Neither the efficiency of the muon-veto system nor the neutron flux from the dominant neutron production from muons within the lead castle can be much affected by the gap in the shielding. And, in contrast to the lead castle, the PE shield was
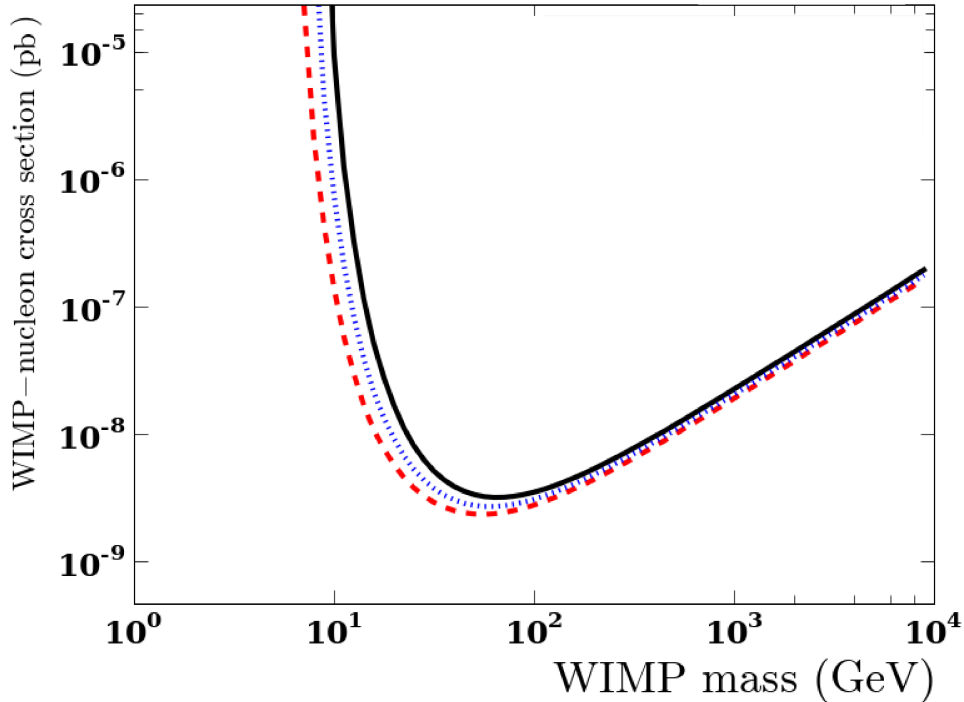
Figure 5.1.: Projections of the EDELWEISS sensitivity on the spin independent WIMP-nucleon scattering cross-section on the Ge nuclei for an exposure of $3000\,\mathrm{kg\cdot d}$, for three different analysis (γ discrimination) thresholds. The cross-section is normalized to nucleons. Projections for $13.1\,\mathrm{keV}$ (solid black), $10\,\mathrm{keV}$ (dotted blue) and $7.5\,\mathrm{keV}$ (dashed red) threshold have been calculated with the micrOMEGAs [91] tool from the DAMNED online tool set [260].

designed with a large overlap of the two movable wagons. Thus, a much higher neutron flux from the laboratory walls and the rock can be excluded. For a better quantitative estimate, detailed simulations including the exact geometry and material budget of EDELWEISS-III are needed. Until the results of this analysis are thoroughly investigated, we rely on the EDELWEISS-II extrapolation of $\Gamma_{amb-n} = (0.8 - 1.9) \cdot 10^{-4}$ events/kg/d (sec. 2.4.1).

5.1. Sensitivity for O(100 GeV/c^2) WIMPs

In spite of individual background limits as high as $N_\gamma < 1.08$ events for the γ background (eq. 5.1) and $N_{\mu-n} < 0.6$ events [159], the sensitivity of the EDELWEISS-III experiment is discussed for the assumption of a background free data taking of $3000\,\mathrm{kg\cdot d}$ of exposure. This is motivated by the fact that especially the largest background limits from muon-induced events and γ events are only upper limits and can easily be a magnitude better. Neither the γ discrimination nor the μ-tagging efficiency and neutron yield from muons in the EDELWEISS-III setup are known precisely enough, but so far no misidentified γ event was observed in the region of interest during calibration and internal PE and higher granularity of the detectors can only lower the background from muon-induced events.

To calculate the projected sensitivity, full efficiency above the 99.99% C.L. gamma discrimination threshold is assumed. The mean ionization and heat resolutions of $707\,\mathrm{eV}$ ionization on $\mathrm{E_{Col}}$ and $984\,\mathrm{eV}$ on heat that were measured in this commissioning run correspond to a γ discrimination threshold of $E_{\mathrm{Rec}} \geq 13.1\,\mathrm{keV}$. The best ionization and heat resolutions of $550\,\mathrm{eV}$ ionization and $490\,\mathrm{eV}$ heat achieved within this thesis yield full γ discrimination above $E_{\mathrm{Rec}} \geq 7.5\,\mathrm{keV}$. Limits on the spin independent WIMP-nucleon scattering cross-section have been calculated with the micrOMEGAs [91] software package.

They are given for the 13.1 keV threshold (solid black) and for the 7.5 keV threshold in dashed red in fig. 5.1. For comparison, the reference EDELWEISS-III projection from 2012 has been added (dashed blue) [261, 262].

While there is only a minor influence on the sensitivity for large WIMP masses, the impact of resolution and threshold is huge for lower mass WIMPs. For WIMPs with $m_\chi = 10 \, \frac{\text{GeV}}{\text{c}^2}$ almost a factor 100 in sensitivity is present between data taking with a 7.5 keV threshold and 13.1 keV threshold. The projected 90% C.L. limits are $1.4 \cdot 10^{-7}$ pb, $7.5 \cdot 10^{-7}$ pb (for the reference projection) and $9.4 \cdot 10^{-6}$ pb.

For the WIMP data taking, it is unrealistic to assume that all detectors achieve the same resolutions and the same γ discrimination threshold. Thus it is unlikely to reach the red sensitivity as long as one does not exploit the data below the 99.99% γ discrimination threshold. On the other hand, the limit calculated from the 13.1 keV threshold corresponds to a worst case scenario. The threshold has been calculated without the selection of low noise periods and without any likely benefits from stable continuous data taking. Hence a realistic sensitivity is expected in between these boundaries.

In order to go beyond this sensitivity for low WIMP masses, background event populations and efficiencies for the various cuts need to be analyzed and modeled carefully to extract maximal information from the lowest energy region. Within the EDELWEISS collaboration two independent analyses are being prepared using Bayesian maximum likelihood methods and multivariate techniques.

5.2. Low mass WIMP analysis with advanced statistical techniques

In order to exploit the data below the gamma discrimination threshold, backgrounds have to be considered more carefully. The characterization of not only acceptance but also discrimination efficiencies for known backgrounds becomes important. The work on the maximum likelihood analysis [263] and on the multivariate analysis using a boosted decision tree (BDT) [233] is not part of this thesis. However, the maximum likelihood analysis already uses data from this processing, and in the BDT analysis several studies on the influence of the ionization resolution on the low mass sensitivity have been performed given the current backgrounds. These studies are hence closely linked and highlight the relevance of this work for the future WIMP search analysis in the EDELWEISS experiment.

Both of these analyses focus on the low WIMP mass region, where the event discrimination becomes more difficult. They do not use the standard plot of ionization yield versus recoil energy which has been discussed vigorously in this thesis. Instead, they rely on the more basic heat and ionization energies or individual energy estimates. The maximum likelihood analysis is defined in the ionization (E_{Col}) versus nuclear recoil energy ($E_{\text{Rec}}^{\text{NR}}$) plane. The uncertainties of events in this plot are thus given by the uncertainties on ionization on the y-axis and the uncertainties from heat propagated accordingly on the x-axis without intermingling the errors via eq. 3.25 for the "true" recoil energy and for the following calculation of the ionization yield. Additional sensitivity can be gained through the modeling of the backgrounds in probability density functions and through removing of the γ discrimination thresholds. The WIMP search data from this commissioning run has been used as a test case for this analysis [263], and the low energy data of detector FID818 has been plotted in fig. 5.2.

It is worth to note that the recoil energy scale is only exact for events that follow the quenched ionization yield of nuclear recoils as parametrized by the Lindhard model. The energy of events with larger ionization yield is overestimated as can be seen by the comparison of the ionization energy and the recoil energy for γ events. On the other hand, the
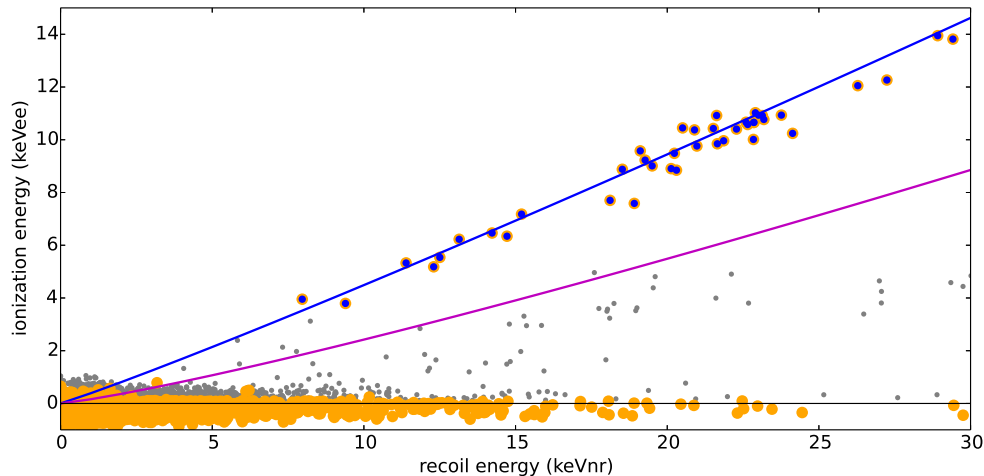
Figure 5.2.: Ionization energy (electron equivalent) versus recoil energy (nuclear recoil) for 5 days of WIMP search data at 8 V bias for detector FID818. All events before cuts in gray, after fiducial cut in yellow, after fiducial and threshold cuts (1 keV on heat and ionization in blue). The position of the γ band and the nuclear recoil band are indicated by their central lines in blue and purple.

recoil energy of events with lower ionization yield than that of nuclear recoils is underestimated. The following event populations can be identified. The events that survive fiducial and threshold cuts shown in blue all follow the blue line indicating the γ band. Before fiducial cut, a set of events with reduced but non zero charge yield becomes apparent (gray dots) that can be associated to interactions in the surface region of the detectors. Finally, a dominant population of events with zero charge yield becomes apparent. This population has a Gaussian distribution of the ionization signal around zero and an exponentially decreasing energy spectrum. At low heat signal they are comprised of noise triggers but especially the higher energy tail is incompatible with this explanation. The origin of these events is not yet understood, but a decrease in time has been observed and several hypotheses like stress induced relaxations are being discussed and different holding structures will be evaluated in the future. This event population is overlapping with the WIMP signal region up to $E_{\mathrm{Rec}} \approx 4\,\mathrm{keV}$-$5\,\mathrm{keV}$ and is thus limiting the sensitivity for low mass WIMPs. With the development of an analysis with a boosted decision tree (see fig. 5.3), this event population was studied more closely. The BDT analysis was trained on several different event populations from the data of this commissioning run to project the set of six initial energy variables onto a single variable with maximal discrimination between signal and background. An example output from a first analysis of 2014 WIMP search data is given in fig. 5.3. In addition to the data (black points), the signal distribution of a simulated WIMP with $m_\chi = 6\,\mathrm{GeV/c^2}$ (gray) has been added for visualization. Individual background event populations are modeled as Pb recoils (brown), surface β's (green), fiducial γ's (cyan) and heat only events (red). It can be clearly seen that the heat-only events are the dominating background population. During the study of this event population it was found that a 15% improvement in the ionization resolution E_{Col} can significantly improve the separation between nuclear recoil events and the heat only events and can lead to up to a factor 10 improvement in sensitivity for WIMP masses below $10\,\mathrm{GeV}$ [233].

Improvements from the software processing as discussed in chapter 3 are of the order of 20% on individual ionization channels and 10% on the sum of ionization, see sec. 4.1.2. A similar 10% improvement on E_{Col} should be achievable in this processing by the tuning of the decorrelation or even simply by the omission of the full decorrelation for the calculation of E_{Col}. With respect to the additional potential of optimization of this processing as dis-
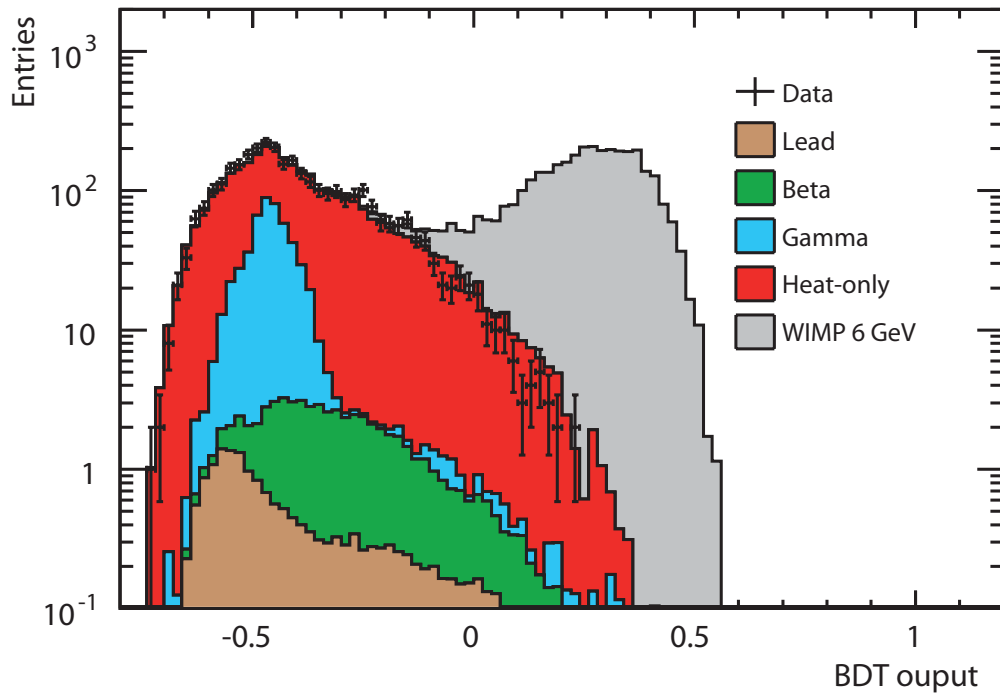
Figure 5.3.: Example output of a multivariate analysis with a boosted decision tree. In this study the boosted decision tree was trained on the data from this commissioning run to project the 6 individual energy variables from the ionization and heat signals onto a single variable (Neural Net Response) with maximal discrimination power between signal and background events. The potential signal of a $6\,\mathrm{GeV/c^2}$ WIMP is shown in gray and individual background components can be distinguished by color. For details see text. Plot from the Saclay multivariate analysis [233].

cussed in chapter 3, also a 15% improvement seems feasible without too much effort. This work can thus culminate in a factor 10 improvement in the sensitivity of the EDELWEISS experiment for low mass WIMPs.

6. Conclusions

Dark matter searches together with neutrino oscillation experiments, the search for neutrinoless double β decay and proton decay are leading the non-accelerator based effort to discover and illuminate the nature of particle physics beyond the standard model. The problem of missing (dark) matter was first noticed in the study of the motion of stars in our galaxy by J. Jeans 1922 [12] and then, with high significance, in the Coma galaxy cluster in 1933 by F. Zwicky [13]. Observational evidence for an additional matter component in form of dark matter has now been found on all scales from galaxies [14] via galaxy clusters [23, 19, 24] to cosmology and the evolution of the Universe [42, 264]. First experiments searching directly for dark matter signals used simple setups with a single ionization Ge detector and passive shielding [1] trying to detect the scattering of dark matter particles off nuclei. Since then, experiments have evolved to more complex setups with active veto detectors, large shielding layers and dual signal readout of massive arrays with tens of kg of target crystals [2, 107] and hundreds of kg of liquid noble gas targets [115, 136]. Up to ton scale experiments are already planned or under construction for both cryogenic and liquid noble gas experiments [209].

In this evolution, it is not only the target mass which scales, but also the complexity and size of the experimental data and often also the number of collaborating groups. This challenges existing data acquisition and processing solutions as well as the distribution of information and data. For the EDELWEISS experiment this was especially pronounced since both muon-veto system and Ge bolometer DAQ and data processing were completely independent and separated between different working groups. Furthermore, the 1st phase of the experiment had been small enough for a single person to implement data backup, processing and analysis without the need for much automatization and online documentation. However, with the current installation of 36 individual detectors with 6 channels each and the active muon-veto system of 46 plastic scintillator modules, this approach reaches its limit. With respect to future ton scale experiments, the group at KIT took over the task to build a sustainable and scalable analysis framework, KData. The completion of this framework and the validation with a first analysis of the EDELWEISS-III background discrimination is an integral part of this thesis. Originally, the work on this framework was started in 2010 when already processed EDELWEISS-II data existed. Thus, we first implemented an event based high level data structure to allow easy data access and to create an environment to facilitate the analysis of muon-induced background and the correlation with other subdetectors like a dedicated radon monitor. Within my Diploma thesis [4], I implemented the event building for this project and used the new KData data structure for

the measurement of the muon-induced background in EDELWEISS-II. Starting this PhD thesis I completed this study to extract an estimate of the muon-induced background for EDELWEISS-III. In addition, based on the results of another Diploma thesis [174] a first measurement of the muon flux from EDELWEISS data was obtained. To finish this task, a detector response model of the muon-veto system system needed to be built and interfaced into an existing detailed Geant4 simulation of the EDELWEISS experiment [5, 6]. The extracted muon flux of

$$\Phi_\mu = 5.4 \pm 0.2(\text{stat})^{+0.5}_{-0.9}(\text{syst.}) \, \mu/\text{m}^2/\text{d} \qquad (6.1)$$

through a horizontal plane was published together with all details of the analysis of the muon-induced background in EDELWEISS-II in [7]. A first projection of the muon-induced background in an exposure of $3000 \, \text{kg·d}$ in EDELWEISS-III was evaluated to yield $N_{\mu-\text{induced}} < 0.6$ events as an upper limit. Potentially large benefits are expected from an additional internal PE shield and the higher granularity of detectors and the subsequent rejection of multiple scatter events.

However, the neutron background from ambient radioactivity as well as from muon-induced events is not the only possible background which has to be evaluated for the EDELWEISS-III data taking. Especially the surface event background is a prime concern for crystal based rare event search detectors. Various effects like recombination of charges in the electrodes, surface defects and the different band structure at the surface can influence the charge yield for surface events and can hence lead to misidentification of surface events as signal events. The study of this background is thus of prime importance for the analysis of EDELWEISS-III data and is the main topic of this thesis. To complete this goal the KData framework had to be improved and validated against a pre-existing processing.

With the modifications of the experiment towards EDELWEISS-III it became apparent that it would be best to start the development of the KData processing and analysis framework anew focusing on the automatization of basic data organization and backup tasks first, and then building the software towards the analysis. The framework was developed on the basis of ROOT and CouchDB, featuring several key design goals like full data encapsulation, data access independent of the framework libraries, high modularity and reusability. A detailed description together with some performance measurements of the CouchDB throughput has been published in [3].

As part of my thesis, several pulse processing algorithms, the high level data analysis tier as well as calibration routines have been coded in this project. Data distribution from the underground lab to the computing centers in Lyon and Karlsruhe as well as the automated backup on HPSS tape drives of 7.5 TB of 1 year of EDELWEISS-III commissioning data have been supervised. The fully implemented processing chain has been validated with an analysis of the data from the last EDELWEISS-III commissioning run from October 2013 to January 2014. The event rate above $E_{\text{Rec}} = 100 \, \text{keV}$ of two randomly selected detectors out of twelve fully working detectors has been compared to an independent pre-existing processing to ensure the consistency of the new processing. No indication of data loss or another problem could be observed. A difference of the event rate of less than 2.5% (sec. 4.2.2) was measured. This difference can well be explained by different acceptances of cuts and accounting for uncertainties in the calculation of the live time. Including a typical uncertainty of less than 3% for the calibration of the detectors, the difference in the event rate completely vanishes.

The performance of the processing was evaluated in terms of a comparison of the energy resolution for noise events, the baseline resolution, of all twelve fully operational detectors of the same commissioning data set. The baseline resolutions determine the discrimination capabilities of the detectors for lowest energy interactions. Better resolutions reduce the

threshold above which a background event identification between γ-, surface-, heat-only-events and the signal of nuclear recoils is possible. These resolutions are hence a measure for the sensitivity to detect WIMPs, especially with low mass.

Within this work, an overall improvement of 22% down to $\sigma_i = 920\,\text{eV}$ was achieved on the individual baseline resolution of the ionization channels. This overall resolution is computed as an average over all datasets, detectors and channels. The improvement has been measured against the independent analysis from the Lyon analysis group of the same commissioning data. Out of these data, only the datasets with relevant operating conditions at 8 V bias were used, adding up to 12 days of γ calibration data and 5 days of background data taking. A significant part of the measured improvement in the baseline resolution is understood as a result of the additional decorrelation procedure of the ionization channels (sec. 3.3.2.2). No further benefit of this procedure was expected on the energy resolution of the total ionization and bulk ionization measured on the collecting electrodes. Nevertheless, the adaptive-time-dependent selection of the optimal bandpass filter parameters still showed an improvement of 9.7% to $\sigma_{\text{ion}} = 1023\,\text{eV}$ for the resolution of the total ionization signal $E_{\text{ion}} = \frac{1}{2} \cdot \Sigma_{i=1}^{4} E_i$. The bulk ionization E_{Col} however showed no improvement at all. This is understood in terms of a noise injection from the veto channels to the collecting ionization channels due to the newly introduced decorrelation procedure. We expect that the improvement of 10% on σ_{ion} will lead to the same improvement in the energy resolution of the bulk ionization with a reprocessing of the data without the decorrelation procedure. Additional potential for improvements, e.g. an adaptive noise detection and a simultaneous fitting of several ionization channels has been discussed (sec. 3.3.4). It is thus expected that continued development on the data processing will be able to boost the EDELWEISS-III sensitivity for low mass WIMPs by up to a factor 10 [233].

In the analysis of this commissioning data set, background discrimination capabilities of FID detectors in the EDELWEISS-III setup were checked for three different event classes:

In a bachelor thesis [252] supervised within this thesis, the available WIMP search data was used to verify the detection of muon-induced events. To achieve this, the analysis routines were updated to the new KData high level data structure and the timing and consistency of the processing were checked. In the analysis, 10 coincidence events were found, 5 multiple and 5 single events. The resulting rate of $\Gamma_{\mu-\text{ind}} = (0.09 \pm 0.03)$ evts/kg·d is slightly lower than the rate measured in EDELWEISS-II: $\Gamma_{\mu-\text{ind}} = (0.15 \pm 0.01)$ [4]. However, considering systematic uncertainties in the calculation of the live time of this analysis, the rates are in statistical agreement and no effect of the additional internal PE shield could be identified. In addition, the derived exact event time of the processing could be checked and was found to be in excellent agreement with previous results. In a second bachelor thesis [251], the integration of the muon-veto system DAQ into the bolometer DAQ was tested. In addition to the verification of muon-tagging with this much simpler method, the new data was used to deduce the dead time of the muon-veto system to $\langle t_P \rangle = (0.143 \pm 0.001)\,\text{ms}$. The validity of this result was checked using a conventional statistical approach.

The second background population that has been investigated consists of bulk γ events. Three out of the twelve fully operational detectors of this commissioning run were carefully calibrated including a logarithmic correction of the heat signal amplitudes and a reiteration over the calibration of background and γ calibration data to account for systematic differences. With a γ discrimination expected from the resolution functions above recoil energies of 11 keV (compared to 15 keV for FID detectors in the EDELWEISS-II setup) of better than 99.99% for each of the three detectors, the discrimination could be probed with 27% lower threshold than before. Taking these data, a discrimination in terms of

remaining signal event candidates R of

$$R_\gamma^{11\,\mathrm{keV}} < 2.0 \cdot 10^{-5} \quad (90\% \,\mathrm{C.L.}) \tag{6.2}$$

WIMP candidates per γ-evt was measured. An additional result from a previous analysis with a larger dataset exists. However, the cuts used in this thesis are not exactly the same as in the previous analysis [250]. Thus, in general one has to be careful in combining these results. Especially, one has to ensure that both analyses feature a similar acceptance after cuts, which should be flat in energy so that no bias is introduced. In this analysis, the dominant influence on the acceptance comes from the fiducial cut with a 50% efficiency at $E_{\mathrm{Col}} = 4.1\,\mathrm{keV}$. Since this is far below the analysis threshold of the previous analysis $E_{\mathrm{Rec}} = 15$ keV, a statistical combination of the datasets seems well justified. The combination of the results improves the previous limit by 22% to a rejection above 15 keV of

$$R_\gamma^{15\,\mathrm{keV}} < 4.4 \cdot 10^{-6} \quad (90\% \,\mathrm{C.L.}). \tag{6.3}$$

The central background component that was studied in this thesis is the background from surface events. Surface events suffer from an ionization quenching similar to nuclear recoils and can thus easily mimic the signal. This background component is also difficult to model due to the intricate details of surface defects, due to different thicknesses of additional dead layers in form of the Al electrodes on the detectors as well as due to possible charge sharing between bulk and surface regions. As an example, an unaccounted incomplete rejection of surface events in the CRESST and CoGeNT experiments together with an over-simplified modeling of this event population has led to an erroneous preference of a DM signal hypothesis in the past [8, 9, 10].

In this thesis, the surface event rejection has been measured experimentally with a ^{210}Pb source implanted on copper tape glued to the detector holders of a single detector. With the improved resolutions in the EDELWEISS-III setup, a remaining rate of misidentified signals of

$$R_{\mathrm{surface}}^{10.5\,\mathrm{keV}} < 1.5 \cdot 10^{-4} \quad (90\% \,\mathrm{C.L.}) \tag{6.4}$$

events per decay from $^{210}\mathrm{Pb} \to \cdots \to^{206}$ Pb could be demonstrated down to a recoil energy of $E_{\mathrm{Rec}} = 10.5\,\mathrm{keV}$. It is only limited by statistics. The analysis does not achieve a full acceptance at the analysis threshold of 10.5 keV. It has an efficiency increase with a width of 1.1 keV which reaches 50% efficiency at $E_{\mathrm{Col}} = 4.1\,\mathrm{keV}$ ionization energy. For charge quenched nuclear recoils, this translates to a 50% efficiency at $E_{\mathrm{Rec}} = 15\,\mathrm{keV}$ recoil energy and full efficiency above $E_{\mathrm{Rec}} = 20\,\mathrm{keV}$. The efficiency loss is dominated by a coincidence requirement on the signal of the collecting electrodes sampled at 100 kHz. This requirement ensures a reliable estimate of the pulse time which in turn is needed for a correlation and detailed study of muon-induced events. However, this requirement can certainly be relaxed for a low mass WIMP analysis with lower exposure, where larger coincidence windows for muon-induced events can be accepted. Additionally, the threshold can be improved by the simultaneous fitting of ionization channels foreseen for the next release of the KData processing.

Accounting for this efficiency loss and conservatively neglecting any efficiency below 15 keV the results from this commissioning data set have been combined with previous measurements in a long term data taking giving

$$R_{\mathrm{surface}}^{15\,\mathrm{keV}} < 3.4 \cdot 10^{-5} \quad (90\%\% \,\mathrm{C.L.}). \tag{6.5}$$

This combined rejection is 12% better, compared to the SCDMS iZIP results validated for a $0.3\,\mathrm{t} \cdot \mathrm{year}$ exposure[1][11]. It is the world's best measured surface event rejection of cryogenic direct dark matter search experiments.

From the rejection capabilities deduced in this work, together with the observed background rates (e.g. a γ rate $\Gamma_\gamma = 82$ events/kg/d higher than originally expected and a surface event rate $\Gamma_{\mathrm{surface}} \approx 4$ events/kg/d), an updated projection of the EDELWEISS-III sensitivity was performed. For the intended exposure of $t_{\mathrm{Exp}} = 3000$ kg·d the expected background components from misidentified γ and surface events as well as from ambient and muon-induced neutrons are (90% C.L.):

$$N_\gamma < \Gamma_\gamma \cdot R_\gamma \cdot t_{\mathrm{Exp}} = 1.08\,\text{events}, \tag{6.6}$$

$$N_{\mathrm{surface}} < \Gamma_{\mathrm{surface}} \cdot R_{\mathrm{surface}} \cdot t_{\mathrm{Exp}} = 0.4\,\text{events}, \tag{6.7}$$

$$N_{\mathrm{amb-n}} < 0.6\,\text{events and} \tag{6.8}$$

$$N_{\mu-\mathrm{n}} < 0.6\,\text{events.} \tag{6.9}$$

However, most limits, especially the largest contribution from γ background, are only upper limits where the MPV is zero. Ongoing measurements and simulations of the discrimination in the complete EDELWEISS-III setting will further improve our understanding of these backgrounds and further constrain the background expectation with higher statistics. Thus, in the projected scenario a background free data taking has been assumed.

Using the measured energy resolutions, earlier EDELWEISS-III projections [262] could be reevaluated and the expected sensitivity of the EDELWEISS-III experiment on the WIMP-nucleon scattering cross-section could be better constrained. It could be demonstrated that the projected 30% improvement on the energy resolution of the ionization channels with respect to EDELWEISS-II was already achieved on some of the 12 detectors in this commissioning run (see fig. 5.1). With such resolutions, a minimal spin independent WIMP-nucleon cross-section of $\sigma = 2.4 \cdot 10^{-9}$ pb can be probed at a WIMP mass of $60\,\mathrm{GeV/c^2}$. With better stability during WIMP data taking, additional improvements on the data processing and including further data quality selections, there is a strong potential to surpass this result, especially for low mass WIMPs.

---

[1]Note that the SCDMS collaboration has a different normalization of the rejection R, and the results need to be scaled accordingly.

Bibliography

[1] Ahlen, S.; Avigone III, F.; Brodzinski, R.; et al. *LIMITS ON COLD DARK MAT-TER CANDIDATES FROM AN ULTRALOW BACKGROUND GERMANIUM SPECTROMETER.* Phys. Lett. B, 195(4):603–608, 1987.

[2] Gascon, J. and Bastidon, N. *The EDELWEISS-III Project and the Rejection Performance of Its Cryogenic Germanium Detectors.* J. Low Temp. Phys., 176(5-6):870–875, February 2014. doi:10.1007/s10909-014-1096-6.

[3] Cox, G.; Armengaud, E.; Augier, C.; et al. *A multi-tiered data structure and process management system based on ROOT and CouchDB.* NIM A, 684:63–72, August 2012. doi:10.1016/j.nima.2012.04.049.

[4] Schmidt, B. *Bestimmung der Rate μ-induzierter Ereignisse bei der Suche nach Dunkler Materie in der EDELWEISS-Messperiode 2009-2010.* Diploma thesis, KIT, Karlsruhe, 2010.

[5] Horn, O.M. *Simulations of the muon-induced neutron background of the EDELWEISS-II experiment for Dark Matter search.* Ph.D. thesis, Karlsruhe TH, 2007.

[6] Kluck, H.M. *Measurement of the cosmic-induced neutron yield at the Modane underground laboratory.* Ph.D. thesis, KIT, 2013.

[7] Schmidt, B.; Armengaud, E.; Augier, C.; et al. *Muon-induced background in the EDELWEISS dark matter search.* Astropart. Phys., 44:28–39, April 2013. doi:10.1016/j.astropartphys.2013.01.014.

[8] Angloher, G.; Bauer, M.; Bavykina, I.; et al. *Results from 730 kg days of the CRESST-II Dark Matter search.* Eur. Phys. J. C, 72(4):1971, April 2012. doi:10.1140/epjc/s10052-012-1971-8.

[9] Aalseth, C.E.; Barbeau, P.S.; Colaresi, J.; et al. *CoGeNT: A search for low-mass dark matter using p-type point contact germanium detectors.* Phys. Rev. D, 88(1):012002, July 2013. doi:10.1103/PhysRevD.88.012002.

[10] Davis, J.H.; McCabe, C.; and Bœhm, C. *Quantifying the evidence for dark matter in CoGeNT data.* J. Cosmol. Astropart. Phys., 08(014):1–26, August 2014. doi:10.1088/1475-7516/2014/08/014.

[11] Agnese, R.; Anderson, A.J.; Asai, M.; et al. *Search for Low-Mass Weakly Interacting Massive Particles Using Voltage-Assisted Calorimetric Ionization Detection in the SuperCDMS Experiment.* Phys. Rev. Lett., 112(4):041302, January 2014. doi:10.1103/PhysRevLett.112.041302.

[12] Jeans, J.H. *The motions of stars in a Kapteyn universe.* MNRAS, 82(122):122–132, 1922.

[13] Zwicky, F. *Die Rotverschiebung von extragalaktischen Nebeln.* Helv. Phys. Acta, 6:110–127, 1933.

[14] Rubin, V.C.; Thonnard, N.; and Ford, W. K., J. *Rotational properties of 21 SC galaxies with a large range of luminosities and radii, from NGC 4605 R = 4kpc to UGC 2885 R = 122 kpc.* Astrophys. J., 238:471, June 1980. doi:10.1086/158003.

[15] White, S.D.M.; Navarro, J.F.; Evrard, A.E.; et al. *The baryon content of galaxy clusters: a challenge to cosmological orthodoxy.* Nature, 366:429–433, 1993. doi: 10.1038/366429a0.

[16] Planck Collaboration. *Planck 2015 results. XIII. Cosmological parameters.* arxiv:1502.01589v1, 2015.

[17] Schneider, P. *Einführung in die Extragalaktische Astronomie und Kosmologie.* Springer Spektrum, korrigiert edition, 2006. ISBN 978-3-540-30589-7.

[18] Briel, U.G.; Henry, J.P.; and Boehringer, H. *Observation of the Coma cluster of galaxies with ROSAT during the all-sky survey.* Astron. Astrophys., 259(2):31–34, 1992.

[19] Clowe, D.; Bradac, M.; Gonzalez, A.H.; et al. *A direct empirical proof of the existence of dark matter.* Astrophys. J. Lett., 648(2, Part 2):109–113, September 2006. doi: 10.1086/508162.

[20] Milgrom, M. *A modification of the Newtionan dynamics as a possible alternative to the hidden mass hypothesis.* Astrophys. J., 270(2):365–370, 1983.

[21] Sanders, R.H. and McGaugh, S.S. *Modified Newtonian Dynamics As an Alternative To Dark Matter.* Ann. Rev. Astron. Astr., 40(1):263–317, September 2002. doi: 10.1146/annurev.astro.40.060401.093923.

[22] Angus, G.W.; Famaey, B.; and Zhao, H.S. *Can MOND take a bullet? Analytical comparisons of three versions of MOND beyond spherical symmetry.* MNRAS, 371(1):138–146, August 2006. doi:10.1111/j.1365-2966.2006.10668.x.

[23] Newman, A.B.; Treu, T.; Ellis, R.S.; et al. *THE DARK MATTER DISTRIBUTION IN A383: EVIDENCE FOR A SHALLOW DENSITY CUSP FROM IMPROVED LENSING, STELLAR KINEMATIC, AND X-RAY DATA.* Astrophys. J., 728(2, L39), February 2011. doi:10.1088/2041-8205/728/2/L39.

[24] Mahdavi, A.; Hoekstra, H.; Babul, A.; et al. *A Dark Core in Abell 520.* Astrophys. J., 668(2):806–814, October 2007. doi:10.1086/521383.

[25] Dawson, W.A.; Wittman, D.; Jee, M.J.; et al. *DISCOVERY OF A DISSOCIATIVE GALAXY CLUSTER MERGER WITH LARGE PHYSICAL SEPARATION.* Astrophys. J. Lett., 747:L42, 2012. doi:10.1088/2041-8205/747/2/L42.

[26] SOFUE, Y. and RUBIN, V. *Rotation Curves of Spiral Galaxies.* Annu. Rev. Astron. Astrophys., 39:137 – 174, 2001. doi:10.1146/annurev.astro.39.1.137.

[27] Corbelli, E. and Salucci, P. *The extended rotation curve and the dark matter halo of M33.* MNRAS, 311(2):441–447, January 2000.

[28] Persic, M.; Salucci, P.; and Stel, F. *The universal rotation curve of spiral galaxies: I. The dark matter connection.* MNRAS, 281(1):27–47, July 1996.

[29] Navarro, J.F.; Frenk, C.S.; and White, S.D.M. *The structure of cold dark matter halos.* Astrophys. J., 462(2, Part 1):563–575, 1996.

[30] Einasto, J. *No Title.* Tartu Astron. Obs. Teated, 17(1).

[31] Merritt, D.; Graham, A.W.; Moore, B.; et al. *Empirical models for Dark Matter Halos. I. Nonparametric Construction of Density Profiles and Comparison with Parametric Models.* Astron. J., 132:2685–2700, 2006. doi:10.1086/508988.

[32] Hezaveh, Y.; Dalal, N.; Holder, G.; et al. *Measuring the power spectrum of dark matter substructure using strong gravitational lensing.* arXiv:1403.2720, 2014.

[33] Sofue, Y. *Grand Rotation Curve and Dark-Matter Halo in the Milky Way Galaxy.* Publ. Astron. Soc. Japan, 64:75–75, 2012. doi:10.1093/pasj/64.4.75.

[34] Bienaymé, O.; Famaey, B.; Siebert, A.; et al. *Weighing the local dark matter with RAVE red clump stars.* Astron. Astrophys., 571(A92):1–13, 2014. doi:10.1051/0004-6361/201424478.

[35] Famaey, B. *Dark matter in the Milky Way.* arXiv:1501.01788, 2015.

[36] Tisserand, P.; Guillou, L.L.; Afonso, C.; et al. *Limits on the Macho Content of the Galactic Halo from the EROS-2 Survey of the Magellanic Clouds.* Astron. Astrophys., 469:387–404, 2007. doi:10.1051/0004-6361:20066017.

[37] Olive, K. *Review of Particle Physics.* Chinese Phys. C, 38(9):090001, August 2014. doi:10.1088/1674-1137/38/9/090001.

[38] Penzias, A.A. and WILSON, R.W. *A measurement of excess antenna temperature at 4080Mc/s.* Astrophys. J., 142:419–421, 1965.

[39] Alpher, R.A.; Bethe, H.; and Gamow, G. *The origin of chemical elements.* Phys. Rev., 73(7):803–804, 1948.

[40] Smoot, G.F.; Bennett, C.L.; Kogut, A.; et al. *Structure in the COBE differential microwave radiometer 1st-year maps.* Astrophys. J., 396(1, Part 2):L1–L5, September 1992.

[41] Komatsu, E.; Smith, K.M.; Dunkley, J.; et al. *SEVEN-YEAR WILKINSON MICROWAVE ANISOTROPY PROBE (WMAP) OBSERVATIONS: COSMOLOGICAL INTERPRETATION.* Astrophys. J. Suppl. Ser., 192(2):18, February 2011. doi:10.1088/0067-0049/192/2/18.

[42] Ade, P.A.R.; Aghanim, N.; Alves, M.I.R.; et al. *Planck 2013 results. I. Overview of products and scientific results.* Astron. Astrophys., 571:A1, October 2014. doi:10.1051/0004-6361/201321529.

[43] Springel, V.; White, S.D.M.; Jenkins, A.; et al. *Simulations of the formation, evolution and clustering of galaxies and quasars.* Nature, 435(7042):629–636, June 2005. doi:10.1038/nature03597.

[44] Klypin, A.A.; Kravtsov, A.V.; Valenzuela, O.; et al. *Where are the missing galactic satellites?* Astrophys. J., 522(1):82–92, 1999. doi:10.1086/307643.

[45] Boylan-Kolchin, M.; Bullock, J.S.; and Kaplinghat, M. *Too big to fail? The puzzling darkness of massive Milky Way subhaloes.* MNRAS Let., 415:L40–L44, 2011. doi:10.1111/j.1745-3933.2011.01074.x.

[46] Bode, P.; Ostriker, J.P.; and Turok, N. *Halo Formation in Warm Dark Matter Models.* Astrophys. J., 556:93–107, 2000. doi:10.1086/321541.

[47] Sawala, T.; Frenk, C.S.; Crain, R.A.; et al. *The abundance of (not just) dark matter haloes.* MNRAS, 431:1366–1382, April 2013. doi:10.1093/mnras/stt259.

[48] Klypin, A.a.; Trujillo-Gomez, S.; and Primack, J. *Dark Matter Halos in the Standard Cosmological Model: Results From the Bolshoi Simulation.* Astrophys. J., 740:102, 2011. doi:10.1088/0004-637X/740/2/102.

[49] Springel, V.; Wang, J.; Vogelsberger, M.; et al. *The Aquarius Project: The subhaloes of galactic haloes.* MNRAS, 391:1685–1711, 2008. doi:10.1111/j.1365-2966.2008. 14066.x.

[50] Viel, M.; Becker, G.D.; Bolton, J.S.; et al. *Warm dark matter as a solution to the small scale crisis: New constraints from high redshift Lyman-α? forest data.* Phys. Rev. D, 88:043502, 2013. doi:10.1103/PhysRevD.88.043502.

[51] Weber, M. and de Boer, W. *Determination of the Local Dark Matter Density in our Galaxy.* Astron. Astrophys., 509(A25):10, 2009. doi:10.1051/0004-6361/200913381.

[52] Chatrchyan, S.; Khachatryan, V.; Sirunyan, A.M.; et al. *Observation of a new boson at a mass of 125 GeV with the CMS experiment at the LHC.* Phys. Lett. B, 716(1):30–61, 2012. doi:10.1016/j.physletb.2012.08.021.

[53] Aad, G.; Abajyan, T.; Abbott, B.; et al. *Observation of a new particle in the search for the Standard Model Higgs boson with the ATLAS detector at the LHC.* Phys. Lett. B, 716(1):1–29, September 2012. doi:10.1016/j.physletb.2012.08.020.

[54] Bergström, L. *Dark matter evidence, particle physics candidates and detection methods.* Ann. Phys., 524:479–496, 2012. doi:10.1002/andp.201200116.

[55] Gardner, S. and Fuller, G.M. *Dark matter studies entrain nuclear physics.* Prog. Part. Nucl. Phys., 71:167–184, 2013. doi:10.1016/j.ppnp.2013.03.001.

[56] Feng, J.L. *Dark Matter Candidates from Particle Physics and Methods of Detection.* Annu. Rev. Astron. Astrophys., 48:494–545, 2010. doi:10.1146/ annurev-astro-082708-101659.

[57] Bertone, G. *Particle dark matter: observations, models and searches.* Cambridge University Press, March 2010. ISBN 0521763681.

[58] Bertone, G.; Hooper, D.; and Silk, J. *Particle dark matter: evidence, candidates and constraints.* Phys. Rep., 405(5-6):279–390, 2005. doi:DOI:10.1016/j.physrep.2004. 08.031.

[59] Peccei, R.D. and Quinn, H.R. *CP conservation in the presence of pseudoparticles.* Phys. Rev. Lett., 38(25):1440–1443, 1977. doi:10.1103/PhysRevLett.38.1440.

[60] Peccei, R.D. and Quinn, H.R. *Constraints imposed by CP conservation in the presence of pseudoparticles.* Phys. Rev. D, 16(1791), 1977. doi:10.1103/PhysRevD.16. 1791.

[61] Ringwald, A. *Exploring the role of axions and other WISPs in the dark universe.* Phys. Dark Universe, 1(1-2):116–135, 2012. doi:10.1016/j.dark.2012.10.008.

[62] Asztalos, S.J.; Rosenberg, L.J.; van Bibber, K.; et al. *Searches for Astrophysical and Cosmological Axions*.* Annu. Rev. Nucl. Part. Sci., 56:293–326, 2006. doi: 10.1146/annurev.nucl.56.080805.140513.

[63] Abe, K.; Hieda, K.; Hiraide, K.; et al. *Search for solar axions in XMASS, a large liquid-xenon detector.* Phys. Lett. B, 724(1-3):46–50, July 2013. doi: 10.1016/j.physletb.2013.05.060.

[64] Armengaud, E.; Arnaud, Q.; Augier, C.; et al. *Axion searches with the EDELWEISS-II experiment.* J. Cosmol. Astropart. Phys., 2013(11):067–067, November 2013. doi: 10.1088/1475-7516/2013/11/067.

[65] Aad, G.; Abbott, B.; Abdallah, J.; et al. *Measurement of the Higgs boson mass from the Hâ$\gamma\gamma$ and HâZZ*â4â channels in pp collisions at center-of-mass energies of 7 and 8 TeV with the ATLAS detector.* Phys. Rev. D, 90:052004, 2014. doi: 10.1103/PhysRevD.90.052004.

[66] Zumino, B. *Supersymmetry Then and Now.* Fortschritte der Phys., 54(2-3):199–204, March 2006. doi:10.1002/prop.200510268.

[67] Wess, J. and Zumino, B. *Supergauge transformation in 4 dimensions.* Nucl. Phys. B, 70(1):39–50, 1974.

[68] Shifman, M. *Reflections and Impressionistic Portrait at the Conference Frontiers Beyond the Standard Model, FTPI, Oct. 2012.* arxiv:1211.0004v1, pages 1–12, 2012.

[69] Hajdukovic, D.S. *The signatures of new physics, astrophysics and cosmology?* Mod. Phys. Lett. A, 28(1350124):1–6, 2013. doi:10.1142/S0217732313501241.

[70] Arkani-Hamed, N.; Gupta, A.; Kaplan, D.E.; et al. *Simply Unnatural Supersymmetry.* arxiv:1212.6971, pages 1–30, 2012.

[71] Ellis, J. *Theory Summary and Prospects.* Proc. Second Annu. LHCP, KCL-PH-TH/2014-35, pages 1–14, 2014.

[72] Chatrchyan, S.; Khachatryan, V.; Sirunyan, a.M.; et al. *Search for dark matter and large extra dimensions in monojet events in pp collisions at $\sqrt{s} = 7$ TeV.* J. High Energy Phys., 09:094, 2012. doi:10.1007/JHEP09(2012)094.

[73] Buchmueller, O.; Cavanaugh, R.; Roeck, a.D.; et al. *The CMSSM and NUHM1 after LHC Run 1.* Eur. Phys. J. C, 74:2922, 2014. doi:10.1140/epjc/s10052-014-2922-3.

[74] Arbey, A.; Battaglia, M.; and Mahmoudi, F. *Combining monojet , supersymmetry , and dark matter searches.* Phys. Rev. D, 89(077701):1–5, 2014. doi:10.1103/PhysRevD.89.077701.

[75] Beskidt, C.; de Boer, W.; and Kazakov, D.I. *The impact of a 126 GeV Higgs on the neutralino mass.* Phys. Lett. B, 738:505–511, 2014. doi:10.1016/j.physletb.2014.08.011.

[76] Malik, S.A.; McCabe, C.; Araujo, H.; et al. *Interplay and Characterization of Dark Matter Searches at Colliders and in Direct Detection.* arXiv:1409.4075, 2014.

[77] Porter, T.A.; Johnson, R.P.; and Graham, P.W. *Dark Matter Searches with Astroparticle Data.* Annu. Rev. Astron. Astrophys., 49:155–194, 2011. doi:10.1146/annurev-astro-081710-102528.

[78] Adriani, O.; Barbarino, G.C.; Bazilevskaya, G.A.; et al. *The PAMELA Mission: Heralding a new era in precision cosmic ray physics.* Phys. Rep., 544:323–370, 2014. doi:10.1016/j.physrep.2014.06.003.

[79] Lopez, A.; Savage, C.; Spolyar, D.; et al. *Fermi/LAT observations of Dwarf Galaxies highly constrain a Dark Matter Interpretation of Excess Positrons seen in AMS-02, HEAT, and PAMELA.* arXiv:1501.01618, December 2015.

[80] Aguilar, M.; Alberti, G.; Alpat, B.; et al. *First result from the alpha magnetic spectrometer on the international space station: Precision measurement of the positron fraction in primary cosmic rays of 0.5-350 GeV.* Phys. Rev. Lett., 110:141102, April 2013. doi:10.1103/PhysRevLett.110.141102.

[81] Calore, F.; Cholis, I.; Mccabe, C.; et al. *A Tale of Tails: Dark Matter Interpretations of the Fermi GeV Excess in Light of Background Model Systematics.* arxiv:1411.4647v1, pages 1–18, 2014.

[82] Ackermann, M.; Albert, A.; Anderson, B.; et al. *Dark matter constraints from observations of 25 Milky Way satellite galaxies with the Fermi Large Area Telescope.* Phys. Rev. D, 89:042001, 2014. doi:10.1103/PhysRevD.89.042001.

[83] Ackermann, M.; Ajello, M.; Albert, A.; et al. *Search for gamma-ray spectral lines with the Fermi Large Area Telescope and dark matter implications.* Phys. Rev. D, 88:082002, 2013. doi:10.1103/PhysRevD.88.082002.

[84] Abramowski, A.; Aharonian, F.; Benkhali, F.A.; et al. *Search for dark matter annihilation signatures in H.E.S.S. observations of dwarf spheroidal galaxies.* Phys. Rev. D, 90(112012), 2014.

[85] Aartsen, M.G.; Abbasi, R.; Abdou, Y.; et al. *IceCube search for dark matter annihilation in nearby galaxies and galaxy clusters.* Phys. Rev. D, 88:122001, 2013. doi:10.1103/PhysRevD.88.122001.

[86] Albuquerque, I.F.M.; Heros, C.P.D.L.; and Robertson, D.S. *Constraints on Self Interacting Dark Matter from IceCube Results.* J. Cosmol. Astropart. Phys., 02:047, 2013. doi:10.1088/1475-7516/2014/02/047.

[87] Lewin, J. *Review of mathematics, numerical factors, and corrections for dark matter experiments based on elastic nuclear recoil.* Astropart. Phys., 6(1):87–112, December 1996.

[88] Savage, C.; Freese, K.; and Gondolo, P. *Annual Modulation of Dark Matter in the Presence of Streams.* Phys. Rev. D, 74(4):27, July 2006. doi:10.1103/PhysRevD.74.043531.

[89] Kurylov, A. and Kamionkowski, M. *Generalized analysis of the direct weakly interacting massive particle searches.* Phys. Rev. D, 69:063503, 2004. doi:10.1103/PhysRevD.69.063503.

[90] Green, A.M. *Dependence of direct detection signals on the WIMP velocity distribution.* J. Cosmol. Astropart. Phys., 10(034):1–24, 2010. doi:10.1088/1475-7516/2010/10/034.

[91] Belanger, G.; Boudjema, F.; Pukhov, A.; et al. *microOMEGAs : a tool for dark matter studies.* arxiv:1005.4133, pages 1–10, May 2010. doi:10.1393/ncc/i2010-10591-3.

[92] Jungman, G.; Kamionkowski, M.; and Griest, K. *Supersymmetric dark matter.* Phys. Rep. - Rev. Sect. Phys. Lett., 267(5-6):195–373, 1996.

[93] Armengaud, E.; Augier, C.; Benoît, A.; et al. *Search for low-mass WIMPs with EDELWEISS-II heat-and-ionization detectors.* Phys. Rev. D, 86(5):1–6, September 2012. doi:10.1103/PhysRevD.86.051701.

[94] Armengaud, E.; Augier, C.; Benoît, A.; et al. *Final results of the EDELWEISS-II WIMP search using a 4-kg array of cryogenic germanium detectors with interleaved electrodes.* Phys. Lett. B, 702(5):329–335, August 2011. doi:10.1016/j.physletb.2011.07.034.

[95] Strege, C.; Bertone, G.; Besjes, G.J.; et al. *Profile likelihood maps of a 15-dimensional MSSM.* J. High Energy Phys., 09(081):1–57, 2014. doi:10.1007/JHEP09(2014)081.

[96] Billard, J.; Figueroa-Feliciano, E.; and Strigari, L. *Implication of neutrino backgrounds on the reach of next generation dark matter direct detection experiments.* Phys. Rev. D, 89(023524):1–15, 2014. doi:10.1103/PhysRevD.89.023524.

[97] Drukier, a.; Freese, K.; Spergel, D.; et al. *New Dark Matter Detectors using DNA for Nanometer Tracking.* arXiv:1206.6809v2, pages 1–18, 2015.

[98] Cooley, J. *Overview of non-liquid noble direct detection dark matter experiments.* Phys. Dark Universe, 4:92–97, September 2014. doi:10.1016/j.dark.2014.10.005.

[99] Bernabei, R. *Dark Matter Particles in the Galactic Halo.* arxiv:1412.6524, pages 1–13, December 2014.

[100] Amaré, J.; Cebrián, S.; Cuesta, C.; et al. *ANAIS: Status and prospects.* arxiv:1501.00104v1, pages 1–5, December 2014.

[101] Cherwinka, J.; Grant, D.; Halzen, F.; et al. *First data from DM-Ice17.* Phys. Rev. D, 90(9):092005, November 2014. doi:10.1103/PhysRevD.90.092005.

[102] Kim, S.C.; Bhang, H.; Choi, J.H.; et al. *New Limits on Interactions between Weakly Interacting Massive Particles and Nucleons Obtained with CsI(Tl) Crystal Detectors.* Phys. Rev. Lett., 108(18):181301, April 2012. doi:10.1103/PhysRevLett.108.181301.

[103] Abe, K.; Hieda, K.; Hiraide, K.; et al. *XMASS detector.* NIM A, 716:78–85, July 2013. doi:10.1016/j.nima.2013.03.059.

[104] Peeters, S.J.M. *DEAP-3600 http://indico.cern.ch/event/278032/session/12/contribution/140/material/slides/0.pdf, Talk at the TeVPA/IDM conference 2014*, 2014.

[105] Monroe, J. *Recent Progress from the MiniCLEAN Dark Matter Experiment.* J. Phys. Conf. Ser., 375(1):012012, July 2012. doi:10.1088/1742-6596/375/1/012012.

[106] Ahmed, Z.; Akerib, D.; Armengaud, E.; et al. *Combined limits on WIMPs from the CDMS and EDELWEISS experiments.* Phys. Rev. D, 84(1):1–5, July 2011. doi:10.1103/PhysRevD.84.011102.

[107] Agnese, R.; Anderson, A.; Asai, M.; et al. *Search for Low-Mass Weakly Interacting Massive Particles with SuperCDMS.* Phys. Rev. Lett., 112(24):241302, June 2014. doi:10.1103/PhysRevLett.112.241302.

[108] Agnese, R.; Ahmed, Z.; Anderson, A.J.; et al. *Silicon detector results from the first five-tower run of CDMS II.* Phys. Rev. D, 88:031104, 2013. doi:10.1103/PhysRevD.88.031104.

[109] Agnese, R.; Ahmed, Z.; Anderson, A.; et al. *Silicon Detector Dark Matter Results from the Final Exposure of CDMS II.* Phys. Rev. Lett., 111(25):251301, December 2013. doi:10.1103/PhysRevLett.111.251301.

[110] Angloher, G.; Bento, A.; Bucci, C.; et al. *Results on low mass WIMPs using an upgraded CRESST-II detector.* Eur. Phys. J. C, 74(12):3184, December 2014. doi:10.1140/epjc/s10052-014-3184-9.

[111] Aprile, E.; Alfonsi, M.; Arisaka, K.; et al. *Dark Matter Results from 225 Live Days of XENON100 Data.* Phys. Rev. Lett., 109(18):181301, November 2012. doi:10.1103/PhysRevLett.109.181301.

[112] Angle, J.; Aprile, E.; Arneodo, F.; et al. *Search for Light Dark Matter in XENON10 Data.* Phys. Rev. Lett., 107(5):051301, July 2011. doi:10.1103/PhysRevLett.107.051301.

[113] Angle, J. *Erratum: Search for Light Dark Matter in XENON10 Data [Phys. Rev. Lett. 107, 051301 (2011)].* Phys. Rev. Lett., 110(24):249901, June 2013. doi:10.1103/PhysRevLett.110.249901.

[114] Akimov, D.; Araújo, H.; Barnes, E.; et al. *WIMP-nucleon cross-section results from the second science run of ZEPLIN-III.* Phys. Lett. B, 709(1-2):14–20, March 2012. doi:10.1016/j.physletb.2012.01.064.

[115] Akerib, D.; Araújo, H.; Bai, X.; et al. *First Results from the LUX Dark Matter Experiment at the Sanford Underground Research Facility.* Phys. Rev. Lett., 112(9):091303, March 2014. doi:10.1103/PhysRevLett.112.091303.

[116] Agnes, P.; Alexander, T.; Alton, A.; et al. *First Results from the DarkSide-50 Dark Matter Experiment at Laboratori Nazionali del Gran Sasso.* arxiv:1410.0653, pages 1–14, October 2014.

[117] Badertscher, A.; Bay, F.; Bourgeois, N.; et al. *ArDM: first results from underground commissioning.* J. Instrum., 8(09):C09005, September 2013. doi:10.1088/1748-0221/8/09/C09005.

[118] Baudis, L. *DARWIN dark matter WIMP search with noble liquids.* J. Phys. Conf. Ser., 375(1):012028, July 2012. doi:10.1088/1742-6596/375/1/012028.

[119] Newstead, J.L.; Jacques, T.D.; Krauss, L.M.; et al. *Scientific reach of multiton-scale dark matter direct detection experiments.* Phys. Rev. D, 88(7):076011, October 2013. doi:10.1103/PhysRevD.88.076011.

[120] Baudis, L.; Ferella, A.; Kish, A.; et al. *Neutrino physics with multi-ton scale liquid xenon detectors.* J. Cosmol. Astropart. Phys., 01:044, January 2014. doi:10.1088/1475-7516/2014/01/044.

[121] Archambault, S.; Behnke, E.; Bhattacharjee, P.; et al. *Constraints on low-mass WIMP interactions on ^{19}F from PICASSO.* Phys. Lett. B, 711(2):153–161, May 2012. doi:10.1016/j.physletb.2012.03.078.

[122] Amole, C.; Ardid, M.; Asner, D.M.; et al. *Dark Matter Search Results from the PICO-2L C_3F_8 Bubble Chamber.* arxiv:1503.00008, pages 1–6, 2015.

[123] Behnke, E.; Behnke, J.; Brice, S.J.; et al. *Erratum: First dark matter search results from a 4-kg CF3I bubble chamber operated in a deep underground site [Phys. Rev. D 86, 052001 (2012)].* Phys. Rev. D, 90(7):079902, October 2014. doi:10.1103/PhysRevD.90.079902.

[124] Felizardo, M.; Girard, T.; Morlat, T.; et al. *The SIMPLE Phase II dark matter search.* Phys. Rev. D, 89(7):072013, April 2014. doi:10.1103/PhysRevD.89.072013.

[125] Cao, X.; Chen, X.; Chen, Y.; et al. *PandaX: a liquid xenon dark matter experiment at CJPL.* Sci. China Physics, Mech. Astron., 57(8):1476–1494, June 2014. doi:10.1007/s11433-014-5521-2.

[126] Xiao, M.; Xiao, X.; Zhao, L.; et al. *First dark matter search results from the PandaX-I experiment.* Sci. China Physics, Mech. Astron., 57(11):2024–2030, September 2014. doi:10.1007/s11433-014-5598-7.

[127] Barbeau, P.S.; Collar, J.I.; and Tench, O. *Large-Mass Ultra-Low Noise Germanium Detectors: Performance and Applications in Neutrino and Astroparticle Physics.* J. Cosmol. Astropart. Phys., 09:009, 2007. doi:10.1088/1475-7516/2007/09/009.

[128] Li, H.B.; Liao, H.Y.; Lin, S.T.; et al. *Limits on Spin-Independent Couplings of WIMP Dark Matter with a p-Type Point-Contact Germanium Detector.* Phys. Rev. Lett., 110(26):261301, June 2013. doi:10.1103/PhysRevLett.110.261301.

[129] Yue, Q.; Zhao, W.; Kang, K.J.; et al. *Limits on light weakly interacting massive particles from the CDEX-1 experiment with a p-type point-contact germanium detector at the China Jinping Underground Laboratory.* Phys. Rev. D, 90(9):091701, November 2014. doi:10.1103/PhysRevD.90.091701.

[130] Henning, R. *MALBEK http://indico.cern.ch/event/278032/session/12/contribution/161 (Talk TeVPA/IDM conference Amsterdam)*, 2014.

[131] Aalseth, C.E.; Barbeau, P.S.; Colaresi, J.; et al. *Search for An Annual Modulation in Three Years of CoGeNT Dark Matter Detector Data.* arXiv:1401.3259, pages 1–8, January 2014.

[132] Li, H.; Singh, L.; Singh, M.; et al. *Differentiation of bulk and surface events in p-type point-contact germanium detectors for light WIMP searches.* Astropart. Phys., 56:1–8, April 2014. doi:10.1016/j.astropartphys.2014.02.005.

[133] Kang, K.J.; Cheng, J.P.; Li, J.; et al. *Introduction to the CDEX experiment.* Front. Phys., 8(4):412–437, August 2013. doi:10.1007/s11467-013-0349-1.

[134] Aguilar-Arevalo, A.A.; Bertou, X.; Butner, M.J.; et al. *DAMIC: a novel dark matter experiment.* arxiv:1310.6688v1, pages 1–4, October 2013.

[135] Kelso, C.; Hooper, D.; and Buckley, M.R. *Toward a consistent picture for CRESST, CoGeNT, and DAMA.* Phys. Rev. D, 85(4):043515, February 2012. doi:10.1103/PhysRevD.85.043515.

[136] Aprile, E.; Arisaka, K.; Arneodo, F.; et al. *The XENON100 dark matter experiment.* Astropart. Phys., 35(9):573–590, April 2012. doi:10.1016/j.astropartphys.2012.01.003.

[137] J. C. Spooner, N. *Direct Dark Matter Searches.* J. Phys. Soc. Japan, 76(11):111016, November 2007. doi:10.1143/JPSJ.76.111016.

[138] Lindhard, J.; Scharff, M.; and Schioett, H. *Range concepts and heavy ion ranges (Notes on atomic collisions, II).* Kgl. Danske Vidensk. Selsk. Mat. Fys. Medd., 33(14):1–42, 1963.

[139] Lindhard, J. *APPROXIMATION METHOD IN CLASSICAL SCATTERING BY SCREENED COULOMB FIELDS.* Kgl. Dan. Vidensk. Selsk., Mat.-Fys. Medd., 36(10):1–32, 1968.

[140] Benoit, A.; Bergé, L.; Blümer, J.; et al. *Measurement of the response of heat-and-ionization germanium detectors to nuclear recoils.* NIM A, 577(3):558–568, July 2007. doi:10.1016/j.nima.2007.04.118.

[141] Armengaud, E.; Augier, C.; Benoîr, A.; et al. *Technical design and performances of the EDELWEISS-II experiment.* (Internal Collab. report), 2012.

[142] Neganov, B. and Trofimov, V. *No Title.* USSR Pat. No 1037771 (1981), Otkrytia i Izobret., 146:215, 1985.

[143] Luke, P.N. *Voltage-assisted calorimetric ionization detector.* J. Appl. Phys., 64(12):6858, 1988. doi:10.1063/1.341976.

[144] Chapellier, M.P.; Chardin, G.; Miramonti, L.; et al. *Physical interpretation of the Neganov-Luke and related effects.* Phys. B Condens. Matter, 284-288:2135–2136, July 2000. doi:10.1016/S0921-4526(99)03053-7.

[145] Alig, R.; Bloom, S.; and Struck, C. *Scattering by ionization and phonon emission in semiconductors.* Phys. Rev. B, 22(12):5565–5582, December 1980. doi:10.1103/PhysRevB.22.5565.

[146] Fano, U. *On the Theory of Ionization Yield of Radiations in Different Substances.* Phys. Rev., 70(1-2):44–52, July 1946. doi:10.1103/PhysRev.70.44.

[147] Fano, U. *Ionization Yield of Radiations. II. The Fluctuations of the Number of Ions.* Phys. Rev., 72(1):26–29, July 1947. doi:10.1103/PhysRev.72.26.

[148] Moszyński, M. and Duchêne, G. *Ballistic deficit correction methods for large Ge detectors.* NIM A, 308:557–567, 1991.

[149] T Yamaya; Asano, R.; H Endo; et al. *MEASUREMENT OF THE FANO FACTOR FOR PROTONS ON SILICON.* NIM A, 159(1):181–187, 1979.

[150] Benoit, A. *Improved exclusion limits from the EDELWEISS WIMP search.* Phys. Lett. B, 545(1-2):43–49, October 2002. doi:10.1016/S0370-2693(02)02238-4.

[151] Sanglard, V.; Benoit, A.; Berge, L.; et al. *Final results of the EDELWEISS-I dark matter search with cryogenic heat-and-ionization Ge detectors.* Phys. Rev. D, 71:122002, 2005.

[152] Shutt, T.; Emes, J.; Haller, E.; et al. *A solution to the dead-layer problem in ionization and phonon-based dark matter detectors.* NIM A, 444(1-2):340–344, April 2000. doi:10.1016/S0168-9002(99)01379-0.

[153] Marnieros, S.; Berge, L.; Broniatowski, a.; et al. *Surface Event Rejection of the EDELWEISS Cryogenic Germanium Detectors Based on NbSi Thin Film Sensors.* J. Low Temp. Phys., 151(3-4):835–840, January 2008. doi:10.1007/s10909-008-9753-2.

[154] Defay, X.; Broniatowski, A.; Juillard, A.; et al. *Cryogenic Ge Detectors for Dark Matter Search: Surface Event Rejection with Ionization Signals.* J. Low Temp. Phys., 151(3-4):896–901, January 2008. doi:10.1007/s10909-008-9762-1.

[155] Brink, P.; Cabrera, B.; Castle, J.; et al. *First test runs of a dark-matter detector with interleaved ionization electrodes and phonon sensors for surface-event rejection.* NIM A, 559(2):414–416, April 2006. doi:10.1016/j.nima.2005.12.026.

[156] Agnese, R.; Anderson, a.J.; Balakishiyeva, D.; et al. *Demonstration of surface electron rejection with interleaved germanium detectors for dark matter searches.* Appl. Phys. Lett., 103(16):1–5, May 2013. doi:10.1063/1.4826093.

[157] Broniatowski, A. *Intervalley Scattering of Hot Electrons in Germanium at Millikelvin Temperatures.* J. Low Temp. Phys., 176(5-6):860–869, January 2014. doi:10.1007/s10909-014-1091-y.

[158] Marnieros, S.; Bergé, L.; Broniatowski, A.; et al. *Controlling the Leakage-Current of Low Temperature Germanium Detectors Using XeF_2 Dry Etching.* J. Low Temp. Phys., 176(3-4):182–187, December 2013. doi:10.1007/s10909-013-0997-0.

[159] Schmidt, B. *The EDELWEISS DM search: Recent results and outlook for 2013.* Cimento, Il Nuovo, 36(06):86–94, 2013. doi:10.1393/ncc/i2014-11620-y.

[160] Bastidon, N. *Etude du rejet β des détecteurs FID de l'expérience EDELWEISS II.* Master thesis, 2013.

[161] Armengaud, E.; Augier, C.; Benoît, A.; et al. *Background studies for the EDELWEISS dark matter experiment.* Astropart. Phys., 47:1–9, July 2013. doi:10.1016/j.astropartphys.2013.05.004.

[162] Mei, D.M. and Hime, A. *Muon-Induced Background Study for Underground Laboratories*, 2006.

[163] Fiorucci, S.; Benoit, A.; Berge, L.; et al. *Identification of backgrounds in the EDELWEISS-I dark matter search experiment.* Astrophys. J., 28(1):143–153, September 2007. doi:10.1016/j.astropartphys.2007.05.003.

[164] Chazal, V.; Brissot, R.; Cavaignac, J.; et al. *Neutron background measurements in the Underground Laboratory of Modane.* Astropart. Phys., 9(2):163–172, August 1998. doi:10.1016/S0927-6505(98)00012-7.

[165] L'Hour, M. *Un site sous-marin sur la côte de l'Armorique. L'épave antique de Ploumanac'h.* Rev. archéologique l'ouest, 4(1):113–131, 1987. doi:10.3406/rao.1987. 908.

[166] Benoit, A.; Berge, L.; Broniatowski, A.; et al. *Calibration of the EDELWEISS Cryogenic Heat-and-ionisation Germanium Detectors for Dark Matter Search*. NIM A, 530(3):426–439, 2003.

[167] Yellin, S. *Finding an upper limit in the presence of an unknown background*. Phys. Rev. D, 66(3):1–7, August 2002.

[168] Ahmed, Z.; Akerib, D.S.; Arrenberg, S.; et al. *Dark Matter Search Results from the CDMS II Experiment*. Science, 327(5973):1619–1621, 2010. doi:10.1126/science.1186112.

[169] Aprile, E.; Arisaka, K.; Arneodo, F.; et al. *Dark Matter Results from 100 Live Days of XENON100 Data*. Phys. Rev. Lett., 107(13):1–6, September 2011. doi:10.1103/PhysRevLett.107.131302.

[170] Bernabei, R.; Belli, P.; Cappella, F.; et al. *Results from DAMA/LIBRA at Gran Sasso*. Found. Phys., 40(7):900–916, October 2009. doi:10.1007/s10701-009-9368-8.

[171] Aalseth, C.E.; Barbeau, P.S.; Colaresi, J.; et al. *Search for an Annual Modulation in a p-Type Point Contact Germanium Dark Matter Detector*. Phys. Rev. Lett., 107(14):141301, September 2011. doi:10.1103/PhysRevLett.107.141301.

[172] Buchmueller, O.; Cavanaugh, R.; Colling, D.; et al. *Supersymmetry and dark matter in light of LHC 2010 and XENON100 data*. Eur. Phys. J. C, 71(8):1722, August 2011. doi:10.1140/epjc/s10052-011-1722-2.

[173] Bertone, G.; Cerdeño, D.G.; Fornasa, M.; et al. *Global fits of the cMSSM including the first LHC and XENON100 data*. J. Cosmol. Astropart. Phys., 01:015, January 2012. doi:10.1088/1475-7516/2012/01/015.

[174] Nieder, H. *Bestimmung des Flusses kosmischer Myonen durch das EDELWEISS-II Experiment*. Diploma thesis, KIT, 2010.

[175] Agostinelli, S.; Allison, J.; Amako, K.; et al. *Geant4 - a simulation toolkit*. NIM A, 506(3):250–303, July 2003. doi:10.1016/S0168-9002(03)01368-8.

[176] Battistoni, G.; Cerutti, F.; Fassò, A.; et al. *The FLUKA code: description and benchmarking*. AIP Conf. Proc., 896(1):31–49, 2007. doi:10.1063/1.2720455.

[177] Araujo, H.; Kudryavtsev, V.; Spooner, N.; et al. *Muon-induced neutron production and detection with GEANT4 and FLUKA*. NIM A, 545(1-2):398–411, June 2005. doi:10.1016/j.nima.2005.02.004.

[178] Araujo, H.; Blockley, J.; Bungau, C.; et al. *Measurements of neutrons produced by high-energy muons at the Boulby Underground Laboratory*. Astropart. Phys., 29(6):471–481, July 2008. doi:10.1016/j.astropartphys.2008.05.004.

[179] Kudryavtsev, V.A.; Pandola, L.; and Tomasello, V. *Neutron- and muon-induced background in underground physics experiments*. Eur. Phys. J. A, 36(2):171–180, April 2008. doi:10.1140/epja/i2007-10539-6.

[180] Lindote, A.; Araújo, H.; Kudryavtsev, V.; et al. *Simulation of neutrons produced by high-energy muons underground*. Astropart. Phys., 31(5):366–375, June 2009. doi:10.1016/j.astropartphys.2009.03.008.

[181] Malgin, a.S. and Ryazhskaya, O.G. *Neutrons from muons underground*. Phys. At. Nucl., 71(10):1769–1781, May 2009. doi:10.1134/S1063778808100116.

[182] Kéfélian, C. *Measurement of the μ-veto system response with an AmBe source (private communication)*, 2014.

[183] Habermehl, F. *Entwicklung der Datenaufnahme und Tests der Vetomodule für das EDELWEISS II μ-Vetozählersystem.* Diploma thesis, Universität Karlsruhe (TH), August 2004.

[184] Reichenbacher, J. *Untersuchung der optischen Eigenschaften grossflächigen Plastikszintillatoren für den KARMEN-Upgrade.* Scientific report fzka6202, FZK, Karlsruhe, 1998.

[185] Allison, J.; Amako, K.; and Apostolakis, J. *Geant4 developments and applications.* IEEE Trans. Nucl. Sci., 53(1):270–278, 2006.

[186] Simard, L. and NEMO-3 SuperNEMO Collaboration. *The NEMO-3 experiment and the SuperNEMO project.* Progr. Part. Nucl. Phys., 64(2):270–272, April 2010. doi:10.1016/j.ppnp.2009.12.026.

[187] Gaisser, T.K. *Cosmic rays and particle physics.* Cambridge University Press, 1990. ISBN 9780521339315.

[188] Wei, Y. *The neutrino induced muon flux at the Fréjus underground experiment.* Ph.D. thesis, Universität Wuppertal, 1993.

[189] Berger, C.; Fröhlich, M.; Mönch, H.; et al. *Experimental study of muon bundles observed in the Frejus detector.* Phys. Rev. D, 40(7):2163, 1989.

[190] *Google Earth Pro.* https://support.google.com/earth/answer/176160?hl=de, 2015.

[191] ICRU. *Report 85 - Fundamental Quantities And Units For Ionizing Radiation (revised).* J. ICRU, 11(1), April 2011. doi:10.1093/jicru/ndr012.

[192] Armengaud, E. *Searching for WIMPs with EDELWEISS.* J. Phys. Conf. Ser., 375(1):012004, July 2012. doi:10.1088/1742-6596/375/1/012004.

[193] *http://www.aurubis.com/de/aurubis-kupfer-kupferrecycling-kupferlegierungen-uw/*, 2015.

[194] Laubenstein, M.; Hult, M.; Gasparro, J.; et al. *Underground measurements of radioactivity.* Appl. Radiat. Isot., 61(2-3):167–72, 2004. doi:10.1016/j.apradiso.2004. 03.039.

[195] Zhang, X. *Laminated cabling - A status report (Talk at the EDELWEISS collaboration meeting, Oxford).* 2014.

[196] *http://www.axon-cable.com/en/00_home/00_start/00/index.aspx*, 2015.

[197] Broniatowski, A.; Defay, X.; Armengaud, E.; et al. *A new high-background-rejection dark matter Ge cryogenic detector.* Phys. Lett. B, 681(4):305–309, November 2009. doi:10.1016/j.physletb.2009.10.036.

[198] Broniatowski, A.; Piro, M.C.; Marnieros, S.; et al. *H^- -Like Centers and Space-Charge Effects in Cryogenic Germanium Detectors for Dark Matter Search.* J. Low Temp. Phys., 176(5-6):802–807, January 2014. doi:10.1007/s10909-013-1060-x.

[199] Gascon, J. *Surface event rejection in EDELWEISS-III (private communication)*, 2014.

[200] Censier, B.; Benoit, A.; Bres, G.; et al. *EDELWEISS Read-out Electronics and Future Prospects.* J. Low Temp. Phys., 167(5-6):645–651, February 2012. doi:10. 1007/s10909-012-0568-9.

[201] Brun, R. and Rademakers, F. *ROOT - An object oriented data analysis framework.* NIM A, 389(1-2):81–86, April 1997. doi:10.1016/S0168-9002(97)00048-X.

[202] Antcheva, I.; Ballintijn, M.; Bellenot, B.; et al. *ROOT - A C++ framework for petabyte data storage, statistical analysis and visualization.* Comput. Phys. Commun., 180(12):2499–2512, December 2009. doi:10.1016/j.cpc.2009.08.005.

[203] *IEEE Standard for Ethernet, IEEE Std 802.3-2012 (Revision to IEEE Std 802.3-2008).* doi:10.1109/IEEESTD.2012.6419735.

[204] Kopmann, A.; Bergmann, T.; Gemmeke, H.; et al. *FPGA-based DAQ system for multi-channel detectors.* 2008 IEEE Nucl. Sci. Symp. Conf. Rec., pages 3186–3190, October 2008. doi:10.1109/NSSMIC.2008.4775027.

[205] Gemmeke, H.; Kleifges, M.; Kopmann, A.; et al. *First measurements with the auger fluorescence detector data acquisition system.* ICRC, pages 769–772, 2001.

[206] Steinbrink, N.; Hannen, V.; Martin, E.L.; et al. *Neutrino mass sensitivity by MAC-E-Filter based time-of-flight spectroscopy with the example of KATRIN.* New J. Phys., 15:113020, 2013. doi:10.1088/1367-2630/15/11/113020.

[207] Gemmeke, H. and Ruiter, N. *3D ultrasound computer tomography for medical imaging.* NIM A, 580(2):1057–1065, October 2007. doi:10.1016/j.nima.2007.06.116.

[208] Hopp, T.; Sroba, L.; Zapf, M.; et al. *Breast Imaging with 3D Ultrasound Computer Tomography: Results of a First In-vivo Study in Comparison to MRI Images.* volume 8539 of *Lecture Notes in Computer Science*, pages 72–79. Springer International Publishing, Cham, 2014. ISBN 978-3-319-07886-1. doi:10.1007/978-3-319-07887-8.

[209] Angloher, G.; Armengaud, E.; Augier, C.; et al. *EURECA Conceptual Design Report.* Phys. Dark Universe, 3:41–74, April 2014. doi:10.1016/j.dark.2014.03.004.

[210] Parks, T.W. and Burrus, C.S. *Digital Filter Design.* John Wiley and Sons, 1987. ISBN 978-0471828969.

[211] Cox, A.; Schmidt, B.; Scorza, S.; et al. *KData homepage https://edwdev-ik.fzk.de/SVN_Repository_for_the_KIT_Dark_Matter_Group/KData.html*, 2015.

[212] *Apache Subversion https://subversion.apache.org/*, 2015.

[213] Pilato, M. *Version Control With Subversion.* O'Reilly & Associates, Inc., 2004. ISBN 0596004486.

[214] *The Apache software foundation, Apache CouchDB project http://couchdb.apache.org/i*, 2015.

[215] Chesneau, B. *Couchdbkit http://couchdbkit.org/*, 2015.

[216] Chilingaryan, S.; Beglarian, A.; Kopmann, A.; et al. *Advanced data extraction infrastructure: Web based system for management of time series data.* J. Phys. Conf. Ser., 219(4):042034, April 2010. doi:10.1088/1742-6596/219/4/042034.

[217] Marino, M.G. *Dark Matter Physics with P-type Point-contact Germanium Detectors: Extending the Physics Reach of the Majorana Experiment.* Ph.D. thesis, University of Wahington, 2010.

[218] Bonicalzi, R.; Collar, J.; Colaresi, J.; et al. *The C-4 dark matter experiment.* NIM A, 712:27–33, June 2013. doi:10.1016/j.nima.2013.02.012.

[219] Hehn, L. *Suche nach einer jahreszeitlichen Modulation der EDELWEISS-2 Ereignisrate als Signal Dunkler Materie.* Diploma thesis, 2012.

[220] Barabash, A.S.; Chernyak, D.M.; Danevich, F.a.; et al. *Enriched $Zn^{100}MoO_4$ scintillating bolometers to search for $0\nu2\beta$ decay of ^{100}Mo with the LUMINEU experiment.* Eur. Phys. J. C, 74:3133, May 2014. doi:10.1140/epjc/s10052-014-3133-7.

[221] Bird, I.; Robertson, L.; and Shiers, J. *Deploying the LHC Computing Grid - The LCG Service Challenges.* 2005 IEEE Int. Symp. Mass Storage Syst. Technol., pages 160–165, 2005. doi:10.1109/LGDI.2005.1612486.

[222] Watson, R. and Coyne, R. *The parallel I/O architecture of the high-performance storage system (HPSS).* Proc. IEEE 14th Symp. Mass Storage Syst., pages 27–44, 1995. doi:10.1109/MASS.1995.528214.

[223] Jordanov, V.T. and Knoll, G.F. *Digital synthesis of pulse shapes in real time for high resolution radiation spectroscopy.* NIM A, 345:337–345, 1994. doi:10.1016/0168-9002(94)91011-1.

[224] Unrau, M. *Kalibration eines EDELWEISS Ge-Bolometers mit unterschiedlichen Filtermethoden zur Extraktion von Signalpulsen.* Ph.D. thesis, KIT, 2012.

[225] Luo, J. *Analysis of EDELWEISS raw data with the wavelet transformation method.* Bachelor thesis, KIT, 2013.

[226] Attisha, M.J. *CDMS-II - Application of Neural Networks and Wavelets to Event Analysis.* Ph.D. thesis, Brown University, 2006.

[227] Butterworth, S. *On the Theory of Filter Amplifiers.* Wirel. Eng., 7:536–541, 1930.

[228] Jones, E.; Oliphant, T.; Peterson, P.; et al. *SciPy: Open Source Scientific Tools for Python, 2001 (http://www.scipy.org/)*, 2015.

[229] Millman, K.J. and Aivazis, M. *Python for Scientists and Engineers.* Comput. Sci. Eng., 13(2):9–12, March 2011. doi:10.1109/MCSE.2011.36.

[230] Wiener, N. *Extrapolation, interpolation, and smoothing of stationary time series with engineering applications.* Cambridge, Technology Press of MIT, 1949. ISBN 978-0262730051.

[231] Golwala, S. *Exclusion Limits on the Wimp-Nucleon Elastic-Scattering Cross Section from the Cryogenic Dark Matter Search.* Ph.D. thesis, University of California at Berkeley, 2000.

[232] Bonhomme, A. *Data analysis of EDELWEISS raw data recorded with FID800 detectors (summer project).* Technical report, KIT, 2014.

[233] Bossière, T. *Heat only events and MVA (Talk, EDELWEISS collaboration meeting Oxford)*, 2014.

[234] Siebenborn, B. *The EDELWEISS-III Dark Matter search (In press).* In *26th Rnecontres Blois "Particle Physiscs Cosmol.* 2014.

[235] Shockley, W. *Currents to Conductors Induced by a Moving Point Charge.* J. Appl. Phys., 9(10):635, 1938. doi:10.1063/1.1710367.

[236] Ramo, S. *Currents Induced by Electron Motion.* Proc. I.R.E., 27(9):584–585, 1939. doi:10.1109/JRPROC.1939.228757.

[237] Arnaud, Q. *Signals Induced by Charge Carrier Trapping.* J. Low Temp. Phys., 176(5-6):924–929, February 2014. doi:10.1007/s10909-014-1106-8.

[238] Little, M.A. and Jones, N.S. *Generalized methods and solvers for noise removal from piecewise constant signals. II. New methods.* Proc. Math. Phys. Eng. Sci., 467(2135):3115–3140, November 2011. doi:10.1098/rspa.2010.0674.

[239] Rudin, L.I.; Osher, S.; and Fatemi, E. *Nonlinear total variation based noise removal algorithms.* Phys. D Nonlinear Phenom., 60(1-4):259–268, November 1992. doi:10.1016/0167-2789(92)90242-F.

[240] Kalafut, B. and Visscher, K. *An objective, model-independent method for detection of non-uniform steps in noisy signals.* Comput. Phys. Commun., 179(10):716–723, November 2008. doi:10.1016/j.cpc.2008.06.008.

[241] Heath, R.L. *Gamma-ray Spectrum Catalogue, Ge (Li) Spectrometry.* USAEC Rep. ANC-1000, 1974.

[242] Hubbell, J.H. and Seltzer, S.M. *Tables of X-ray mass attenuation coefficients and mass energy-absorption coefficients 1 keV to 20 MeV for elements Z=1 to 92 and 48 additional substances of dosimetric interest.* NISTIR-5632, 1995.

[243] Broniatowski, A. *Carrier Anisotropy and Impurity Scattering in Ge at mK Temperatures: Modeling and Comparison to Experiment.* J. Low Temp. Phys., 167(5-6):1069–1074, February 2012. doi:10.1007/s10909-012-0543-5.

[244] Angloher, G.; Bauer, M.; Bavykina, I.; et al. *Commissioning run of the CRESST-II dark matter search.* Astropart. Phys., 31(4):270–276, 2009.

[245] Gascon, J. *Ana - EDELWEISS data analysis and processing solution (private communication).*

[246] Hehn, L. and Armengaud, E. *Hourly baseline resolutions of EDELWEISS II cryogenic Run 12 (private communication).*

[247] Scorza, S. *EDELWEISS-II , direct Dark Matter search experiment: first data analysis and results.* Ph.D. thesis, Université Claude Bernard Lyon I, 2009.

[248] Scorza, S. *Analysis of the γ event rate in Run308 (private communication)*, 2014.

[249] Alessandretti, L. *Gamma background measurement for FID detectors within the EDELWEISS-II experiment.* Master thesis, Université Claude Bernard Lyon I, 2012.

[250] Juillard, A. *Status and prospects of the EDELWEISS direct WIMP search experiment.* J. Low Temp. Phys., 167:1056–1062, January 2012. doi:10.1007/s10909-012-0512-z.

[251] Schipperges, V. *Vermessung der Auslesetotzeit des EDELWEISS-3 Myon-Veto-Systems.* Bachelor thesis, KIT, 2013.

[252] Schreiner, M. and Götz, M. *Identification of muon-induced events in EDELWEISS-III FID800 Ge detectors (In preparation).* Bachelor thesis, KIT.

[253] Kluck, H. *Aufbau und Test eines Prototyp-Neutronendetektors für das EDLEIWESS Experiment.* Diplomarbeit, Universität Karlsruhe (TH), 2007.

[254] Robertson, R.G.H. *Snow Technical Report, SNO-STR-91-071, Electrorefining of Copper.* Technical report, 1991.

[255] Bruemmer, M.; Cooley, J.; Cox, A.; et al. *Community material assay database, http://www.radiopurity.org/*, 2014.

[256] *https://apparentdip.wordpress.com/2007/01/23/u-thhe-thermochronology/*, 2014.

[257] *National Nuclear Data Center, information extracted from the Chart of Nuclides database, http://www.nndc.bnl.gov/chart/*, 2014.

[258] ICRU. *Stopping Powers for Electrons and Positrons, ICRU Report 37.* Technical report, 1984.

[259] ICRU. *Stopping Powers and Ranges for Protons and Alpha Particles, ICRU Report 49.* Technical report, 1993.

[260] *http://pisrv0.pit.physik.uni-tuebingen.de/darkmatter/index1.html (DAMNED Dark Matter Network Exclusion Diagram online tool)*, 2014.

[261] Kozlov, V Y for the EDELWEISS, c. *Recent status of the Dark Matter search with Edelweiss.* arxiv:1305.2808v1, pages 1–4, 2013.

[262] Eitel, K. *https://kicp-workshops.uchicago.edu/IDM2012/program.php - The EDEL-WEISS dark matter search (Talk)*, 2012.

[263] Hehn, L. *The EDELWEISS-III Dark Matter Search: Status and Perspectives (Hamburg, Germany) (In press).* In *Proceedings PANIC 2014* . 2014.

[264] Ade, P.A.R.; Aghanim, N.; Armitage-Caplan, C.; et al. *Planck 2013 results. XVI. Cosmological parameters.* Astron. Astrophys., 571:A16, October 2014. doi:10.1051/0004-6361/201321591.

Appendix

A. Individual muon-veto system calibration results

In the two following tables all individual calibration coefficients as derived from the Landau fit results from MC-simulation and data are given (see sec 2.3.1 for details). The first table documents the results derived for the 2009-2010 data period of EDELWEISS-II. The 2nd one documents the result of the same calibration and fitting method applied on 2010-2011 data after a readjustment of the HV settings. As can be seen the calibration factor decreases as expected from the increase of the HV, which stretches the ADU scales. For three of the modules (9,17,25) no simulation results existed. It was refrained from rerunning the entire MC simulation for computing reasons and instead an average calibration factor was used for these modules. Also for a single module in the 2010-2011 data the Landau fit did not converge and the average calibration factor was used instead. The module numbering used in the table corresponds to the same numbering as in fig. A.1. Note that the calibration can be obtained either from the MPV or the sigma of the Landau fit or from a combination of both. In this work however, we chose to use the MPV of the Landau fit, since it has a better fit accuracy and less variation than the estimated sigma.
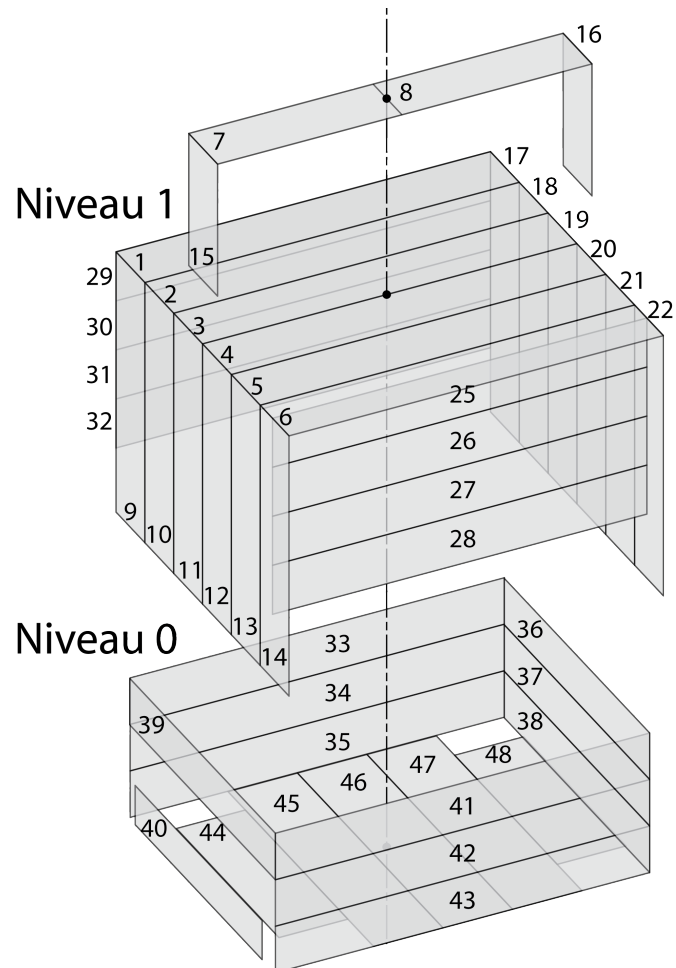
Figure A.1.: Scheme of the EDELWEISS-III muon-veto system . Modules 7,8,15 and 16 were added after the EDELWEISS-II measurement period in 2009-2011 and have not been considered in this analysis.

module	calibration (keV/ADU)	pedestal (ADU)	MPV data (ADU)	MPV error (ADU)	sigma (ADU)	sigma error (ADU)	MPV MC (MeV)	MPV error (MeV)	sigma (MeV)	sigma error (MeV)
1	6.16	177	1819	85	202	25	10.115	0.017	0.810	0.009
2	5.02	110	2101	53	240	24	9.992	0.015	0.749	0.008
3	3.83	91	2709	59	474	37	10.037	0.014	0.761	0.007
4	5.07	122	2089	56	363	28	9.982	0.014	0.739	0.007
5	4.51	106	2316	40	318	24	9.958	0.015	0.755	0.008
6	4.42	86	2358	50	353	30	10.034	0.017	0.796	0.010
9	5.39	84	2610	271	749	124	0.000	0.000	0.000	0.000
10	5.86	130	2956	134	652	68	16.563	0.119	4.048	0.098
11	6.74	109	2559	238	673	78	16.501	0.113	3.823	0.090
12	6.15	147	2807	103	561	72	16.372	0.113	3.778	0.087
13	6.14	212	2894	91	543	49	16.463	0.117	3.795	0.092
14	5.53	166	3171	166	723	103	16.604	0.129	4.087	0.104
17	5.39	129	3272	137	614	80	0.000	0.000	0.000	0.000
18	5.31	143	3570	195	788	132	18.201	0.114	3.950	0.088
19	6.12	192	3146	103	580	59	18.087	0.123	3.724	0.088
20	5.97	195	3230	142	623	88	18.106	0.122	3.823	0.091
21	5.93	150	3184	103	640	65	17.982	0.135	3.959	0.104
22	6.07	120	2629	343	781	110	18.055	0.128	3.866	0.096
25	5.39	194	3921	157	792	149	0.000	0.000	0.000	0.000
26	5.32	164	3639	274	811	200	18.485	0.156	4.458	0.132
27	5.56	174	3510	111	558	80	18.560	0.162	3.768	0.120
28	4.96	179	3909	157	760	135	18.511	0.213	4.948	0.201
29	5.05	150	4175	239	1148	164	20.341	0.240	5.527	0.218
30	7.23	156	2661	541	753	147	21.454	0.273	4.434	0.180
31	4.62	131	4494	470	1340	458	20.141	0.230	3.916	0.158
32	5.10	158	3804	257	1076	242	18.581	0.166	3.864	0.118
33	6.70	116	2857	169	684	122	18.377	0.206	4.758	0.197
34	3.90	156	4675	256	747	236	17.625	0.179	3.434	0.131
35	3.90	146	5273	1919	2204	1893	20.005	0.231	4.524	0.182
36	4.51	153	3703	108	696	102	15.995	0.077	3.030	0.058
37	5.29	127	2919	112	582	53	14.780	0.105	2.814	0.068
38	4.62	123	3098	155	704	108	13.744	0.273	3.617	0.104
39	5.03	120	3421	109	714	64	16.616	0.076	3.177	0.058
40	6.17	138	2908	268	722	115	17.085	0.118	3.699	0.094
41	5.77	114	3319	147	699	105	18.505	0.166	3.950	0.129
42	6.10	133	3263	151	687	107	19.083	0.204	3.433	0.127
43	5.25	132	3876	263	903	246	19.666	0.217	3.701	0.147
44	3.90	147	2682	80	306	51	9.894	0.023	0.691	0.013
45	6.45	132	1641	66	299	38	9.731	0.016	0.658	0.010
46	5.19	97	1962	90	361	39	9.674	0.017	0.622	0.009
47	4.10	124	2501	47	328	27	9.747	0.018	0.687	0.011
48	4.25	123	2435	54	292	31	9.820	0.025	0.670	0.013

module	calibration (keV/ADU)	pedestal (ADU)	MPV data (ADU)	MPV error (ADU)	sigma (ADU)	sigma error (ADU)	MPV MC (MeV)	MPV error (MeV)	sigma (MeV)	sigma error (MeV)
1	4.30	177	2534	37	217	14	10.115	0.017	0.810	0.009
2	5.29	110	1915	46	198	10	9.992	0.015	0.749	0.008
3	4.37	91	2380	36	359	17	10.037	0.014	0.761	0.007
4	3.61	122	2785	105	332	21	9.982	0.014	0.739	0.007
5	3.69	106	2833	30	370	17	9.958	0.015	0.755	0.008
6	3.68	86	2889	38	406	23	10.034	0.017	0.796	0.010
9	4.19	84	4283	85	654	47	0.000	0.000	0.000	0.000
10	4.04	130	4319	93	833	74	16.563	0.119	4.048	0.098
11	4.28	109	3998	82	755	51	16.501	0.113	3.823	0.090
12	3.86	147	4560	99	868	88	16.372	0.113	3.778	0.087
13	4.12	212	4354	119	911	85	16.463	0.117	3.795	0.092
14	4.25	166	4027	187	943	131	16.604	0.129	4.087	0.104
17	4.19	129	4014	173	851	122	0.000	0.000	0.000	0.000
18	3.73	143	5217	230	1036	170	18.201	0.114	3.950	0.088
19	4.05	192	4808	94	652	67	18.087	0.123	3.724	0.088
20	4.64	195	4099	104	688	64	18.106	0.122	3.823	0.091
21	4.75	150	4010	123	818	70	17.982	0.135	3.959	0.104
22	4.19	120	87	299	26	14	18.055	0.128	3.866	0.096
25	4.19	194	3346	168	711	68	0.000	0.000	0.000	0.000
26	4.37	164	4454	246	1114	208	18.485	0.156	4.458	0.132
27	5.04	174	2869	2329	1588	552	18.560	0.162	3.768	0.120
28	4.80	179	3754	357	1011	167	18.511	0.213	4.948	0.201
29	5.35	150	3793	351	1211	205	20.341	0.240	5.527	0.218
30	5.51	156	4453	272	1325	240	21.454	0.273	4.434	0.180
31	4.64	131	4659	266	1192	311	20.141	0.230	3.916	0.158
32	6.11	158	2755	954	885	197	18.581	0.166	3.864	0.118
33	4.96	116	3869	86	634	63	18.377	0.206	4.758	0.197
34	3.91	156	4676	148	586	108	17.625	0.179	3.434	0.131
35	3.71	146	6733	4189	3892	5138	20.005	0.231	4.524	0.182
36	3.94	153	4233	65	649	48	15.995	0.077	3.030	0.058
37	3.62	127	4380	74	663	48	14.780	0.105	2.814	0.068
38	3.18	123	4511	86	683	64	13.744	0.273	3.617	0.104
39	3.93	120	4409	107	807	91	16.616	0.076	3.177	0.058
40	5.13	138	3217	211	767	73	17.085	0.118	3.699	0.094
41	4.53	114	4430	589	1665	581	18.505	0.166	3.950	0.129
42	4.24	133	4810	151	793	116	19.083	0.204	3.433	0.127
43	4.39	132	4722	143	737	98	19.666	0.217	3.701	0.147
44	2.44	147	4270	71	456	49	9.894	0.023	0.691	0.013
45	4.00	132	2561	43	254	19	9.731	0.016	0.658	0.010
46	3.15	97	3184	41	312	19	9.674	0.017	0.622	0.009
47	3.02	124	3350	35	285	18	9.747	0.018	0.687	0.011
48	2.52	123	4079	45	355	28	9.820	0.025	0.670	0.013

A.1. Individual muon-veto system module efficiencies

The trigger efficiency of the individual plastic scintillator modules of the muon-veto system has been determined from data in the 2009-2011 measurement period. By investigation of a certain module and selection of a dataset where any other module triggered the data acquisition, the trigger efficiency of this module could be plotted vs energy (see fig. 2.11). A fit of an error function yielded the following results for the 50% efficiency and sigma values for each individual module (table A.1).

Table A.1.: Trigger probability for all individual muon-veto system modules as determined from an error function fit to data. For details see sec. (2.3.2). The module numbering is consistent with the results given in appendix sec. A and fig. A.1

module	50% efficiency fit value (keV)	50% efficiency fit error (keV)	sigma error function fit value (keV)	sigma error function fit error (keV)
1	13942	290	3300	98
2	11678	333	3588	194
3	4388	227	1106	89
4	6553	320	2051	207
5	7038	299	2158	185
6	6468	326	1937	225
9	6418	640	1940	674
10	6578	643	2021	370
11	6429	547	2064	387
12	5814	668	1961	715
13	5218	918	1015	225
14	8406	614	1774	298
17	5788	784	2175	469
18	6706	817	2087	575
19	9329	763	2729	234
20	8488	702	1374	669
21	7226	790	2277	535
22	9230	167	533	67
25	8337	741	1312	743
26	6685	563	2021	392
27	9396	688	2463	356
28	8428	585	2194	162
29	8447	620	1667	365
30	12468	949	2931	612
31	8130	662	2016	464
32	9674	789	2672	492
33	9973	899	1730	652
34	7348	677	2039	319
35	7196	726	2453	429
36	7204	595	1751	418
37	6641	543	1931	467
38	5767	1104	896	1049
39	7135	754	3477	1057
40	8246	631	2612	671
41	5776	927	2742	688
42	6549	1060	4013	1198
43	8736	1029	3180	942
44	3969	922	1589	873
45	5339	398	1986	270
46	5574	396	1837	438
47	5787	435	1310	270
48	3996	756	1245	807

B. CouchDB example documents

Listing 6.1: JSON document containing all high level analysis results accquired for a specific data run.

```
1
2   {
3       "_id": "run_nk05b000_FID808_kdataOF_v04_02",
4       "_rev": "31-9938643f77ebd1b1e376a9f100cec330",
5       "proc_version": "v04_02",
6       "run": "nk05b000",
7       "bolometer": "FID808",
8       "file": "nk05b000FID808v04.01.NTC.OF.amp.root",
9       "processor": "kanacodewok/kdataExamples/run305processing/
            run_skim_analysis_record_via_DB.py",
10      "submission_date": "2014-09-13 23:56",
11      "file_size_mb": 30.75369930267334,
12      "list_ana_rec": [
13          "chalB FID808 KSeebugKAmpSite11",
14          "slowC FID808 KSeebugKAmpSite12",
15          "chalA FID808 KSeebugKAmpSite11",
16          "ionisA FID808 KSeebugKAmpSite7",
17          "ionisD FID808 KSeebugKAmpSite7",
18          "ionisB FID808 KSeebugKAmpSite7",
19          "slowD FID808 KSeebugKAmpSite7",
20          "slowB FID808 KSeebugKAmpSite7",
21          "slowA FID808 KSeebugKAmpSite7",
22          "ionisC FID808 KSeebugKAmpSite12"
23      ],
24      "n_evts": 52273,
25      "data_partitions": {
26          "nk05b000_009": {
27              "datadb_id": "run_nk05b000_009_kdatascript"
28          },
29          "nk05b000_008": {
30              "datadb_id": "run_nk05b000_008_kdatascript"
31          },
32          "nk05b000_007": {
33              "datadb_id": "run_nk05b000_007_kdatascript"
34          },
35          "nk05b000_003": {
36              "datadb_id": "run_nk05b000_003_kdatascript"
37          },
38          "nk05b000_005": {
39              "datadb_id": "run_nk05b000_005_kdatascript"
40          },
41          "nk05b000_004": {
42              "datadb_id": "run_nk05b000_004_kdatascript"
43          },
44          "nk05b000_010": {
45              "datadb_id": "run_nk05b000_010_kdatascript"
46          },
47          "nk05b000_011": {
48              "datadb_id": "run_nk05b000_011_kdatascript"
49          },
50          "nk05b000_001": {
51              "datadb_id": "run_nk05b000_001_kdatascript"
52          },
53          "nk05b000_000": {
54              "datadb_id": "run_nk05b000_000_kdatascript"
55          },
56          "nk05b000_012": {
57              "datadb_id": "run_nk05b000_012_kdatascript"
58          },
59          "nk05b000_002": {
60              "datadb_id": "run_nk05b000_002_kdatascript"
61          },
62          "nk05b000_006": {
63              "datadb_id": "run_nk05b000_006_kdatascript"
64          }
65      },
66      "proc_rms": { #results of gauss fit to a distirubtion of the RMS of the pretrace
67          "submission_date": "2014-08-28 18:07",
68          "chalB FID808": {
```

```
69              "rms": 1.2797279626612268,
70              "ana_record_name": "KSeebugKAmpSite11",
71              "chi2": 2657.294177454782,
72              "rms_sigma": 0.08032077827469351,
73              "ndf": 31,
74              "rms_error": 0.000500709100768386,
75              "fit_chi2_error": 1
76          },
77          ... # 9 more channels (heatA, 4 ionization channels: once at 100 kHz, once
                 at 500 Hz sampling)
78          "author": "edelweiss",
79          "file": "nk05b000FID808v04.01.amp.root",
80      },
81      "proc_bas_hla": {
82          "submission_date": "2014-09-17 10:01",
83          "processor": "kanacodewok/kdataExamples/update_run_summary.py",
84          "slowB FID808 KSeebugKAmpSite7": {
85              "chi2": 3531.697980272352,
86              "baseline_sigma_error": 0.0043186309761296116,
87              "ndf": 102,
88              "baseline_sigma": 1.0882972892517937
89          },
90          ... # remaing results for the remaining 9 channels
91      },
92      "proc_normalizeTemplateCompression": {
93          "submission_date": "2014-09-10 17:01",
94          "comment": "normalize template_compression",
95          "author": "edelweiss",
96          "file_size_mb": 252.16588687896729,
97          "file": "nk05b000FID808v04.01.NTC.amp.root",
98          "processor": "kanacodewok/kdataExamples/run305processing/
                 run_normalize_template_compression.py"
99      },
100     "proc_normalizeChi2": {
101         "submission_date": "2014-09-14 09:12",
102         "comment": "normalize chi2 with rms of pretrace and template length
103                      for slow and heat channels - original values are copied
104                      to fExtra[5], rms value for nomalization fExtra[6]",
105         "author": "edelweiss",
106         "file_size_mb": 31.392318725585938,
107         "file": "nk05b000FID808v04.01.NTC.OF.RMS.amp.root",
108         "processor": "kanacodewok/kdataExamples/run305processing/run_normalize_chi2.
                 py"
109     },
110     "proc_ampToHLA": {
111         "file_size_mb": 34.21626853942871,
112         "submission_date": "2014-09-17 10:29",
113         "processor": "kanacodewok/kdataExamples/run305processing/run_ampToHLA.py",
114         "file": "nk05b000FID808v04.01.NTC.OF.RMS.hla.root",
115         "author": "edelweiss"
116     },
117     "proc_run_summary": {
118         "data_partitions": {
119             "nk05b000_009": {
120                 "unix_start_time": 1383718137,
121                 "live_time": 3597,
122                 "unix_stop_time": 1383721734,
123                 "stamp_monotonie": false,
124                 "approximate_stamp_monotonie": true,
125                 "evts": [
126                     32041,
127                     36144
128                 ],
129                 "unix_time_monotonie": true
130             },
131             ... # remaing results for the other data partitions
132         },
133         "file_size_mb": 34.21339130401611,
134         "unix_start_time": 1383686037,
135         "channels": {
136             "chalB FID808": 1,
137             "chalA FID808 KSeebugKAmpSite11": {
138                 "index": 0,
139                 "mean_evts": 1305,
```

```
140                    "mean": 346.6841361210264
141                },
142                "ionisD FID808": 5,
143                "chalA FID808": 0,
144                "ionisA FID808": 2,
145                "ionisB FID808": 3,
146                "ionisA FID808 KSeebugKAmpSite7": {
147                    "index": 2,
148                    "mean_evts": 83,
149                    "mean": 369.36993297898624
150                },
151                "slowD FID808": 9,
152                "ionisD FID808 KSeebugKAmpSite7": {
153                    "index": 5,
154                    "mean_evts": 107,
155                    "mean": 363.9184076897452
156                },
157                "slowB FID808 KSeebugKAmpSite7": {
158                    "index": 7,
159                    "mean_evts": 1288,
160                    "mean": 340.7655805030965
161                },
162                "slowA FID808": 6,
163                "slowA FID808 KSeebugKAmpSite7": {
164                    "index": 6,
165                    "mean_evts": 299,
166                    "mean": 344.0679750984728
167                },
168                "list_ana_records": [
169                    "chalA FID808 KSeebugKAmpSite11",
170                    "chalB FID808 KSeebugKAmpSite11",
171                    "ionisA FID808 KSeebugKAmpSite7",
172                    "ionisB FID808 KSeebugKAmpSite7",
173                    "ionisC FID808 KSeebugKAmpSite12",
174                    "ionisD FID808 KSeebugKAmpSite7",
175                    "slowA FID808 KSeebugKAmpSite7",
176                    "slowB FID808 KSeebugKAmpSite7",
177                    "slowC FID808 KSeebugKAmpSite12",
178                    "slowD FID808 KSeebugKAmpSite7"
179                ],
180                "slowB FID808": 7,
181                "ionisB FID808 KSeebugKAmpSite7": {
182                    "index": 3,
183                    "mean_evts": 166,
184                    "mean": 365.17526061276357
185                },
186                "slowC FID808 KSeebugKAmpSite12": {
187                    "index": 8,
188                    "mean_evts": 324,
189                    "mean": 347.1205557364005
190                },
191                "slowC FID808": 8,
192                "ionisC FID808 KSeebugKAmpSite12": {
193                    "index": 4,
194                    "mean_evts": 235,
195                    "mean": 371.5169216724152
196                },
197                "chalB FID808 KSeebugKAmpSite11": {
198                    "index": 1,
199                    "mean_evts": 1298,
200                    "mean": 346.45193260439737
201                },
202                "list_channels": [
203                    "chalA FID808",
204                    "chalB FID808",
205                    "ionisA FID808",
206                    "ionisB FID808",
207                    "ionisC FID808",
208                    "ionisD FID808",
209                    "slowA FID808",
210                    "slowB FID808",
211                    "slowC FID808",
212                    "slowD FID808"
213                ],
```

```
214             "ionisC FID808": 4,
215             "slowD FID808 KSeebugKAmpSite7": {
216                 "index": 9,
217                 "mean_evts": 1282,
218                 "mean": 341.6840109743306
219             }
220         },
221         "rate": 1.022749241317298,
222         "file": "nk05b000FID808v04.01.NTC.OF.RMS..hla.root",
223         "stamp_start": 355873053800,
224         "run": "nk05b000",
225         "stamp_stop": 360324614600,
226         "unix_time_monotonie": false,
227         "author": "Benjamin",
228         "unix_stop_time": 1383730553,
229         "submission_date": "2014-09-16 15:34",
230         "run_condition": "\"calibration gamma\"",
231         "evts": 45497,
232         "live_time": 44485,
233         "approximate_stamp_comment": "True if there is no occurrence of
234                                       stamp - last_stamp > 1 s",
235         "voltages": {
236             "slowA": -1.5,
237             "slowB": 4,
238             "slowC": 1.5,
239             "slowD": -4
240         },
241         "stamp_monotonie": false,
242         "unix_delta_t": 44516,
243         "approximate_stamp_monotonie": true,
244         "processor": "kanacodewok/kdataExamples/run305processing/run_summary.py"
245     },
246     "author": "edelweiss",
247     "proc_bas": {
248         "submission_date": "2014-09-13 14:14:56.956201",
249         "author": "Benjamin",
250         "file": "nk05b000FID808v04.01.amp.root",
251         "chalB FID808": {
252             "chi2": 2431.690158209012,
253             "baseline_sigma": 2.663062535698798,
254             "baseline_sigma_error": 0.005563295789301148,
255             "ana_record_name": "KSeebugKAmpSite11",
256             "ndf": 97
257         },
258         ... # results from remaining channels
259     },
260     "proc_bas_hla_after_chi2": {
261         "submission_date": "2014-09-21 22:25",
262         "processor": "kanacodewok/kdataExamples/update_run_summary.py",
263         "slowB FID808 KSeebugKAmpSite7": {
264             "chi2": 350.7910733929181,
265             "baseline_sigma_error": 0.003599020536313169,
266             "ndf": 60,
267             "baseline_sigma": 0.9177641962001744
268         },
269         ... # results from remaining channels
270
271     },
272     "proc_bas_bana_after_chi2": {
273         "submission_date": "2014-09-21 19:40",
274         "processor": "kanacodewok/kdataExamples/update_run_summary.py"
275         "Bas_Heat_WA": {
276             "chi2": 581.4683309561314,
277             "baseline_sigma_error": 0.0065573350076091885,
278             "baseline_sigma": 1.7356431350076729,
279             "ndf": 183
280         },
281         ... # baseline results for various combined ionization quantities
282     },
283     "proc_magic_point": {
284         "submission_date": "2014-09-17 16:11",
285         "author": "Benjamin",
286         "sum_ion_MP": 26.50690375360404,
287         "sum_ion_Par": [
```

```
288                   0.8332110298222808,
289                   4.471856501692201,
290                   0.8146677617214906,
291                   4.30383342240958
292             ],
293             "weighted_average_Par": [
294                   0.45933114749932863,
295                   4.4197978136730915,
296                   0.7547282895870603,
297                   4.298181392070393935
298             ],
299             "processor": "kanacodewok/kdataExamples/run305processing/update_run_summary.
                   py",
300             "weighted_average_MP": 19.035360003910245
301       },
302       "proc_calib": {
303             "submission_date": "2014-09-16 20:44",
304             "comment": "lin_gain_I corrected over ana_record and voltages (8,12,20V)
305                         via kanacodewok/kdataExamples/run305processing/
                            update_run_summary.py
306                         on 2014-09-16 20:44",
307             "processing_type": "optimal_freq",
308             "run_condition": "calibration gamma",
309             "parameters": {
310                   "log_corr_H": {
311                         "chalB": {
312                               "par3": 0.8836099642087694,
313                               "par2": 1.2244536493628435,
314                               "par1": -0.1307509412085402,
315                               "par0": 1.4513733281818977
316                         },
317                         "chalA": {
318                               "par3": 0.882379789393566,
319                               "par2": 1.2356329277790223,
320                               "par1": -0.13109490139713678,
321                               "par0": 1.4536903200383158
322                         }
323                   },
324                   "lin_gain_H": {
325                         "chalB": -1.1793120363187957,
326                         "chalA": 0.46846800370473757,
327                         "num_evts_B": 1355,
328                         "num_evts_A": 1355
329                   },
330                   "lin_gain_I": {
331                         "slowA": 0.2181220633097068,
332                         "slowB": -0.19206028085760118,
333                         "slowC": -0.3018430433635349,
334                         "slowD": 0.18606777465612695
335                   },
336                   "order_chal": -99,
337                   "order_slow": -99,
338                   "order_ionis": -99,
339                   "frequency_ionis": -99,
340                   "frequency_slow": -99,
341                   "frequency_chal": -99,
342                   "cross_talk": {
343                         "BD": 0,
344                         "AC": 0,
345                         "AB": 0.2779068832063332,
346                         "BA": 0,
347                         "BC": 0,
348                         "CB": 0,
349                         "CA": 0,
350                         "DB": 0,
351                         "DC": 0,
352                         "DA": 0,
353                         "CD": 0.23094481166376576,
354                         "AD": 0
355                   }
356             },
357             "run_date": "2013-11-05 00:00:00",
358             "author": "Benjamin",
359             "_rev": "1-3d03ee990bada2026c5bb170467a5724",
```

```
360          "bolometer": "FID808",
361          "voltage": {
362              "ionisD": -4,
363              "ionisA": -1.5,
364              "ionisB": 4,
365              "ionisC": 1.5
366          },
367          "run_name": "nk05b000",
368          "comment_heat": "Lin heat calibration added on 2014-09-16 15:18 by Benjamin"
             ,
369          "calibration_version": "R305",
370          "_id": "b3c001ca51be72fe8781833f2de386da",
371          "FWHM": {
372              "comment": "Width (1sigma) of the gaussian fit to the 356 keV peak
373                          entire (8V,12V,20V) data sets",
374              "ionisD": 0.5,
375              "ionisA": 0.5,
376              "ionisB": 0.5,
377              "ionisC": 0.5,
378              "slowA": 0.5,
379              "slowB": 6.788220195357564,
380              "slowC": 0.5,
381              "slowD": 5.823235257676522,
382              "chalB": 5.928574960960489,
383              "chalA": 6.240506986108691
384          },
385          "temperature": {
386              "temperature": 68
387          }
388      },
389      "proc_OptimalFrequency": {
390          "submission_date": "",
391          "selected_anaRecord": {
392              "chalB FID808": 11,
393              "slowC FID808": 12,
394              "chalA FID808": 11,
395              "ionisA FID808": 7,
396              "ionisD FID808": 7,
397              "ionisB FID808": 7,
398              "slowD FID808": 7,
399              "slowB FID808": 7,
400              "slowA FID808": 7,
401              "ionisC FID808": 12
402          },
403          "author": "edelweiss",
404          "OF_doc_id": "run_nk05b000_FID808_kdataOF_v04_02",
405          "file": "nk05b000FID808v04.01.NTC.OF.amp.root",
406          "processor": "kanacodewok/kdataExamples/run305processing/
                 run_skim_analysis_record_via_DB.py"
407      }
408 }
```

C. Alternative choices of Butterworth filter parameters

The choice of the best set of Butterworth filter parameters (sec. 3.3.3) within this work is a rather aggressive selection optimized for resolution. It does not take into account any quality criteria other than the χ^2 of the Gauss fit to the baseline amplitude distribution. One might however also check the amplitude spectra at high energy and not only the width of the amplitude estimate for 0 keV events. An investigation of the effect of the different cutoff frequencies of the filtering on the amplitude spectra is shown in fig. C.2.

The 0.25, 2.0 and 15 Hz, 1st order Butterworth filters, produce very similar spectra for the population of well reconstructed physical events from the ^{133}Ba calibration source. The dominant 356 keV photopeak is clearly visible at ~1800 ADU, followed by the compton spectrum below. There is however, a large contribution of unphysical events reconstructed with a huge wrong signed amplitude for the lowest highpass cutoff frequencies as can be seen in fig. C.2. This unphysical event population can be suppressed going from a 1st order Butterworth filter with 0.25 Hz (black) to a 15 Hz highpass cutoff frequency (red).
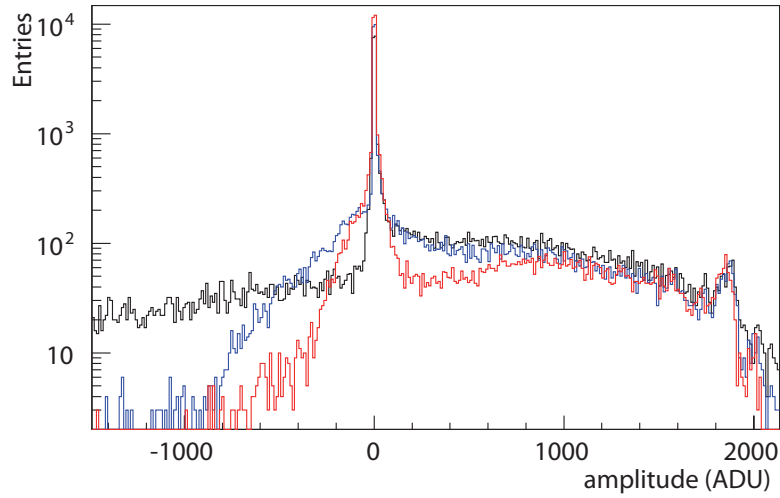
Figure C.2.: Amplitude spectra estimated from filtering with three different highpass cutoff frequencies (0.25 Hz - black, 2.0 Hz - blue, 15 Hz red). Only 1st order Butterworth filters are shown. The dataset is a one day gamma calibration from 5th November 2013 for the hole collecting electrode of detector FID823.

These events also exhibit some very peculiar features in their peak position distribution. Fig. C.3 shows the reconstructed peak position vs. the amplitude of the events. All of these large negative amplitude events have a precise pulse localization far off the central trigger position at only a few possible positions within the trace. A possible way to remove these events from the further analysis is thus to cut on the peak position within the trace and only allow pulses with a sensible timing of ±2.5 ms around the trigger. Resulting spectra (fig. C.4) are almost entirely free of unphysical events. The acceptance of this cut can be estimated from the 356 keV peak which shows that this has only a minor impact.

A further analysis of WIMP search data showed that the unphysical event population at negative energies completely disappeared with this much lower rate of data taking. This is also compatible with the observation that this event population is strongly suppressed
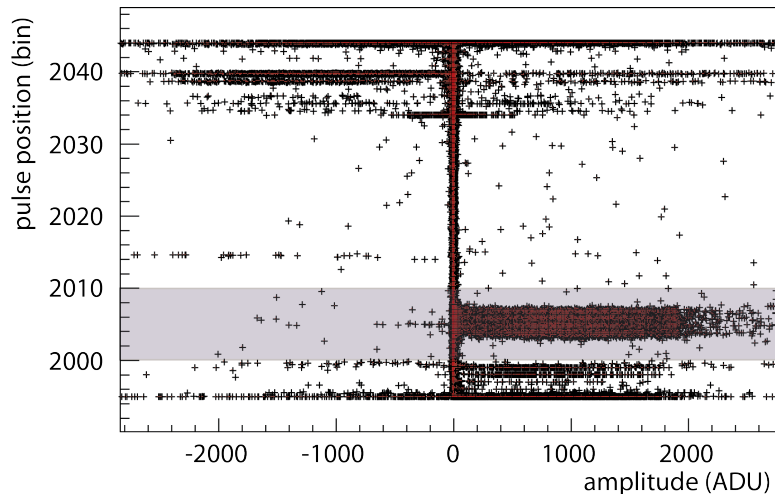

Figure C.3.: Peak position vs amplitude for an analysis with a 0.25 Hz highpass cutoff frequency in black. Amplitude estimates where our minimizer TMinuit reported a successful fit convergence have been marked in red. The dataset is a one day gamma calibration from 5th November 2013 for the hole collecting electrode of FID823. The blue band is positioned around the trigger position and can be used to subtract unphysical technically misreconstructed pulses.
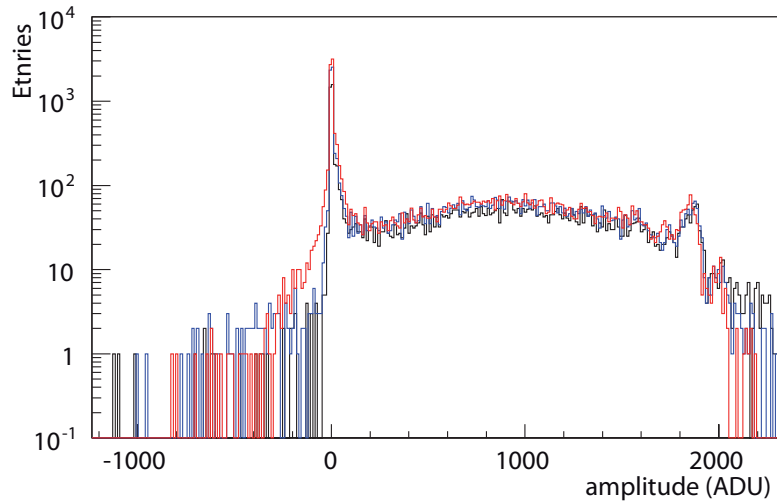
Figure C.4.: Amplitude spectra estimated from filtering with three different highpass cutoff frequencies 0.25 Hz - black, 2.0 Hz - blue, 15 Hz red. A sensible peak position around the trigger position (blue band in fig.C.3 has been required. The dataset is a one day gamma calibration from 5th November 2013 for the hole collecting electrode of detector FID823.

by higher cutoff frequencies. The pulse shaping implied by higher Butterworth cutoff frequencies leads to an effective shortening of the pulses and thus to less pile-up and less misreconstructed pulses.

D. Heat calibration differences between calibration and WIMP search data
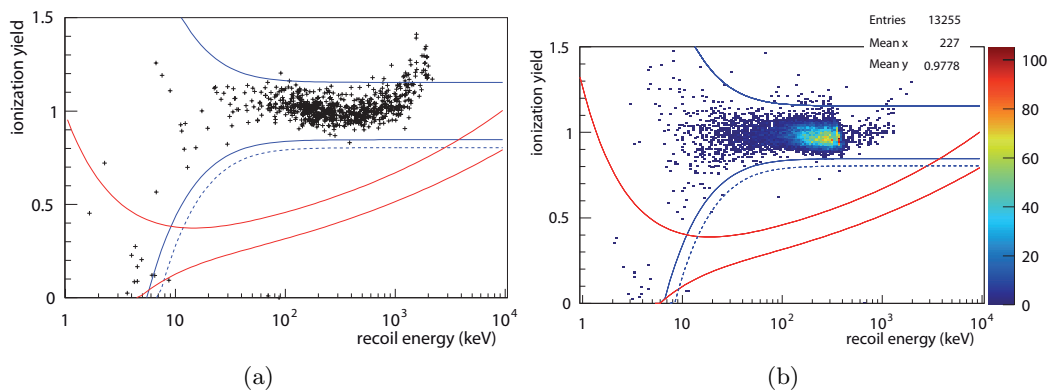

(a) (b)

Figure D.5.: (a) Ionization yield versus recoil energy for the entire WIMP search data at 8V bias for detector FID808. (b) Gamma calibration data at 8V bias for detector FID808. Logarithmic heat calibration has been performed on the WIMP search data. Using this set of coefficients the mean Q-value of the γ calibration data abounts to 0.978 instead of 1.0.

In the processing discussed within this thesis the linear gain of each of the heat channels is determined automatically on a run by run (usually 8-20 h) basis. The non-linearity in the response of the NTDs is corrected after the linear gain has been determined for all datasets. This poses the following problem: The energy spectra between calibration and WIMP search data are quite different with energies up to 384 keV during ^{133}Ba-calibration and energies up to the MeV scale during WIMP search data taking. Consequently the linear gain of the heat channels which are calibrated such that the mean heat energy of a dataset

corresponds to the mean ionization energy of that dataset are different for calibration and WIMP search data. This effect has been visualized in fig. D.5 and fig. D.6 for FID808 and FID823.
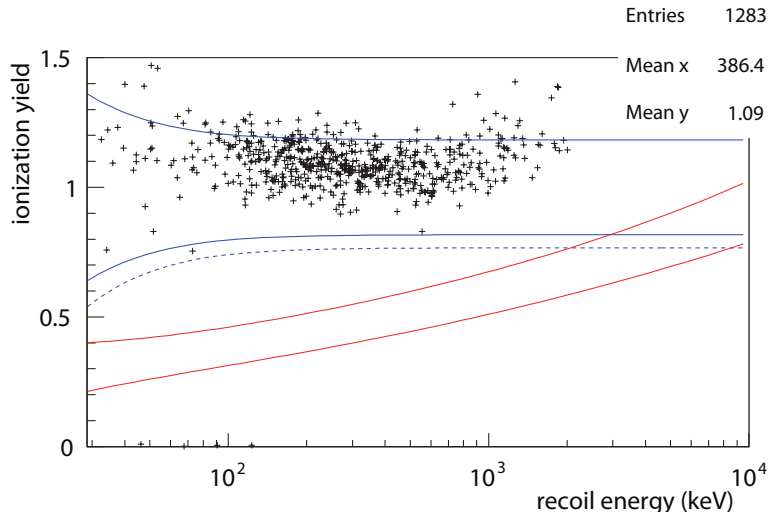

Figure D.6.: Background data at 8V bias for detector FID823. Logarithmic heat calibration has been performed on the gamma calibration data set. There is a similar albeit much stronger evidence for a linear shift in the heat calibration that was not taken into account correctly.

While it should be possible to account for this difference with a single multiplicative factor a slightly different approach has been pursued in this thesis. In the process of the non-linearity correction all heat signals are effectively corrected such that the ionization/heat ratio is equal to one independent of the energy. In order to account for the difference in linear gain the process of non-linearity correction is carried out twice: Once for the γ-calibration data and once for the WIMP search data. Fit results of the piece-wise defined non linearity correction are summarized in table D.2. A larger spread of the parameters is expected for WIMP search data since the parameter estimates have to be performed from less statistics. Compatibility of the shape of the correction has been verified by calibration of WIMP search data with parameter estimates from γ calibration data (fig. D.6)and vice versa (fig.D.5 (b)). The piece wise defined second order polynomial parametrization is certainly only valid up to energies of 600 - 800 keV. For higher energies an additional tilt of the γ population away from unity can be observed. Hence it would be interesting to study different parametrizations of the non linearity that can better describe the data at high energy and maybe even reduce remaining uncertainties at lower energy.

Table D.2.: Best fit values for the parametrization of the heat non linearity according to eq. 3.15. The fit has been done on γ calibration data and WIMP search data independently for FID808 and FID823. For FID818 one of the heat channels is broken and the logarithmic heat correction has only been estimated from γ calibration data for the remaining heat channel.

| detector, channel and datatype	p0	p1	p2	p3
FID808, heatA, γ	1.451	-0.131	1.224	0.884
FID808, heatA, WIMP	1.417	-0.121	1.194	0.654
FID808, heatB, γ	1.454	-0.131	1.236	0.882
FID808, heatB, WIMP	1.421	-0.121	1.381	1.570
FID823, heatA, γ	1.493	-0.139	1.212	0.849
FID823, heatA, WIMP	1.531	-0.142	1.230	0.6767
FID823, heatB, γ	1.463	-0.133	1.190	0.746
FID823, heatB, WIMP	1.484	-0.132	1.147	-1.754
FID818, heatB, γ	1.521	-0.145	1.209	0.724

Enlarging the particle zoo
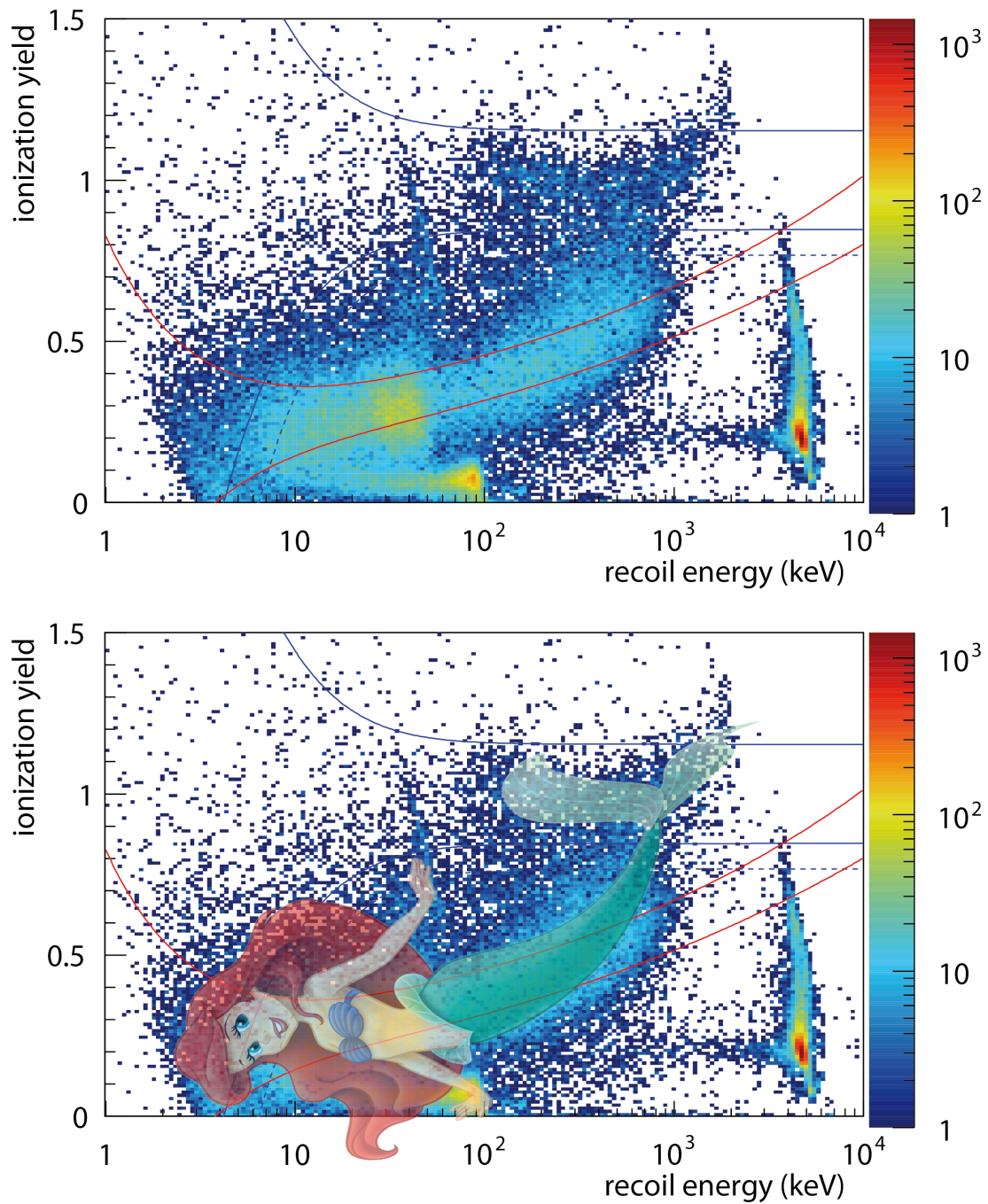
Figure D.7.: Event distribution in ionization yield versus recoil energy for 5 days of surface event calibration data of FID808. Whoever made it this far here is a discovery: Ariel the mermaid, first seen by L. Hehn.

Acknowledgement

The completion of this work has only been possible through the collaboration and help of many people.
First of all I want to thank Prof. Dr. Johannes Blümer, my supervisor, for the possibility to pursue my PhD thesis at the institute of nuclear physics in the EDELWEISS direct dark matter search experiment. Secondly special thanks go to Prof. Dr. Wim de Boer, for accepting to act as co-referee for my thesis. The KSETA courses preparing for exam level particle physics were very much appreciated, as was the concise and effective communication.

I want to express my appreciation and deep gratitude to Dr. Klaus Eitel, whose steady support and suggestions strongly influenced and improved this thesis. There was never a day when Klaus would not make time for a discussion. In addition, to his wealth of knowledge about physics and comma placement, his insights into wine and cheese were very welcome at numerous conferences and several Suisse Fondue and Itialian Tiramisu evenings at the institute. This in turn requires me to thank Dr. Silvia Scorza, not only for making those marvelous Tiramisu, but much more importantly for all the common days fighting to calibrate bolometers with insufficient statistics and catching up with the Lyon analysis. This thesis would not be finished without her contributions. I'm indebted to Dr. Adam Cox for technical advice on software development and for setting the basis for this thesis through his work on the KData software project. I learned a lot on modern software design from his example and his expertise was strongly missed at the institue. All the best to you and your family in the United States of America.

I want to specially thank Prof. Dr Jules Gascon, who was my host during a one month stay at the EDELWEISS dark matter group in Lyon. I will always remember the many hours of discussion which made us (almost) forget dinner. His knowledge of all the kinks of inidividual bolometers is amazing and proved extremely valuable for the comparison of the developed data processing.

Thanks also to Dr. Eric Armengaud and Prof. Dr. Gilles Gerbier for various discussions on the performance of the experiment and on the topics of filtering and data analysis.
A very special thank you goes to Dr. Valentin Kozlov for the installation of numerous computing libraries, for the creation of dozens of accounts and all his work as administrator of the Tesla computing cluster. I very much enjoyed our discussions on physics and the in depth test of the Opel Insignia after the Lyon collaboration meeting.

Finally, I want to express my gratitude to my fellow PhD students for the very enjoyable last four years. Lukas, you were an extremely agreeable office mate, and I have to say thanks again for your and Cecile's efforts in fitting an uncounted number of 356 keV peaks. Thanks to Bernhard for his numerous quests in enlightening my ignorance about the EDELWEISS electronics and to Holger for setting me up with the Geant4 MC simulation code of the EDELWEISS-II experiment. Thanks to all of you and especially to Nadine and Geertje for many enjoyable after work get together.

Last I want to thank my girlfriend who had to endure me during the final month of my thesis, my family, and especially my parents. Not only did they support and finance my studies in Karlsruhe, but their unconditional encouragement was invaluable. While their joy in proofreading incomprehensible physics texts is probably very limited, they still spent a number of evenings reading this manuscript, instead of enjoying an evening at the sea of Gibraltar. I am very grateful for all the love and caring they gave me during my whole life and dedicate this thesis to them.